

STATE OF THE ART CHEMODYNAMICAL SIMULATIONS OF THE  
FIRST METALS IN THE UNIVERSE

DYNA IBRAHIM

CENTRE FOR ASTROPHYSICS RESEARCH  
SCHOOL OF PHYSICS, ASTRONOMY AND MATHEMATICS  
UNIVERSITY OF HERTFORDSHIRE

*Submitted to the University of Hertfordshire in partial fulfilment of the requirements of the degree  
of Doctor of Philosophy.*

SUPERVISORS:

PROF. CHIAKI KOBAYASHI

PROF. JAMES E. GEACH

DR. EMMA C. LAKE

MARCH 2025



*“The universe exists because we are aware of it.”*

*LDR*

# *Abstract*

We live in a Universe filled with an infinite variety of shapes and structures: stars, planets, mountains, clouds, oceans, flowers, — and humans, to name a few. One fascinating truth connects them all: everything is made from the same basic building blocks — atoms. These atoms, composed of subatomic particles, interact to form molecules, the foundation of life as we know it. Yet, perhaps even more remarkable is that many of the atoms within us were forged billions of years ago in the hearts of ancient stars. This thesis is dedicated to understanding the origin of these first elements and how they came to be distributed throughout the cosmos.

To trace the origin of the elements, we must understand how galaxies became chemically enriched in the early Universe. This process, known as chemical enrichment, depends on a complex combination of physical mechanisms, such as stellar nucleosynthesis, gas inflows and outflows, star formation, and most importantly, feedback from stars and active galactic nuclei (AGNs). Among these, stellar feedback, which refers to the energy released from supernova explosions at the end of their lives, remains one of the most uncertain processes in galaxy formation theory. In the first part of this thesis, I focus on constraining its role by implementing and comparing four supernova feedback models: thermal, stochastic, kinetic, and mechanical in state-of-the-art cosmological hydrodynamical simulations.

To test these models, we use two key observational diagnostics: the mass–metallicity relation (MZR) and metallicity gradients, for both stars and gas, across a wide range of galaxy masses and redshifts. These chemical signatures act as fossil records of how efficiently galaxies formed stars, retained metals, and redistributed them over cosmic time. Our analysis shows that mechanical feedback best reproduces the observed MZR and metallicity gradients within galaxies up to redshift  $z = 5$ , providing the most realistic balance between star formation regulation and metal retention.

Having constrained stellar feedback using recent observations, we return to our core question: how were the first elements produced? Observational data from the James Webb Space Telescope (JWST) has revealed surprisingly high elemental abundance ratios in some of the earliest observed galaxies, patterns that were not expected to appear so early in cosmic history. These findings challenge existing theories and raise important questions about the nature of the first stars and galaxies. Several hypotheses have been proposed to explain these enhanced ratios, including enrichment by very massive stars or massive rotating Wolf-Rayet (WR) stars.

To address this, we take the novel step of simulating these scenarios in a fully cosmological context. For the first time, we implement nucleosynthetic yields from rotating Population III stars, specifically, WR stars up to  $120 M_{\odot}$ , faint supernovae, and rotating Pair-Instability Supernovae (PISNe) up to  $300 M_{\odot}$ . These yields are incorporated self-consistently into our simulations to study their impact on the chemical evolution of early galaxies. My results suggest that rotating WR stars are the most likely source of the enhanced nitrogen and other elemental abundances seen in high-redshift galaxies such as GN-z11.

This thesis offers a new perspective on the chemical evolution of the Universe by combining detailed feedback modeling with early Universe nucleosynthesis in a cosmological framework. From constraining feedback models using present-day and high-redshift observations, to exploring the fingerprints of the first stars, this work brings us closer to understanding how the elements that make up our world — and ourselves — came into being.

# Declaration

I declare that no part of this work is being submitted concurrently for another award of the University or any other awarding body or institution. This thesis contains a substantial body of work that has not previously been submitted successfully for an award of the University or any other awarding body or institution.

The following parts of this submission have been published previously and/or undertaken as part of a previous degree or research programme:

1. Chapter 3: Published as [Ibrahim and Kobayashi \(2024\)](#), *Monthly Notices of the Royal Astronomical Society*. [527, 3276](#).
2. Chapter 4: Submitted as [Ibrahim and Kobayashi \(2025\)](#) to *Monthly Notices of the Royal Astronomical Society* and is under review. [arXiv](#).

Except where indicated otherwise in the submission, the submission is my own work and has not previously been submitted successfully for any award.

# *Acknowledgements*

First and foremost, I would like to express my deep gratitude to my supervisor, Professor Chiaki Kobayashi, for her guidance, support, and inspiration throughout my PhD. Her vast knowledge and contagious energy have greatly shaped both this thesis and my overall research journey.

I am sincerely thankful to my secondary supervisors, Professor Jim Geach and Dr. Emma Curtis Lake, for their valuable insights and thoughtful comments, which greatly contributed to improving this work. I would also like to acknowledge Dr. Chris Lovell, my former supervisor, for his support and guidance at the beginning of this project.

I am grateful to the members of the Z group — Dr. Federico Sestito, Dr. Souradeep Bhattacharya, Madeline Silcock, Alice Ferreira, and Dr. Darshan Kakkad — as well as to Dr. Rob Yates, for the engaging discussions and for creating a stimulating research environment.

Thank you to my fellow postgraduates — Soumyadeep Das, Kasia Nowak, Sayan Baig, and Thomas Wocial — and all my UoH PhD colleagues, for the conversations, support, and good company throughout this journey. A special thank you to Chloe Bosomworth — meeting someone who shares the same interests made this experience even more enjoyable.

I gratefully acknowledge the University of Hertfordshire for providing access to its high-performance computing facilities, which were essential for the simulations carried out in this research. I also extend my gratitude to the DiRAC High Performance Computing Facility at Durham University for additional computational support.

Finally, this thesis is dedicated to my family. Thank you for your unconditional support, patience, and love. To my mom, thank you for always being there through both the frustrations and the moments of joy. I'm also thankful to my friends for their steady encouragement along the way. A heartfelt thank you to my uncle, whose passion and curiosity sparked my own.

# Contents

<b>Abstract</b>	<b>I</b>
<b>Acknowledgements</b>	<b>IV</b>
<b>1 Introduction</b>	<b>1</b>
1.1 Cosmic Evolution . . . . .	1
1.1.1 Early Universe . . . . .	1
1.1.2 First stars. . . . .	3
1.1.3 First galaxies . . . . .	5
1.1.4 Galaxy evolution. . . . .	5
1.2 Chemical Evolution. . . . .	8
1.2.1 Metallicity definitions. . . . .	8
1.2.2 Mass-Metallicity Relation . . . . .	9
1.2.3 Metallicity gradients . . . . .	9
1.3 Nucleosynthesis Yields . . . . .	10
1.3.1 Big Bang Nucleosynthesis . . . . .	10
1.3.2 Stellar Nucleosynthesis . . . . .	10
1.3.3 Neutron capture process . . . . .	12
1.4 Simulations of chemical enrichment . . . . .	14
1.4.1 Previous work. . . . .	14
1.4.2 Analytic Models of Enrichment with Feedback . . . . .	16
1.5 Thesis outline . . . . .	17
<b>2 Code and simulations</b>	<b>19</b>
2.1 Cosmological simulations . . . . .	20
2.2 Hydrodynamics . . . . .	22
2.3 Baryon physics . . . . .	24
2.4 Initial Mass Function . . . . .	25
2.5 Cumulative Function . . . . .	26
2.6 Stellar Lifetime . . . . .	27
2.7 Yield Tables. . . . .	28
2.7.1 Yields from AGB and sAGB Stars. . . . .	30
2.7.2 Yields from ccSNe . . . . .	31
2.7.3 Yields from HNe . . . . .	32
2.7.4 Yields from WR stars. . . . .	33
2.7.5 Yields from PISNe . . . . .	34
2.7.6 Other Yield Tables . . . . .	35
2.8 Supernova Feedback . . . . .	35
2.9 Galaxy properties . . . . .	37
2.9.1 Star Formation Rates . . . . .	38
2.9.2 Galaxy Stellar Mass Function. . . . .	39
2.9.3 Galaxy Luminosity Function . . . . .	39
2.9.4 Size-Mass Relation. . . . .	40
2.9.5 Mass-Metallicity Relation . . . . .	41
2.9.6 Metallicity gradients . . . . .	44
2.10 Summary . . . . .	45
<b>3 Mass-Metallicity relations</b>	<b>46</b>

3.1	Introduction . . . . .	46
3.2	Model . . . . .	48
3.2.1	Baryonic Physics . . . . .	49
3.2.2	Stellar Feedback . . . . .	50
3.2.3	Initial Conditions . . . . .	53
3.2.4	Fiducial parameters . . . . .	53
3.3	Results . . . . .	54
3.3.1	Density and Temperature evolution . . . . .	54
3.3.2	Gas-phase diagram . . . . .	55
3.3.3	Cosmic Star Formation Rate . . . . .	57
3.3.4	Redshift evolution . . . . .	58
3.3.5	Mass–Metallicity Relations . . . . .	60
3.4	Conclusions . . . . .	66
<b>4</b>	<b>Metallicity gradients</b>	<b>68</b>
4.1	Introduction . . . . .	68
4.2	Methods . . . . .	71
4.2.1	Our Model . . . . .	71
4.2.2	Galaxy sample . . . . .	72
4.2.3	Metallicity gradients . . . . .	73
4.3	Results . . . . .	74
4.3.1	Metallicity maps . . . . .	74
4.3.2	Radial stellar metallicity profiles . . . . .	79
4.3.3	Radial gas-phase metallicity profiles . . . . .	80
4.3.4	Present-day gradients vs mass . . . . .	82
4.4	Redshift Evolution . . . . .	84
4.4.1	Stellar Gradients vs Mass . . . . .	84
4.4.2	Gas-phase Gradients vs Mass . . . . .	86
4.4.3	Time evolution of metallicity gradient . . . . .	87
4.5	Galaxy type dependence . . . . .	92
4.6	Discussion . . . . .	93
4.6.1	Present-day gradients . . . . .	93
4.6.2	Overall evolution of gradients . . . . .	96
4.6.3	Gradient evolution in an individual galaxy . . . . .	97
4.7	Conclusions . . . . .	99
<b>5</b>	<b>Nucleosynthesis yields from Population III stars</b>	<b>102</b>
5.1	Introduction . . . . .	102
5.2	Method . . . . .	103
5.2.1	Model . . . . .	104
5.2.2	Pop III nucleosynthesis yields . . . . .	104
5.2.3	Pop III IMF . . . . .	105
5.3	Results . . . . .	105
5.3.1	N/O . . . . .	105
5.3.2	Other elemental abundance ratios . . . . .	107
5.3.3	Pop III IMF dependence . . . . .	109
5.4	Conclusions . . . . .	115
<b>6</b>	<b>Conclusions</b>	<b>116</b>

6.1 Future work . . . . . 118

Appendix – MZR

A.1 Star formation rates . . . . . 120  
 A.2 Stellar Metallicities. . . . . 122  
 A.3 Age dependence of the stellar MZR . . . . . 124

Appendix – Metallicity gradients

B.1 Kinematics . . . . . 126  
 B.2 Star Formation Main Sequence . . . . . 128  
 B.3 Tracking individual galaxies . . . . . 130

Appendix – Computation time

C.1 Resolution convergence tests . . . . . 135

Part Bibliography

# List of Figures

1.1	Schematic figure of the cosmic history of the universe. . . . .	2
1.2	Schematic figure of chemical enrichment from different types of stars. . . . .	11
2.1	Projected density map of our cosmological simulations in $25 h^{-1} \text{Mpc}^3$ box with our fiducial mechanical feedback model, at $z = 0$ . High density regions are shown in green. . . . .	21
2.2	Diagram summarizing the methods used in our hydrodynamical simulation based on the GADGET-3 code. . . . .	22
2.3	The contribution of the nucleosynthesis yields cumulative function from the previous timestep with $M=tm2$ to the current timestep with $M=tm1$ , as a function of the synchronised individual timestep $dti$ (left panel) and Nitrogen fraction per unit stellar mass (right panel) . . . . .	26
2.4	The lifetime of stars depending on the main sequence metallicity. . . . .	27
2.5	Upper table: Mass ranges of different stellar yields from our table “SN2SAGBYIELD” used in the cosmological simulations. Lower table: Mass ranges of stellar yields including our new tables “WRSN2SAGBYIELD” and “PISNYIELD”. . . . .	29
2.6	Mass fractions relative to Fe, normalized by the solar ratio, as a function of atomic number for AGB and sAGB stars. We compare stars with different progenitor masses: $M = 1M_{\odot}$ (blue), $M = 6M_{\odot}$ (orange), and $M = 7.5M_{\odot}$ (green). Each panel corresponds to a different metallicity $Z$ . Note that AGB yields for Fe are not available at $Z = 0$ . . . . .	30
2.7	Same as Figure 2.6, but showing yields from ccSN used in C5 (solid lines, without WR), ccSN used in C6 (dashed lines, with WR) and faint supernovae (thick solid lines at $Z = 0$ ). We compare stars with progenitor mass $M = 20M_{\odot}$ (blue) and $30M_{\odot}$ (orange). . . . .	31
2.8	Same as Figure 2.6, but showing yields from HNe used in C5 (solid lines), HNe used in C6 (dashed lines). We compare stars with progenitor mass $M = 20M_{\odot}$ (blue), $30M_{\odot}$ (orange) and $40M_{\odot}$ (green). . . . .	33
2.9	Same as Figure 2.6, but showing yields from WR stars from our WRSN2SAGBYIELD table (solid lines) and PISNYIELD table (thick solid lines, at $Z = 0$ ). We compare stars with progenitor mass $M = 60M_{\odot}$ (blue), $80M_{\odot}$ (orange) and $120M_{\odot}$ (green). . . . .	34

- 2.10 Mass fraction relative to Fe, normalized by the solar ratio, as a function of atomic number for PISN stars. We compare stars with different progenitor masses:  $M = 160M_{\odot}$  (blue),  $M = 180M_{\odot}$  (orange), and  $M = 240M_{\odot}$  (green) and  $M = 280M_{\odot}$  (red). Each panel corresponds to a different model: non-rotating stars (left), non-magnetic rotating stars (middle), and magnetic rotating stars (right). . . . . 35
- 2.11 Schematic representation of the four supernova feedback models employed in this study. . . . . 36
- 2.12 Cosmic star formation rate history of our  $25 h^{-1}$  Mpc simulations with different feedback models: thermal (blue), stochastic (orange), kinetic (green), and mechanical (red). Observational data are taken from [Madau and Dickinson \(2014\)](#), grey cross), [\(Driver et al., 2018\)](#), pink plus), and [\(Leroy et al., 2024\)](#), purple line). 38
- 2.13 Evolution of the galaxy stellar mass function from  $z = 5$  to  $z = 0.7$  in a  $25 h^{-1}$  Mpc box volume. The solid lines are our simulations with the thermal (blue), stochastic (orange), mechanical (red) feedback models. The dashed lines are observational data from [Baldry et al. \(2012\)](#); [Tomczak et al. \(2014\)](#); [McLeod et al. \(2021\)](#); [Navarro and White \(1993\)](#). . . . . 39
- 2.14 Evolution of the rest-frame V-band luminosity function from  $z = 5$  to  $z = 0.7$  in a  $25 h^{-1}$  Mpc box volume. The solid lines are our simulations with the thermal (blue), stochastic (orange), mechanical (red) feedback models. The purple dashed line is observational data from [Marchesini et al. \(2012\)](#) . . . . . 40
- 2.15 Evolution of the galaxy size–mass relation in a  $25 h^{-1}$  Mpc box. The dots show individual simulated galaxies at each redshift, color-coded by feedback model (thermal: blue; stochastic: orange; mechanical: red), the solid lines represent the median for the corresponding model. Dashed lines are observational data from [van der Wel et al. \(2014\)](#), [Mowla et al. \(2019\)](#), and [Ward et al. \(2024\)](#). Panels from left to right show  $z=0.7, 2, 3$ , and  $5$ . . . . . 40
- 2.16 Top panel: Redshift evolution of the luminosity-weighted stellar MZR of galaxies for the thermal (blue, solid), stochastic (orange, dash-dotted), kinetic (green, dashed), and mechanical (red, dash-dotted) feedback models in a  $25 h^{-1}$  Mpc box volume. The solid lines are for the medians, and the shaded areas show the  $1\sigma$  scatter of individual galaxies. Observational data are taken from [Gallazzi et al. \(2014,  \$z = 0.7\$ \)](#), and [Cullen et al. \(2019,  \$z = 3\$ , with +0.5 dex shift for \[O/Fe\]\)](#). Bottom panel is the same but for the SFR-weighted gas-phase MZR. Observational data (dotted with different symbols) are from [Maiolino et al. \(2008,  \$z \sim 0.7\$ \)](#), [Savaglio et al. \(2005,  \$z \sim 0.4 - 1\$ \)](#), [Guo et al. \(2016,  \$z \sim 0.5 - 0.7\$ \)](#), [Sanders et al. \(2021,  \$z \sim 2 - 3\$ \)](#), [Li et al. \(2022,  \$z \sim 2 - 3\$ \)](#), and [Curti et al. \(2024b,  \$z \sim 3 - 6\$ \)](#). . . . . 42

2.17	SFR-weighted gas-phase metallicity gradient as a function of redshift, for all galaxies in our simulations with the thermal (blue solid line), kinetic (green dashed), stochastic (orange dash-dotted), and mechanical (red dense dash-dotted) feedback models, in a $25 h^{-1}$ Mpc box volume. The shaded areas are $1\sigma$ scatter of the individual galaxies. The symbols are observational data from Yuan et al. (2011, black cross) using AO-assisted spectroscopy OSIRIS on Keck II on a face-on spiral galaxy at $z \sim 1.5$ , Jones et al. (2013, magenta diamonds) using AO-assisted spectroscopy OSIRIS on Keck on gravitationally lensed systems, and Curti et al. (2020a, cyan triangle) using KMOS KLEVER survey on 42 gravitationally lensed galaxies. . . . .	44
3.1	Density evolution of our cosmological simulations in $10 h^{-1}$ Mpc <sup>3</sup> box for our four feedback (FB) models: thermal, kinetic, stochastic, and mechanical in the 1st, 2nd, 3rd, and 4th columns, respectively, with the fiducial parameters in section 3.2.4. We show projected gas density at $z = 0, z = 1$ , and $z = 2$ in the top, middle and bottom rows, respectively. . . . .	55
3.2	The same as Figure 3.1 but for temperature maps of our cosmological simulations for the four feedback models at $z = 0$ . . . . .	56
3.3	The same as Figure 3.1 but for the gas-phase metallicity, $\log Z_g/Z_\odot$ , in our cosmological simulations for the four feedback models at $z = 0$ . . . . .	56
3.4	Density-temperature phase space diagrams for thermal (panel a), kinetic (panel b), stochastic (panel c), and mechanical (panel d) feedback models. Each panel shows the temperature as a function of hydrogen number density with the colour contour indicating the number density of the gas particles in the entire simulation volume at $z = 0$ . . . . .	57
3.5	The same as Figure 3.4 for $z = 1$ . . . . .	57
3.6	Cosmic star formation rate history of our $10 h^{-1}$ Mpc simulations with our different feedback models: thermal (blue), stochastic (orange), kinetic (green), and mechanical (red). The observational data are taken from Madau and Dickinson (2014, grey cross) and Driver et al. (2018, pink plus). . . . .	58
3.7	(a) Stellar mass density as a function of redshift, comparing to the observational data (grey square) taken from Madau and Dickinson (2014). (b) Cosmic gas fraction $f_g \equiv M_g/(M_g + M_* + M_{\text{BH}})$ for all gas (solid lines), hot gas ( $T > 10^6$ K, dashed lines), and cold gas ( $T < 1.5 \times 10^4$ K, dotted lines). (c) Cosmic stellar metallicity evolution. (d) Gas-phase oxygen abundances evolution for all gas (solid lines), ISM (dotted lines), and IGM (dashed lines). In all panels, the thermal, stochastic, kinetic, and mechanical feedbacks are always shown in blue, orange, green, and red, respectively. . . . .	58

- 3.8 Stellar mass–metallicity relations with thermal (blue), stochastic (orange), kinetic (green), and mechanical (red) feedback models. The stellar metallicity is V-band luminosity-weighted. The lines are for medians and the shaded areas show the  $1\sigma$  scatter. The observational data are taken from [Zahid et al. \(2017\)](#), (grey dashed line, with  $1\sigma$  scatter). . . . . 61
- 3.9 Gas-phase mass–metallicity relations with thermal (blue; triangles), stochastic (orange; diamonds), kinetic (green; squares), and mechanical (red; circles) feedback models. The SFR-weighted, gas-phase oxygen abundances of galaxies (number ratios relative to hydrogen) are shown. The observational data (grey dashed line) are from [Tremonti et al. \(2004\)](#) with the ‘KD02’ scale in [Kewley and Ellison \(2008\)](#), and from [Curti et al. \(2020b\)](#), (brown dashed line). . . . . 62
- 3.10 Evolution of the luminosity-weighted stellar MZR with thermal (blue), stochastic (orange), kinetic (green), and mechanical (red) feedback models. The solid lines are for the medians, and the shaded areas show the  $1\sigma$  scatter. Observational data are taken from [Zahid et al. \(2017,  \$z = 0\$ \)](#), [Gallazzi et al. \(2005,  \$z = 0\$ \)](#), [Gallazzi et al. \(2014,  \$z = 1.2\$ \)](#), and [Cullen et al. \(2019,  \$z = 3\$ , with +0.5 dex shift for \[O/Fe\]\)](#). 63
- 3.11 Evolution of the SFR-weighted gas-phase MZR with thermal (blue; triangles), stochastic (orange; diamonds), kinetic (green; squares), and mechanical (red; circles) feedback models. The solid lines indicate the linear fit to the individual galaxies shown by the symbols with the same colour. Observational data are from [Tremonti et al. 2004 \( \$z = 0\$ \)](#) with the KD02 scale in [Kewley and Ellison \(2008,  \$z = 0\$ \)](#), [Curti et al. \(2020b,  \$z = 0\$ \)](#), [Yabe et al. \(2012,  \$z = 1.4\$ \)](#), [Sanders et al. \(2021,  \$z \sim 2-3\$ \)](#), [Li et al. \(2022,  \$z \sim 2-3\$ \)](#). . . . . 64
- 3.12 Evolution of the young stellar MZR (solid lines) comparing to the gas-phase metallicities (symbols, the same as in Fig. 3.11). The solid lines are the medians of the luminosity-weighted stellar MZR for stars younger than 0.1 Gyr, and the shaded areas show the  $1\sigma$  scatter. . . . . 64
- 4.1 Stellar (blue) and gas (orange) distribution for the same massive galaxy A ( $M_* \sim 10^{11} M_\odot$ ) with the thermal, stochastic and mechanical feedback models (1st, 2nd and 3rd panels, respectively). The grey solid and dashed circles represent  $1R_e$  and  $2R_e$ , respectively. Panels (b) and (c) show the stellar and gas-phase metallicity distributions, respectively, along the  $x$  axis. The solid blue and orange lines are the median metallicity in each bin of  $x$  (see main text for details) for stellar and gas-phase metallicity, respectively. Panels (d) and (e) are the same as panels (b) and (c) but along the  $y$  axis. . . . . 74

- 4.2 (a) V-band luminosity-weighted (solid lines) and mass-weighted (dashed lines) stellar metallicity profiles for Galaxy A at  $z = 0.7$  for the thermal (blue), stochastic (orange) and mechanical (red) feedback models. We show the profiles with measurable gradients along the total projected radius  $\alpha$ , the inner gradient  $\alpha_{*,\text{in}}$  within  $R_e = 4.59$  kpc, and the outer gradient  $\alpha_{*,\text{out}}$  between  $R_e$  and  $2R_e$  (vertical dashed grey lines). (b) SFR-weighted (solid lines) and mass-weighted (dashed lines) gas-phase metallicity profiles for Galaxy A at  $z = 0.7$  with measurable gradients  $\alpha_{\text{g,in}}$  in 8 kpc (vertical dashed grey lines). The dotted lines show the best linear regression fits. . . . . 76
- 4.3 Same as Fig. 4.1 but for an intermediate-mass galaxy B ( $M_* \sim 10^{10} M_\odot$ ). . . . . 77
- 4.4 Same as Figure 4.2, but for Galaxy B with  $R_e = 3.74$  kpc. . . . . 78
- 4.5 (a) V-band luminosity-weighted stellar metallicity profiles for lower-mass galaxies ( $M_* < 10^{10} M_\odot$ ) with measurable gradients at  $z = 0.7$  in our simulations. The solid lines are the median for the thermal (blue), stochastic (orange), and mechanical (red) feedback models. The shaded areas are  $1\sigma$  scatter. The dotted lines are the best linear fit of the medians for a single slope  $\alpha_*$ , the inner gradient  $\alpha_{*,\text{in}}$  within  $1R_e$ , and the outer gradient  $\alpha_{*,\text{out}}$  between  $1R_e$  and  $2R_e$ . The vertical grey solid lines represent  $1R_e$  and  $2R_e$ . (b) The same as (a), but for SFR-weighted gas-phase oxygen abundance profiles. The medians are fitted with a single slope  $\alpha_{\text{g,in}}$  (dotted line) within 8kpc, indicated by the vertical grey solid line. . . . . 80
- 4.6 Same as Figure 4.5, but for massive galaxies with  $M_* > 10^{10} M_\odot$ . . . . . 81
- 4.7 *Top panel:* V-band luminosity weighted stellar metallicity gradients measured within  $1.5 R_e$  as a function of the galaxy's total stellar mass at  $z = 0$  in our simulation with the mechanical feedback model (red circles). The red line shows the median value at a given mass. Observational data are taken from the SAURON survey (Kuntschner et al. 2010, black squares), the CALIFA survey (Sánchez-Blázquez et al. 2014, black triangles; and González Delgado et al. 2015, black dashed line), and from the ATLAS<sup>3D</sup> survey (grey shading, Kuntschner et al., priv. comm.). *Bottom panel:* Same, but for the SFR-weighted gas-phase oxygen abundance gradients measured within 8 kpc. Observational data are taken from Sánchez-Menguiano et al. (2016, CALIFA, black square), Poetrodjojo et al. (2018, SAMI, black circle) and Khoram and Belfiore (2024, MaNGA, black line). 83

- 4.8 Upper panels: The V-band luminosity weighted stellar metallicity inner gradients  $\alpha_{*,\text{in}}$  within  $1.5 R_e$  as a function of the galaxy total stellar mass at  $z = 0.7$  (a),  $z = 2$  (b), and  $z = 5$  (c) for all galaxies in our simulations with the thermal (blue), stochastic (orange), and mechanical (red) feedback models (see main text). The solid lines are the median at a given mass. The dashed lines are the metallicity gradients  $\alpha_*$  along the total projected radius. The lower panels (d, e, and f) are the same, but for the SFR-weighted gas-phase oxygen abundance gradients  $\alpha_g$  within 8 kpc (solid lines) and total gradients (dashed lines). The distributions of simulated galaxies are shown with hexagonally binned density maps at  $z = 0.7$  and 2, while with scattered points at  $z = 5$ , with the same colour. The black/gray symbols are observational data from Carton et al. (2018) at  $0.5 < z < 0.8$  (circles), Simons et al. (2021) at  $0.6 < z < 1.5$  and  $1.2 < z < 2.6$  (squares), Curti et al. (2020b) at  $1.2 < z < 2.5$  (triangles), and Ju et al. (2024) at  $0.5 < z < 1.7$  (diamonds). 84
- 4.9 *Top panel:* SFR-weighted gas-phase metallicity gradient in [dex/kpc] as a function of redshift for all galaxies in our simulations with the thermal (blue solid line), stochastic (orange), and mechanical (red) feedback models. The shaded areas are  $1\sigma$  scatter. The black/gray symbols are observational data from Yuan et al. (2011, circle) using AO-assisted spectroscopy OSIRIS on Keck II on a face-on spiral galaxy at  $z \sim 1.5$ , Jones et al. (2013, Square) using AO-assisted spectroscopy OSIRIS on Keck on gravitationally lensed systems, Curti et al. (2020a, right-pointing triangles) using KMOS KLEVER survey on 42 gravitationally lensed galaxies, Wang et al. (2022, upward-pointing triangle) with NIRISS, early result from GLASS-JWST and Ju et al. (2024, diamonds) with the JWST/NIRSpec Slit-stepping Spectroscopy. *Bottom panel:* Same as the top panel but for massive galaxies ( $M_* > 10^{10} M_\odot$ ) only. . . . . 88
- 4.10 Same as Figure 4.9, but in [dex/ $R_e$ ] measured within  $2.5 R_e$ . . . . . 89
- 4.11 *Top panel:* V-band luminosity weighted stellar metallicity gradients measured within  $1.5 R_e$  as a function of redshift for all galaxies in our simulations with the thermal (blue), stochastic (orange), and mechanical (red) feedback models. Gradients are measured for each galaxy, normalized by the effective radius  $R_e$ , and then the median is calculated at a given redshift (solid lines). The shaded areas are  $1\sigma$  scatter. Observational data are taken from Kobayashi and Arimoto (1999, black point with error bar), the SAURON survey (Kuntschner et al. (2010, light gray square with error bar); and the ATLAS<sup>3D</sup> survey (Kuntschner et al., priv. comm; gray diamond with error bar). *Bottom panel:* Same as top panel but for massive galaxies with  $M_* > 10^{10} M_\odot$ . . . . . 91

- 4.12 The SFR-weighted gas-phase oxygen abundance gradients as a function of redshift for all galaxies in our simulations with the thermal (blue, top panel), stochastic (orange, middle panel), and mechanical (red, bottom panel) feedback models. The dashed and dotted lines show the medians of earlier-type galaxies ( $\Delta\text{SFMS} < -0.5$ ) and later-type galaxies ( $\Delta\text{SFMS} > -0.5$ ), respectively. The shaded areas are  $1\sigma$  scatter. . . . . 92
- 4.13 Radial gas number density profiles for galaxies grouped by different bins of gas-phase metallicity gradients  $\alpha_{\text{g,in}}$  within 8 kpc. Each line represents the median profile within a given gradient range. The shaded area is the  $1\sigma$  scatter. Results are shown for  $z = 0$  with the mechanical feedback. . . . . 95
- 4.14 Same as Fig. 4.13, but for radial star formation rate profiles. . . . . 95
- 4.15 Evolution of the SFR-weighted gas-phase metallicity profile of Galaxy A with the mechanical feedback, at redshifts  $z = 0.7, 2, 3,$  and  $5$ . The slope of each profile,  $\alpha_{\text{g,in}}$  [dex/kpc], is obtained within 8 kpc and is listed in the legend. . . . . 98
- 4.16 Same as Fig. 4.15 but for the luminosity-weighted stellar metallicity profile of Galaxy A. The slope of each profile  $\alpha_{*,\text{in}}$  [dex/kpc], is obtained within  $1.5 R_e$  (at each redshift) and is listed in the legend. . . . . 98
- 5.1 The evolution of SFR-weighted gas-phase N/O abundance ratios compared to oxygen abundances with Pop III nucleosynthesis yields from WR (circles), WR and PISN (triangles) and without (cross), including faint supernovae. We compare with observational data of from Cameron et al. (2023, GNz-11 ( $z = 10.6$ ); pink area), Isobe et al. (2023, orange circle), Marques-Chaves et al. (2024, purple diamond), Topping et al. (2024a, cyan triangle), Topping et al. (2024b, magenta triangle), Curti et al. (2024a, red circle), Castellano et al. (2024a, brown star), Schaerer et al. (2024a, yellow square), and Dopita et al. (2016, gray line). . . . . 106
- 5.2 Same as Figure 5.1, but for (A): carbon to oxygen ratio, (B): neon to oxygen ratio, (C): argon to oxygen ratio, (D): sulfur to oxygen ratio. Observational data are from Marques-Chaves et al. (2024, purple), Isobe et al. (2023, orange), Topping et al. (2024a, cyan), Rogers et al. (2024, yellow), D'Eugenio et al. (2024, magenta symbol), Cameron et al. (2023, pink area), and Arellano-Córdova et al. (2024, orange area;  $0.02 < z < 0.18$ ). . . . . 108
- 5.3 Redshift evolution of the SFR in our cosmological simulations with thermal FB in a  $(10h^{-1} \text{ Mpc})^3$  box. We compare SFRs with various Pop III IMF slopes ( $x_{\text{imf}3} = 0.3, 1.3, 2.3$ ; shown in blue, pink, yellow, respectively) with yields from WR and PISN (C6; solid lines) and without (C5; dashed lines). The left panel corresponds to the Pop III IMF mass range  $M_* = [0.01, 120]M_\odot$ , and the right panel to  $M_* = [15, 300]M_\odot$ . Observational data are taken from Madau and Dickinson (2014, gray cross symbols) and Driver et al. (2018, pink plus symbols). . . . . 110

- 5.4 Same as Figure 5.3, but showing the impact of the Pop III initial metallicity threshold  $Z_{max3}$  on the cosmic SFR for C6, with a fixed Pop III IMF slope of  $x_{imf3} = 1.3$ . . . . . 111
- 5.5 Upper panels: Luminosity-weighted stellar MZR in our cosmological simulations at  $z = 0$ , within a  $(10h^{-1} \text{ Mpc})^3$  box. We compare MZR for different Pop III IMF slopes ( $x_{imf3} = 0.3, 1.3, 2.3$ , in blue, pink, and yellow, respectively) with C5 (dashed lines) and C6 (solid lines) models. The left panel corresponds to an initial mass range of  $M_* = [0.01, 120]M_\odot$ , and the right panel to  $M_* = [15, 300]M_\odot$ . Observational data are taken from Zahid et al. (2017, gray line). Bottom panels: Same as the upper panels, but for SFR-weighted gas-phase MZR. . . . . 113
- 5.6 Same as Figure 5.5, but with a fixed  $x_{imf3} = 1.3$ , for various  $Z_{max3}$ . . . . . 114
- A.1 Cosmic SFRs for thermal, kinetic, stochastic and mechanical feedback models in panels (a), (b), (c) and (d) respectively. For each model we explore a wide range of feedback parameter  $f$ . The grey line in panel (a) shows a run where supernova energy feedback is completely switched off (while retaining chemical feedback). The grey cross and magenta plus are observational data taken from Madau and Dickinson (2014) and Driver et al. (2018), respectively, from far UV to mid IR. 120
- A.2 Stellar MZR for thermal, kinetic, stochastic and mechanical feedback models are shown in panels (a), (b), (c) and (d), respectively. For the thermal feedback (panel (a)), we compare luminosity-weighted metallicity (blue) with mass-weighted metallicity (orange). For panels (b), (c) and (d), we explore a wide range of feedback parameters  $f$ , at  $z = 0$ . The black dashed line and shaded are optical observational data taken from Zahid et al. (2017) of star-forming galaxies in the SDSS at  $z = 0$ . . . . . 123
- A.3 Evolution of luminosity-weighted stellar MZR of galaxies with different ages of star particles:  $< 0.1$  (blue),  $0.1-1$  (orange),  $1-2$  (green), and  $5-6$  Gyr (red), comparing to the gas-phase metallicities of galaxies (grey points). From top panel to bottom, the figure shows thermal, stochastic, kinetic and mechanical feedback models. The solid lines are for medians, and the shaded areas show the  $1\sigma$  scatter. The dashed lines represent the same observational data for the gas-phase MZR as in Fig. 3.11. . . . . 124

B.1	Stellar kinematic maps of a massive galaxy A with the thermal, stochastic, and mechanical feedback simulations in the top, middle, and bottom rows, respectively. Each panel shows a projection along 20 kpc in the x and y axis for a map of the line of sight velocity $\langle V_z \rangle$ (first column), velocity dispersion $\sigma_z$ (second column), radial velocity $V_{xy} = \sqrt{\langle V_x \rangle^2 + \langle V_y \rangle^2}$ (third column), the angle $\phi = \tan^{-1}(\langle V_y \rangle / \langle V_x \rangle)$ showing the direction of motion in the plane (fourth column). . . . .	127
B.2	Same as Figure B.1 but for gas kinematic maps of Galaxy A. . . . .	127
B.3	The same stellar kinematic maps as Figure B.1 but for an intermediate-mass galaxy B. . . . .	128
B.4	The same gas kinematic maps as Figure B.1 but for Galaxy B. . . . .	129
B.5	<i>Left:</i> SFMS for all galaxies in our simulations with the thermal (blue), stochastic (orange), and mechanical (red) feedback models at $z = 0.7$ . The solid lines show the best fit to the data. The dotted lines are the perpendicular shift of the solid lines by $-0.5$ dex. The square and diamond symbols represent galaxy A and B in each model. <i>Right:</i> Distribution of the perpendicular distances from the SFMS ( $\Delta$ SFMS) in our simulations with the thermal (blue), stochastic (orange), and mechanical (red) feedback models. . . . .	129
B.6	Same as Figure 4.8, but for the thermal feedback only, colour-mapped by $\Delta$ SFMS for ETGs (red) and LTGs (blue). . . . .	131
B.7	Same as Figure B.6, but for the stochastic feedback. . . . .	131
B.8	Same as Figure B.6, but for the mechanical feedback. . . . .	131
B.9	Formation history of Galaxy A across cosmic time with the mechanical feedback. Each panel shows a projected view of the simulation volume in a box of $4 \times 3$ Mpc <sup>2</sup> in side, with gas particles in orange, star particles in blue, and the central Friends-of-Friends group marked with a black cross. The white circle shows the selected descendant of Galaxy A. The panels are ordered chronologically from top left ( $z = 5$ ) to bottom right ( $z = 0$ ). . . . .	132
C.1	Time taken (in minutes) to complete simulation runs as a function of the number of CPU cores, for different box sizes and resolutions on UHHPC (solid lines) and DiRAC HPC (dashed lines) systems. The 10mpc96 and 10mpc128 labels indicate the simulation box size (10 Mpc) and grid resolution ( $96^3$ and $128^3$ particles, respectively). . . . .	133
C.2	Resolution convergence tests. <b>**Left:**</b> Cosmic star-formation history for 10 Mpc boxes at three resolutions ( $96^3$ , $128^3$ , and $192^3$ ) compared with observational compilations (Madau and Dickinson, 2014; Driver et al., 2018). <b>**Right:**</b> Stellar mass–metallicity relation for the same runs at $z = 0$ , compared with Zahid et al. (2017). . . . .	136

# List of Tables

- |     |   |     |
|-----|---|-----|
| 3.1 | Cosmic stellar mass density $\log \rho_*$ , gas fraction $f_g$ (for all gas, hot gas, and cold gas), stellar metallicity $Z_*/Z_\odot$ , and gas-phase oxygen abundances $[O/H]_g$ (for all gas, ISM, and IGM) of the thermal, stochastic ( $f = 50$ ), kinetic ( $f = 1\%$ ) and mechanical ( $f = 1\%$ ) feedback models at $z = 0$ . . . . .   | 60  |
| 4.1 | The median of the SFR-weighted gas-phase oxygen abundance gradients in dex/kpc (upper table) and dex/ $R_e$ (middle table), and the V-band luminosity-weighted stellar metallicity gradients (bottom table), as a function of redshift $z$ for all galaxies in our simulations with the thermal, stochastic, and mechanical feedback models. The $1\sigma$ scatters are also given. . . . . | 90  |
| 5.1 | Table summarizing properties of JWST observed galaxies with high nitrogen-to-oxygen ratios at $z > 6$ . . . . .   | 103 |

# ACRONYMS

---

<b><math>\Lambda</math>CDM</b>	$\Lambda$ -Cold Dark Matter
<b>AGB</b>	Asymptotic Giant Branch
<b>AGN</b>	Active Galactic Nuclei
<b>BBN</b>	Big Bang Nucleosynthesis
<b>BH</b>	Black Hole
<b>BPASS</b>	Binary Population and Spectral Synthesis
<b>CALIFA</b>	Calar Alto Legacy Integral Field spectroscopy Area
<b>CANDELS</b>	Cosmic Assembly Near-infrared Deep Extragalactic Legacy Survey
<b>ccSN</b>	Core-Collapse Supernovae
<b>CGM</b>	Circumgalactic Medium
<b>CLEAR</b>	CANDELS Lyman- $\alpha$ Emission at Reionization
<b>COSMOS</b>	Cosmic Evolution Survey
<b>DM</b>	Dark Matter
<b>EAGLE</b>	Evolution and Assembly of GaLaxies and their Environments
<b>ETG</b>	Early Type Galaxies
<b>FB</b>	FeedBack
<b>FIRE</b>	Feedback In Realistic Environments
<b>FoF</b>	Friend-of-Friends
<b>GADGET</b>	GAxaxies with Dark matter and Gas intEracT
<b>GLASS</b>	Grism Lens-Amplified Survey from Space
<b>GLF</b>	Galaxy Luminosity Function
<b>GSMF</b>	Galaxy Stellar Mass Function
<b>HN</b>	Hypernova
<b>HORIZON-AGN</b>	Hydrodynamical cosmological simulation with Active Galactic Nuclei
<b>HST</b>	Hubble Space Telescope
<b>IFU</b>	Integral Field Unit
<b>IGM</b>	Intergalactic Medium
<b>IllustrisTNG</b>	Illustris: The Next Generation

---

<b>IMF</b>	Initial Mass Function
<b>ISM</b>	Interstellar Medium
<b>JWST</b>	James Webb Space Telescope
<b>KLEVER</b>	Kmos LEnsEd Velocity and Emission line Review
<b>KMOS</b>	K-band Multi Object Spectrograph
<b>LTG</b>	Late Type Galaxies
<b>MaNGA</b>	Mapping Nearby Galaxies at APO
<b>MOSDEF</b>	MOSFIRE Deep Evolution Field survey
<b>MUSE</b>	Multi Unit Spectroscopic Explorer
<b>MZR</b>	Mass – Metallicity (Z) Relation
<b>NDW</b>	Neutrino-Driven Wind
<b>NIRISS</b>	Near Infrared Imager and Slitless Spectrograph
<b>NIRSpec</b>	Near-Infrared Spectrograph
<b>NS</b>	Neutron Stars
<b>OSIRIS</b>	Optical System for Imaging and low Resolution Integrated Spectroscopy
<b>PISN</b>	Pair Instability Supernova
<b>PM</b>	Particle-Mesh
<b>SAMI</b>	Sydney – Australian Astronomical Observatory Multi-Object Integral Field Spectrograph
<b>SAMs</b>	Semi-Analytic Models
<b>SAURON</b>	Spectroscopic Areal Unit for Research on Optical Nebulae
<b>SDSS</b>	Sloan Digital Sky Survey
<b>SFMS</b>	Star Formation Main Sequence
<b>SFR</b>	Star Formation Rate
<b>SIMBA</b>	Simulating galaxies with MUltiphase gas and Black hole Accretion
<b>SPH</b>	Smoothed-Particle Hydrodynamics
<b>SW</b>	Stellar Winds
<b>VLT</b>	Very Large Telescope
<b>WD</b>	White Dwarf
<b>WR</b>	Wolf Rayet

## CHAPTER 1

# INTRODUCTION

---

## 1.1 Cosmic Evolution

### 1.1.1 Early Universe

The prevailing consensus in cosmology is that the Universe emerged from a hot, dense state approximately 13.8 billion years ago, in an event known as the Big Bang, marking the beginning of space, time, and the observable Universe (Planck Collaboration et al., 2020). Shortly after, the Universe underwent a brief period of rapid expansion known as inflation. As it continued to expand and cool, it transitioned into a hot plasma composed of quarks, antiquarks, and gluons.

Within the first second after the Big Bang, the Universe was an opaque plasma, cool enough for nuclear fusion to begin and for various subatomic particles to form, including matter (protons, neutrons, and electrons) and antimatter.

Within the next  $\sim 3$  minutes, conditions finally became suitable for Big Bang Nucleosynthesis (BBN) to occur (Alpher et al., 1948). During this phase, nearly all neutrons and about 25% of the protons fused into the first elements, forming  $^1\text{H}$ ,  $^2\text{H}$ ,  $^3\text{He}$ ,  $^4\text{He}$  and  $^7\text{Li}$  (Copi et al., 1995; Coc et al., 2013). At this stage, the Universe was cool enough for baryons to be stable and still hot enough for them to fuse, mainly consisting of an ionized plasma of protons, helium nuclei, electrons, and photons. However, the Universe also cooled too rapidly for complex nuclear reactions to proceed beyond a certain point. In particular, the absence of stable nuclei with mass numbers 5 and 8 (like  $^5\text{He}$  and  $^8\text{Be}$ ) created a “mass gap”, making it extremely difficult to build up heavier elements like C directly from He in the Big Bang environment. As a result, Big Bang nucleosynthesis could not produce significant amounts of C or any heavier elements. At the same time, with the Universe dominated by photons, there was way too much energy for neutral atoms to form.

After  $\sim 20$  minutes, the Universe had cooled and expanded to a diameter of roughly 600 light-years. By this point, almost all of the hydrogen and helium (and a small fraction of lithium) that would eventually form stars and galaxies in the Solar System had already been created.

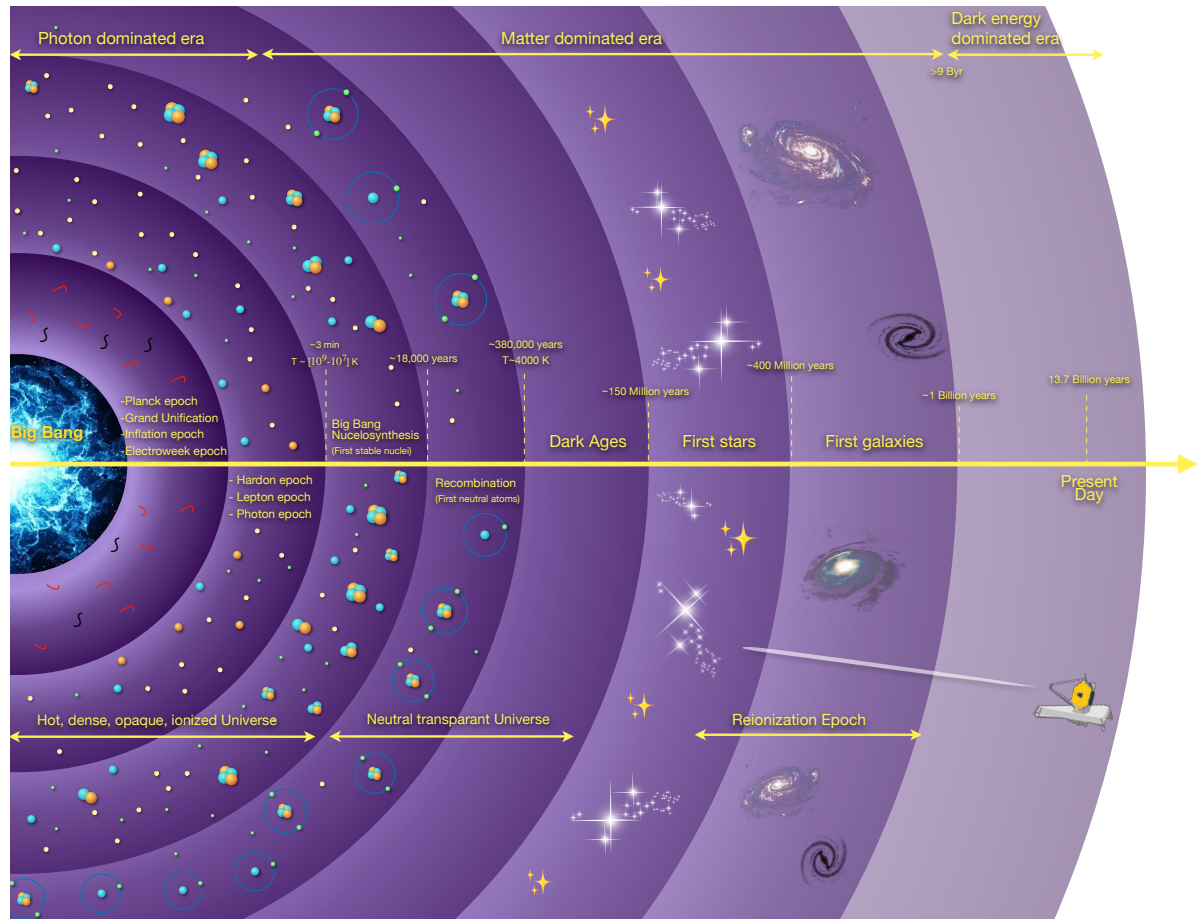


FIGURE 1.1: Schematic figure of the cosmic history of the universe.

As time passed, photons were redshifted and gradually lost energy. After  $\sim 40,000$  years, the radiation energy density becomes lower than the matter density. This transition to a matter-dominated era allowed dark matter to begin clumping under gravity, attracting more and more matter. With insufficient radiation pressure to resist gravitational collapse, these clumps continued to grow, forming the first structure in the Universe.

By  $\sim 380,000$  years after the Big Bang, the Universe had cooled enough for free electrons to combine with nuclei and form atoms. Moreover, these newly formed atoms (mostly H, He, and Li) quickly reached their lowest energy state (deionized), forming the first neutral atoms and also releasing photons in the process. These photons had existed since the hot plasma era and were simply set free to travel across the Universe once the electron density declined sufficiently to make Thomson scattering inefficient. Once scattering ceased, photons began to travel freely through space in a process known as photon decoupling. For the first time, the Universe became transparent, with an observable surface roughly 100 million light-years in diameter (Planck Collaboration et al., 2020).

Over the next few million years, these photons redshifted into non-visible wavelengths, leaving the Universe dark in the absence of visible light. These same photons were the only light source and

can still be observed today as the Cosmic Microwave Background (CMB). This period, known as the Dark Ages, spanned from the end of the Recombination Epoch until the formation of the first stars (Furlanetto et al., 2006).

These processes and epochs are summarized in Figure 1.1, where I highlight the main contributors to the formation of elements across cosmic time.

### 1.1.2 First stars

After a few hundred million years, clouds of primordial hydrogen began to collapse under gravity, eventually forming the first stars. The first generation of stars, known as population III stars (Pop III), formed from pristine gas composed of light elements synthesized during BBN. These stars are predicted to have formed in dark matter (DM) halos with masses  $\sim 10^6 M_\odot$ , often referred to as minihalos (Bromm and Yoshida, 2011), which collapsed at redshifts  $z \simeq 20\text{--}30$  (e.g., Tegmark et al., 1997; Yoshida et al., 2003). Pop III stars are believed to have been very massive, with typical masses  $\gtrsim 100 M_\odot$  (Bromm et al., 1999; Bromm and Larson, 2004; Nakamura and Umemura, 2001; Abel et al., 2000, 2002). However, later studies suggest that lower-mass Pop III stars may also have formed (Greif et al., 2011; Hirano et al., 2014; Rossi et al., 2021) and could even have existed as binaries (Stacy and Bromm, 2013). These stars impacted their environments by emitting intense ultraviolet radiation, which ionized the surrounding neutral hydrogen, initiating the cosmic Reionization era (Robertson, 2022), around  $\sim 400$  million years after the Big Bang.

The Reionization Era marks the period during which the intergalactic medium (IGM) transitioned from being predominantly neutral to fully ionized due to the emergence of the first luminous sources, effectively ending the cosmic Dark Ages. As ionizing photons escaped into the IGM, they created expanding ionized bubbles around their host halos. Over time, these bubbles grew and overlapped, reionizing most of the hydrogen in the Universe. Recent constraints from the Planck mission indicate that approximately half of the intergalactic hydrogen was ionized by  $z \sim 7.7$  (Planck Collaboration et al., 2020), although the process likely began as early as  $z \sim 10\text{--}12$ . In addition to massive stars, other sources like accreting black holes and X-ray binaries may have contributed to the ionizing photon budget (Mirabel et al., 2011).

Understanding the nature of Pop III stars remains a great challenge, as they formed under much simpler physical conditions than those found in present-day molecular clouds. The primordial gas in which they formed has a characteristic temperature of  $T_c \sim 200\text{--}300$  K and densities of  $n_c \sim 10^4 \text{cm}^{-3}$ , in contrast to the much colder ( $T \sim 10$  K) environments of present-day star-forming regions.

If these first stars were very massive ( $M \sim 140\text{--}300 M_\odot$ ) and experienced little mass loss, they would have ended their lives in supernovae explosions triggered by pair-creation instability known as Pair-Instability Supernovae (PISNe; Barkat et al., 1967; Heger and Woosley, 2002; Takahashi

et al., 2018), ejecting large amounts of heavy elements into the interstellar medium (ISM). Stars with masses exceeding  $300 M_{\odot}$  are expected to have collapsed directly into black holes (BH).

These primitive star-forming regions ultimately served as the seeds for the formation of the first galaxies.

### Stellar populations

In the early 1950s, the terms population I and Population II (Pop I and II) stars were introduced by Baade (1944), who categorized stellar populations primarily based on age and chemical composition, with Pop I being metal-rich and Pop II metal-poor. Later in the 1970s, astronomers realized that certain stars did not fit into this classification. In particular, even the most metal-poor Pop II stars have metallicities significantly higher than the pristine gas left from the Big Bang. Therefore, a third category of stars is introduced: Population III (Pop III) stars, thought to be composed entirely of primordial gas.

Population I stars are relatively young, formed between approximately  $10^6$  and  $10^{10}$  years ago. Stars younger than  $10^6$  years are sometimes referred to as extreme Population I stars. These stars are commonly found in the spiral arms of the Milky Way galaxy and in dwarf irregular galaxies such as the Magellanic Clouds. They form from metal-rich ISM gas that has been enriched by earlier generations of stars through processes like supernova explosions. As a result, they contain heavy elements such as Fe, Ni and C, but they still mainly consist of H and He. The sun is a typical example of a pop I star, formed about 4.6 billion years ago (Bahcall et al., 1995).

Population II stars are among the oldest observed stars, formed roughly 10-13 billion years ago. Since they formed in earlier times, they originated in environments where heavy elements had not yet been formed in large quantities. Therefore, they are described as metal-poor stars, typically containing 10 to 100 times fewer heavy elements than Population I.

Population III stars are hypothetical and represent the very first generation of stars to form in the Universe, originating from gas clouds that collapsed shortly after the Big Bang. These stars would have formed in pristine gas composed only of hydrogen and helium, with no heavier elements (i.e., zero metallicity; e.g., Bond, 1981; Carr and Hawking, 1974). Their remnants likely contributed to the enrichment of the ISM, providing the building blocks for Pop II stars. To date, Pop III stars have never been directly observed, and no truly metal-free star have been found in the Milky Way. This is likely because they were very massive (on the order of a few hundred  $M_{\odot}$ ), had short lifetimes, and had already ended their lives as stellar remnants, BHs or neutron stars (NS). The most metal-poor star discovered so far, SMSS0313-6708, has an iron abundance of  $[Fe/H] \lesssim -7$  and is carbon-enhanced (Keller et al. 2014; Nordlander et al. 2017).

### 1.1.3 First galaxies

Over time, the earliest generations of stars began to cluster and merge, accreting surrounding gas through gravitational attraction to form the first protogalaxies. These primitive structures, hosted in DM halos, were likely small, low-mass systems dominated by Pop III and early Pop II stars. They represent the building blocks of larger galaxies seen today (Bromm and Yoshida, 2011).

In the present day, telescopes like the JWST have revolutionized our understanding of this era. JWST has detected galaxies at redshifts  $z \gtrsim 10$  (e.g., Naidu et al. 2022; Bunker et al. 2023; Curtis-Lake et al. 2023; Castellano et al. 2024a), corresponding to just 300–400 million years after the Big Bang. These observations offer unprecedented insights into the formation and evolution of the first galaxies. Surprisingly, many of these early galaxies already show signs of metal enrichment and exhibit unexpected chemical abundances (e.g., Cameron et al. 2023; Schaerer et al. 2024a; Topping et al. 2024a,b; D’Eugenio et al. 2024) challenging existing models of early star formation and chemical enrichment.

### 1.1.4 Galaxy evolution

The formation and growth of galaxies in the early Universe is governed by the framework of hierarchical structure formation, where small-scale structures formed first and merged over time to build larger systems (Rees and Ostriker, 1977; White, 1978). In this scenario, dark matter halos collapsed under gravity, accreting baryonic matter that cooled and condensed to form stars. This continuous buildup led to galaxies with diverse sizes, morphologies, and chemical compositions, all shaped by their unique histories of accretion, star formation, and feedback.

By  $\sim 1$  billion year after the Big Bang, galaxies begun to look like those we observe today, with morphologies including ellipticals, spirals and irregulars. Spiral galaxies, such as the Milky Way, are characterized by well-defined rotating disks that host ongoing star formation. In contrast, elliptical galaxies tend to be more massive, spheroidal systems with older stellar populations, and are often formed through major mergers.

Cosmological simulations such as Illustris (Vogelsberger et al., 2014), FIRE (Hopkins et al., 2014), EAGLE (Schaye et al., 2015) and SIMBA (Davé et al., 2019) have shown that mergers, feedback, and gas accretion play crucial roles in shaping galaxy morphology, stellar content, and chemical evolution, giving rise to more complex galaxies.

There are various scaling relations used to understand galaxy formation and evolution, from which model parameters in cosmological simulations are determined. Below, we describe some of the most commonly studied ones.

#### 1.1.4.1 Star Formation Rate

The Star Formation Rate (SFR) measures the rate at which new stars form in a galaxy and is expressed in  $M_{\odot}/\text{yr}$  (e.g., [Madau and Dickinson 2014](#)). It depends on various quantities such as gas temperature and density. It is also impacted by stellar and AGN feedback, which heats the gas and suppresses star formation. The SFR increased through cosmic time, peaking at cosmic noon ( $\sim 10$  billion years ago) and declining since. For instance, the Milky Way forms stars at  $\sim 1.6 M_{\odot}/\text{yr}$  ([Licquia and Newman, 2015](#)), which is a low rate compared to starburst galaxies and galaxies in the early universe.

#### 1.1.4.2 Galaxy Luminosity Function

The Galaxy Luminosity Function (GLF) describes the number density of galaxies as a function of their luminosity. Early studies of the GLF date back to Edwin Hubble, but it was [Schechter \(1976\)](#) who introduced the Schechter function, which accurately describes the observed distribution of galaxy luminosities. The function typically features a power-law behaviour at the faint end, an exponential cutoff at the bright end, and a characteristic luminosity that marks the transition between the two regimes. Surveys such as SDSS, COSMOS, and CANDELS have measured the GLF across a wide range of redshifts (e.g., [Montero-Dorta and Prada 2009](#); [Finkelstein et al. 2012, 2022](#); [Donnan et al. 2023](#)), revealing that galaxy number densities evolve with cosmic time, particularly at the bright end, where massive galaxies grow through mergers and accretion. In cosmological simulations, reproducing the observed GLF serves as a key test for models of galaxy formation, as it is closely linked to the Galaxy Stellar Mass Function (GSMF) and the physics of baryonic processes such as supernova feedback, AGN, and gas accretion.

#### 1.1.4.3 Galaxy Stellar Mass Function

The Galaxy Stellar Mass Function (GSMF) describes the number density of galaxies as a function of their stellar mass. Studies of the GLF ([Schechter, 1976](#)) laid the foundation for understanding the distribution of galaxy masses. The GSMF is a fundamental observable, often characterized by a power law at the low-mass end and an exponential cutoff at the high-mass end, resembling the Schechter function. It reflects the efficiency of star formation and feedback processes, where low-mass galaxies are more affected by supernova-driven winds, while massive galaxies experience quenching due to AGN feedback. Observations from large surveys like SDSS and CANDELS (e.g., [Silk 2013](#); [Grazian et al. 2015](#); [Stefanon et al. 2021](#)) have allowed for precise measurements of the GSMF across cosmic time, revealing that the number density of massive galaxies evolves significantly, with rapid buildup in the early universe. Our simulations with AGN feedback give a good match to observational data ([Taylor and Kobayashi, 2016](#)).

While the GLF and GSMF have similar forms and both trace galaxy number densities, they serve different purposes and offer complementary views. The GLF is more straightforward for observers, as luminosity can be directly measured, while the GSMF is preferred in theoretical models, providing a more physical measure of stellar content such as star formation history under assumptions of the IMF and dust attenuation.

#### 1.1.4.4 Galaxy Size-Mass Relation

The Galaxy Size-Mass Relation describes the correlation between a galaxy's stellar mass and physical size. More massive galaxies tend to be larger, following a power-law relation where size ( $R_e$ , the effective radius, defined as the projected radius that encloses half of the total stellar mass, see section 4.2 for details) scales with stellar mass ( $M_*$ ). This relation helps us understand where stars formed within the original collapsing gas cloud, and can give constraints about star formation timescales (Kormendy and Bender, 1996; Kobayashi, 2005; Trujillo-Gomez et al., 2011). For star-forming galaxies, the relation exhibit a shallower slope due to continuous gas accretion and inside-out growth, while quiescent galaxies tend to be more compact. Observational data from HST, and JWST (e.g., van der Wel et al. 2014; Ward et al. 2024) showed an evolution of the size-mass relation across cosmic time, where high-redshift galaxies tend to be significantly more compact than local galaxies due to stellar feedback and minor mergers (Naab et al., 2009). To reproduce this relation in cosmological simulations, we incorporate various baryonic physics like AGN-driven feedback (Taylor and Kobayashi, 2015), gas accretion, and environmental effects (Kobayashi, 2004).

#### 1.1.4.5 Star Formation Main Sequence

The Star Formation Main Sequence (SFMS) describes the tight, nearly linear correlation between a galaxy's SFR and its stellar mass ( $M_*$ ). Actively star-forming galaxies follow a tight correlation between stellar mass and SFR, while quiescent galaxies lie well below this sequence (Renzini and Peng, 2015). First identified in large galaxy surveys such as SDSS, CANDELS, and COSMOS (e.g., Noeske et al. 2007; Whitaker et al. 2012), the SFMS suggests that most star-forming galaxies grow in a regulated manner, they evolve steadily through continuous gas accretion and star formation rather than through stochastic bursts. The normalization of the SFMS evolves with cosmic time, with higher SFRs at earlier epochs (e.g.,  $z \sim 2$ ) due to the greater availability of cold gas (Speagle et al., 2014). However, massive galaxies tend to quench as they move off the sequence, possibly due to AGN feedback. JWST has extended SFMS studies to  $z > 6$ , revealing that early galaxies formed stars more efficiently than previously thought (e.g., Clarke et al. 2024).

## 1.2 Chemical Evolution

### 1.2.1 Metallicity definitions

It is important to begin by introducing the concept of metallicity,  $Z$ , which is used extensively throughout this thesis. In astronomy, *metals* refer to all elements heavier than hydrogen and helium. Consequently, metallicity describes the abundance of all such heavy elements.

One common way to define metallicity is through the mass fraction, using the relation:

$$X + Y + Z = 1,$$

where  $X$ ,  $Y$ , and  $Z$  are the mass fractions of hydrogen, helium, and all metals, respectively. These are given by:

$$X \equiv \frac{m_{\text{H}}}{M}, \quad Y \equiv \frac{m_{\text{He}}}{M}, \quad Z \equiv \sum_{i>\text{He}}^N \frac{m_i}{M},$$

where  $M$  is the total baryonic mass and  $m_i$  is the mass of the  $i^{\text{th}}$  element heavier than helium.

This definition is more commonly used in galaxy formation simulations, where the full mass budget of each element is known. However, in observations, measuring the total metallicity is difficult because not all heavy elements can be detected simultaneously. As a result, observers typically use the abundance of a single element as a proxy for total metallicity.

Another commonly used approach is to express metallicity in terms of chemical abundance ratios, particularly relative to solar composition. These are denoted using square brackets, for example:

$$\left[ \frac{\text{Fe}}{\text{H}} \right] = \log_{10} \left( \frac{n_{\text{Fe}}}{n_{\text{H}}} \right)_{\star} - \log_{10} \left( \frac{n_{\text{Fe}}}{n_{\text{H}}} \right)_{\odot}, \quad (1.1)$$

where  $n_{\text{Fe}}$  and  $n_{\text{H}}$  are the number densities of iron and hydrogen, respectively. The subscript  $\star$  refers to the object of interest, and  $\odot$  denotes solar values.

Iron is commonly used as a reference element for stellar metallicity because it exhibits many strong absorption lines in the optical spectrum, making it relatively easy to observe. While it is not the most abundant metal, it serves as a reliable proxy for overall metallicity.

The interpretation of  $[\text{Fe}/\text{H}]$  is as follows:

$$\left[ \frac{\text{Fe}}{\text{H}} \right] = \begin{cases} > 0 & \text{Higher than solar metallicity} \\ = 0 & \text{Solar metallicity} \\ < 0 & \text{Lower than solar metallicity} \end{cases}$$

In gas-phase environments, it is more common to use oxygen as a proxy for metallicity, since it is the most abundant heavy element. The oxygen abundance is expressed as:

$$12 + \log_{10}(\text{O}/\text{H}) \equiv 12 + \log_{10}\left(\frac{n_{\text{O}}}{n_{\text{H}}}\right), \quad (1.2)$$

where  $n_{\text{O}}$  and  $n_{\text{H}}$  are the number densities of oxygen and hydrogen atoms. The “+12” is a standard convention in astronomy to bring the values into a readable scale. For example, if  $\log_{10}(\text{O}/\text{H}) \sim -4$ , then  $12 + \log_{10}(\text{O}/\text{H}) \sim 8$ , which is easier to interpret and compare.

Throughout this work, we adopt the solar abundances mainly from [Asplund et al. \(2009\)](#), but for oxygen we use  $\log_{10}(\text{O}/\text{H})=8.76\pm 0.02$  as in [Kobayashi et al. \(2020a\)](#).

### 1.2.2 Mass-Metallicity Relation

The Mass-Metallicity Relation (MZR) describes the correlation between galaxy stellar mass and its metal content, and is crucial for understanding galaxy evolution and chemical enrichment over cosmic time. This relation shows that massive galaxies are more metal rich, meaning they contain more heavy elements in their gas and stars. Whereas, low-mass galaxies have lower metallicities due to metal loss through supernova-driven winds ([Kobayashi et al., 2007](#)) and metal ejection by AGN winds ([Taylor et al., 2020](#)). The MZR is impacted by supernova feedback which we focus on in Chapter 3. In addition to the MZR, the Fundamental Metallicity Relation (FMR) describes the correlation between galaxy stellar mass, gas-phase metallicity, and SFR. The FMR is introduced by [Mannucci et al. \(2010\)](#), suggesting that at fixed stellar mass, galaxies with higher SFRs tend to have lower metallicities.

### 1.2.3 Metallicity gradients

Metallicity gradients in galaxies describe how elemental abundances vary as a function of radius. Most local star-forming galaxies exhibit negative gradients for both stars and gas, where metallicity decreases with increasing radius, indicating that the central regions are more metal-rich. However, some galaxies show flat or even positive (inverted) gradients, where the metallicity is uniform or increases toward the outskirts. These patterns can result from processes such as radial gas flows, mergers, or strong feedback redistributing metals. Both gas-phase and stellar metallicity gradients are active areas of research, offering valuable insights into galaxy evolution. We explore these topics in more detail in Chapter 4.

## 1.3 Nucleosynthesis Yields

### 1.3.1 Big Bang Nucleosynthesis

The Big Bang nucleosynthesis (BBN) is the process that formed the first atomic nuclei ( $^1\text{H}$ ,  $^3\text{He}$ ,  $^4\text{He}$  as well as a small amount of  $^7\text{Li}$  and  $^7\text{Be}$ ) in the early universe. This model occurred between  $\sim 1$  second and  $\sim 20$  minutes after the Big Bang, in a hot ( $\sim 10^9\text{K}$ ) and dense environment. And it is one of the key pillars supporting the Big Bang theory, providing an independent confirmation of early Universe physics.

One of the few remaining tensions in BBN is the so-called lithium problem, which is a discrepancy between the predicted and observed abundance of  $^7\text{Li}$ . The combination of BBN with the baryon-to-photon ratio ( $\eta$ ) derived from the CMB accurately predicts the primordial abundances of H,  $^4\text{He}$ , and D. However, it overestimates the amount of  $^7\text{Li}$  (Coc et al., 2013). This issue may be due to an incomplete understanding of stellar lithium depletion or uncertainties in nuclear reactions. We use the same initial composition as in Kobayashi et al. (2020a), including a theoretical value of  $^7\text{Li}/\text{H} = 5.623 \times 10^{-10}$  (Pitrou et al., 2018).

All other elements are synthesized later in stars, which we focus on in the following section.

### 1.3.2 Stellar Nucleosynthesis

Stellar nucleosynthesis is the process by which elements are formed through nuclear fusion in the cores of stars. It is responsible for producing all chemical elements heavier than H and He. Stellar nucleosynthesis is summarized in Figure 1.2, depending on the stellar progenitor mass and various processes, and is described in more details below.

#### Low-mass stars

Low-mass stars with initial mass  $M_* < 8M_\odot$  at  $Z = Z_\odot$  (such as the Sun) can only fuse elements up to N and C, then die as White Dwarfs (WD), a core of nitrogen and carbon slowly cooling and contracting. These low-mass stars also play a role in forming heavy elements, with the condition that at least a few heavy elements were already present when they are born.

#### Intermediate/high mass stars

In intermediate/high mass stars with  $10M_\odot < M_* < 40M_\odot$ , elements beyond C and N (from O to Ni) can be fused with a process called the alpha-ladder, which is achieved by fusing each new element with He to form heavier elements.

#### Type II supernovae

The energy required to keep the star in equilibrium against gravity is produced by the fusion of elements up to Nickel. However, the fusion energy is not enough to form elements after Nickel, which drains the core from its energy resulting in a core-collapse supernovae (ccSN) explosion.

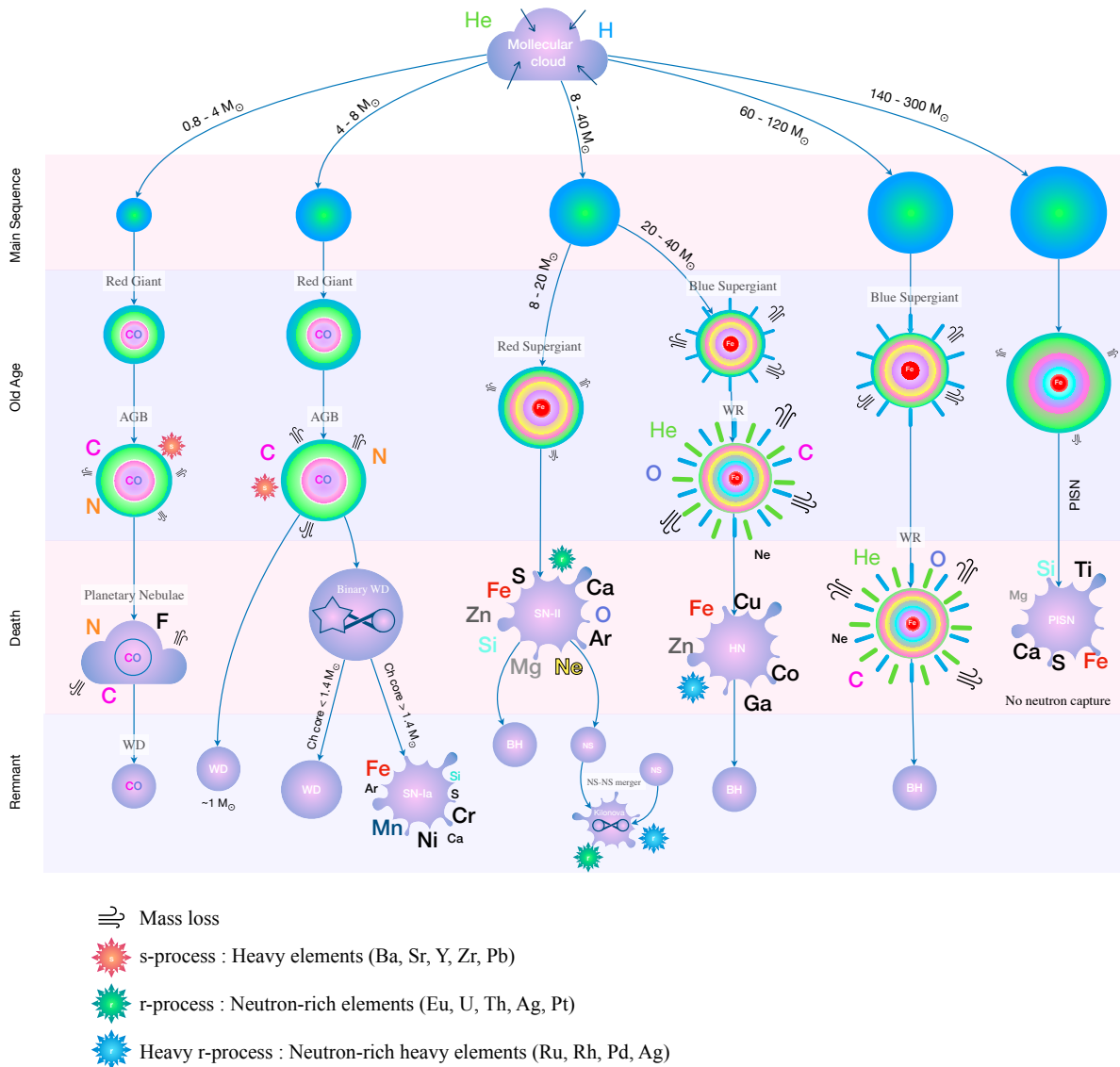


FIGURE 1.2: Schematic figure of chemical enrichment from different types of stars.

While the contribution to the periodic table of ccSNe is from Ni to Kr, it mainly produces the so-called  $\alpha$  elements (O, Ne, Mg, Si, S, Ar, and Ca).

### Hypernovae

Among ccSNe, hypernovae (HN; explosions with energies  $> 10^{52}$  erg), which are observed as broad-line Type Ibc supernovae (Nomoto et al., 2013), are known to produce a large amount of Fe, Co and Zn. A significant fraction of massive stars ( $> 20M_{\odot}$ ) are predicted to explode as HN in order to explain the galactic chemical evolution (Kobayashi et al., 2006a). We assume 50% of stars with  $M > 20M_{\odot}$  to explode as HNe (depending on the metallicity  $Z$ ), while the remaining stars at  $> 30M_{\odot}$  end their lives as failed supernovae.

### Type Ia supernovae

So far, we have covered the formation of light elements by the Big Bang Nucleosynthesis and

individual stars. However, we are still missing all the heavy elements in the periodic table. In fact, these are produced by multiple stellar interactions. For example, in a close binary system a white dwarf can accrete mass from its companion until it surpasses the Chandrasekhar mass and can no longer support itself, resulting in a thermonuclear explosion known as a Type Ia supernova (SN-Ia). These explosions produce huge fractions of iron peak elements (Cr, Mn, Fe, and Ni; [Kobayashi et al., 2020b](#)). The amount of element produced depends on the mass of WD progenitors, and a large fraction of SNe-Ia should come from near-Chandrasekhar (Ch) mass explosions (see [Kobayashi et al., 2020a](#)), which are included in our simulations.

### Beyond Iron: Neutron Capture Elements

The nuclear reactions happening in stars and during their explosions produce a significant amount of neutrons. These neutrons can be captured by nuclei and produce more and more heavy elements (ex: In-115 absorbs a neutron and becomes In-116). This is known as the neutron capture process. On the other hand, when an element is unstable, it decays to form a different heavy element (ex: In-116 is unstable and decays to form Sn-116). This is known as the  $\beta$  decay. These two processes happen in the different supernovae, and NS mergers considered above and are responsible for producing an essential amount of heavy elements.

More details about neutron-capture processes are discussed in the following section.

### 1.3.3 Neutron capture process

Understanding how each chemical element is produced is fundamental to understanding the formation of the Universe. H, He and Li were the first elements produced by the Big Bang nucleosynthesis. After that, the so-called light elements (up to iron peak elements) are synthesised in stars by the fusion process, where they release energy that balances the gravity force of stars. Later on, heavy elements are formed by the neutron capture process ([Burbidge et al., 1957](#); [Cameron, 1957](#)).

Neutron Capture is a nuclear reaction in which a neutron collides with a seed nucleus to form a heavier one (an isotope with one higher atomic mass).



If the resulting isotope is stable, this reaction will keep happening. If it is unstable, the  $\beta$ -decay process occurs:



The original element X becomes a new chemical element Y with an unchanged mass number A and an atomic number Z that rises by one.

### **The slow neutron-capture process (s-process)**

When the neutron capture process is slow, and there is enough time for the  $\beta$ -decay to happen before another neutron is captured, the neutron capture is defined as s-process. This occurs mainly in AGB stars (e.g., [Karakas and Lattanzio, 2014](#)) and lasts thousands of years ([Lugaro et al., 2003](#)). This process produces half of the chemical elements heavier than iron.

### **The rapid neutron-capture process (r-process)**

When successive neutrons are captured rapidly, such that the  $\beta$ -decay does not have enough time to occur, the neutron capture is defined as r-process. This series proceeds through increasingly neutron-rich isotopes until reaching nuclei so unstable that their rapid  $\beta$ -decay outpaces any further neutron captures. The cosmic regions where this process happens are still debated. It must happen in regions with a high density of free neutrons.

Below we discuss the regions where the r-process may occur:

- **Neutron Star Mergers**

Neutron-star mergers (NSM, e.g., [Wanajo et al., 2014](#)) are a candidate for the r-process site. The merger of the binary system ejects neutron-rich material from the gravitational fields of the NS to the ISM, allowing the r-process to occur in this dynamic ejecta (initially predicted in [Lattimer and Schramm, 1974](#) and later studied in [Symbalisty and Schramm, 1982](#)).

- **Neutrino Driven Winds**

After a supernova explosion, the core of the proto-neutron star cools by emitting neutrinos. The energy from these neutrinos causes an expanding supersonic outflow known as the neutrino-driven winds. The neutrino-driven wind lasts for several seconds and even minutes after the explosion, and are suggested to produce a weak r-process ([Qian and Woosley, 1996](#); [Qian and Wasserburg, 2007](#)).

- **Electron Capture Supernovae**

Inside the core of a super-AGB star are O, Ne and Mg atoms. The Ne and Mg atoms absorb their electrons when the core gets too dense. This absorption of electrons is known as an electron-capture reaction. The electrons typically kept the core pressure up. Their capture reduces support and causes gravitational collapse, followed by explosive oxygen burning, leading to r-process in the ejecta. ECSNe are probably only able to produce a

weak r-process (Wanajo et al., 2011).

- **Rapidly Rotating Magnetised Massive Stars**

Magneto-rotational supernovae (MRSNe, e.g., Nishimura et al., 2015; Limongi and Chieffi, 2018b) are a hypothetical category of cc-SNe implicating magnetic rotating stars. The core collapses and forms a neutron star. The rapid rotation is responsible for forming a high-density accretion disk. This high density increases the electron-capture rate, which increases the conversion of protons to neutrons in the nuclei. When these neutron-rich nuclei reach the neutron drip line, they enrich the system with free neutrons (Symbalisky, 1984; Cameron, 2001). A strong magnetic field is also responsible for driving jets at the poles of the NS and ejecting r-processed material from the accretion disc.

## 1.4 Simulations of chemical enrichment

### 1.4.1 Previous work

Simulating the chemical enrichment of galaxies is especially challenging, as it adds further complexity to the already difficult problem of modelling their formation and evolution. The build-up of dark matter is relatively straightforward to follow, since it interacts only through gravity and can be traced from initial conditions set by the CMB. In contrast, the baryonic component is enriched through a variety of small-scale astrophysical processes, including star formation, stellar winds, supernovae, and the growth of supermassive black holes. These mechanisms not only regulate the flow of gas but also determine how metals are produced, ejected, and recycled within and between galaxies. Feedback processes play a central role in shaping chemical enrichment. In the simplest analytic models, the metallicity of a galaxy depends on the balance between metal production from stars, dilution by pristine gas inflows, and removal of enriched gas through outflows (Finlator and Davé, 2008; Davé et al., 2011). Stronger feedback drives more efficient outflows, lowering the metallicity at fixed stellar mass and redistributing metals into the circumgalactic and intergalactic medium. Conversely, weaker feedback allows galaxies to retain a larger fraction of their metals, producing higher enrichment but less consistency with observed mass–metallicity relations. Thus, understanding the link between feedback and enrichment is essential.

Capturing the link between large-scale structure and local enrichment events in one cosmologically representative simulation remains a major challenge, making the use of approximations and sub-grid models necessary. The two main approaches used to study these processes are semi-analytic models (SAMs) and hydrodynamical simulations (see Section 2.1 for details, along with the classic chemical evolution models (e.g. Tinsley 1980; Matteucci and Francois 1989).

### Semi-analytic models (SAMs)

SAMs remain an important tool for studying galaxy formation and enrichment because of their efficiency and flexibility. They were first introduced by [White and Frenk \(1991\)](#), who used the Press–Schechter formalism ([Press and Schechter, 1974](#); [Narayan and White, 1988](#)) to describe the abundance of dark matter haloes and linked baryonic evolution to halo properties under simple assumptions.

In these models, chemical enrichment is typically implemented through parameterised prescriptions that track how stars form, evolve, and release metals into their surroundings. Their efficiency allows the exploration of large parameter spaces, making them valuable tools for interpreting observed galaxy properties such as cosmic SFR and the global metallicity evolution.

Early implementations provided only average predictions, but later refinements extended the technique to individual haloes through Monte Carlo realisations of merger histories (e.g. [Cole et al., 1994](#); [Heyl et al., 1995](#); [Kauffmann et al., 1993](#)). With increasing computational resources, SAMs were increasingly complemented by large N-body simulations of dark matter, such as the Millennium series ([Springel et al., 2005](#); [Boylan-Kolchin et al., 2009](#); [Angulo et al., 2012](#); [Ferlito et al., 2023](#)), which provided realistic merger trees on which more sophisticated baryonic and enrichment models could be built (e.g. [Fanidakis et al., 2011](#); [Fu et al., 2013](#)). Prominent examples with explicit chemical-evolution modules include those by [De Lucia et al. \(2004\)](#); [Somerville et al. \(2004\)](#); [Fu et al. \(2013\)](#); [Yates and Kauffmann \(2014\)](#); [Belfiore et al. \(2019\)](#); [Yates et al. \(2021\)](#); [Sharda et al. \(2021\)](#); [Murphy et al. \(2022\)](#); [Behling et al. \(2025\)](#), each tuning free parameters to match the slope and redshift evolution of the mass–metallicity relation. Nevertheless, SAMs are limited by the fact that baryonic physics is not evolved self-consistently with the dark matter, restricting their output to global or average enrichment properties rather than detailed chemical structures.

### Hydrodynamical simulations

Hydrodynamical simulations provide a complementary approach to SAMs by treating enrichment processes directly, following the evolution of both dark matter and baryons in a cosmological framework. These simulations build on N-body calculations of structure formation, tracing the collapse of matter into haloes and their growth through mergers and accretion. Gas physics is then solved using particle-based, mesh-based, or hybrid schemes ([Frenk et al., 1999](#); [O’Shea et al., 2005](#); [Agertz et al., 2007](#)), each with their own strengths and limitations (see section 2.1 for more details). Sub-grid models are then required to capture unresolved processes such as star formation, stellar yields, and feedback from supernovae (e.g. [Finlator and Davé, 2008](#); [Davé et al., 2011](#)). A key strength of hydrodynamical simulations is their ability to follow not only global enrichment but also the internal distribution of metals within galaxies, such as spatial gradients and the kinematics of the star and gas particles. These predictions can now be compared

with observations from integral-field and multi-object spectrographs, which provide detailed metallicity maps of galaxies across cosmic time.

A variety of codes have been developed for this purpose, applied both to isolated galaxies (e.g. [Katz, 1992](#); [Mihos and Hernquist, 1994](#); [Kawata and Gibson, 2003](#); [Kobayashi, 2004](#)) and to cosmological studies, from individual systems ([Navarro and White, 1993](#)) to galaxy populations on large scales ([Cen and Ostriker, 1999](#); [Springel and Hernquist, 2003](#)). A fundamental limitation is the balance between resolution and simulated volume: higher spatial and mass resolution are restricted to smaller cosmological boxes, while larger-volume runs sacrifice small-scale detail. To overcome this, many projects run suites of simulations with same physical prescriptions but different box sizes and resolutions (e.g. [McAlpine et al., 2016](#)).

In the past decade, improvements in both computational power and physical modeling have enabled these codes to reproduce a wide range of observed galaxy properties. Several collaborations now provide public access to their outputs. Prominent examples include Illustris ([Vogelsberger et al., 2014](#); [Genel et al., 2014](#)), IllustrisTNG ([Springel et al., 2018](#); [Pillepich et al., 2018](#); [Torrey et al., 2019](#); [Hemler et al., 2021](#); [Garcia et al., 2023](#)), EAGLE ([Schaye et al., 2015](#); [Crain et al., 2015](#); [McAlpine et al., 2016](#); [De Rossi et al., 2017](#); [Tissera et al., 2022](#)), HORIZON-AGN ([Dubois et al., 2014](#); [Dubois et al., 2016](#)), FIRE ([Hopkins et al., 2014](#); [Ma et al., 2016](#)), and MUFASA ([Davé et al., 2016, 2017](#)). In contrast, some specialized codes sacrifice cosmological volume to achieve sub-parsec resolution in individual galaxies (e.g. [Kobayashi et al., 2011a](#); [Pallottini et al., 2017](#); [Katz et al., 2015](#); [Costa et al., 2015](#)). A comprehensive overview of these approaches and their comparative strengths is given by [Somerville and Davé \(2015\)](#).

## 1.4.2 Analytic Models of Enrichment with Feedback

To capture these processes in a simplified way, analytic models often follow the formalism of [Tinsley \(1980\)](#), where a galaxy is treated as a well-mixed “box” of total mass  $M = M_s + M_g$  (stars + gas) with:

$$\frac{dM_s}{dt} = \Psi(t) - E(t), \quad (1.5)$$

$$\frac{dM_g}{dt} = -\Psi(t) + E(t) + f(t) - \dot{M}_{\text{out}}(t), \quad (1.6)$$

where  $\Psi$  is the star formation rate,  $E$  the mass return from dying stars,  $f$  the infall rate, and  $\dot{M}_{\text{out}} = \lambda \Psi$  the outflow rate (mass-loading  $\lambda$ ).

The total mass of metals  $Z M_g$  in the gas then evolves as

$$\frac{d(Z M_g)}{dt} = -Z \Psi + E_Z + Z_f f - Z \dot{M}_{\text{out}}, \quad (1.7)$$

where  $E_Z$  is the metal ejection rate from stars and  $Z_f$  the metallicity of the inflow.  $Z$  denotes the metallicity of the ISM of the system considered, while stellar metallicities are inherited from the

gas at birth.

In the common *instantaneous recycling* and no-infall limit ( $f, E_Z \rightarrow 0$ ), this reduces to

$$\frac{dZ}{dt} = \frac{\Psi}{M_g} [y - Z(1 + \lambda)],$$

with  $y$  the net nucleosynthetic yield averaged by IMF per stellar population (the mass of newly produced metals returned to the ISM per unit mass locked into long-lived stars and remnants), so that a steady-state (“equilibrium”) metallicity is

$$Z_{\text{eq}} = \frac{y}{1 + \lambda}.$$

Thus, stronger feedback (larger  $\lambda$ ) yields lower retained metallicity (Tinsley, 1980).

## 1.5 Thesis outline

Understanding how galaxies form and evolve requires addressing one of the main uncertainties in astrophysics: stellar feedback. The energy and matter released by stars, particularly through supernova explosions, play a critical role in regulating star formation and distributing metals throughout the interstellar and intergalactic medium. This chemical enrichment is, in turn, essential to tracing the origin of elements and interpreting the observed properties of galaxies across cosmic time.

Using cosmological hydrodynamical simulations based on the GADGET-3 code, I first implement and compare four feedback models: thermal, stochastic, kinetic, and mechanical to understand their impact on the distribution of metals in galaxies. Chapter 2 introduces the theoretical framework, detailing the simulation methods, physical processes, feedback mechanisms and nucleosynthesis yields used in this study.

In Chapter 3, we constrain supernova feedback in our cosmological simulations using stellar and gas-phase mass–metallicity relations, this work has been published in Ibrahim and Kobayashi (2024). We extend this investigation for the impact of supernova feedback on metallicity radial gradients (Chapter 4), a study that has been submitted to MNRAS and is currently under review (Ibrahim and Kobayashi, 2025).

In Chapter 5, we investigate the origin of elements by incorporating nucleosynthesis yields from Population III stars, specifically rotating Wolf–Rayet stars and pair-instability supernovae, into our cosmological simulations. I present the resulting elemental abundances and compare them with recent observations from the James Webb Space Telescope.

In Chapter C, I conduct a performance benchmark of our simulation code across different resolutions, volumes, and high-performance computing environments, optimizing for both accuracy and efficiency.

Finally, Chapter 6 summarizes the key findings of this thesis, highlighting the progress made in understanding the origin and distribution of elements in the Universe. It also outlines potential directions for future work.

## CHAPTER 2

# CODE AND SIMULATIONS

---

<b>2.1</b>	<b>COSMOLOGICAL SIMULATIONS</b> . . . . .	<b>20</b>
<b>2.2</b>	<b>HYDRODYNAMICS</b> . . . . .	<b>22</b>
<b>2.3</b>	<b>BARYON PHYSICS</b> . . . . .	<b>24</b>
<b>2.4</b>	<b>INITIAL MASS FUNCTION</b> . . . . .	<b>25</b>
<b>2.5</b>	<b>CUMULATIVE FUNCTION</b> . . . . .	<b>26</b>
<b>2.6</b>	<b>STELLAR LIFETIME</b> . . . . .	<b>27</b>
<b>2.7</b>	<b>YIELD TABLES</b> . . . . .	<b>28</b>
2.7.1	YIELDS FROM AGB AND SAGB STARS . . . . .	30
2.7.2	YIELDS FROM CCSNE . . . . .	31
2.7.3	YIELDS FROM HNE . . . . .	32
2.7.4	YIELDS FROM WR STARS . . . . .	33
2.7.5	YIELDS FROM PISNE . . . . .	34
2.7.6	OTHER YIELD TABLES . . . . .	35
<b>2.8</b>	<b>SUPERNOVA FEEDBACK</b> . . . . .	<b>35</b>
<b>2.9</b>	<b>GALAXY PROPERTIES</b> . . . . .	<b>37</b>
2.9.1	STAR FORMATION RATES . . . . .	38
2.9.2	GALAXY STELLAR MASS FUNCTION . . . . .	39
2.9.3	GALAXY LUMINOSITY FUNCTION . . . . .	39
2.9.4	SIZE-MASS RELATION . . . . .	40
2.9.5	MASS-METALLICITY RELATION . . . . .	41
2.9.6	METALLICITY GRADIENTS . . . . .	44
<b>2.10</b>	<b>SUMMARY</b> . . . . .	<b>45</b>

---

## 2.1 Cosmological simulations

Our simulation code is based on the "GALaxies with Dark matter and Gas intERacT 3" code known as GADGET-3 (Springel et al., 2005). It uses TreeSPH (Lucy 1977, Gingold and Monaghan 1977, and Hernquist and Katz 1989) which combines the *smoothed particle hydrodynamics* (SPH) in order to follow the gas dynamics, with the *hierarchical tree algorithm* to compute the N-body gravitational interactions. The tree algorithm organizes all particles into a hierarchical, space-filling structure (an oct-tree in 3D). The simulation volume is first divided into one large cube, then each cube is split into eight child cubes, and so on, until each leaf node contains a single particle. To compute the gravitational force on a given particle, the code “walks” the tree: if a node is sufficiently far away (its size divided by its distance is below a chosen opening-angle threshold), the node’s total mass is treated as a single point located at its centre of mass; otherwise the node is opened and its children are examined in turn. By approximating distant groups of particles in bulk and only resolving nearby neighbours exactly, the tree algorithm reduces the force calculation from  $O(N^2)$  to  $O(N \log N)$  operations, while maintaining high accuracy for close interactions (Springel et al., 2005).

We use an improved version of the code that contains several physical processes related to galaxy formation and evolution, such as radiative cooling, star formation, supernovae feedback (Kobayashi et al., 2007; Ibrahim and Kobayashi, 2024), and black hole physics (Taylor and Kobayashi, 2014). Figure 2.1 shows the projected gas density map from our simulation in a  $25 h^{-1} \text{Mpc}^3$  comoving volume. The filamentary structures trace the underlying DM distribution, while the high-density regions (shown in green) correspond to the locations of galaxy formation.

The simulation of galaxy formation and evolution remains a significant challenge as it extends from large-scale structures along dark matter filaments to star formation scales. Assumptions and approximations are therefore necessary and depend on the scale we want to resolve. For instance, the *semi-analytic models* SAMs (White and Frenk, 1991) compute the baryonic physics separately from the dark matter (which only interacts by gravity). Unlike in SAMs, the *hydrodynamical simulations*, can simulate the baryonic physics simultaneously with the dark matter self-consistently. The latter can also predict the internal structure of galaxies (i.e. kinematics and spatial distributions), while SAMs can only predict the total or average quantities (Somerville and Davé, 2015).

Different methods are used in current hydrodynamical simulations; two main approaches are mesh-based and particle-based:

- *Mesh-based* codes are mostly Eulerian, where the space is discretized, and the fluid is described at fixed mesh as a function of time. These codes offer a high resolution for the evaluation of hydrodynamical shocks. However, they lack Galilean-invariance.

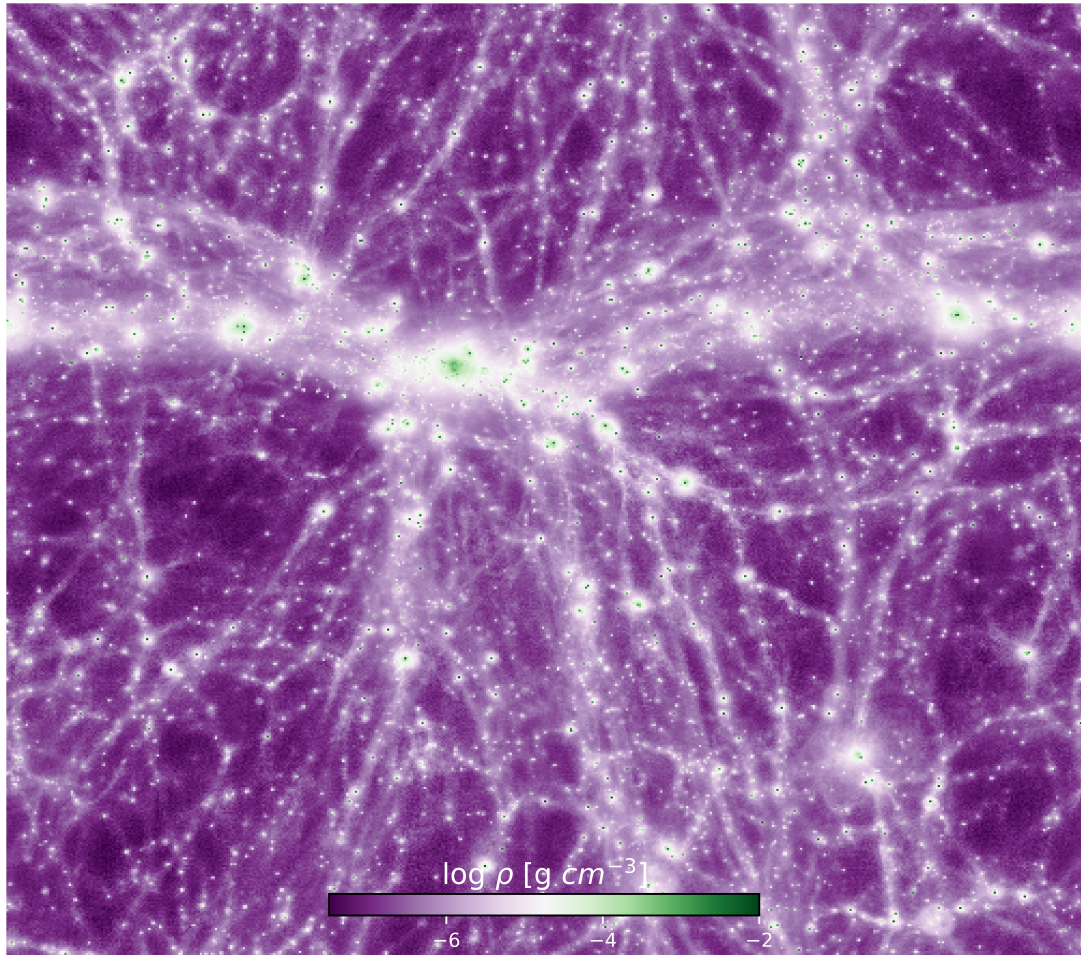


FIGURE 2.1: Projected density map of our cosmological simulations in  $25 h^{-1} \text{Mpc}^3$  box with our fiducial mechanical feedback model, at  $z = 0$ . High density regions are shown in green.

- *Particle-based* codes are mainly Lagrangian, where the mass is discretized, and the fluid particle's trajectory is followed over time. This approach is the fastest method for gravitational field computations. However, it usually does not suit work requiring high spatial resolution.

GADGET uses TreePM hybrid methods (Bagla, 2002), which combines the best features by using the Tree algorithm at short scales and the Particle-Mesh (PM) algorithm at large scales for the gravitational forces. The method used in our hydrodynamical simulations are summarized in Figure 2.2.

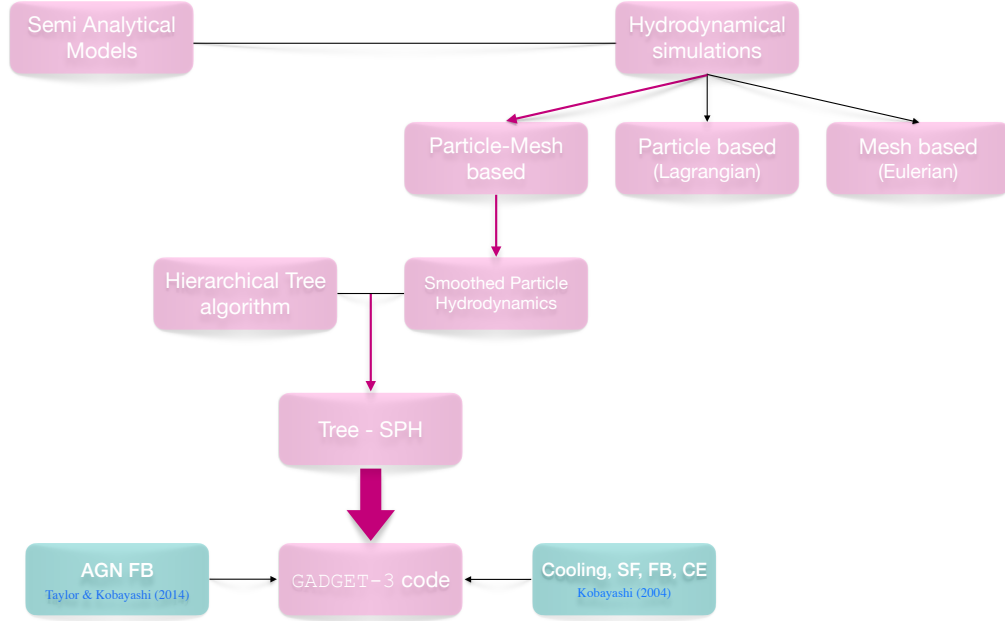


FIGURE 2.2: Diagram summarizing the methods used in our hydrodynamical simulation based on the GADGET-3 code.

## 2.2 Hydrodynamics

We define the Lagrangian derivative as

$$\frac{D}{Dt} = \frac{\partial}{\partial t} + \mathbf{v} \cdot \nabla.$$

The basic equations of hydrodynamics are as follows:

$$\text{Continuity equation : } \frac{D\rho}{Dt} + \rho \nabla \cdot \mathbf{v} = 0, \quad (2.1)$$

$$\text{Conservation of momentum: } \frac{D\mathbf{v}}{Dt} = -\frac{1}{\rho} \nabla P - \nabla \Phi, \quad (2.2)$$

$$\text{Thermal energy equation: } \frac{Du}{Dt} = \frac{P}{\rho^2} \frac{D\rho}{Dt} + \frac{1}{\rho} \nabla \cdot (\kappa \nabla T) + \frac{H - \Lambda}{\rho}, \quad (2.3)$$

$$\text{Poisson's equation: } \nabla^2 \Phi = 4\pi G \rho. \quad (2.4)$$

Here,  $\rho$  is the mass density,  $\mathbf{v}$  the velocity of the fluid,  $u$  the specific thermal energy,  $P$  the pressure,  $\Phi$  the gravitational potential,  $G$  the gravitational constant,  $\kappa$  the coefficient of thermal

conductivity,  $T$  the temperature,  $H$  the heating function, and  $\Lambda$  the cooling function. The equation of state of an ideal gas is used with adiabatic index  $\gamma = 5/3$ :

$$P = (\gamma - 1) \rho u.$$

Note that GADGET-3 solves the entropy equation instead of energy equation (Springel and Hernquist, 2002).

## Smoothed-particle hydrodynamics

This section introduces the SPH equations used to resolve the evolution of the fundamental hydrodynamical equations. A brief overview of the baryonic physics used in our simulation is also provided.

SPH is a Lagrangian computational method used to simulate continuum fluid flows. Originally developed for astrophysical applications (Monaghan, 2005), it has since been adopted across various fields. The smoothly averaged value of any physical quantity  $f(r)$  at a given location  $r$  is given by

$$\langle f(r) \rangle = \int f(r') W(r - r', h) dr' \quad (2.5)$$

Where  $h$  is the characteristic radius known as the *smoothing length*, and  $W(r)$  is the *smoothing kernel*, which is normalised as

$$\int W(r - r', h) dr' = 1 \quad (2.6)$$

with

$$\lim_{h \rightarrow 0} W(r - r', h) = \delta(r - r') \quad (2.7)$$

The gradient of  $f(r)$  is then

$$\nabla \langle f(r) \rangle = \int f(r') \nabla W(r - r', h) dr' \quad (2.8)$$

The equations above describe a continuous fluid. In practice, we approximate this fluid by a set of discrete particles, by replacing the integral with a summation over all particles within a volume  $V_j = \frac{m_j}{\rho_j}$ . As a result, equation 2.5 is modified as

$$f(r_i) = \sum_{j \in \Omega} f(r_j) W(|r_i - r_j|, h) V_j \quad (2.9)$$

With  $r_i$  and  $r_j$  the locations of particle  $i$  and neighbour particles  $j$  respectively.  $\Omega$  is a set of neighbours of particle  $i$ . We simplify the notation such that:

$$f_i = \sum_{j \in \Omega} \frac{m_j}{\rho_j} f_j W_{ij} \quad (2.10)$$

With the same logic, equation 2.8 is obtained as

$$\nabla f_i = \sum_{j \in \Omega} \frac{m_j}{\rho_j} f_j \nabla W_{ij} \quad (2.11)$$

In our simulations, equations 2.10 and 2.11 are applied for the basic equations of hydrodynamics by replacing  $f_i$  with the appropriate physical quantity.

## 2.3 Baryon physics

We use cosmological hydrodynamical simulations based on the GADGET-3 code (Springel et al., 2005) in a comoving  $10h^{-1}\text{Mpc}$  or  $25h^{-1}\text{Mpc}$  cubic boxes with periodic boundary conditions. Details regarding the box size, as well as the number and mass of gas and dark matter particles are provided in the relevant sections. Details about the initial conditions and physical processes are given in Section 3.2, where we use metallicity-dependent radiative cooling, stellar feedback (Kobayashi, 2004), black hole physics (Taylor and Kobayashi, 2014), and chemical enrichment (Kobayashi et al., 2020a,b). The AGN parameters are kept unchanged throughout this work.

### Star Formation

We use the star formation criteria used in (Katz, 1992) with (1) converging, (2) dynamical and (3) sound crossing (i.e. Jeans unstable) times:

1. *Converging flows*: Star formation is only allowed in convergent flows. The  $(\nabla \cdot v)_i$  term accounts for the local radial velocity dispersion that should be converging such as

$$(\nabla \cdot v)_i < 0 \quad (2.12)$$

2. *Rapid cooling*: Star formation is only allowed in regions where the cooling time is less than the dynamical time

$$t_{\text{cool}} < t_{\text{dyn}} \quad (2.13)$$

3. *Jeans instability*: The gas has to be locally Jeans unstable

$$t_{\text{dyn}} < t_{\text{sound}} \quad (2.14)$$

Where  $t_{\text{cool}}$  is the cooling time (the time it would take for the gas to radiate away its energy),  $t_{\text{dyn}}$  is the dynamical time, and  $t_{\text{sound}}$  is the sound crossing time such as:

$$t_{\text{cool}} = \frac{\rho u}{\Lambda} \quad (2.15)$$

$$t_{\text{dyn}} = \frac{1}{\sqrt{4\pi G \rho}} \quad (2.16)$$

$$t_{\text{sound}} = \frac{h_i}{c_s} \quad (2.17)$$

With  $u$  the specific thermal energy with unit energy per density.  $c_s$  is the local sound speed,  $h_i$  the smoothing length and  $\Lambda$  the cooling rate (as a function of  $Z$ ).

One of the most uncertain phenomena remains supernova feedback. To constrain supernova feedback in our simulations, we study its impact on the mass–metallicity relation (Chapter 3) and metallicity radial gradients (Chapter 4).

## 2.4 Initial Mass Function

The initial mass function (IMF) describes the initial distribution of stellar masses for a population of stars during star formation. Since stellar properties and evolution depend on the mass, the IMF is an essential tool for studying stars. While it is relatively invariant across different stellar groups, observational evidence suggests that the IMF may depend on environmental conditions (Hsu et al., 2013; Damian et al., 2021). As such, the IMF could differ significantly in early galaxies dominated by massive stars.

In this work, we adopt the Kroupa IMF (Kroupa, 2008) for Population I and II stars, spanning a mass range of  $[0.01, 120], M_{\odot}$  with a slope of  $x_{\text{imf}} = 1.3$ . For Population III stars, we conduct a parameter study by varying the upper mass range up to  $[15, 300], M_{\odot}$ , as well as by adjusting the slope  $x_{\text{imf}3}$  and the metallicity threshold  $Z_{\text{max}3}$ .

The IMF  $\phi(m)$  is given by

$$\phi(m) \propto m^{-x_{\text{imf}}} \quad (2.18)$$

where  $x_{\text{imf}}$  is the slope for a given mass range, which, for the Kroupa IMF is as follow

$$\phi(m) \propto \begin{cases} m^{-0.3}, & 0.01 \leq m/M_{\odot} < 0.08 \\ m^{-1.3}, & 0.08 \leq m/M_{\odot} < 0.50 \\ m^{-2.3}, & 0.50 \leq m/M_{\odot} < 120 \end{cases} \quad (2.19)$$

## 2.5 Cumulative Function

The nucleosynthesis yields cumulative function represents the integrated production of chemical elements over time within the simulation, tracing the contribution of nucleosynthetic yields from various processes, such as AGB, cc-SN (including SN-II and HN), WR stars and PISN. This function accumulates the total mass of newly synthesized elements as a function of cosmic time. A star produces elements at the end of its life, with its nucleosynthetic output depending on its initial mass. The mass of stars in a star particle is controlled by the IMF, while its stellar lifetime is controlled by the LIFETIME.DAT table. Within each star particle, a simple stellar population (SSP) forms at  $t = 0$ , consisting of stars of the same age and metallicity but with different masses. The most massive stars evolve and die first, followed by progressively lower-mass stars over time. The key step in constructing the cumulative function is summing these contributions at each timestep  $dt$ . Once the cumulative function is computed for each star particle—taking into account its birth time (or age), the timestep of its formation, and the corresponding turnoff mass—we obtain the total nucleosynthetic yield at a given timestep as a function of cosmic time by summing across all contributing star particles.

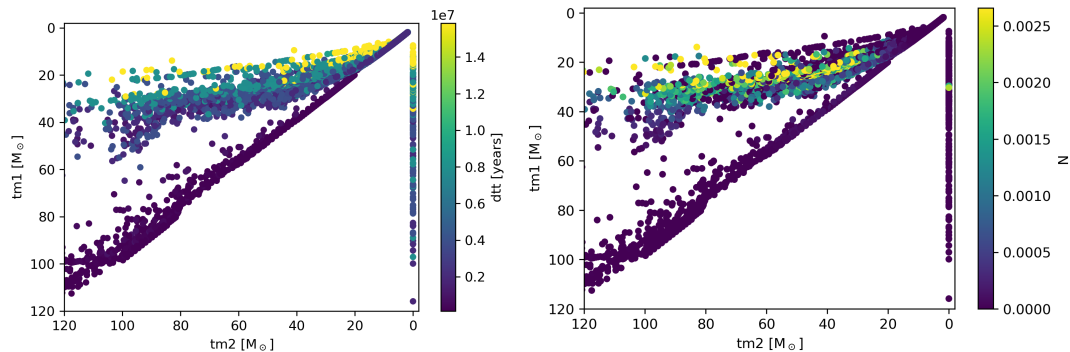


FIGURE 2.3: The contribution of the nucleosynthesis yields cumulative function from the previous timestep with  $M=tm2$  to the current timestep with  $M=tm1$ , as a function of the synchronised individual timestep  $dt$  (left panel) and Nitrogen fraction per unit stellar mass (right panel)

By tracking the cumulative yield, we can determine the efficiency of metal production in different environments. For example, in right panel of Figure 2.3 we use it to track the production of Nitrogen. In our simulation,  $tm1$  is the mass of a star particle at the current timestep ( $t = \text{age}$ ), and  $tm2$  is the mass at the previous timestep ( $t = \text{age} - dt$ ). Left panel of Figure 2.3 shows the timestep from  $tm2$  to  $tm1$  for each star particles, while the right panel shows the Nitrogen fraction per unit stellar mass from  $tm2$  to  $tm1$ . Note that at a given timestep  $dt$ , the function is called for all star particles, meaning, in this plot, multiple points may correspond to the same star particle at different timesteps. In this example, we use an upper mass  $120M_{\odot}$  to focus on the impact of WR stars. Since massive stars die first, all particles have  $tm2 \geq tm1$ , except  $tm2=0$  which is a default

value for new born star particles with age smaller than the timestep (they do not have a previous timestep).

$dt=0$  for  $tm_2=tm_1$  because there is no timestep for the star particle to evolve to its own mass, similarly the metal mass is very small as shown for Nitrogen in the right panel. The cumulative function initially starts at  $M=120M_{\odot}$  for all star particles, so particles with  $tm_2=120M_{\odot}$  are young and just started their contribution. Small  $tm_2$  means the routine already run for a long time, so the star is old and not producing much metals at  $tm_2 \sim 0$ .

Even when two points share nearly identical  $tm_2$  and  $tm_1$ , they can differ in both  $dt$  and  $N$  because the nitrogen yield per unit mass depends sensitively on a star particle's initial metallicity and dominant ejecta channel (primary SN versus secondary AGB). Additionally, our use of adaptive timesteps means that fast SN driven mass loss occurs over short  $dt$ , whereas slower AGB wind mass loss spans much longer  $dt$ .

## 2.6 Stellar Lifetime

Stars return enriched material to the ISM through stellar winds and supernova explosions at the end of their lifetimes. The chemical enrichment model adopted in our simulation follows the prescriptions of Kobayashi (2004). We implement metallicity-dependent main sequence lifetimes from Kodama and Arimoto (1997), as shown in Figure 2.4. Assuming that stars die shortly after leaving the main sequence, these lifetimes determine the stellar mass range of stars ending their lives at each simulation timestep. Within this mass range, the IMF is used to compute the total mass and distribution of stars dying during this timestep.

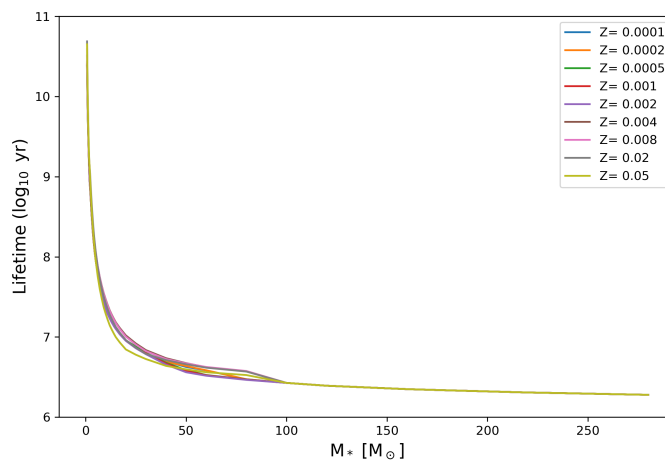


FIGURE 2.4: The lifetime of stars depending on the main sequence metallicity.

## 2.7 Yield Tables

In this section, we describe the yield tables used in our simulation and present the resulting chemical abundances for a selection of elements. We compare how these abundances vary across different yield models, considering variations in progenitor mass and initial metallicity.

### Interpolations

The yield tables are three-dimensional tables that provide the mass yield of each element as a function of the stellar initial mass and metallicity. Since the stellar mass and metallicity do not exactly match in all the yield tables, we use a linear interpolation such as:

$$\frac{y - y_a}{y_b - y_a} = \frac{x - x_a}{x_b - x_a} \quad (2.20)$$

Where  $x$  and  $y$  are the two missing values between  $(x_a, x_b)$  and  $(y_a, y_b)$ , respectively ( $x$  and  $y$  are for yield and stellar metallicity, or yield and stellar mass). The yields are interpolated in both  $M$  and  $Z$  for each element. These yields are then used to create the cumulative function (Section 2.5), from which metal ejection is calculated at each timestep. Finally, the amount of metal ejection are distributed to the ISM using a kernel weighting.

We use several yield tables as functions of the main-sequence mass of the progenitor  $M$  and metallicity  $Z$ , including mass loss. Our SN2SAGBYIELD table contains yields from [Nomoto et al. \(2006\)](#); [Kobayashi et al. \(2006a\)](#), and the three updated models of [Kobayashi et al. \(2011b\)](#) and [Kobayashi et al. \(2020a\)](#). In this table, the effect of rotation is not included. Its content is summarized in the upper table of Figure 2.5, and is described below:

- For AGB yields,  $M = (1.0, 1.25, 1.5, 1.75, 1.9, 2.0, 2.25, 2.5, 3.0, 3.5, 4.0, 4.5, 5.0, 5.5, 6.0, 6.5) M_{\odot}$  and  $Z = (0.0001, 0.004, 0.008, \text{ and } 0.02)$  from [Karakas \(2010\)](#).
- For normal ccSN,  $E_{51} = 1$  is assumed. The supernova tables for  $Z = (0, 0.001, 0.004, 0.008, 0.02, 0.05)$  give yields for  $M = (13, 15, 18, 20, 25, 30, 40) M_{\odot}$ .  $M=40M_{\odot}$  corresponds to failed supernovae, which “fail” to explode and become BHs (they don’t produce iron-peak elements).
- For HNe, a relation between the mass and energy ( $M$ - $E$ ) is used (as estimated from observations and models of supernovae). Hence, the hypernova tables for  $Z = (0.001, 0.004, 0.008, 0.02, \text{ and } 0.05)$  are given for a set of  $(M/ M_{\odot}, E_{51}) = (20, 10), (25, 10), (30, 20), \text{ and } (40, 30)$ .

This table is used in Chapters 3 and 4 (in our simulation C5), while in Chapter 5 we implement two new yield tables (to our new simulation C6), which are summarized in the lower table of Figure 2.5 and described below:

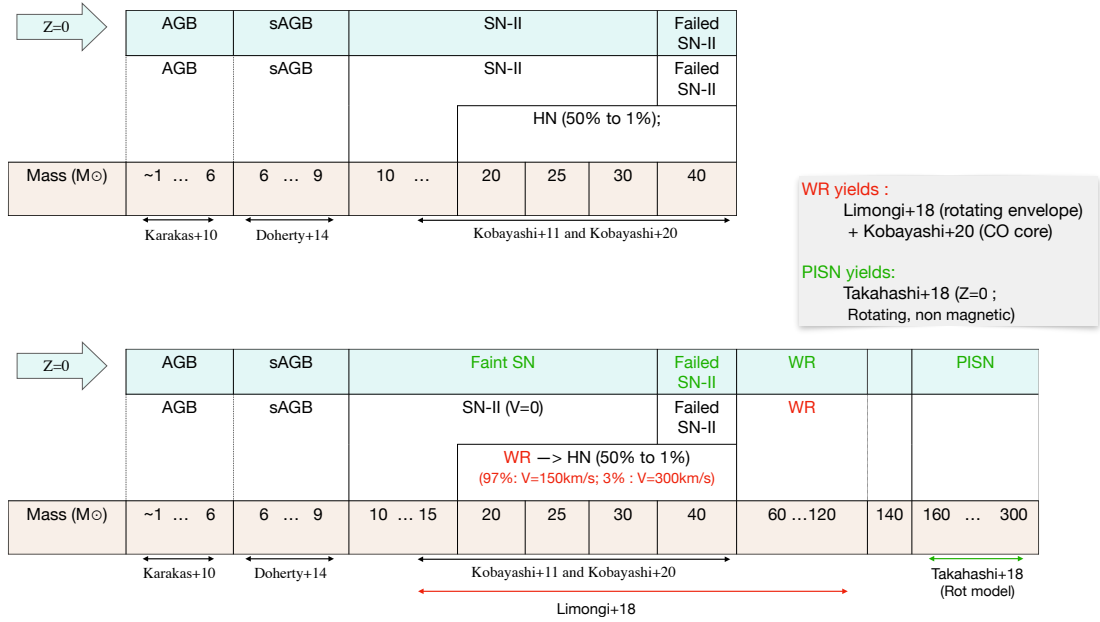


FIGURE 2.5: Upper table: Mass ranges of different stellar yields from our table “SN2SAGBYIELD” used in the cosmological simulations. Lower table: Mass ranges of stellar yields including our new tables “WRSN2SAGBYIELD” and “PISNYIELD”.

- WRSN2SAGBYIELD table, which includes nucleosynthesis yields from Pop III rotating WR up to  $120M_{\odot}$ . It combines the CO core yields from Kobayashi et al. (2020a) with the contributions of C and N from rotating stellar envelopes and winds from Limongi and Chieffi (2018b).
- PISNYIELD table, includes nucleosynthesis yields from Pop III faint SN (cc-SNe with  $M > 15M_{\odot}$  and  $Z = 0$  (Umeda and Nomoto, 2002), with relatively low explosion energies  $E_{51} < 1$ ), as well as WR, and PISNe up to  $300M_{\odot}$ .

Models with  $Z = 0$  represent the very first generation of stars, formed from pristine, metal-free gas. In cosmological simulations, inhomogeneous enrichment occurs, where localized regions receive significant enrichment from earlier supernovae. As a result, even at high redshift, small pockets of metal-rich star formation can emerge. In contrast,  $Z = 0.02$  corresponds to solar metallicity and reflects the typical metallicity of stars forming in the present-day Universe. A metallicity of  $Z = 0.05$  is more than twice the solar value and is referred to as super-solar metallicity; such stars are rarely observed and are often limited to chemically enriched regions in massive galaxies. For comparison, the solar abundance table is taken from Kobayashi et al. 2020a (mostly Asplund et al. 2009).

Yield tables are generated for isotopes up to mass number  $A=35$ . This upper limit reflects the fact that, beyond  $A=35$ , experimentally and theoretically derived reaction-rate data are not well constrained, which would introduce large uncertainties in the calculated stellar yields. Numerous nucleosynthesis codes similarly restrict their output to  $A \leq 35$

### 2.7.1 Yields from AGB and sAGB Stars

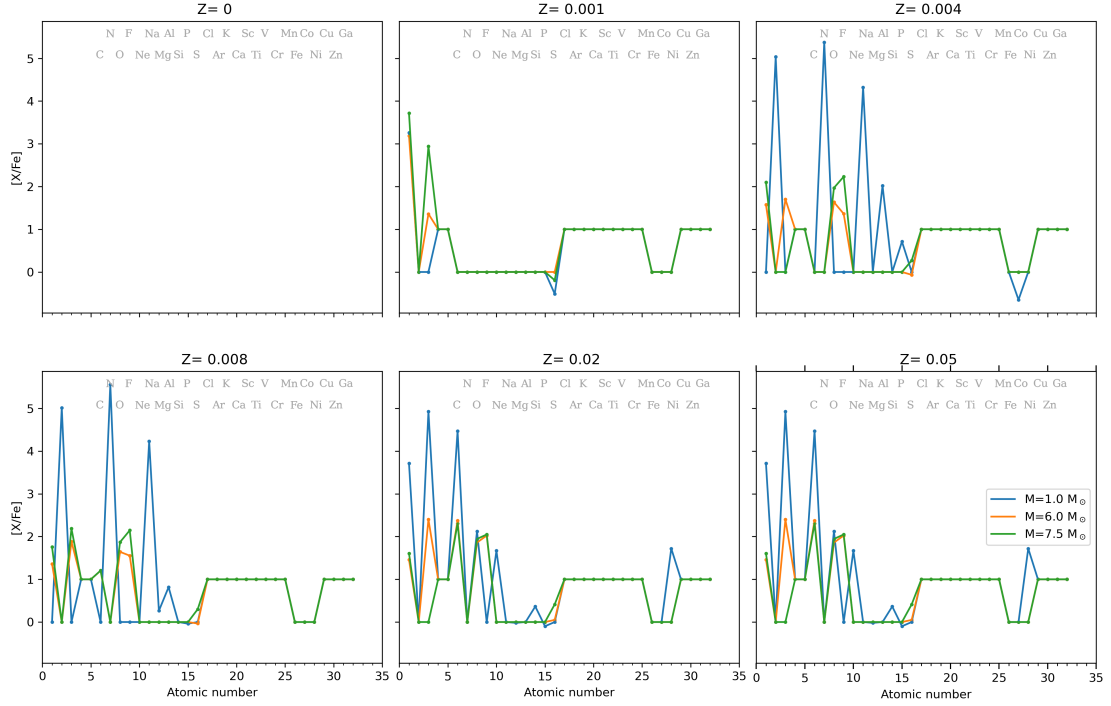


FIGURE 2.6: Mass fractions relative to Fe, normalized by the solar ratio, as a function of atomic number for AGB and sAGB stars. We compare stars with different progenitor masses:  $M = 1M_{\odot}$  (blue),  $M = 6M_{\odot}$  (orange), and  $M = 7.5M_{\odot}$  (green). Each panel corresponds to a different metallicity  $Z$ . Note that AGB yields for Fe are not available at  $Z = 0$ .

The nucleosynthesis yields for AGB stars were initially calculated in [Karakas \(2010\)](#) and [Karakas and Lugaro \(2016\)](#), while yields from super-AGB (sAGB) are from [Doherty et al. \(2014\)](#). We use the latest set introduced in [Kobayashi et al. \(2020b\)](#). These yields are from single stars with progenitor mass  $\lesssim 8 M_{\odot}$ .

Figure 2.6 shows abundance patterns  $[X/Fe]$  as a function of the atomic number for AGB and sAGB stars. We show the yields for models with  $M = 1.0, 6.0,$  and  $7.5 M_{\odot}$  (in blue, orange, and green, respectively). Each panel is for a different metallicity  $Z = (0, 0.001, 0.004, 0.008, 0.02, 0.05)$ .

AGB yields tables contain net yields, i.e. zero and negative values, so to best represent the yields in this figure, we set the following default values :

- If  $X/Fe < 0$ , then we set  $X/Fe = 1$  by default, so that log values become 0.

- If  $X/Fe = 0$ , then we set  $X/Fe = 10$  by default, so that log values become 1.

(i.e., in this figure,  $[X/Fe] = 0$  represents negative yields ( $X/Fe < 0$ ), and  $[X/Fe] = 1$  represent the zero yields ( $X/Fe = 0$ )). When the net yields are between  $0 < Yields < 1$ , we obtain negative  $[X/Fe]$ , which means that proportionally more iron is produced than element X.

Zero metallicity AGB yields are incomplete in the literature. We use models from [Campbell and Lattanzio \(2008\)](#), who discuss metal-free AGB star for  $M = (0.85, 1, 2, \text{ and } 3)M_{\odot}$ . We also use  $M = 0.9M_{\odot}$ , which is interpolated from these original values. On the other hand, more

calculations are available for metal-poor AGB stars ( $Z \sim 0.0001$ ), and for higher metallicities which are self-consistent models.

From this model examples, we see AGB production of light elements such as N and C. No heavy metal is produced for  $M > 3.5 M_{\odot}$ , this assumption may be invalid but does not affect the average chemical evolution of galaxies.

## 2.7.2 Yields from ccSNe

ccSNe originate from stars with masses  $M \gtrsim 8 M_{\odot}$ . “Normal” ccSNe are characterized by explosion energies  $E_{51} \equiv E/10^{51}$  ergs  $\sim 1$  (while HNe are  $\gtrsim 10$  (Section 2.7.3)).

In our model, ccSNe span a progenitor mass range of  $10\text{--}40 M_{\odot}$ . Yields for these events were first calculated in Kobayashi et al. (2006a) and later updated in Kobayashi et al. (2011a). In this work, we adopt a more recent set of yields that includes the effects of failed supernovae (no Fe production at  $40 M_{\odot}$ ), as introduced in Kobayashi et al. (2020b).

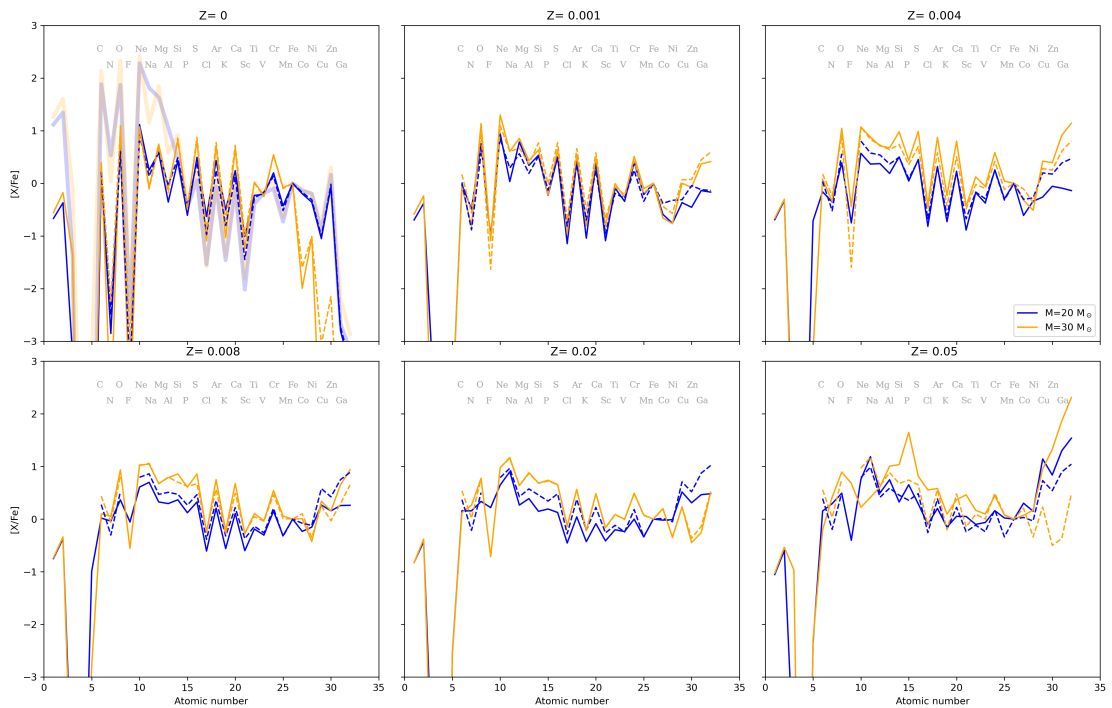


FIGURE 2.7: Same as Figure 2.6, but showing yields from ccSN used in C5 (solid lines, without WR), ccSN used in C6 (dashed lines, with WR) and faint supernovae (thick solid lines at  $Z = 0$ ). We compare stars with progenitor mass  $M = 20 M_{\odot}$  (blue) and  $30 M_{\odot}$  (orange).

Figure 2.7 shows the abundance patterns  $[X/Fe]$  as a function of atomic number for supernova ejecta. The results are shown for progenitor masses of  $M = 20 M_{\odot}$  (blue) and  $30 M_{\odot}$  (orange) and metallicities  $Z = (0, 0.001, 0.004, 0.008, 0.02, 0.05)$ . We compare different supernova models: solid lines represent normal cc-SNe with  $E_{51} = 1$ , dashed lines correspond to cc-SNe with WR progenitors, and thick solid lines in the top-left panel ( $Z = 0$ ) show yields from faint supernovae

(see Table 2.5). Faint supernova models exhibit strong production of  $\alpha$ -elements, particularly with prominent peaks in C and O.

At metallicities  $Z = 0$  and  $Z = 0.0001$ , we observe a pronounced zigzag pattern in the elemental abundances, which arises from the so-called odd- $Z$  effect, a contrast between elements with odd and even atomic numbers ( $Z$ ). Odd- $Z$  elements are primarily produced through secondary nucleosynthesis, which depends on the presence of pre-existing C and O. As a result, their production increases with higher initial metallicity. In contrast, even- $Z$  elements are predominantly produced through primary nucleosynthesis, and their yields remain relatively constant across different metallicities (Kobayashi et al., 2006a). This difference leads to the characteristic zigzag pattern in elemental abundances. As metallicity increases, the contrast between odd- $Z$  and even- $Z$  elements becomes less pronounced, as shown in the figure.

In our model, the yields from faint supernovae (represented by thick solid lines) and HNe are applied exclusively at  $Z = 0$ . These events predominantly produce C and O elements, while contributing only small amounts of iron-peak elements due to larger fallback.

### 2.7.3 Yields from HNe

HNe are extremely energetic ccSN explosions, typically associated with the deaths of massive stars ( $M_* > 20, M_\odot$ ). They release significantly more energy than normal supernovae, often exceeding  $10^{52}$  ergs, corresponding to  $E_{51} \geq 10$ . Hypernovae are important contributors to the nucleosynthesis of heavy elements, particularly iron and some  $r$ -process elements.

In this work, we adopt the updated yield set from Kobayashi et al. (2006a), as presented in Kobayashi et al. (2020b). The fraction of stars exploding as HNe depends on metallicity, with values of  $f_{\text{HNe}} = (0.01, 0.01, 0.23, 0.4, 0.5, 0.5)$  for  $Z = (0.05, 0.02, 0.008, 0.004, 0.001, 0.0)$ , respectively, and is linearly interpolated for metallicities in between (Kobayashi and Nakasato, 2011a). Stars with  $M=40 M_\odot$  explode only as HNe (otherwise are failed supernovae, Section 2.7.2)

Figure 2.8 presents the abundance patterns ( $[X/\text{Fe}]$  as a function of atomic number) of HNe at metallicities  $Z = (0, 0.001, 0.004, 0.008, 0.02, 0.05)$ , for progenitor masses of  $M=20, 30$  and  $40, M_\odot$  (blue, orange, and green, respectively). HN yields show a small dependence on progenitor mass, though the variation is less pronounced compared to other supernova models. Lower-mass hypernovae (e.g.,  $M=20M_\odot$ ) tend to produce slightly more light elements. Models that include WR progenitors (dashed lines) produce more element such as N and F due to stellar rotation.

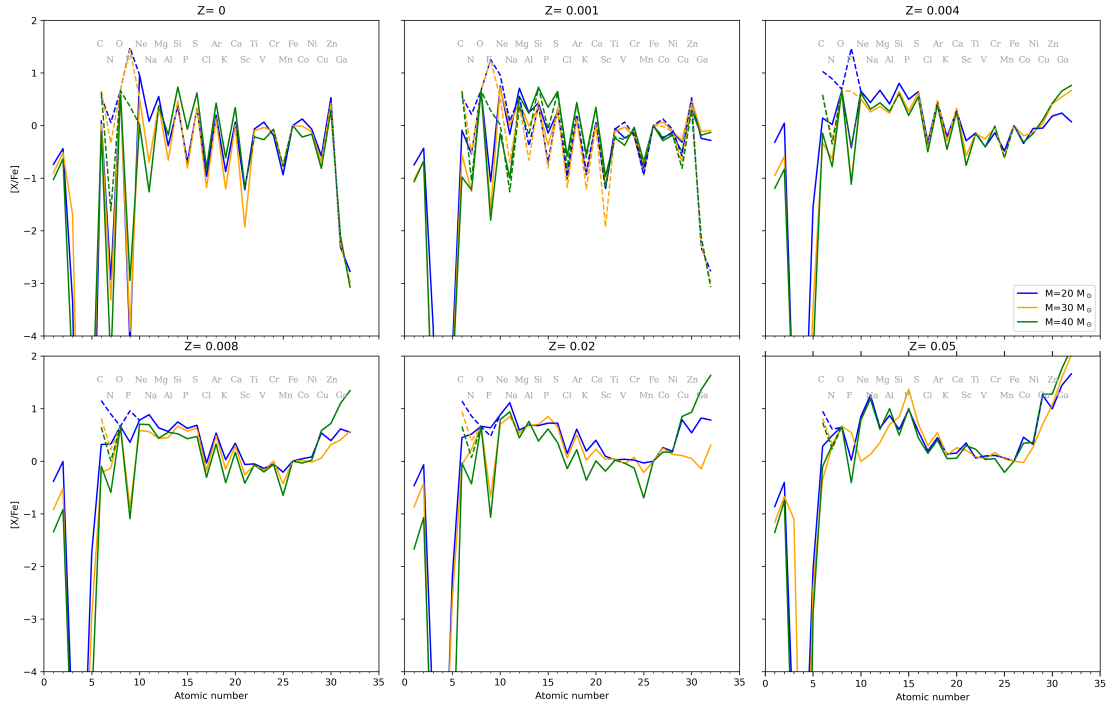


FIGURE 2.8: Same as Figure 2.6, but showing yields from HNe used in C5 (solid lines), HNe used in C6 (dashed lines). We compare stars with progenitor mass  $M = 20M_{\odot}$  (blue),  $30M_{\odot}$  (orange) and  $40M_{\odot}$  (green).

## 2.7.4 Yields from WR stars

Figure 2.9 is the same as Figure 2.8, but for WR stars with progenitor masses of  $M=60, 80,$  and  $120 M_{\odot}$  (blue, orange, green, respectively). It shows that WR stars primarily produce light elements, particularly C and N. Since these massive WR stars do not explode, they do not contribute significantly to the production of iron-peak elements, which are typically formed during explosive nucleosynthesis. However, WR stars evolve in non-zero metallicity environments, meaning they already contain some iron. This pre-existing iron explains the small Fe content seen in their ejecta.

The WR yield tables include negative yields for certain elements, representing net destruction during stellar evolution. To visualize this, we adopt the same convention used for AGB stars: in the figure,  $[X/Fe] = 0$  corresponds to negative yields, and  $[X/Fe] = 1$  indicates zero net production.

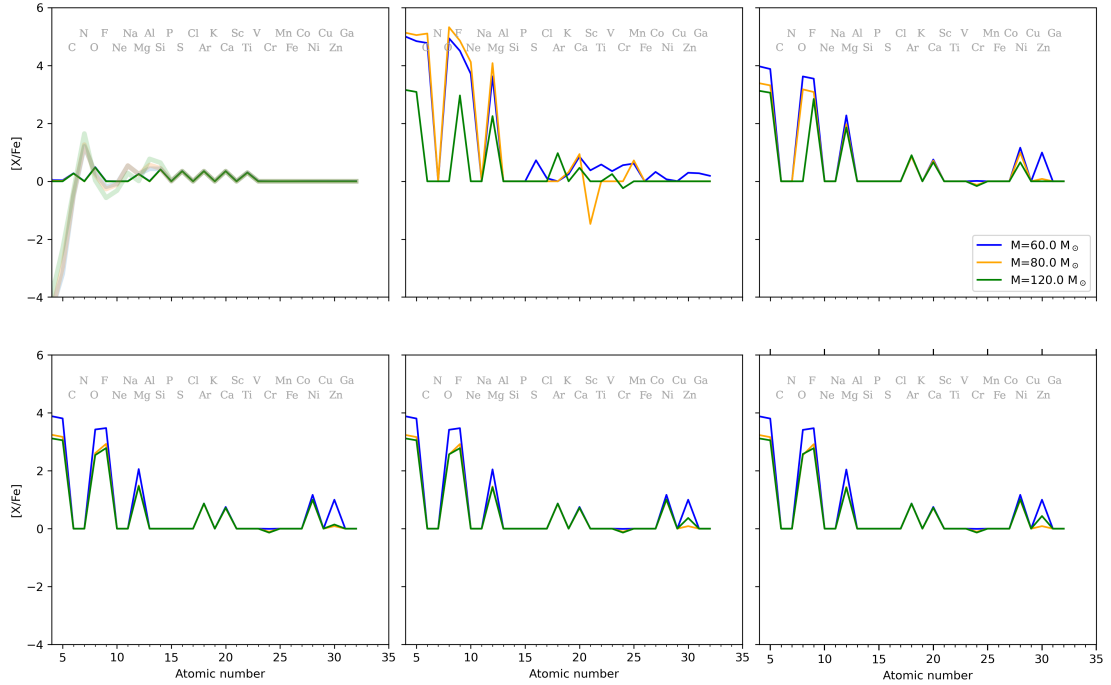


FIGURE 2.9: Same as Figure 2.6, but showing yields from WR stars from our WRSN2SAGBYIELD table (solid lines) and PISNYIELD table (thick solid lines, at  $Z = 0$ ). We compare stars with progenitor mass  $M = 60M_{\odot}$  (blue),  $80M_{\odot}$  (orange) and  $120M_{\odot}$  (green).

### 2.7.5 Yields from PISNe

Figure 2.10 presents the abundance patterns ( $[X/Fe]$  as a function of atomic number) of PISNe at zero metallicity ( $Z = 0$ ) for progenitor masses of  $M=160, 180, 240,$  and  $280 M_{\odot}$ . The yields are shown for three types of stellar models from Takahashi et al. (2018): non-rotating (left panel), non-magnetic rotating (middle panel), and magneto-rotating stars (right panel). A notable feature of these models is the low production of iron-peak elements such as Zn and Co, which results from the relatively low central temperatures at core bounce during collapse (Umeda and Nomoto, 2002; Heger and Woosley, 2002). In contrast, the large abundances of Si, S, and Ca are attributed to explosive oxygen burning.

A characteristic of PISN yields is the pronounced odd-even effect, which is significantly stronger than that seen in cc-SN. This zigzag pattern arises due to the efficient production of iron-group elements in a stable environment. Despite their predicted high luminosities, due to the large amount of Fe produced, PISNe have yet to be observed.

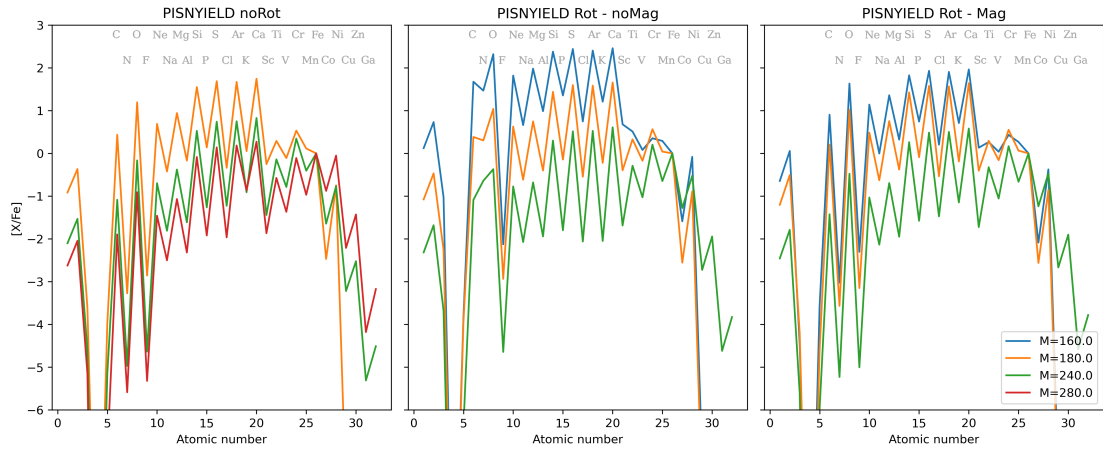


FIGURE 2.10: Mass fraction relative to Fe, normalized by the solar ratio, as a function of atomic number for PISN stars. We compare stars with different progenitor masses:  $M = 160M_{\odot}$  (blue),  $M = 180M_{\odot}$  (orange),  $M = 240M_{\odot}$  (green) and  $M = 280M_{\odot}$  (red). Each panel corresponds to a different model: non-rotating stars (left), non-magnetic rotating stars (middle), and magnetic rotating stars (right).

### 2.7.6 Other Yield Tables

Nucleosynthesis yields from SN-Ia are included in our simulations, following the models of [Kobayashi et al. \(2020b\)](#). In contrast, models of NSM, MRSNe, ECSNe, and neutrino-driven wind (NDWs) have not yet been observed at high redshift and are therefore not included in our cosmological simulation. However, even if they were included, we expect their contribution to the chemical enrichment of elements up to Zn (which can be observed in high-redshift galaxies) to be minor, and their impact on elements beyond Zn to be negligible. To quantitatively assess this assumption, we plan to incorporate these enrichment channels in future work.

## 2.8 Supernova Feedback

Supernova feedback is a crucial mechanism in galaxy formation and evolution, regulating star formation and shaping gas and stellar distribution within galaxies. It originates from the explosive deaths of massive stars, which inject energy, momentum, and enriched material into the surrounding interstellar medium. Without supernova feedback, simulations predict an overabundance of compact, massive galaxies with unrealistically high star formation rates, contradicting observations. This process heats and disperses gas, reducing star formation in low-mass galaxies and driving galactic outflows that redistribute metals.

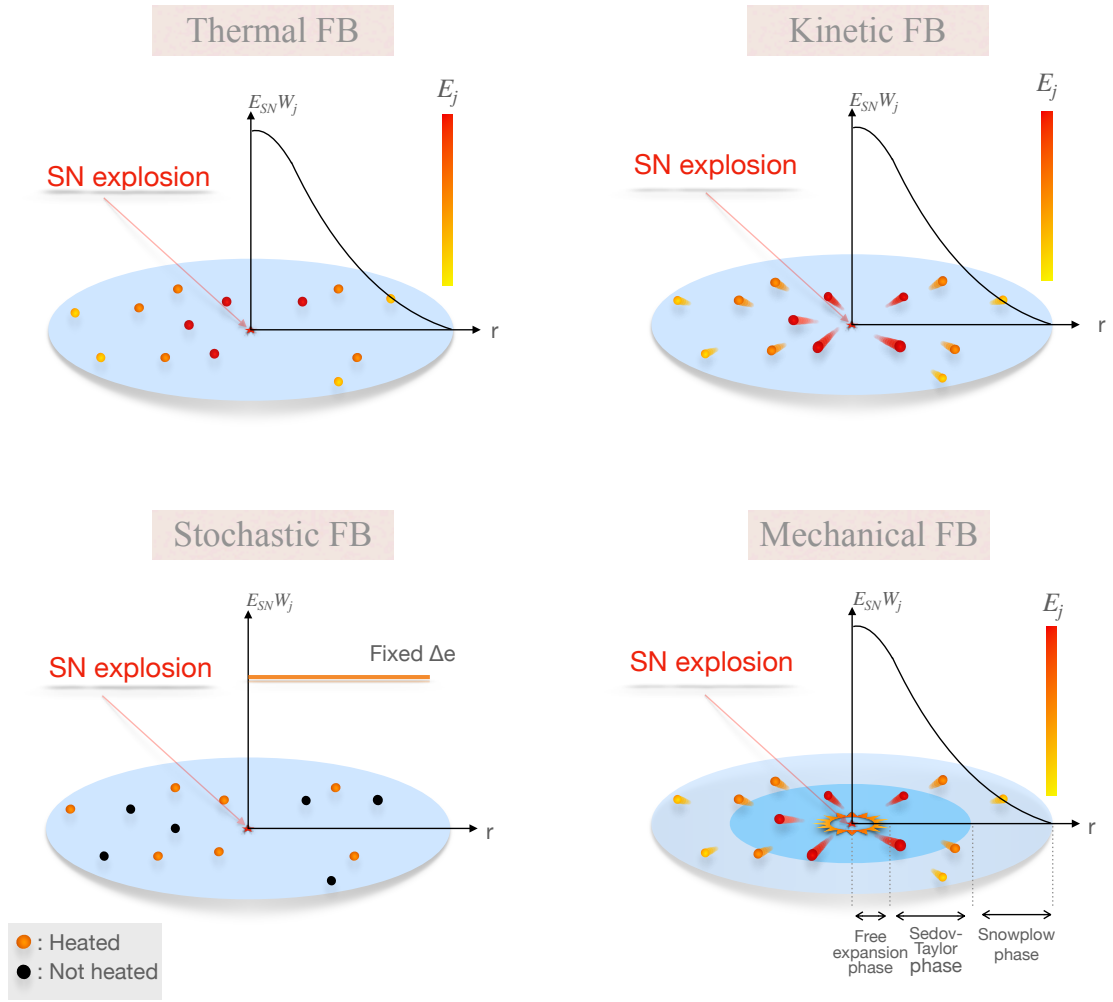


FIGURE 2.11: Schematic representation of the four supernova feedback models employed in this study.

### Metal distribution

In this work, we distribute metals to the ISM following the same criteria as Kobayashi (2004), where element ejections from stellar winds (SW;  $E_{SW}$ ) and from ccSN ( $E_{SNcc}$ ) for a single star particle at a given timestep can be calculated as

$$E_{SW} = \int_{tm2}^{tm1} (1 - w_m - p_{z_i, m, \Pi}) Z_i \phi(m) dm, \quad (2.21)$$

$$E_{SNcc} = \int_{tm2}^{tm1} p_{z_i, m, \Pi} \phi(m) dm. \quad (2.22)$$

Where the mass fraction of each element  $i$  in the gas-phase increases via element ejections from  $E_{SW}$  and  $E_{SNcc}$ .  $tm1$  and  $tm2$  represent the turnoff mass at the current and previous timestep, respectively.  $w_m$  is the remnant mass fraction, it equals the mass fraction of a WD (for stars with initial masses  $m \lesssim 8M_{\odot}$ ), a NS (for  $\sim 8 - 20M_{\odot}$ ) or a BH (for  $m \gtrsim 20M_{\odot}$ ).  $p_{z_i, m, \Pi}$  is the

nucleosynthesis yields of cc-SN, as a function of  $m$ ,  $Z$ , and explosion energy.  $Z_i$  is the metallicity of a star particle  $\phi(m)$  is the IMF.

For energy production, we calculate the event rates (the number of events per timestep) of SWs ( $\mathcal{R}_{\text{SW}}$ ), ccSNs ( $\mathcal{R}_{\text{SNcc}}$ ) as

$$\mathcal{R}_{\text{SW}} = \int_{\max[tm2, 8]}^{tm1} \frac{1}{m} \phi(m) dm, \quad (2.23)$$

$$\mathcal{R}_{\text{SNcc}} = \int_{\max[tm2, 8]}^{\min[tm1, 50]} \frac{1}{m} \phi(m) dm. \quad (2.24)$$

For ccSNe, we set the lower and upper mass limits as (8 and 50  $M_{\odot}$ ) or IMF limits, while SWs use the IMF upper limit. SNIa ( $\mathcal{R}_{\text{Ia}}$ ) also produce energy following similar equations (Kobayashi and Taylor, 2023).

### Energy distribution

Different implementations of energy feedback influence the efficiency of this process, impacting the structure, metallicity, and stellar mass function of galaxies. In this work, we use (1) the thermal feedback distributing pure thermal energy to the neighbour gas particles, (2) the stochastic feedback (similar to Dalla Vecchia and Schaye 2012) distributing thermal energy in a stochastic way to a random number of particles with the probability parameter, (3) the kinetic feedback (Navarro and White, 1993) partially converting the thermal energy into kinetic energy, and (4) the mechanical feedback (Hopkins et al., 2018), which accounts the physics during the Sedov-Taylor phase of supernova expansion, using the fraction parameter. Of the four supernova feedback schemes implemented in this work, the mechanical feedback model is the most astrophysically realistic. Unlike purely thermal or kinetic prescriptions, mechanical feedback explicitly injects the terminal momentum of a supernova remnant calibrated to the Sedov-Taylor phase, ensuring that the momentum-driven snowplough phase is captured even when unresolved by the simulation's resolution (Kimm et al., 2015; Martizzi et al., 2015). By injecting momentum directly (rather than relying exclusively on thermal energy, which can be rapidly radiated away in dense gas) this model preserves the correct momentum budget of individual explosions, driving more realistic galactic outflows and suppressing artificial overcooling. As a result, it naturally reproduces key observables such as the normalization and slope of the mass-metallicity relation and the redshift evolution of metallicity gradients, without the need for arbitrary cooling shut-off times or fixed wind velocities (Hopkins et al., 2018). These models are cartooned in Figure 2.11 and described in details in Chapter 3.

## 2.9 Galaxy properties

Dark matter halos are found in each snapshot using the Friends-of-Friends algorithm with a linking length of  $b=0.2$  times the mean inter-particle spacing (Springel et al., 2005). Once a halo

is identified, we define its galaxy simply by collecting all gas and star particles within a 20 kpc radius of the halo's centre. Galaxy properties (stellar mass, SFR, metallicity, size, etc.) are then measured from those particles.

### 2.9.1 Star Formation Rates

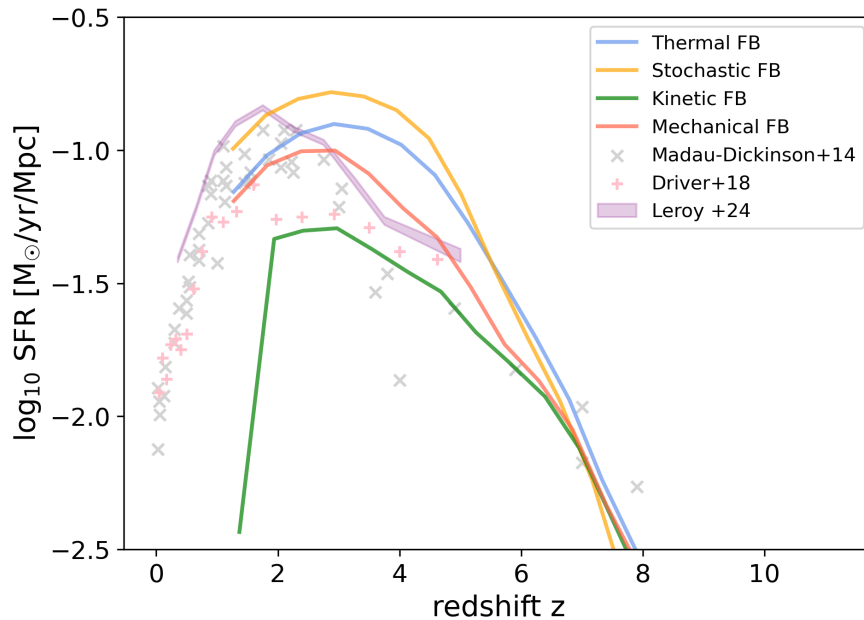


FIGURE 2.12: Cosmic star formation rate history of our  $25 h^{-1}$  Mpc simulations with different feedback models: thermal (blue), stochastic (orange), kinetic (green), and mechanical (red). Observational data are taken from [Madau and Dickinson \(2014, grey cross\)](#), [\(Driver et al., 2018, pink plus\)](#), and [\(Leroy et al., 2024, purple line\)](#).

Figure 3.6 shows the cosmic SFR history obtained using four different feedback models with fiducial parameters in our  $25 h^{-1}$  Mpc simulation volume. The SFR increases with time, peaking at the so-called cosmic noon around redshift  $z \sim 2$ , where star formation was at its highest. It then declines toward lower redshifts due to the depletion of cold gas and the increasing influence of feedback from supernovae and AGN, which suppress further star formation.

In this figure, we present the currently available simulation outputs, which extend down to  $z = 1.5$ . Lower redshift evolution, with in a smaller volume box, is shown and discussed in Chapter 3.

Among the models, thermal and stochastic feedback produce relatively high SFRs due to weaker feedback. Kinetic feedback performs well at high redshift ( $z > 2$ ) but suppresses star formation too strongly at  $z = 1.5$ , leading to a premature quenching of galaxy growth. In contrast, the mechanical feedback model provides a more balanced regulation of star formation and shows the best agreement with observational data across redshift. Observational data are taken from [Madau and Dickinson \(2014, grey crosses\)](#), [\(Driver et al., 2018, pink plus\)](#), and [\(Leroy et al., 2024, purple line\)](#).

At  $z \geq 6$  all feedback models produce nearly identical cosmic star-formation rates. In this regime the high gas densities and rapid accretion overwhelm or rapidly radiate away injected energy, so the details of the feedback implementation matter little. At redshifts below  $z \sim 4$ , however, halo gas densities drop and cooling times increase, while cosmic inflow slows. Under these conditions feedback energy is retained longer and drives more efficient outflows, so differences between the four models become more pronounced, leading to the growing separation of the curves.

## 2.9.2 Galaxy Stellar Mass Function

Figure 2.13 shows the evolution of the GSMF in the cosmological hydrodynamical simulations with the thermal (blue), stochastic (orange), and mechanical (red) feedback models from  $z = 5$  to  $z = 0.7$ . It shows a general decline in number density  $\Phi$  with increasing redshift, consistent with the hierarchical growth of galaxies.

At  $z = 0.7$ , the simulations reasonably agree with observational data (dashed lines). At the high-mass end, they tend to underpredict the GSMF due to the relatively small box volume used here ( $25 h^{-1}$  Mpc); this also causes the simulated GSMF to fall below observational estimates (e.g., Tomczak et al. 2014) at higher redshifts ( $z \geq 2$ ), particularly for  $\log(M_*) > 10.5 M_\odot$ , suggesting an overestimation of feedback efficiency or insufficient early star formation. The mechanical feedback results in the strongest suppression of massive galaxies, while the stochastic feedback enhances star formation, leading to a higher GSMF at intermediate masses.

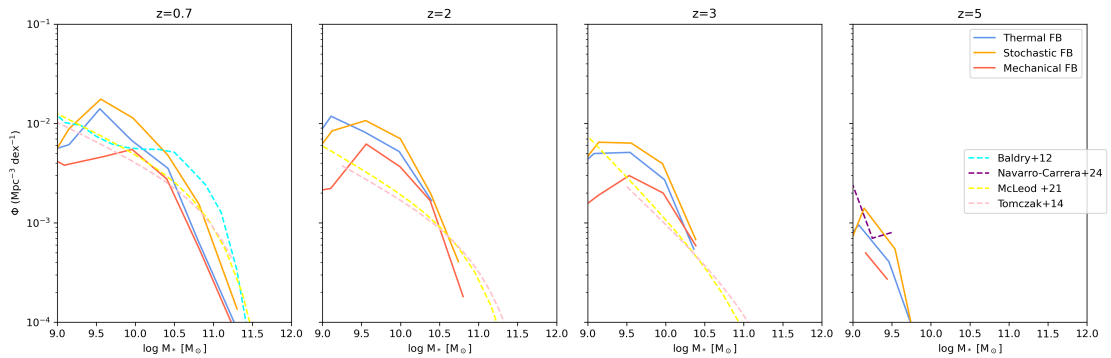


FIGURE 2.13: Evolution of the galaxy stellar mass function from  $z = 5$  to  $z = 0.7$  in a  $25 h^{-1}$  Mpc box volume. The solid lines are our simulations with the thermal (blue), stochastic (orange), mechanical (red) feedback models. The dashed lines are observational data from Baldry et al. (2012); Tomczak et al. (2014); McLeod et al. (2021); Navarro and White (1993).

## 2.9.3 Galaxy Luminosity Function

Figure 2.14 shows the evolution of the rest frame V-band luminosity function from with the thermal (blue), stochastic (orange), and mechanical (red) feedback models, demonstrating a general decline in the number density ( $\Phi_V$ ) of galaxies with increasing redshift.

At  $z = 0.7$ , the simulated luminosity function is in reasonable agreement with the observational data from [Marchesini et al. \(2012\)](#) at magnitudes  $M_V \sim -19$ , and shows a lower number of bright galaxies (with  $M_V < -18$ ), suggesting a suppression of high-luminosity systems due to strong feedback effects.

At higher redshifts ( $z \geq 2$ ), the luminosity functions with all feedback models show lower densities than the observation, especially at the bright end. The stochastic feedback results in the highest galaxy number densities, while mechanical feedback shows the strongest suppression of bright galaxies, suggesting stronger feedback.

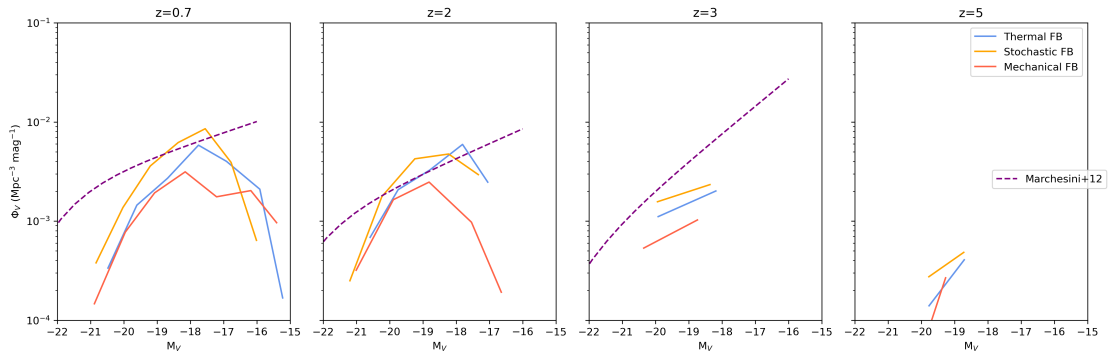


FIGURE 2.14: Evolution of the rest-frame V-band luminosity function from  $z = 5$  to  $z = 0.7$  in a  $25 h^{-1}$  Mpc box volume. The solid lines are our simulations with the thermal (blue), stochastic (orange), mechanical (red) feedback models. The purple dashed line is observational data from [Marchesini et al. \(2012\)](#)

## 2.9.4 Size-Mass Relation

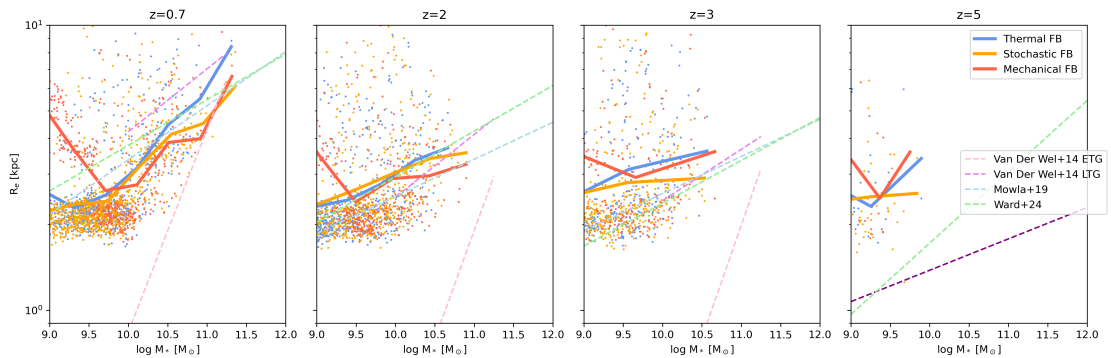


FIGURE 2.15: Evolution of the galaxy size–mass relation in a  $25 h^{-1}$  Mpc box. The dots show individual simulated galaxies at each redshift, color-coded by feedback model (thermal: blue; stochastic: orange; mechanical: red), the solid lines represent the median for the corresponding model. Dashed lines are observational data from [van der Wel et al. \(2014\)](#), [Mowla et al. \(2019\)](#), and [Ward et al. \(2024\)](#). Panels from left to right show  $z=0.7, 2, 3$ , and  $5$ .

Figure 2.15 shows the evolution of the size-mass relation with the thermal (blue), stochastic (orange), and mechanical (red) feedback models. It shows a general trend of increasing galaxy effective radius ( $R_e$ , see Chapter 4) with stellar mass, consistent with observational constraints.

At  $z = 0.7$ , the simulations are in agreement with observational data from [van der Wel et al. \(2014\)](#) and [Ward et al. \(2024\)](#) for  $\log(M_*) > 10.5$ , but at lower mass, the simulations predict smaller galaxy sizes. Under mechanical feedback, galaxies with  $\log(M_*/M_\odot) \lesssim 10$  exhibit larger  $R_e$  at fixed mass compared to thermal or stochastic models. This is because mechanical feedback model injects momentum that more efficiently evacuates central gas and redistributes it to larger radii. Early central star formation is thus delayed, and subsequent star formation occurs farther out, producing a more extended stellar component. At higher redshifts ( $z \geq 2$ ), the simulated galaxies continue to follow a mass–size relation, with effective radii increasing systematically with stellar mass. The scatter is larger at the low-mass end, while the relation becomes tighter for massive galaxies. In our simulations, the overall galaxy mass–size relation is well reproduced, but the evolution of galaxy sizes with redshift appears weaker than in observations. While observational studies typically find that galaxy sizes evolve approximately as  $R_e \propto (1+z)^{-1}$  (e.g. [van der Wel et al. 2014](#); [Mo et al. 1998](#)), our results show comparatively weak redshift dependence, consistent with earlier findings by [Taylor and Kobayashi \(2016\)](#), who reported similarly subtle evolution at the massive end. This discrepancy is likely linked to numerical resolution, which limits the ability of cosmological simulations to capture the compactness of high-redshift systems and the subsequent size growth at later times. Moreover, galaxy size is sensitive to the development of extended stellar disks, which at low redshift can substantially increase the effective radius. However, the accretion of cold gas onto the disk plane occurs on small physical scales that are not fully resolved in our runs, leading to an underprediction of size growth.

### 2.9.5 Mass-Metallicity Relation

All stellar metallicities in this work are luminosity-weighted, matching the fact that integrated-light abundance measurements from absorption features are dominated by the brightest stars. Gas-phase metallicities are SFR-weighted, since emission-line diagnostics preferentially sample the H II regions around young, massive stars where star-formation (and hence line luminosity) is highest. The top panels of [Figure 2.16](#) show the V-band luminosity-weighted stellar MZR for the thermal (blue, solid line), stochastic (orange, dash-dotted), kinetic (green, dashed) and mechanical (red, dense dash-dotted) feedback models from  $z = 0.7$  to 5. The lines show the medians of all individual galaxies identified in our simulations, while the shaded areas show the  $1\sigma$  scatter of the individual galaxy measurements at each redshift. The dotted lines and symbols are observational data. We use a solar metallicity  $Z_\odot = 0.015$ .

At  $z = 0.7$ , our kinetic model seems too strong and does not produce enough metals to explain the observations ([Chapter 3](#)). Despite no overlap in the mass range, this model seems consistent with data from [Gallazzi et al. \(2014\)](#). However, we note its large error bar of  $\sim 1$  dex. The thermal and stochastic models overproduce metals compared to the mechanical feedback for low-mass galaxies ( $M < 10^{10}M_\odot$ ), which result in significantly higher metallicities than in [Gallazzi et al. \(2014\)](#) for massive ones. These models suggest that the stellar mass–metallicity relation has not

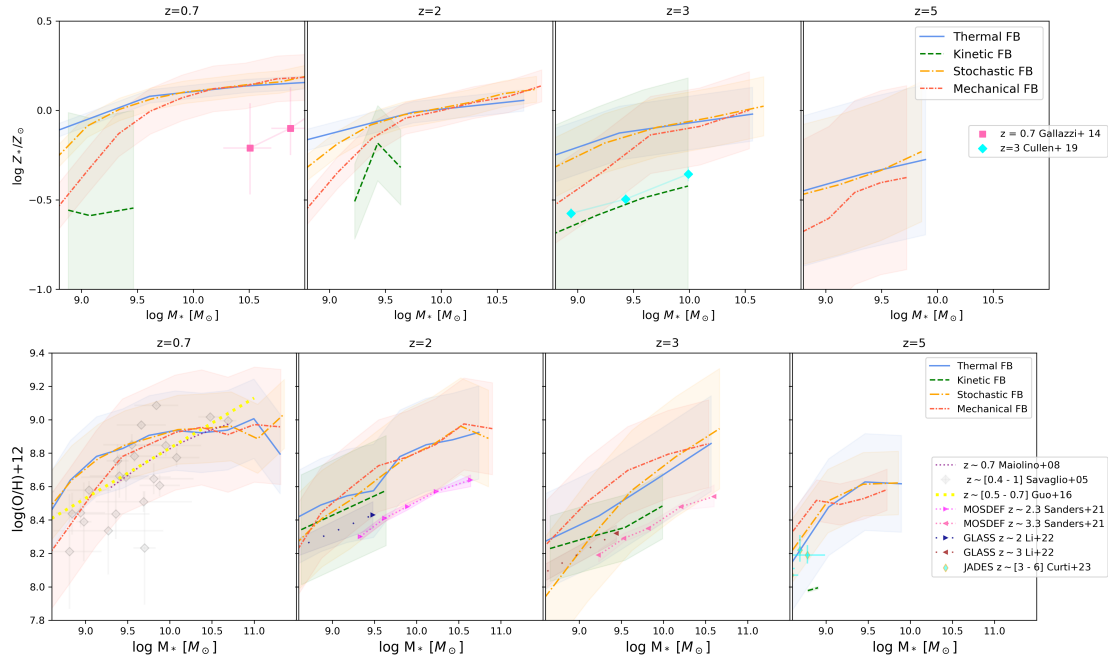


FIGURE 2.16: Top panel: Redshift evolution of the luminosity-weighted stellar MZR of galaxies for the thermal (blue, solid), stochastic (orange, dash-dotted), kinetic (green, dashed), and mechanical (red, dash-dotted) feedback models in a  $25 h^{-1}$  Mpc box volume. The solid lines are for the medians, and the shaded areas show the  $1\sigma$  scatter of individual galaxies. Observational data are taken from Gallazzi et al. (2014,  $z = 0.7$ ), and Cullen et al. (2019,  $z = 3$ , with  $+0.5$  dex shift for  $[O/Fe]$ ). Bottom panel is the same but for the SFR-weighted gas-phase MZR. Observational data (dotted with different symbols) are from Maiolino et al. (2008,  $z \sim 0.7$ ), Savaglio et al. (2005,  $z \sim 0.4 - 1$ ), Guo et al. (2016,  $z \sim 0.5 - 0.7$ ), Sanders et al. (2021,  $z \sim 2 - 3$ ), Li et al. (2022,  $z \sim 2 - 3$ ), and Curti et al. (2024b,  $z \sim 3 - 6$ ).

significantly evolved between  $z \sim 0.7$  and  $z \sim 3$ , at least at the massive end, contrary to the kinetic model. At  $z = 3$ , the UV observations from Cullen et al. (2019) for Fe abundances are shifted by  $+0.5$  dex, taking into account the typical  $[O/Fe]$  enhancement, and seem to nicely match our kinetic model, but again, we note the large error bar of  $\sim 1$  dex for this model. The shift is necessary because Cullen et al. (2019) measure Fe abundances directly from UV absorption lines, whereas in our simulations we track the total metal content. Since oxygen and other  $\alpha$ -elements dominate the overall metal budget and are enhanced relative to Fe in young stellar populations, a correction of  $\sim 0.5$  dex is applied to bring the observed Fe abundances onto a comparable total-metallicity scale. At  $z = 5$ , the kinetic model only produces two low-mass galaxies, which explains the absence of MZR for this model. At high redshifts, we retrieve the MZR for thermal, stochastic and mechanical models. The metallicity at a given mass increases by  $\sim 0.3$  dex from  $z = 5$  to  $z = 0.7$ . The thermal feedback always produces slightly more metals than the other models for  $M < 10^{10} M_{\odot}$ , and the kinetic feedback results in significantly lower stellar metallicities than in the other models. Overall, the supernova feedback has a more significant impact on the metallicity at the low-mass end, where low-mass galaxies eject more metals into the intergalactic medium (Kobayashi et al., 2007).

The bottom panel of Figure 2.16 is the same but for the gas-phase MZR with SFR-weighted gas oxygen abundance from  $z = 0.7$  to 5 for the same four feedback models. The lines show the medians of individual galaxies in our simulations. The kinetic-feedback curves at  $z = 0$  and  $z = 5$  are omitted due to the small number of galaxies in those snapshots (more detail in Chapter 3). The dotted lines and symbols represent observational data at various redshifts. All observational data have been converted for the Kroupa IMF.

At  $z = 0.7$ , our kinetic feedback has no star-forming galaxies, which explains the absence of MZR. While our mechanical feedback model most agrees with observed data from Maiolino et al. (2008), Savaglio et al. (2005) and Guo et al. (2016). With this resolution, we have a limited sample, but we still retrieve the MZR at all redshifts with thermal, stochastic and mechanical. At higher redshifts, the metallicities at a given mass are considerably lower for the kinetic feedback due to the suppression of star formation, leading to few metal-poor low-mass galaxies. At  $z = 5$ , the sample of galaxies with the kinetic feedback is too limited to show the MZR. We find a significant evolution from  $z \sim 5$  to 0.7 for the gas-phase MZR in the thermal, stochastic and mechanical feedbacks ( $\sim 0.2$  dex). At higher redshifts, the MOSDEF (Sanders et al., 2021) and GLASS survey with NIRISS slitless spectroscopy on JWST (Li et al., 2022) showed  $\sim 0.1$  and  $\sim 0.07$  dex evolution from  $z \sim 2$  to  $z \sim 3$ , respectively, which is larger than in all our models ( $\sim 0.07$  dex), except for the kinetic. The kinetic feedback model fits well with the later, but as discussed previously, this model is underproducing stars, so this matching does not necessarily support the kinetic feedback of supernovae. At  $z = 5$ , the JADES survey (Curti et al., 2024b) with JWST/NIRSpec at  $3 < z < 6$  for low mass galaxies show a nice match with our thermal model.

## 2.9.6 Metallicity gradients

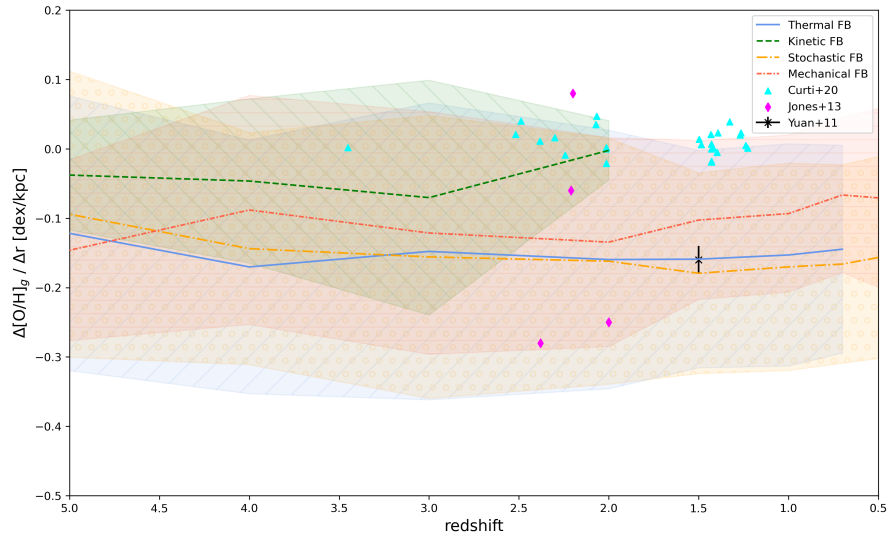


FIGURE 2.17: SFR-weighted gas-phase metallicity gradient as a function of redshift, for all galaxies in our simulations with the thermal (blue solid line), kinetic (green dashed), stochastic (orange dash-dotted), and mechanical (red dense dash-dotted) feedback models, in a  $25 h^{-1}$  Mpc box volume. The shaded areas are  $1\sigma$  scatter of the individual galaxies. The symbols are observational data from Yuan et al. (2011, black cross) using AO-assisted spectroscopy OSIRIS on Keck II on a face-on spiral galaxy at  $z \sim 1.5$ , Jones et al. (2013, magenta diamonds) using AO-assisted spectroscopy OSIRIS on Keck on gravitationally lensed systems, and Curti et al. (2020a, cyan triangle) using KMOS KLEVER survey on 42 gravitationally lensed galaxies.

Figure 2.17 shows the SFR-weighted gas-phase metallicity gradients as a function of redshift for all our galaxies with the thermal (blue solid line), kinetic (green, dashed), stochastic (orange, dash-dotted), and mechanical (red, dense dash-dotted) feedback models. The gradient is measured within  $2R_e$  where  $R_e$  is the effective radius of each galaxy. We show the redshift evolution from  $z = 5$  up to  $z = 0.5$  for the stochastic and mechanical models, to  $z = 0.7$  for the thermal model, and to  $z = 2$  for the kinetic feedback which stops forming stars after  $z = 2$  with this resolution. The shaded areas show the  $1\sigma$  scatter of the individual galaxies at each redshift.

The symbols represent observational data from Curti et al. 2020a (cyan triangle), Yuan et al. 2011 (black cross), Jones et al. 2013 (magenta diamonds). These observational data nicely match our gradients with the kinetic feedback near  $z \sim 2$ . The gradients with the mechanical feedback is flatter than those with thermal and stochastic feedback, but with all three supernovae feedback models, the median gradients remain mostly negative at all redshifts, suggesting that galactic centers are more metal-rich than the outskirts. A detailed analysis of both of the stellar and gas-phase metallicity gradients will be discussed in Chapter 4.

## 2.10 Summary

In this chapter, we have described the numerical framework and physical ingredients forming the basis of our chemodynamical simulations. We use the GADGET-3 code with smoothed-particle hydrodynamics (SPH) to follow dark matter and gas in comoving volumes of  $10\text{--}25 \text{ Mpc h}^{-1}$  per side. Gas cooling, star formation, and an evolving stellar IMF set the timing and locations of metal production, while detailed yield tables for AGB stars, cc-SN and PISN, and rotating WR stars determine element-by-element enrichment.

We introduced four different supernova feedback implementations (thermal, stochastic, kinetic, and mechanical) and explained how energy and metals are deposited into the surrounding gas. Haloes are identified via a FoF algorithm, and each galaxy is defined by all gas and star particles within 20 kpc of the halo centre. From these particles we measure stellar masses, star formation rates, metallicities, and sizes.

These choices establish a consistent platform for the results in Chapters 3–5. In particular, the contrasting feedback schemes provide the variation we need to test how outflows and chemical yields shape the mass–metallicity relation and radial abundance gradients. The next chapter is the first of those diagnostics, comparing our four feedback models against observed mass–metallicity relation.

## CHAPTER 3

# MASS-METALLICITY RELATIONS

---

<b>3.1</b>	<b>INTRODUCTION</b>	<b>46</b>
<b>3.2</b>	<b>MODEL</b>	<b>48</b>
3.2.1	BARYONIC PHYSICS	49
3.2.2	STELLAR FEEDBACK	50
3.2.3	INITIAL CONDITIONS	53
3.2.4	FIDUCIAL PARAMETERS	53
<b>3.3</b>	<b>RESULTS</b>	<b>54</b>
3.3.1	DENSITY AND TEMPERATURE EVOLUTION	54
3.3.2	GAS-PHASE DIAGRAM	55
3.3.3	COSMIC STAR FORMATION RATE	57
3.3.4	REDSHIFT EVOLUTION	58
3.3.5	MASS-METALLICITY RELATIONS	60
<b>3.4</b>	<b>CONCLUSIONS</b>	<b>66</b>

---

### 3.1 Introduction

The evolution of elemental abundances in the universe across cosmic time is essential to understand the formation and evolution of galaxies (e.g., [Kobayashi and Taylor, 2023](#), for a review). While the evolution of dark matter in the standard  $\Lambda$  cold dark matter ( $\Lambda$ -CDM) cosmology is well understood, one of today’s greatest challenges is understanding the evolution of baryonic matter from primordial elements produced in the Big Bang nucleosynthesis to elements heavier than helium produced in stars. Metals are observed in the local to the distant galaxies. The abundances of metals in galaxies give information about the star formation rate (SFR), gas outflows, and inflow during the galaxies’ histories. The study of metallicity also provides crucial information about the exchange of metals between stars, the cold interstellar gas, and the diffuse surrounding gas.

Understanding the origin and behaviour of elements is subject to several studies. Chemical elements are produced during different astronomical events. Hydrogen and helium form through the Big Bang nucleosynthesis, while carbon and heavier elements form in stellar nucleosynthesis from core-collapse supernovae (SNe), asymptotic giant branch (AGB) stars, thermonuclear explosions observed as Type Ia supernovae (SNe Ia), and neutron star mergers observed as kilonovae (Kobayashi et al., 2020a). Metals are produced in stars and are ejected into the interstellar medium (ISM), circumgalactic medium (CGM), and the intergalactic medium (IGM) (e.g., Péroux and Howk, 2020). This ejection happens through losing the outer gaseous envelopes of old/dying stars or the explosion of massive stars as supernovae (with initial masses  $\gtrsim 10M_{\odot}$ ). The energy released through stellar winds and supernovae explosions is known as stellar feedback (e.g., Larson, 1974). Feedback can efficiently suppress star formation by heating and evaporating dense, star-forming clouds, generating turbulent supersonic shocks, and generating outflows that eject gas from the galaxy. At low halo masses, the dominant feedback is from massive stars (stellar winds, supernova explosions, photoionization, and radiation pressure). Whereas at higher masses, active galactic nucleus (AGN) feedback dominates (e.g., Silk 2013; Taylor and Kobayashi 2015). Different feedback methods are used in different cosmological simulations, such as thermal feedback (e.g., Katz 1992) kinetic feedback (Navarro and White, 1993), stochastic feedback (Dalla Vecchia and Schaye, 2012), and mechanical feedback (Hopkins et al., 2018; Smith et al., 2018). In this paper we investigate the impact of supernova feedback on the metallicities of galaxies using the same stellar yields in our cosmological simulations.

Cosmological simulations consider two different processes for the evolution of galaxies over cosmic time: (1) The hierarchical growth of dark-matter structures on timescales proportional to redshift (Press and Schechter, 1974). (2) The baryonic physics on timescales that are impacted by the processes such as radiative cooling, star formation, and feedback (White and Rees, 1978). The simulation of galaxy formation and evolution remains a significant challenge as it extends from large-scale structures along dark matter filaments to star formation scales. Assumptions and approximations are therefore necessary and depend on the scale we want to resolve. For instance, the semi-analytic models (SAMs) (White and Frenk, 1991) compute the baryonic physics separately from the dark matter. SAMs treat each galaxy as an unresolved object and provide a statistical sample of galaxies. On the other hand, hydrodynamical simulations model the hydrodynamics and gravitational laws and can simulate the baryonic physics simultaneously with the dark matter self-consistently. These simulations can also predict the internal structure of galaxies (i.e., kinematics and spatial distributions). However, the results are still limited to a finite resolution. Therefore, all currently available hydrodynamical models implement analytical laws to attempt to capture the effects of the above mentioned sub-galactic processes on a galaxy scale. Several hydrodynamical simulations are used to predict the evolution in galaxies, with very different input physics in each simulation. For example, the EAGLE simulations (Schaye et al., 2015) use stochastic feedback (Dalla Vecchia and Schaye, 2012). Illustris uses bipolar winds,

IllustrisTNG (Pillepich et al., 2018) uses isotropic, kinetic (wind) feedback from Springel and Hernquist (2003), SIMBA (Davé et al., 2019) uses stellar kinetic feedback with decoupled wind particles, HORIZON-AGN (Dubois et al., 2016) uses thermal energy injection to model stellar feedback. In this paper, we use our own chemodynamical code (Taylor and Kobayashi, 2014) based on the GADGET hydrodynamical code (Springel et al., 2001b, 2005) to systematically investigate the effects of supernova feedback on the chemical evolution of galaxies.

Measuring metallicity from observed spectra of galaxies is subject to many previous studies, is an ongoing effort, and is available for stellar populations (e.g., Worthey et al., 1992; Conroy, 2013) and the ISM (e.g., Maiolino and Mannucci, 2019; Kewley and Ellison, 2008). The stellar mass–metallicity relation (MZR) was first discovered in local elliptical galaxies by studying the colour-magnitude diagram (McClure and van den Bergh, 1968). The relation for the ISM was first observed in a small sample of nearby star-forming galaxies by Lequeux et al. (1979). Later on, using the Sloan Digital Sky Survey (SDSS), several authors derived a clearer MZR for stars (e.g., Gallazzi et al. 2006; Zahid et al. 2017) and the ISM (Tremonti et al., 2004; Curti et al., 2020b), where galaxy metallicity increases with stellar mass. Various methods are used to infer the metallicity of the gaseous phase. The main ones are different calibrations with the photoionization models (Kewley and Ellison, 2008), strong line calibration (Curti et al., 2020b), and direct method based on electron temperature (Curti et al., 2023).

In this paper, we implement and compare four models of stellar feedback in our cosmological simulations. The physical processes included in our simulation are described in section 2. The results of the different feedback models on the MZR are presented in section 3. Comparing with the observed MZRs, we discuss our results and give our perspectives in section 4.

## 3.2 Model

Our simulation code is based on the "GALaxies with Dark matter and Gas intEracT 3" code known as GADGET-3 (Springel et al., 2005). It uses TreeSPH (Hernquist and Katz, 1989), which combines the smoothed particle hydrodynamics (SPH) (Lucy, 1977; Gingold and Monaghan, 1977) to follow the gas dynamics, with the hierarchical tree algorithm to compute the N-body gravitational interactions. The long-range force is calculated with the PM-algorithm using Fourier techniques. We use an improved version of the code that contains several physical processes related to galaxy formation and evolution, such as radiative cooling, star formation, supernovae feedback (Kobayashi et al., 2007), and black hole (BH) physics (Taylor and Kobayashi, 2014).

### 3.2.1 Baryonic Physics

Gravitational instability physics (i.e. dark matter structures) is an important starting point in galaxy formation models. However, one of today’s greatest challenges in cosmological simulations is implementing the baryonic astrophysical processes that describe the galaxy population. The key difference between dark and baryonic matter is that the latter can dissipate energy through radiative processes. In what follows, we discuss the main processes involved in galaxy formation.

**Radiative Cooling:** Radiative cooling is a process that allows a space object to lose heat by thermal radiation. It uses the cooling function  $\Lambda(T)$ , which expresses gas cooling by thermal radiation. This function assumes that the gas is optically thin (i.e. an emitted photon can typically leave the cloud). An example of a set of cooling curves is given by [Sutherland and Dopita \(1993\)](#) where  $\Lambda(T)$  has multiple peaks and valleys because the emission mechanisms are most efficient at specific temperatures. For instance, it is characterised by a big bump at low temperature produced by line radiation and a tail at high temperature (above  $10^7$  K) produced by Bremsstrahlung. We also include Compton heating. In this work, we use the same metallicity-dependent cooling function implemented by [Kobayashi \(2004\)](#), which is computed with the MAPPINGS-III software ([Sutherland and Dopita, 1993](#)).

**Star Formation:** In galaxy simulations the formation of star particles is only allowed in a gas that obeys certain conditions, stars are formed in cool dense gas. As in [Kobayashi et al. \(2007\)](#), we use the star formation criteria used in [Katz \(1992\)](#), which are: (1) Star formation is only allowed in convergent flows, (2) Star formation is only allowed in regions where the cooling time is less than the dynamical time (rapid cooling), and (3) The gas has to be locally Jeans unstable.

**Stellar Feedback:** Stars account for less than 10% of the baryonic matter in the observable Universe ([Madau and Dickinson, 2014](#)), yet cosmic microwave background (CMB) models predict that nearly all gas should have cooled and formed stars by today. Early galaxy-formation theories ([White and Rees 1978](#), [Dekel and Silk 1986](#)) identified this “overcooling” problem and invoked supernova feedback as a remedy. In addition to stellar feedback, we include Compton cooling of the CMB, in which hot, free electrons transfer energy to CMB photons ([Kobayashi et al., 2007](#)). The energy released by supernovae heats and expels gas from galaxies, lowering their baryon fractions and suppressing further star formation. At the same time, gravitational heating, arising from virial shocks as gas falls into massive halos, can raise gas temperatures and further delay cooling (although this shock is not resolved in any SPH calculation). Additionally, the simulation includes photo-heating by a uniform UV background radiation ([Haardt and Madau, 1996](#)), implemented in equation 2.3. Feedback processes fall into two broad classes: ejective feedback, which drives gas out of the interstellar medium (ISM), and preventive feedback, which stops gas accretion onto the ISM. On the other hand, dying stars and supernovae also enrich the ISM with metals, enhancing radiative cooling and thereby promoting star formation (e.g., [Kobayashi et al., 2007](#)). In our model, we include both the heating and the metal-enrichment effects self-consistently; see Sect. 3.2.2 for further details.

**AGN Feedback:** In addition to supernova feedback, feedback from AGNs is essential in suppressing star formation in massive galaxies (e.g., [Silk, 2013](#); [Taylor and Kobayashi, 2015](#)). In a star-forming galaxy (with cool and dense gas) where the BH is not yet active, part of the gas produces stars, and the other part falls into the BH. After accreting enough gas, the BH becomes active and ejects outflows and radio jets. This mechanism, known as AGN feedback, heats and pushes the gas away, which slows down star formation and stops the BH from growing. No more fuel will cause the BH to deactivate, meaning nothing will heat the gas anymore (for it to expand), so it returns to the initial BH stage. At this stage, the gas can cool again. However, stars only form if the gas is dense enough, which is usually not the case.

As in [Taylor and Kobayashi \(2014\)](#), AGN feedback in our simulation is modelled as (1) BH seed formation: the seed BHs are formed with the first stars, any gas particle with a density higher than the specified critical density and with zero metallicity ( $Z = 0$ ) is converted into a BH particle with a seed mass of  $1000h^{-1}M_{\odot}$ . (2) Growth: The seed BHs grow by accreting gas and by merging with other BHs. (3) AGN feedback: In each timestep, a certain amount of energy is produced by the BH and is distributed in a thermal form to a fixed number of neighbour gas particles.

**Chemical Enrichment:** In our simulations, a star particle is not a single star but a set of many. We consider a star particle as a simple stellar population (SSP, i.e. stars with the same age and metallicity but different masses) and include a chemical enrichment model that tracks the enrichment of the gas with all elements up to zinc. Oxygen, carbon and iron abundances are mainly produced by core-collapse SNe, AGB stars, and SNe Ia, respectively ([Kobayashi et al., 2020a](#)). The initial mass function (IMF) of stars is taken from [Kroupa \(2008\)](#). We compute oxygen abundance for the ISM to compare with observations of metallicities weighted by SFRs. And we use total metals for stellar metallicities weighted by V-band luminosities.

### 3.2.2 Stellar Feedback

In hydrodynamical simulations, gas particles are affected by nearby star particles locally. We also follow the cooling of the gas particles after the feedback. These are fundamentally different from the loading factor in previous work (e.g., [Belfiore et al., 2016](#); [Lian et al., 2018](#); [Lin and Zu, 2023](#)), which is the measure for the average effect of or within the galaxy (see [Taylor et al. 2020](#) for comparison between simulations and observations). In the following, we describe four feedback methods proposed for hydrodynamical simulations.

**Thermal feedback:** The classical stellar feedback method used in galaxy simulations consists of the distribution of thermal energy from supernova explosions into the surrounding gas (e.g., [Katz 1992](#)), namely, to the neighbour particles in a fixed radius or with a fixed number, using a smoothing kernel  $W_j$ .

$$\Delta E = E_{\text{SN}}W_j \quad (3.1)$$

Where  $\Delta E$  is the weighted fraction of the supernova energy received by the  $j^{\text{th}}$  gas particle, and  $E_{\text{SN}}$  is the total energy ejected by supernovae from an evolving star particle in a given time step. In our simulations,  $N_{\text{ngb}}$  nearest neighbour gas particles are selected and receive the supernova energy weighted by the smoothing kernel. Then at each time step, the total ejected energy  $E_{\text{SN}}$  is divided accordingly to the weighting to heat the gas particles individually.

Our simulations also include hypernova feedback (Kobayashi et al., 2007). Since the energy of hypernovae is more than ten times larger than the supernova energy ( $10^{51}$  erg), the temperature increase can be much more significant and can reach  $\sim 10^6$  K. Once the gas particles are heated to this temperature, they do not cool rapidly due to the low cooling rate. As a result, this reduces the SFR significantly, and the hypernova feedback is expected to be more efficient than supernova-only feedback.

**Kinetic feedback:** This method consists of implementing outflows where the energy input is partially converted to kinetic energy (Navarro and White, 1993). The thermal energy ejected by each supernova explosion is partially reduced by a parameter  $f$  ( $0 \leq f \leq 1$ ), representing the fraction of energy distributed as kinetic energy. This model simulates a shocked gas with a kinetic kick of velocity  $v$  such as:

$$v = \sqrt{2f E_{\text{SN}} W_j / M_j} \quad (3.2)$$

where  $M_j$  is the mass of the  $j^{\text{th}}$  gas particle that receives the energy, and  $E_{\text{SN}} W_j$  is the weighted fraction of the supernova energy received by the  $j^{\text{th}}$  gas particle. This velocity is added to the original velocity of neighbour particles isotropically.

**Stochastic feedback:** This approach was first implemented by Kay et al. (2003) in galaxy simulations, and generalised by Dalla Vecchia and Schaye (2012) to complete the thermal feedback method and efficiently suppress star formation. Thermal feedback may be inefficient because the thermal energy is mostly radiated away before it can be turned into kinetic energy. This may be because the mass of the gas receiving the supernova energy is too large. Without hypernovae the energy emitted by supernovae is not enough to efficiently heat these gas particles; hence the gas temperature remains too low and the cooling time too short. Another reason for the thermal feedback inefficiency may be the lack of resolution: the energy is mainly distributed to a high-density gas because the simulation does not resolve the hot and low-density areas (which remain missing).

The temperature jump of the neighbour gas can be increased by reducing the mass of the heated gas with respect to the star particle. This can be done by reducing the number of heated gas particles or by specifying the temperature jump of the heated gas. The first idea may cause an issue if even one gas particle is too massive. The second way can be done using stochastic feedback, where the probability of the gas particle being heated depends on the star-to-gas mass ratio and the specified temperature jump. For the stochastic feedback, the idea is to select a random number of nearby particles (instead of heating all the neighbour particles as in the thermal feedback model).

We use the same model as in [Dalla Vecchia and Schaye \(2012\)](#) where we define an energy increase  $\Delta e$  used to heat the neighbour gas particles.

$$\Delta e = f \frac{E_{\text{SN}}}{N_{\text{ngb}}} \quad (3.3)$$

where  $E_{\text{SN}}$  is the total supernova energy ejected by an evolving star particle in a given timestep,  $N_{\text{ngb}}$  is the number of neighbour gas particles, and  $f$  is a parameter which is introduced to hold the probability that each of the  $N_{\text{ngb}}$  particles receives an energy increase of  $\Delta e$  (i.e.,  $\Delta e > \frac{E_{\text{SN}}}{N_{\text{ngb}}}$ , hence  $f > 1$ ).  $\Delta e$  is the total energy a single gas particle will receive from the supernovae independently from the distance to the star particle. To determine if a gas particle will receive the energy or not, a random number  $0 < r < 1$  is compared to the condition:

$$r < \frac{E_{\text{SN}} M_*}{\Delta e \sum_j^{N_{\text{ngb}}} M_j} \quad (3.4)$$

with  $M_*$  the mass of the star particle and  $M_j$  the mass of the  $j^{\text{th}}$  gas particle receiving the energy. The gas particle receives an energy increase of  $\Delta e$  only if this condition is satisfied. Larger  $f$  results in a smaller number of gas particles heated with a larger energy  $\Delta e$ . Note that  $M_j$  and  $M_*$  are not constant in our simulations.

**Mechanical feedback:** Mechanical feedback takes into account the supernova shock wave applied to gas particles. This model uses assumptions depending on the structure of the ISM at small scales and its interaction with the supernova remnants. As the supernova shock wave propagates, it accelerates particles, radiating energy away. There are mainly three phases in the life of a supernova: i) the free expansion phase, ii) the adiabatic or Taylor-Sedov phase ([Taylor, 1950](#); [Sedov, 1959](#)), where the expansion proceeds adiabatically into the surroundings, and radiative losses are negligible. And iii) the radiative or ‘snowplough’ phase, where the gas temperature in the shock wave drops as the cooling function increases and the shock slows until it merges with the surroundings and disappears.

We implement mechanical feedback similar to [Hopkins et al. \(2014\)](#) and [Smith et al. \(2018\)](#), where the supernova shock wave is considered to occur during the Sedov-Taylor phase of expansion, during which the shock wave is energy conserving. As in the kinetic model, a fraction  $f$  ( $0 \leq f \leq 1$ ) of supernova energy  $E_{\text{SN}}$  is ejected in a kinetic form, but is converted to a momentum kick. The total momentum injected in the rest frame of the star particle is

$$P_{\text{tot}} = \sqrt{2m_{\text{ej}} f E_{\text{SN}}} \quad (3.5)$$

with  $m_{\text{ej}}$  the total mass ejected by the supernovae in a given timestep. Following [Kimm et al. \(2015\)](#), the momentum as the remnant transitions to the snowplough phase is given as

$$P_{\text{fin}} = 3 \times 10^5 \text{ km s}^{-1} M_{\odot} E_{51}^{16/17} n_{\text{H}}^{-2/17} Z'^{-0.14} \quad (3.6)$$

with  $E_{51} \equiv E_{\text{SN}}/10^{51}$  erg,  $n_{\text{H}}$  is the hydrogen number density, and  $Z'$  the metallicity in solar units ( $Z' \equiv \max(Z/Z_{\odot}, 0.01)$ ). The correct momentum, therefore, depends on the stage of the expansion. We calculate both forms of momentum in the code for each star particle during each timestep, and choose as

$$\Delta P = W_j P_{\text{tot}} \min(\delta M, \delta P). \quad (3.7)$$

Where  $\delta M = \sqrt{1 + \frac{m_j}{\Delta m_j}}$  is associated to the resolved Sedov-Taylor phase, with  $m_j$  the initial mass of the  $j^{\text{th}}$  gas particle receiving the energy, and  $\Delta m_j$  the mass received by the  $j^{\text{th}}$  gas particle from supernovae in nearby star particles. And  $\delta P = \frac{P_{\text{th}}}{P_{\text{tot}}}$  is associated with the unresolved exit of the Sedov-Taylor phase.  $W_j P_{\text{tot}}$  is the portion of momentum received by  $j^{\text{th}}$  gas particle.

### 3.2.3 Initial Conditions

We use  $\Lambda$ CDM cosmology with  $h = 0.68$ ,  $\Omega_m = 0.31$ ,  $\Omega_{\Lambda} = 0.69$  and  $\Omega_b = 0.048$  (Planck Collaboration, 2020). The simulations presented in this paper are run at the same resolution with the same initial conditions (as in Kobayashi et al. (2007) with updated cosmological parameters): Same number of dark matter and gas with a resolution of  $N_{\text{gas}}=N_{\text{DM}}=128^3$  with mass  $M_{\text{DM}} = 3.47 \times 10^7 h^{-1} M_{\odot}$  and  $M_{\text{gas}} = 6.35 \times 10^6 h^{-1} M_{\odot}$ . The simulation is run in a periodic, comoving, cubic box volume of  $10 h^{-1} \text{Mpc}$  on a side, with a gravitational softening lengths of  $\epsilon_{\text{DM}} = 1.6875$  and  $\epsilon_{\text{gas}} = 0.84375 h^{-1} \text{kpc}$ . We use the Friend-of-Friends (FoF) algorithm to locate galaxies as in Taylor and Kobayashi (2014).

### 3.2.4 Fiducial parameters

We run our simulation with the same initial conditions and different parameter values  $f$ . For the kinetic feedback we run  $f=[0, 1, 0.5, 1, 2, 3, 5, 10, 30, 50, 70, 90]\%$  and find that the larger is  $f$ , the stronger the feedback. A large  $f$  suppresses star formation too much, while  $f < 1$  gives very similar results as the thermal feedback (see Appendix A.1). For these reasons, we decide to use  $f = 1\%$  as our fiducial parameter. For the mechanical feedback, we run  $f=[1, 2, 5, 10, 30, 50, 70]\%$ , and with the same reasoning as for the kinetic feedback, we choose  $f = 1\%$  as our fiducial parameter.

For the stochastic feedback,  $f$  is the fraction of total energy ejected from supernovae and is proportional to the probability that a gas particle is heated by the supernovae. A large  $f$  is equivalent to a large  $\Delta e$  which yields the right-hand side of Equation 3.4 to be small. Therefore, for a large  $f$ , Equation 3.4 is rarely satisfied, as only a small number of particles receive the energy increase and are impacted by the supernova feedback. We ran the values  $f = [1, 3, 5, 10, 30, 50, 70, 90]$  (see Appendix. A.1) and found that for  $f < 50$  the impact of  $f$  is not significant, and for  $f > 50$  the feedback is too weak. Therefore, we choose to use  $f = 50$  as our fiducial

parameter for the stochastic feedback as it is our largest supernova energy fraction where enough particles are heated for the feedback to be effective.

We have verified that our results are numerically robust by performing resolution convergence tests. These are presented in Appendix C.1, where we show that the cosmic star-formation history and the stellar mass–metallicity relation are well converged at the resolutions adopted in this work.

## 3.3 Results

### 3.3.1 Density and Temperature evolution

Figure 3.1 shows the redshift evolution of the gas density in our cosmological simulations from the same initial conditions for the four feedback models with our fiducial parameters. At  $z = 2$  (bottom row), the density distribution is similar for all models. At  $z = 1$  (middle row), the kinetic feedback starts to behave differently. For example, if we focus on the top left region of the map, we can notice a large ring-like structure that is not occurring for the other models.

At  $z = 0$  (top row), one can distinguish a rich filamentary structure for the thermal, stochastic, and mechanical feedbacks (columns 1, 2, and 4, respectively); however, with the kinetic feedback, the density becomes very diffuse. There is no significant difference in the dark matter structure. The gas in our simulations is accreted along the filaments falling toward a central node with higher density; this triggers star formation, enhances supernova feedback, and drives galactic winds. The supernova feedback starts earlier in the kinetic model, which explains the “rings” at  $z = 1$ . This pushed gas keeps moving away from galaxies, which causes the diffuse structure at  $z = 0$ . There are no significant differences among the three other models.

Figure 3.2 shows the gas temperature in our simulations for the four models at  $z = 0$ . Here again, we see a drastic behaviour with the kinetic feedback, which overheats the gas above  $10^6$  K. The temperature is similarly high also with the stochastic feedback. Therefore, it is expected that the stochastic feedback model will have diffuse density structure similarly to the kinetic feedback model in the future time. On the other hand, the gas temperature in the thermal and mechanical feedback models ranges from  $\sim 2000$  K in low-density regions to  $\sim 6000$  K in dense regions. Overall, the mechanical feedback results in colder gas, and the cold areas are more extended than in the case with the thermal feedback.

Figure 3.3 shows the gas metallicity for the four models at  $z = 0$ . The metallicity is distributed similarly for the thermal, stochastic and mechanical feedbacks, but stochastic feedback gives slightly less extended metallicity distribution. The supernova feedback enhances the production of galactic winds, which mainly enriches the ISM and only slightly the IGM. On the other hand, the kinetic feedback produces much stronger galactic winds and strongly enriches the IGM.

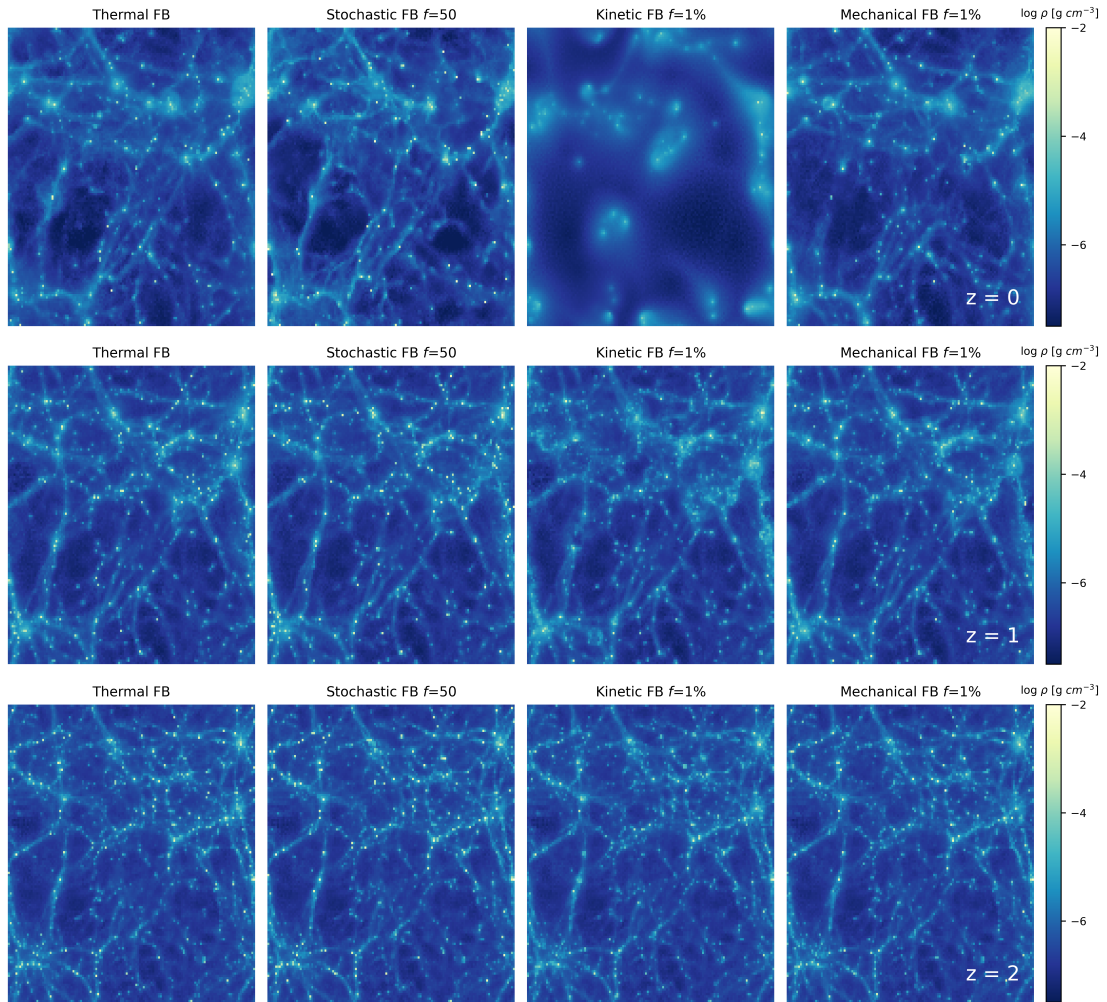


FIGURE 3.1: Density evolution of our cosmological simulations in  $10 h^{-1} \text{Mpc}^3$  box for our four feedback (FB) models: thermal, kinetic, stochastic, and mechanical in the 1st, 2nd, 3rd, and 4th columns, respectively, with the fiducial parameters in section 3.2.4. We show projected gas density at  $z = 0, z = 1$ , and  $z = 2$  in the top, middle and bottom rows, respectively.

### 3.3.2 Gas-phase diagram

As described in [Davé et al. \(2001\)](#), the baryons in the universe are found in four different regions of the gas phase diagram: (1) The *diffuse region* (low temperature  $T < 10^5 \text{K}$  and low density  $\rho$ ) contains adiabatic gas outside galaxies with no specific role. (2) The *condensed region* (low temperature  $T < 10^5 \text{K}$  and high density  $\rho$ ) contains stars and cool gas inside galaxies. (3) The *hot region* ( $T > 10^7 \text{K}$ ) contains the hot gas in galaxy clusters. (4) The *warm-hot region* ( $10^5 \text{K} < T < 10^7 \text{K}$ ) contains the baryons in the IGM. Such matter surrounding galaxies more closely can be observed with metal absorption lines and called CGM ([Péroux and Howk, 2020](#)).

Figure 3.4 shows the density-temperature phase space diagram at  $z = 0$  for the four feedback models with our fiducial parameters. The main noticeable feature is the different behaviours of the warm hot region. The diagrams of the thermal and mechanical models show two bumps at two different temperatures: the first bump is at  $T \sim 10^4 \text{K}$  which corresponds to the peak of

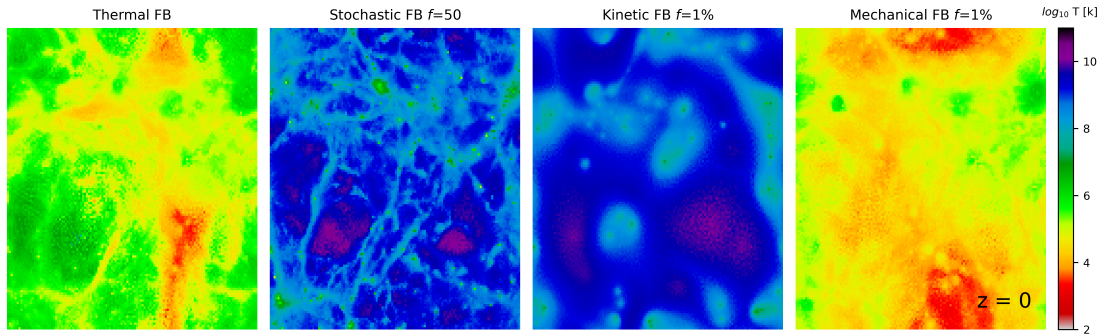


FIGURE 3.2: The same as Figure 3.1 but for temperature maps of our cosmological simulations for the four feedback models at  $z = 0$ .

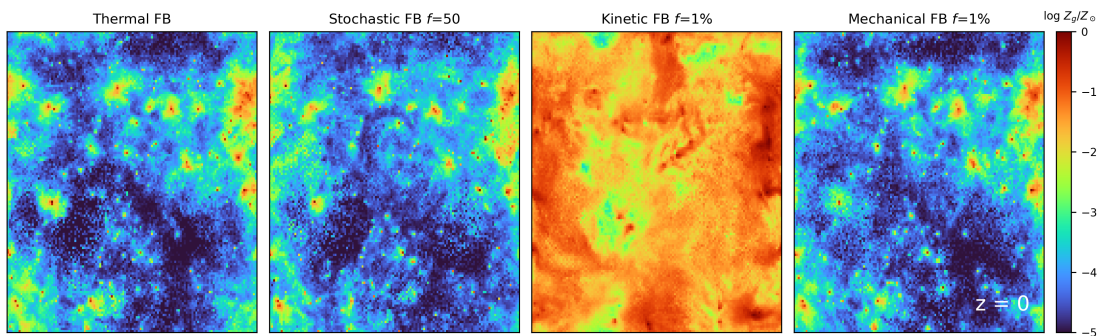


FIGURE 3.3: The same as Figure 3.1 but for the gas-phase metallicity,  $\log Z_g/Z_\odot$ , in our cosmological simulations for the four feedback models at  $z = 0$ .

hydrogen cooling temperature, and the second bump is at  $T \sim 10^5$  K which corresponds to the peak of helium cooling.

The straight horizontal line at temperature  $T \sim 10^4$  K is caused by the cooling function sharply dropping below  $T \sim 10^4$  K (see Fig.13 of Kobayashi and Taylor 2023), which prevents gas cooling until it reaches very high density. Note that molecular cooling is not included, which would weaken this behaviour. At high densities, there are more star-forming particles in the stochastic feedback model than in the other models.

The gas phase temperature-density diagram for the kinetic feedback has a strange behaviour as most of the gas is hot and diffuse; this is due to the cooling function used in our simulations, which drops down when the particles are heated beyond  $\sim 3 \times 10^5$  K. This figure supports the prediction that the stochastic feedback will end up with the same behaviour as the kinetic one. These diagrams indicate that the mechanical feedback is a better model for this resolution.

The drastic changes for the kinetic and stochastic feedback happen after  $z = 1$  (see section 3.3.4), and Fig. 3.5 shows the gas phase diagram of the four models at  $z = 1$  where there is no significant difference between the models. If we look closer, the mechanical feedback has a slightly larger amount of warm gas (at  $T \sim 10^5$  K); this is due to its efficiency, making the non-star forming gas particles either heated or ejected.

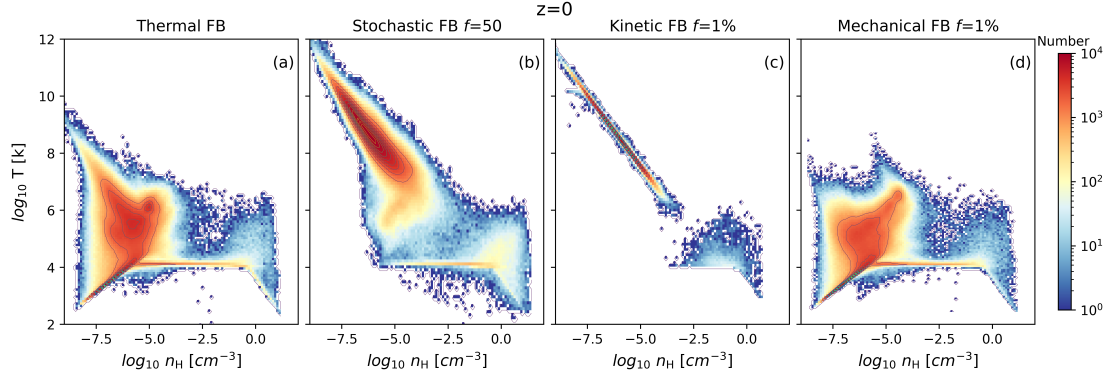


FIGURE 3.4: Density-temperature phase space diagrams for thermal (panel a), kinetic (panel b), stochastic (panel c), and mechanical (panel d) feedback models. Each panel shows the temperature as a function of hydrogen number density with the colour contour indicating the number density of the gas particles in the entire simulation volume at  $z = 0$ .

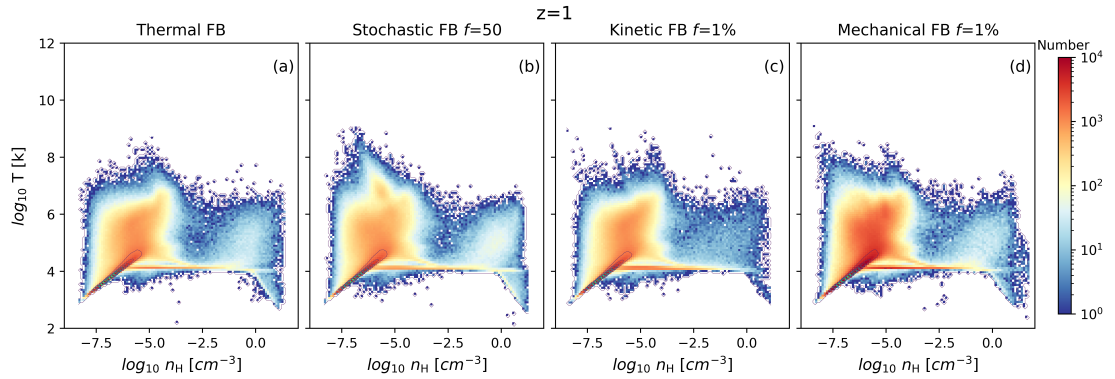


FIGURE 3.5: The same as Figure 3.4 for  $z = 1$ .

### 3.3.3 Cosmic Star Formation Rate

Figure 3.6 shows the cosmic SFR history obtained with each of the four feedback models with fiducial parameters. The SFR increases with time until the cosmic noon at redshift  $\sim 2$ , where the SFR was at its maximum. It decreases from  $z \sim 2$  to the present day because most of the cold gas has already turned into stars, but also because the formation of stars is suppressed by the presence of more supernova and AGN feedback. These test runs with a limited box size do not have very massive galaxies and galaxy clusters, which may explain our SFRs are lower at  $z \lesssim 2$  than observed. The stochastic feedback shows a similar behaviour with a slightly higher SFR (due to weaker feedback). In the kinetic case, the feedback impact can only be seen after sufficient star formation has occurred (i.e. at  $z \lesssim 6$ ). After  $z = 6$ , the feedback is too strong, and star formation is suppressed too much, compared with the observations. We retrieve the same behaviour for the mechanical feedback with a less strong suppression of SFRs. Observational data are taken from Madau and Dickinson (2014) (grey cross) and Driver et al. (2018) (pink plus).

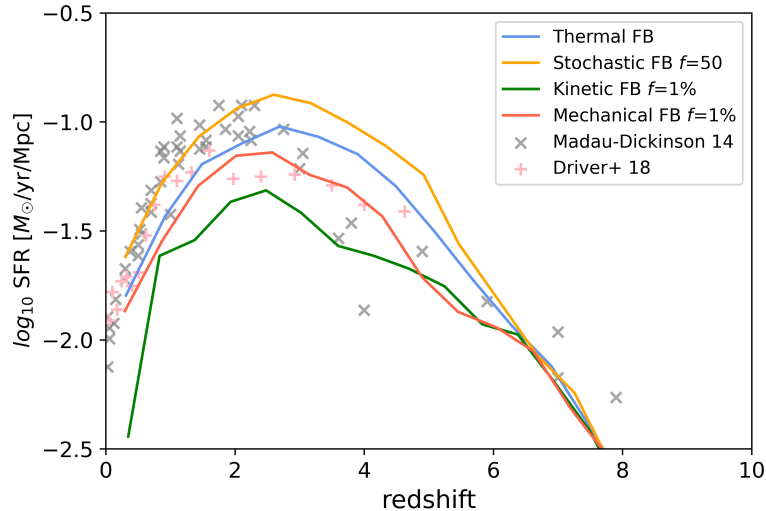


FIGURE 3.6: Cosmic star formation rate history of our  $10 h^{-1}$  Mpc simulations with our different feedback models: thermal (blue), stochastic (orange), kinetic (green), and mechanical (red). The observational data are taken from [Madau and Dickinson \(2014, grey cross\)](#) and [Driver et al. \(2018, pink plus\)](#).

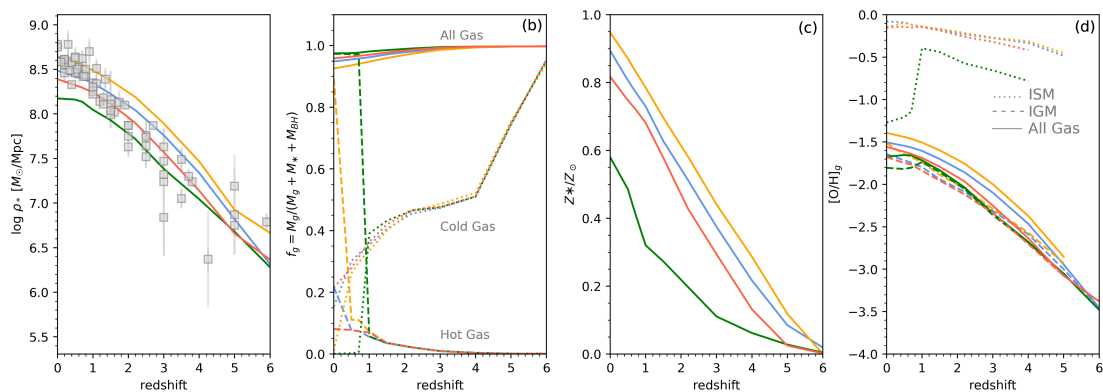


FIGURE 3.7: (a) Stellar mass density as a function of redshift, comparing to the observational data (grey square) taken from [Madau and Dickinson \(2014\)](#). (b) Cosmic gas fraction  $f_g \equiv M_g / (M_g + M_* + M_{BH})$  for all gas (solid lines), hot gas ( $T > 10^6$  K, dashed lines), and cold gas ( $T < 1.5 \times 10^4$  K, dotted lines). (c) Cosmic stellar metallicity evolution. (d) Gas-phase oxygen abundances evolution for all gas (solid lines), ISM (dotted lines), and IGM (dashed lines). In all panels, the thermal, stochastic, kinetic, and mechanical feedbacks are always shown in blue, orange, green, and red, respectively.

### 3.3.4 Redshift evolution

In Figure 3.7, we investigate the redshift evolution of different cosmic quantities of the gas and stars in our simulations. The panel 3.7a shows the stellar mass density as a function of redshift, obtained with our four feedback models. The kinetic model has the lowest stellar density at all redshifts plotted here since, as shown in the cosmic SFR, it is the strongest feedback that suppresses star formation the most. Our simulations follow a similar trend as observational data from [Madau and Dickinson \(2014\)](#). However, at  $z > 1$ , the kinetic and mechanical feedback seems to fit better, while at  $z < 1$ , the thermal and stochastic feedback work better.

The panel 3.7b shows the gas fraction defined as  $f_g \equiv M_g / (M_g + M_* + M_{\text{BH}})$  as a function of redshift for the four feedback models. At  $z > 4$ , the total gas fraction (solid lines) is  $f_g \sim 100\%$  for all models. From  $z = 4$ , the total gas fraction decreases to  $f_g = 94\%$ ,  $92\%$ ,  $97\%$ , and  $96\%$  at  $z = 0$ , respectively for thermal, stochastic, kinetic, and mechanical feedback. All these are comparable with the observational estimates (e.g.,  $f_g = 0.91\text{--}0.95$  in [Madau and Dickinson 2014](#)). The stochastic feedback gives the smallest total gas fraction, and despite the large amount of hot gas in Figure 3.4, more gas is turned into stars overall (as shown in Fig. 3.7a). The kinetic feedback has the largest total gas fraction.

The dashed and dotted lines show the hot and cold gas fractions with  $T > 10^6$  and  $T < 1.5 \times 10^4$  K, respectively. At  $z > 6$ , most of the gas was cold in all models. The cold gas fraction decreases with time while the hot gas fraction increases, mainly due to stellar and AGN feedback. At  $z \leq 2$ , the cold gas fraction differs depending on the feedback models. The kinetic model has the highest cold gas fraction, which may be explained by the lower SFR than the other models. The gas is drastically heated in the kinetic model at exactly  $z = 1$  due to the high efficiency of stellar feedback, this transition is not caused by our redshift binning but is real due to the nature of this feedback model. Around this redshift, a large number of gas particles are heated above  $10^5$  K, where the cooling rate is low (as explained in section 3.3.2), and are ejected from galaxies, suddenly increasing the hot gas fraction. A similar behaviour is observed for the stochastic feedback later on at  $z = 0.5$ , however, it is less sharp and evolves up to  $z = 0$ . This extreme temperature change starts exactly at  $z < 1$  and  $z < 0.5$  for the kinetic and stochastic feedback, respectively. And the difference between  $z = 0$  and  $z = 1$  is clearly observed in the gas-phase density-temperature diagrams in Fig. 3.4 and Fig. 3.5.

The panel 3.7c shows the stellar metallicity across cosmic time for the four models, which increases as time followed by star formation. The kinetic model has the lowest stellar metallicity at all redshifts since fewer stars are produced than in any other models. It is clear that the supernova feedback model has an impact on the present-day stellar metallicity, with  $Z_*/Z_\odot = 0.89$ ,  $0.94$ ,  $0.57$ ,  $0.81$  at  $z = 0$  for thermal, stochastic, kinetic, and mechanical feedback, respectively.

The panel 3.7d shows the evolution of oxygen abundance with time with the four feedback models for all the gas (solid lines), the ISM (dotted lines) and the IGM (dashed lines), separately. As defined in [Kobayashi et al. \(2007\)](#) and [Taylor and Kobayashi \(2016\)](#), the ISM is all gas particles in galaxies identified by the Friend of Friend algorithm ([Springel et al., 2001a](#)), and the IGM is all the other gas particles. The kinetic feedback has a lower oxygen abundance because it has less star formation, therefore fewer heavy elements are produced by supernovae. From  $z = 1$ , the oxygen abundance is reduced in the ISM due to the winds that eject the oxygen-enhanced gas outside the galaxy, but also due to dilution, where all matter is mixed up and fills the ISM with hydrogen, which explains the drop in the plot.

Table 3.1 summarizes the values of the cosmic stellar mass density  $\log \rho_*$ , gas fraction  $f_g$  (for all

FB Model	Thermal	Stochastic	Kinetic	Mechanical
$\log \rho_*$	8.483	8.642	8.173	8.389
$f_g$ (All Gas)	0.948	0.925	0.974	0.958
$f_g$ (Cold Gas)	0.154	0.0103	0.0007	0.215
$f_g$ (Hot Gas)	0.216	0.893	0.973	0.081
$Z_*/Z_\odot$	0.893	0.947	0.974	0.816
$[\text{O}/\text{H}]_g$ (ISM)	-0.080	-0.148	-1.272	-0.152
$[\text{O}/\text{H}]_g$ (IGM)	-1.643	-1.512	-1.805	-1.676
$[\text{O}/\text{H}]_g$ (All Gas)	-1.506	-1.393	-1.674	-1.557

TABLE 3.1: Cosmic stellar mass density  $\log \rho_*$ , gas fraction  $f_g$  (for all gas, hot gas, and cold gas), stellar metallicity  $Z_*/Z_\odot$ , and gas-phase oxygen abundances  $[\text{O}/\text{H}]_g$  (for all gas, ISM, and IGM) of the thermal, stochastic ( $f = 50$ ), kinetic ( $f = 1\%$ ) and mechanical ( $f = 1\%$ ) feedback models at  $z = 0$ .

gas, hot gas, and cold gas), stellar metallicity  $Z_*/Z_\odot$ , and gas-phase oxygen abundance  $[\text{O}/\text{H}]_g$  (for all gas, ISM, and IGM) at  $z = 0$ , for the four feedback models.

### 3.3.5 Mass–Metallicity Relations

#### 3.3.5.1 Stellar Populations

Figure 3.8 shows the stellar mass–metallicity relations (MZRs) for the four feedback models, with the integrated metallicity of stars in galaxies weighted by the V-band luminosity of star particles. In our simulations, a star particle is not a single star but a set of many. We consider a star particle a simple stellar population (SSP, i.e. stars with the same age and metallicity but different masses). V-band luminosities of star particles are calculated using the Binary Population and Spectral Synthesis (BPASS) code version 2.2.1 (Stanway and Eldridge, 2018). The stellar metallicity of galaxies is measured in a 15 kpc projection from the galactic centre. The lines in Figure 3.8 represent the median of the simulated galaxies, while the shaded areas display the  $1\sigma$  scatter. The solar metallicity used in the figure is  $Z_\odot = 0.015$ .

Our thermal and stochastic models tend to overproduce metals compared with the local observations (black dashed line, with the grey shade for  $1\sigma$ ) taken from Zahid et al. (2017). Our kinetic feedback is not producing enough metals due to the lower SFR and not keeping enough metals in stars because of the kick velocity that drives the metals out of the galaxy. Among our four models, mechanical feedback gives the closest matches to the observed relation from Zahid et al. (2017) at  $z = 0$ , with this resolution. We aim to confirm this by running even higher resolution in a larger volume of cosmological simulations in our future work.

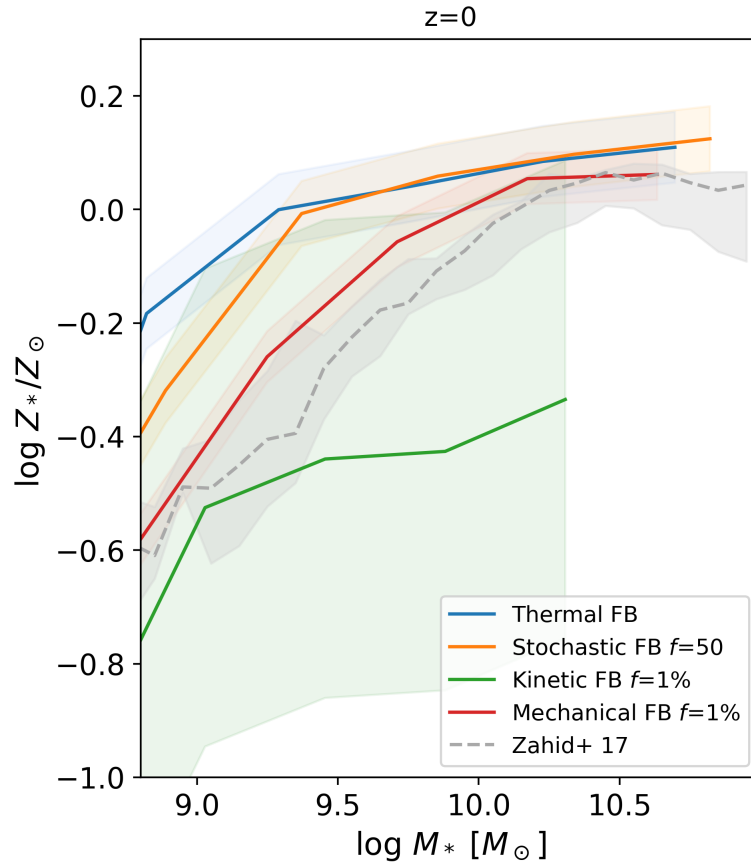


FIGURE 3.8: Stellar mass–metallicity relations with thermal (blue), stochastic (orange), kinetic (green), and mechanical (red) feedback models. The stellar metallicity is V-band luminosity-weighted. The lines are for medians and the shaded areas show the  $1\sigma$  scatter. The observational data are taken from [Zahid et al. \(2017\)](#), (grey dashed line, with  $1\sigma$  scatter).

### 3.3.5.2 Gas phase

Figure 3.9 shows the gas-phase MZR with our four feedback models. We calculate the gas-phase “metallicity” of galaxies by measuring the gas oxygen abundance within 15 kpc from each galactic centre, weighted by the SFRs of gas particles to compare with observations, which are weighted by emission lines. Not many gas particles are forming stars with the current simulation volume and resolution, particularly at the massive end. Therefore, we have limited data points for SFR-weighted gas-phase metallicities. Consequently, we show the metallicities of galaxies (points), in addition to a fit (linear fit of medians; solid lines) in Fig. 3.9. The solar oxygen abundance adopted for our nucleosynthesis yields is  $\sim 8.76$ . At  $z = 0$ , the kinetic feedback gives the highest gas-phase metallicity ( $\sim 9.1$  dex), which is possibly due to the strong ejection of metal-poor gas. From this figure (namely scatter plot), we can conclude that for relatively low-mass galaxies at  $\sim 10^9 M_\odot$ , the thermal and mechanical feedbacks are in reasonably good agreement with the observed gas-phase MZR from [Kewley and Ellison \(2008\)](#) (grey dashed line). The stochastic feedback seems to give a shallower slope than observed. With the mechanical feedback, higher-mass galaxies ( $\sim 10^{10} M_\odot$ ) tend to have slightly lower metallicities than in

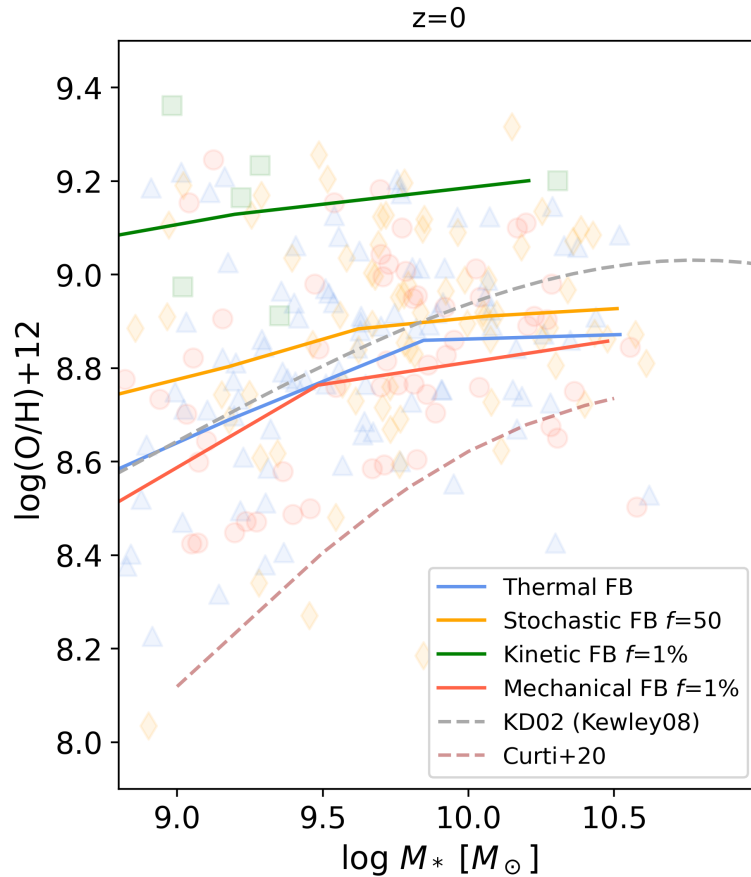


FIGURE 3.9: Gas-phase mass–metallicity relations with thermal (blue; triangles), stochastic (orange; diamonds), kinetic (green; squares), and mechanical (red; circles) feedback models. The SFR-weighted, gas-phase oxygen abundances of galaxies (number ratios relative to hydrogen) are shown. The observational data (grey dashed line) are from Tremonti et al. (2004) with the ‘KD02’ scale in Kewley and Ellison (2008), and from Curti et al. (2020b, brown dashed line).

Kewley and Ellison (2008), and are more comparable with Curti et al. (2020b)’s observation (brown dashed line). This offset reflects the well-known calibration differences: the KD02 scale used in Kewley and Ellison (2008), based on photoionisation models, systematically yields higher oxygen abundances at fixed stellar mass than the direct-method,  $T_e$ -anchored calibration of Curti et al. (2020b).

It is important to note that while the shape of the stellar and gas-phase MZR is relatively robust against the methods used for the metallicity determination, the absolute amplitude of the stellar and gas-phase metallicity measurement of galaxies are still quite uncertain (e.g., Goddard et al. 2017 for stellar metallicity measurements with different stellar population synthesis codes and stellar templates and Maiolino and Mannucci 2019 for a review of the various methods for the gas-phase metallicity determination). This can also be seen in Fig. 3.10 and 3.11, where multiple sources of the metallicity measurements are included. It is very important to obtain the absolute values of metallicities of both stellar and gas-phase in observations.

### 3.3.5.3 Stellar MZR evolution

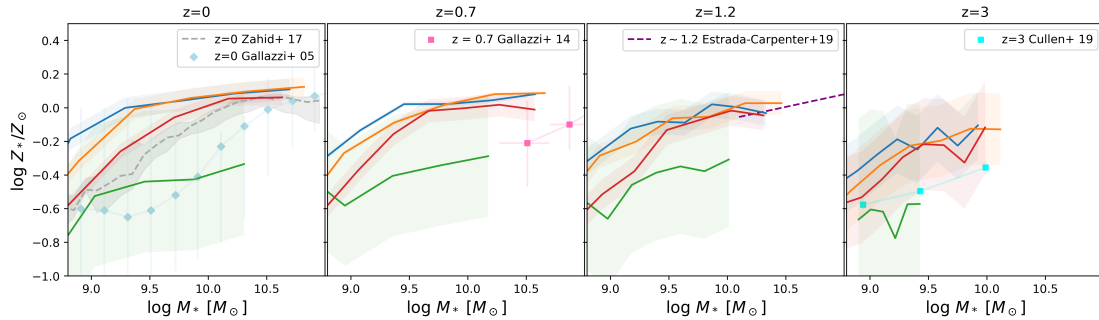


FIGURE 3.10: Evolution of the luminosity-weighted stellar MZR with thermal (blue), stochastic (orange), kinetic (green), and mechanical (red) feedback models. The solid lines are for the medians, and the shaded areas show the  $1\sigma$  scatter. Observational data are taken from [Zahid et al. \(2017,  \$z = 0\$ \)](#), [Gallazzi et al. \(2005,  \$z = 0\$ \)](#), [Gallazzi et al. \(2014,  \$z = 1.2\$ \)](#), and [Cullen et al. \(2019,  \$z = 3\$ , with +0.5 dex shift for \[O/Fe\]\)](#).

Figure 3.10 shows the stellar MZR from  $z = 0$  to 3 for the four feedback models. At higher redshifts, all models systematically give lower metallicities at a given mass, showing very similar differences among the models ( $\sim 0.2$  dex from  $z = 3$  to 0). At all shown redshifts, the thermal feedback always produces slightly more metals than the other models. The low cosmic SFR with the kinetic feedback results in significantly lower stellar metallicities than in the other models. At the low-mass end, the stochastic feedback gives metallicities slightly lower than the thermal feedback by  $\sim 0.1$  dex. Overall, the supernova feedback has a more significant impact on the metallicity at the low-mass end where low-mass galaxies eject more metals ([Kobayashi et al., 2007](#)).

The mechanical feedback seems to give the best match to the observations at  $z = 0$ , although the observed stellar metallicities at higher redshifts are either lower or of galaxies with limited overlap in mass compared to the model prediction. In the observations, massive galaxies have super-solar metallicities at  $z = 0$ , which disappear at  $z = 3$ . At  $z = 0$ , as already shown in Fig. 3.8, our model agrees well with the latest analysis by [Zahid et al. \(2017\)](#), although these give significantly higher metallicities than in [Gallazzi et al. \(2005\)](#). At  $z = 0.7$ , although there is no overlap in the mass range, data from [Gallazzi et al. \(2014\)](#) is more consistent with our kinetic model. However, this data set does not reject the other models if we consider the significant offset between [Zahid et al. \(2017\)](#) and [Gallazzi et al. \(2005\)](#) data at  $z = 0$ . We also note the large error bars of  $\sim 0.2$  dex for these data. Our mechanical model seems consistent with the Hubble Space Telescope observations at  $z = 1.1$ – $1.6$  ([Estrada-Carpenter et al., 2019](#)). These data suggest that the mass–metallicity relation has not significantly evolved since  $z \sim 0$  at least at the massive end, contrary to [Gallazzi et al. \(2014\)](#) at  $z \sim 0.7$ . At  $z = 3$ , the UV observations from [Cullen et al. 2019](#) are for Fe abundances, are shifted by +0.5 dex taking account of [O/Fe], but still about 0.2 dex lower than our predicted metallicities.

### 3.3.5.4 Gas phase MZR evolution

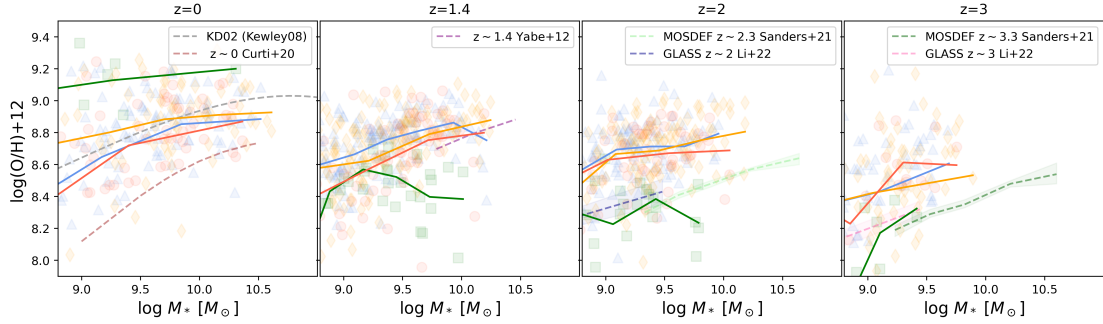


FIGURE 3.11: Evolution of the SFR-weighted gas-phase MZR with thermal (blue; triangles), stochastic (orange; diamonds), kinetic (green; squares), and mechanical (red; circles) feedback models. The solid lines indicate the linear fit to the individual galaxies shown by the symbols with the same colour. Observational data are from Tremonti et al. 2004 ( $z = 0$ ) with the KD02 scale in Kewley and Ellison (2008,  $z = 0$ ), Curti et al. (2020b,  $z = 0$ ), Yabe et al. (2012,  $z = 1.4$ ), Sanders et al. (2021,  $z \sim 2-3$ ), Li et al. (2022,  $z \sim 2-3$ ).

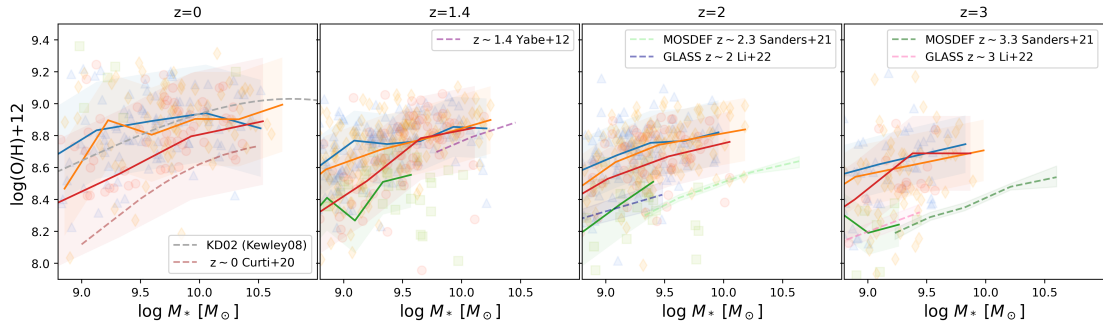


FIGURE 3.12: Evolution of the young stellar MZR (solid lines) comparing to the gas-phase metallicities (symbols, the same as in Fig. 3.11). The solid lines are the medians of the luminosity-weighted stellar MZR for stars younger than 0.1 Gyr, and the shaded areas show the  $1\sigma$  scatter.

Figure 3.11 shows the SFR-weighted gas-phase MZR for the four feedback models at  $z = 0, 1.4, 2,$  and  $3$ . Points are individual simulated galaxies (thermal: blue triangles; stochastic: orange diamonds; kinetic: green squares; mechanical: red circles), and the solid lines are linear fits to the points of the same colour. Dashed curves are observational median relations from Tremonti et al. (2004) and Curti et al. (2020b) at  $z \sim 0$ , Yabe et al. (2012) at  $z \sim 1.4$ , and MOSDEF/GLASS (Sanders et al., 2021; Li et al., 2022) at  $z \sim 2-3$ . Despite the significant scatter and finite resolution of our sample, an MZR is present at all redshifts. At  $z = 0$ , the mechanical model aligns well with the Tremonti et al. (2004) KD02 calibration, while Curti et al. (2020b) lies lower owing to calibration differences. At  $M_{\star} \sim 10^{10} M_{\odot}$ , the simulated scatter points span  $\sim 8.7-9.0$  dex in  $12 + \log(\text{O}/\text{H})$ . For reference, the intrinsic  $1\sigma$  scatter within a single strong-line calibration is  $\sim 0.1$  dex (e.g. KD02; Kewley and Ellison 2008; see also Curti et al. 2020b). Our simulated spread ( $\sim 0.3$  dex) is therefore larger, primarily due to finite resolution and small-number statistics

in some bins. These limitations are reduced in our larger-volume and higher-resolution run (see Fig. 2.16).

The evolution of the dashed observational relations with redshift illustrates the well-established trend that galaxies at earlier epochs are more metal-poor at fixed stellar mass. From  $z = 0$  to  $z \sim 3$ , our simulations also show a decrease in metallicity: the kinetic feedback produces the strongest change ( $\sim 1.4$  dex), the stochastic and mechanical feedbacks have a moderate evolution ( $\sim 0.2$  dex), while the thermal feedback only has a mild evolution ( $\sim 0.05$  dex). This behaviour is consistent with the picture of progressively less chemically enriched gas reservoirs at high redshift (e.g. Yabe et al. 2012; Sanders et al. 2021; Li et al. 2022). Overall, the simulated MZR reproduces this observed downward shift with increasing redshift, although the precise normalization depends on the metallicity calibration adopted in each observational study.

At high redshifts, most low-mass galaxies have fast star formation enriching their ISM. However, the kinetic feedback suppresses this star formation, which leads to only a few metal-poor low-mass galaxies. As discussed previously, the drastic change in the kinetic feedback model, which occurs exactly after  $z = 1$  removing metal-poor gas and causing the metal-rich ( $\sim 9.1$  dex) galaxies (green squares) at  $z = 0$ .

To verify the consistency between the stellar and gas-phase metallicities, we also show the metallicities of young stars since these are expected to be consistent with the metallicities of gas from which the stars were born. In Figure 3.12, we show the MZR of young stars ( $<0.1$  Gyr), comparing to the simulated gas-phase metallicities (symbols) and the observed gas-phase MZR (dashed lines) at each redshift. The young stellar MZR (solid lines) agree well with the simulated gas-phase metallicities. At  $z = 0$ , the mechanical feedback increases with mass, similar to the observed MZR. At higher redshifts, the kinetic feedback fits better, as in Figure 3.11. Note that no line is plotted for the kinetic feedback at  $z = 0$  because not many young stars form with the kinetic feedback.

The dashed lines represent observational data at various redshifts, which may be suffered by the uncertainties of the analysis methods, as already discussed. All observational data have been converted for the Kroupa IMF. At  $z = 0$ , our mechanical feedback model most agrees with observed data from Tremonti et al. (2004) with the KD02 scale in Kewley and Ellison (2008), which gives 0.5–0.6 dex higher metallicities than in Curti et al. (2020b). At  $z = 1.4$ , although we only have galaxies at the low-mass end, we compare with observational data from Yabe et al. (2012) (converted to the method from Kewley and Dopita 2002 with the procedure given by Kewley and Ellison 2008) for massive galaxies. Then we find that the metallicity trend is comparable to our models. At higher redshifts, the MOSDEF (Sanders et al., 2021) and GLASS survey with NIRISS slitless spectroscopy on the James Webb Space Telescope (JWST) (Li et al., 2022) showed  $\sim 0.1$  and  $\sim 0.07$  dex evolution from  $z \sim 2$  to  $z \sim 3$ , respectively, which is larger than in all our models ( $\sim 0.07$  dex), except for the kinetic. The kinetic feedback model fits well

with the latter, but as discussed previously, this model is underproducing stars, so this matching does not necessarily support kinetic feedback of supernovae.

### 3.4 Conclusions

Implementing four different methods of supernova feedback into our self-consistent cosmological chemodynamical simulations, we confirm that the modelling of feedback has a great impact on the mass–metallicity relations (MZR), and can be constrained by spectroscopic observations of galaxies. In order to minimise other uncertainties, we have used the latest nucleosynthesis yields that can reproduce the observed elemental abundances of stars in the Milky Way (Kobayashi et al., 2020a,b), and aim to reproduce the stellar and gas-phase metallicities simultaneously.

We compare four supernova feedback models: The classic thermal and kinetic models, where supernova energy is either ejected in pure thermal form or with a partial kinetic kick; The stochastic model, similar to Dalla Vecchia and Schaye (2012), which heats a random number of neighbour gas particles with a fixed energy increase; And the mechanical model from Hopkins et al. (2018), which considers the work done during the Sedov-Taylor phase of supernova expansion. After performing a parameter study (Appendix A.1), we choose the following fiducial parameters from the observed cosmic SFRs (section 3.2.4):  $f = 1\%$ ,  $f = 50$ , and  $f = 1\%$  for kinetic, stochastic, and mechanical feedback models, respectively. Cosmic SFRs are significantly reduced with the kinetic feedback, which is too strong and is not producing enough stars, even with only a tiny fraction of supernova energy converted to a kick velocity. On the other hand, thermal and stochastic models are slightly overproducing stars at  $z \gtrsim 2$ . Mechanical feedback gives a better match to the observed cosmic SFRs (Fig. 3.6).

Despite fairly similar cosmic SFRs, we find a drastic change in the heating history of the ISM at  $z \sim 1$  with the kinetic feedback, and at  $z \sim 0.5$  with the stochastic feedback. This can be clearly seen in the gas-phase space diagram (Figs. 3.4 and 3.5) as the hot diffused gas, as well as in the spatial distribution of temperatures (Fig. 3.2). The spatial distribution of metals (Fig. 3.3) are fairly similar, except for the kinetic feedback.

Galaxy MZR are greatly affected by the supernova feedback models. Strong supernova feedback makes star formation inefficient in the galaxy, which results in lower stellar metallicities of galaxies (Fig. 3.8). However, this is not the case for gas-phase metallicities, particularly with kinetic feedback (Fig. 3.9). We find that young ( $< 0.1$  Gyr) stellar metallicities are consistent with the gas-phase metallicities. Considering both stellar and gas-phase MZR, our mechanical feedback seems the most plausible in order to explain the observational data of present-day galaxies.

Finally, we show the time evolution of the MZR. As expected, both stellar and gas-phase metallicities become lower at higher redshifts in all feedback models. With our mechanical

feedback, the predicted evolution of stellar MZR is in reasonably good agreement with the observations up to  $z \sim 3$  (Fig.3.10). Our kinetic feedback model gives too low stellar metallicities at all redshifts. For the gas-phase MZR, we find too large evolution in the kinetic model from  $z \sim 3$  to 0, and less prominent evolution for the other models (Fig.3.11). The available observations at  $z > 1$  seem rather consistent with the kinetic model, and we will investigate this further by comparing higher resolution and larger volume simulations to distant galaxies with the JWST as well as those of a large sample from ongoing and future spectroscopic galaxy surveys on ground-based telescopes.

## CHAPTER 4

# METALLICITY GRADIENTS

---

<b>4.1</b>	<b>INTRODUCTION</b>	<b>68</b>
<b>4.2</b>	<b>METHODS</b>	<b>71</b>
4.2.1	OUR MODEL	71
4.2.2	GALAXY SAMPLE	72
4.2.3	METALLICITY GRADIENTS	73
<b>4.3</b>	<b>RESULTS</b>	<b>74</b>
4.3.1	METALLICITY MAPS	74
4.3.2	RADIAL STELLAR METALLICITY PROFILES	79
4.3.3	RADIAL GAS-PHASE METALLICITY PROFILES	80
4.3.4	PRESENT-DAY GRADIENTS VS MASS	82
<b>4.4</b>	<b>REDSHIFT EVOLUTION</b>	<b>84</b>
4.4.1	STELLAR GRADIENTS VS MASS	84
4.4.2	GAS-PHASE GRADIENTS VS MASS	86
4.4.3	TIME EVOLUTION OF METALLICITY GRADIENT	87
<b>4.5</b>	<b>GALAXY TYPE DEPENDENCE</b>	<b>92</b>
<b>4.6</b>	<b>DISCUSSION</b>	<b>93</b>
4.6.1	PRESENT-DAY GRADIENTS	93
4.6.2	OVERALL EVOLUTION OF GRADIENTS	96
4.6.3	GRADIENT EVOLUTION IN AN INDIVIDUAL GALAXY	97
<b>4.7</b>	<b>CONCLUSIONS</b>	<b>99</b>

---

## 4.1 Introduction

The chemical composition of galaxies provides key insights into galaxy formation and evolution and has been intensively studied with large-scale galaxy surveys. For example, the correlation between galaxy stellar mass and metallicity (MZR), which we focused on in our previous paper (Ibrahim and Kobayashi, 2024), is important to explain global galaxy properties over cosmic time.

Moreover, studying the spatial distribution of metals inside galaxies gives more constraints on the chemical enrichment and star formation histories in the galaxies. Namely, radial metallicity gradients can constrain the growth of disc galaxies (e.g. Larson 1976; Kobayashi and Nakasato 2011b; Pilkington et al. 2012; Vincenzo and Kobayashi 2020), and the merging histories of the early-type galaxies (e.g. White 1978; Kobayashi 2004; Hopkins et al. 2009).

Present-day metallicity gradients in galaxies seem to depend on various properties such as galaxy stellar mass, which was studied with slit observations of a limited sample of early-type galaxies (ETGs) (e.g. Davies et al. 1993; Kobayashi and Arimoto 1999; Spolaor et al. 2010), the merging histories of galaxies (Rich et al., 2012), galaxy type (Kuntschner et al., 2010; Goddard et al., 2017), and environment (Zheng et al. 2017).

For further studies of the internal structure of galaxies, large-scale observational surveys have been performed with integral field units (IFU) such as SAURON (e.g. Kuntschner et al. 2010), CALIFA (e.g. Sánchez et al. 2012), MaNGA (e.g. Bundy et al. 2015), SAMI (e.g. Ho et al. 2014) and its successor HECTOR (e.g. Bland-Hawthorn 2015), and MUSE with higher resolution (Bacon et al. 2010; Sánchez-Menguiano et al. 2018), where metallicity gradients are obtained for thousands of nearby galaxies.

Metallicity gradients have been extensively studied using hydrodynamical simulations, including Taylor and Kobayashi (2017), IllustrisTNG (Hemler et al., 2021; Garcia et al., 2023), EAGLE (Tissera et al., 2022), CIELO (Tapia-Contreras et al., 2025), FIRE (Ma et al., 2017), and FOGGIE (Acharyya et al., 2025), in addition to isolated galaxy simulations Kobayashi (2004), Kobayashi and Nakasato (2011b), MUGS and MaGICC (Gibson et al., 2013). These studies consistently find that gradients are typically negative at  $z = 0$ , flatten with increasing stellar mass and are shaped by inside-out growth, stellar feedback, radial mixing, and gas accretion. At higher redshifts, however, the picture becomes more varied: some simulations predict flatter gradients such as EAGLE (Tissera et al., 2022) and enhanced MaGICC (Gibson et al., 2013), while others find steeper gradients, e.g., TNG50 (Hemler et al., 2021) and MUGS (Gibson et al., 2013). Some studies also report breaks between inner and outer metallicity profiles, linked to structural and dynamical transitions in galaxies (Garcia et al., 2023). While quantitative differences exist depending on the feedback models and resolution, the qualitative trends across simulations remain consistent. Semi-analytical models have also explored the origin and evolution of metallicity gradients in galaxies (e.g., Lian et al., 2018; Belfiore et al., 2019; Yates et al., 2021; Sharda et al., 2021, 2024; Stevens et al., 2024), offering complementary insights on the roles of star formation efficiency, gas inflows, and outflows. These models are particularly useful for isolating the effects of feedback strength, enrichment timescales, and metal mixing processes such as turbulent diffusion, which can be parameterized to explore a wider range of physical scenarios.

In the nearby universe, the inner regions of most spiral galaxies are more chemically enriched than the outskirts, which produces *negative* metallicity gradients (e.g. Searle 1971; Belfiore et al.

2017). The negative gradient is observed for individual H II regions, planetary nebulae, Cepheids, and open clusters in the Milky Way (e.g., Magrini et al. 2010; Stanghellini and Haywood 2010), and in nearby galaxies (e.g. Zaritsky et al. 1994; Kewley et al. 2010; Bresolin 2011; Berg et al. 2015). One way to explain negative gradients of gas-phase (and also stellar) metallicity is the ‘inside-out’ growth scenario of galaxy formation (Larson 1974; Matteucci and Franco 1989; Samland et al. 1997; Portinari and Chiosi 1999; Prantzos and Boissier 2000; Kobayashi and Nakasato 2011b). Several physical processes can ‘invert’ this negative gas gradient, making the outskirts equally or more metal-enriched than the centre of the galaxy. The gas-phase gradient can be flattened due to the accretion of metal-enriched gas into the outskirts (Bresolin et al., 2012), supernova-driven winds (Gibson et al., 2013; Ma et al., 2017), or galactic mergers and interactions (Rich et al., 2012). Finally, the gas-phase gradients can become positive (inverted) due to the accretion of pristine gas to the galactic centre (e.g., Jones et al. 2013; Sánchez Almeida et al. 2018) or strong metal-rich galactic outflows (e.g. Tissera et al. 2022).

Merging histories of galaxies, notably major mergers, can also impact the flattening of the *stellar* metallicity gradients. However, gas-rich galaxy mergers can cause central star formation from metal-rich gas, recreating negative gradients of stars. Kobayashi (2004) studied these effects in a cosmological context.

Therefore, tracing the evolution of the metallicity gradients across cosmic time is crucial to understanding the role of star formation, gas flows, and feedback processes during galaxy evolution. Despite being well observed in the nearby universe, metallicity gradients remain poorly constrained at higher redshifts, giving diverse conclusions (e.g. Cresci et al. 2010; Queyrel et al. 2012; Yuan et al. 2011; Jones et al. 2013; Wang et al. 2017, 2022; Venturi et al. 2024; Ju et al. 2024). Direct measurements of metallicity gradients at high redshifts require the near-infrared IFU (e.g., KMOS on the Very Large Telescope (VLT); Sharples et al. 2013; Curti et al. 2020a), with surveys targeting hundreds of galaxies at  $z \sim 1-2$  (e.g. Stott et al. 2014a; Wuyts et al. 2016). Furthermore, NIRSpect IFU on the James Webb Space Telescope (JWST) can expand this study including higher redshifts  $z > 6$  (e.g., Venturi et al. 2024; Ju et al. 2024).

To predict and constrain chemical enrichment within galaxies, hydrodynamical simulations are necessary. In Ibrahim and Kobayashi (2024), we implemented and compared four models of supernova feedback (thermal, stochastic, kinetic, and mechanical) with our cosmological hydrodynamical simulations, and concluded that the mechanical feedback model gives the best match with the local stellar and gas-phase MZR, as well as the observed cosmic star formation rates (SFRs). Similar comparative studies of supernova feedback have also been carried out in other cosmological simulations (e.g. Gentry et al., 2017; Chaikin et al., 2022), highlighting the importance of feedback modeling in reproducing observed galaxy properties.

In this paper, we use these supernova feedback models to investigate their impact on the metallicity gradients of galaxies while keeping all the other physical processes unchanged. We present both

stellar and gas-phase metallicity gradients of the galaxies in our simulations, where various types and masses of galaxies are included based on  $\Lambda$  cold dark matter ( $\Lambda$ CDM) cosmology. Therefore, our prediction can be statistically compared with the ongoing and future observational surveys.

This paper is arranged as follows: In Section 4.2, we describe our galaxy samples and define the stellar and gas-phase metallicity gradients used for our simulated galaxies. In Section 4.3, we present an example of two galaxies at  $z = 0.7$  and discuss their stellar and gas-phase gradient and kinematics depending on supernova feedback in detail. Then, we analyze the stellar and gas-phase gradients for all galaxies in our simulations at  $z = 0.7$ , depending on galaxy stellar mass. We also show the stellar mass dependence of metallicity gradients at  $z = 0$  with our best feedback model. In Section 4.4, we present the evolution of the metallicity gradients up to  $z = 5$ . In Section 4.5, we study the evolution of the gas-phase metallicity gradient depending on galaxy type. Finally, our conclusions are given in Section 4.7.

## 4.2 Methods

### 4.2.1 Our Model

We perform chemodynamical simulations with our own code based on the GALaxies with Dark matter and Gas intEract 3 (GADGET-3) code (Springel et al., 2005) including various baryon physics as in our previous work (Ibrahim and Kobayashi, 2024).

In this paper, the simulations are run with the same initial conditions and resolution but in a larger volume, commoving  $25h^{-1}$ Mpc cubic box, with periodic boundary conditions. The number of gas and dark matter particles is  $N_{\text{gas}} = N_{\text{DM}} = 320^3$ , with mass  $M_{\text{gas}} = 9.34 \times 10^6 h^{-1} M_{\odot}$  and  $M_{\text{DM}} = 5.1 \times 10^7 h^{-1} M_{\odot}$ . We use the same cosmological parameters as in Ibrahim and Kobayashi (2024):  $\Lambda$ CDM cosmology with  $h = 0.68$ ,  $\Omega_m = 0.31$ ,  $\Omega_{\Lambda} = 0.69$  and  $\Omega_b = 0.048$  (Planck Collaboration, 2020). The gravitational softening lengths are  $\epsilon_{\text{gas}} = 0.84375 h^{-1}$  kpc and  $\epsilon_{\text{DM}} = 1.6875 h^{-1}$  kpc for gas and dark matter/stars, respectively. In this study, we use the same cosmological simulation framework as described in Ibrahim and Kobayashi (2024), with key physical prescriptions summarized here for completeness. SFR are calculated based on local gas conditions, following a dynamical timescale as described in Kobayashi (2004). We adopt a Kroupa (2008) initial mass function (IMF) that is fixed throughout the simulation and does not vary with galaxy mass or redshift. The initial gas composition assumes primordial abundances, with 75.3% hydrogen and 24.7% helium by mass, as in Kobayashi et al. (2020a).

Our cosmological simulations include various physical processes relevant to galaxy formation and evolution: metallicity-dependent radiative cooling (Kobayashi, 2004), star formation (Kobayashi et al., 2007), black hole physics (Taylor and Kobayashi, 2014), and element and energy production from asymptotic giant branch stars, Type Ia, Type II supernovae (Kobayashi, 2004). Our simulations also include hypernovae (HNe), which are energetic core-collapse supernovae from

massive progenitors ( $20\text{--}50M_{\odot}$ ) often associated with gamma-ray bursts (Kobayashi et al., 2006b). Each HN event releases more energy and metals compared to a typical SN, thereby enhancing the effects of stellar feedback and chemical enrichment, particularly in low-metallicity environments. We adopt the same metallicity-dependent HN fraction and explosion energy as in Kobayashi and Nakasato (2011b), calibrated to reproduce elemental abundance patterns in the Milky Way. These values are fixed in our model and not treated as free parameters in this study. Including HNe improves the realism of the simulations and contributes to the regulation of star formation.

Supernovae feedback modelling was described in detail in Ibrahim and Kobayashi (2024); we summarize the key points below.

To study the impact of supernova feedback on the metallicity gradients, we use three out of the four feedback models studied in our previous work (Ibrahim and Kobayashi, 2024) since we found that the kinetic feedback model cannot reproduce the global observations of present-day galaxies. In this paper, we use (1) the thermal feedback distributing pure thermal energy to the neighbour gas particles, (2) the stochastic feedback (similar to Dalla Vecchia and Schaye 2012) distributing thermal energy in a stochastic way to a random number of particles with the probability parameter  $f=50$ , and (3) the mechanical feedback (Hopkins et al., 2018), which accounts the physics during the Sedov-Taylor phase of supernova expansion, using the fraction parameter  $f=1\%$ . Note that the Sedov-Taylor phase and superbubble evolution are not explicitly resolved due to the resolution limits inherent in cosmological simulations. Similarly, we do not include a sub-grid turbulent metal diffusion model. These physical limitations are discussed further in Section 4.6 in the context of their potential impact on metallicity gradients.

## 4.2.2 Galaxy sample

As in Ibrahim and Kobayashi (2024), galaxies are identified using the friends-of-friends (FoF) algorithm based on the code used in Springel et al. (2001a). The total stellar mass,  $M_*$ , is defined within 20 kpc. From the FoF centres, the centres of galaxies are re-defined as the centre of mass of star particles. We use these galactic centres also for gas-phase gradients at high redshifts, although it is not always possible in observations (e.g. Venturi et al., 2024). We only use galaxies with more than 100 star particles in the 20 kpc radius.

In the case of ongoing mergers or galaxies with satellite companions, our analysis can confound the system with a single galaxy, which can bias our estimation of the metallicity profiles and gradients. To eliminate these contaminations, we apply the following criteria: It is considered a single galaxy only if the total stellar mass within  $2R_e$  from the galactic centre is larger than 75% of the total stellar mass of the galaxy, otherwise we ignore this object:

$$M_{*,2R_e} > 0.75M_*. \quad (4.1)$$

$M_{*,2R_e}$  is the stellar mass within the projected radius  $r < 2R_e$ , where  $R_e$  is the effective radius, i.e. the radius containing half the total stellar mass.

As a result, 838, 1119, and 591 galaxies with  $M_* \sim 10^{8.5-11} M_\odot$  are obtained for our thermal, stochastic, and mechanical feedback models, respectively (more details in Section 4.3.2). In §4.5, we discuss the dependence of gradients on the galaxy types defined from the star formation main sequence (also in Appendix B.2).

All radial gradients in this work are measured in the projected galaxy plane (i.e. using the simulation’s native  $x$ – $y$  coordinates) without rotating each galaxy to a face-on orientation. Observational surveys typically estimate galaxy inclinations from axis ratios and apply inclination corrections to their measurements accordingly. We therefore caution that direct comparisons with fully inclination-corrected observational gradients should account for this difference, and a future update of this analysis will include an explicit rotation of each galaxy to face-on prior to gradient fitting.

### 4.2.3 Metallicity gradients

In this paper, we investigate the radial metallicity profiles although the metallicity distributions can show more detailed structures depending on galaxy types. For each galaxy, we compute the projected radius  $r$  with respect to the galactic centre in the  $(x, y, z)$  space. Along  $z$ -axis, all particles in  $\pm 20$  kpc are projected on the  $x$ – $y$  plane.

To compare with observations, the stellar metallicity at a given  $r$  is weighted by the rest-frame V-band luminosity  $L_V$  of star particles, where are located most of the absorption lines used in the observations, such as

$$Z_{*w} = \frac{\sum(Z_* \times L_V)}{\sum L_V}. \quad (4.2)$$

The gas-phase metallicity at a given  $r$  is weighted by the SFR of gas particles, as observed with emission lines, such as

$$Z_{gw} = \frac{\sum(Z_g \times \text{SFR})}{\sum \text{SFR}}. \quad (4.3)$$

We then produce the metallicity profiles of the gas-phase metallicities against linear  $r$  and the stellar metallicity profile against  $\log(r/R_e)$ . When we estimate the overall metallicity profile for all the galaxies in our simulations at a given redshift  $z$  (Sections 4.3.2 and 4.3.3), we first produce the profile for each individual galaxy, bin along  $\log(r/R_e)$  for stars and  $r$  for gas, and then calculate the median value of the metallicity in each bin.

Using the median radial profiles obtained, we measure the slope of the profile, which equals the metallicity gradient. Before the weighting, the stellar ( $\alpha_{*,nw}$ ) and gas-phase ( $\alpha_{g,nw}$ ) metallicity gradient are given by:

$$\alpha_{*,nw} = \frac{\Delta \log Z_*}{\Delta \log(r/R_e)} [\text{dex dex}^{-1}] \quad (4.4)$$

and

$$\alpha_{g,nw} = \frac{\Delta \log Z_g}{\Delta r} \quad [\text{dex kpc}^{-1}]. \quad (4.5)$$

Replacing the (mass-weighted) metallicities by the weighted metallicities in equations 4.4 and 4.5, we obtain:

$$\alpha_* = \frac{\Delta \log(\sum(Z_* \times L_V)/\sum L_V)}{\Delta \log(r/R_e)} \quad [\text{dex dex}^{-1}] \quad (4.6)$$

and

$$\alpha_g = \frac{\Delta \log(\sum(Z_g \times \text{SFR}_g)/\sum \text{SFR}_g)}{\Delta r} \quad [\text{dex kpc}^{-1}]. \quad (4.7)$$

Finally, to calculate the gradient values, the inner and outer boundaries are applied for stars and gas separately (Section 4.3.1 for more details). When we compare to observations (Section 4.3.4) with a different definition of gradients in  $[\text{dex } R_e^{-1}]$ , we divide our gradients by  $R_e$  [kpc] of individual galaxies to make them in  $[\text{dex } R_e^{-1}]$ . It is harder for stars, but since the stellar metallicity is flattened around  $0.1R_e$ , the metallicity difference from  $r = 0$  to  $r = R_e$  [dex  $R_e^{-1}$ ] is approximately  $\alpha_*$ .

## 4.3 Results

### 4.3.1 Metallicity maps

#### Galaxy A

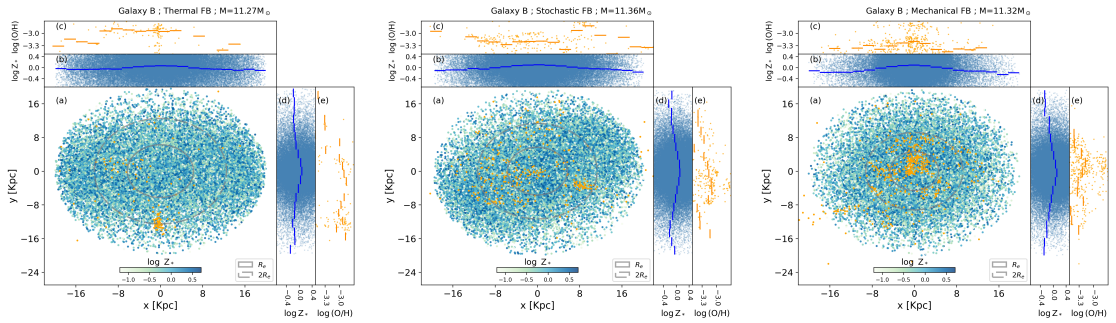


FIGURE 4.1: Stellar (blue) and gas (orange) distribution for the same massive galaxy A ( $M_* \sim 10^{11} M_\odot$ ) with the thermal, stochastic and mechanical feedback models (1st, 2nd and 3rd panels, respectively). The grey solid and dashed circles represent  $1R_e$  and  $2R_e$ , respectively. Panels (b) and (c) show the stellar and gas-phase metallicity distributions, respectively, along the  $x$  axis. The solid blue and orange lines are the median metallicity in each bin of  $x$  (see main text for details) for stellar and gas-phase metallicity, respectively. Panels (d) and (e) are the same as panels (b) and (c) but along the  $y$  axis.

Panels (a) of Figure 4.1 show the stellar (blue) and gas-phase (orange) distributions for an example massive galaxy (Galaxy A) with  $M_* \sim 10^{11} M_\odot$  in our cosmological simulations at  $z = 0.7$ , with the same initial conditions for the thermal (left panels), stochastic (middle panels), and mechanical (right panels) feedback models. The individual stellar particles on the map are colour-coded

with the stellar metallicity  $\log Z_*$ . The grey solid and dashed circles on each map represent  $1R_e$  and  $2R_e$ , respectively. The upper histograms on each map represent the radial metallicity profiles along the  $x$ -axis for stellar (blue) and gas-phase (orange) metallicities in panels (b) and (c), respectively. The right-side histograms (d) and (e) represent the radial metallicity profiles along the  $y$ -axis for stars and gas, respectively. The solid lines in the histograms are the median metallicity in each bin of  $x$  or  $y$  (20 bins within the total diameter of 40 kpc).

The stellar distribution in this massive galaxy is similar among the three feedback models. No specific pattern is distinguished from the stellar metallicity map either. However, the gas phase distribution is considerably impacted by the supernova feedback. The gas particles are non-uniformly distributed in all models, but with the thermal model (left), they are concentrated in one region at the bottom, and with the mechanical model (right), they are more centred around the centre of the stellar component. The stellar and gas-phase metallicity histograms show the presence of a gradient along both the  $x$  and  $y$  axes. Gas gradients show more azimuthal variations than stellar gradients.

To compare with observations, we use the V-band luminosity-weighted (solid lines) and mass-weighted (dashed lines) stellar metallicity profiles against projected radius  $r$ , as shown in Figure 4.2(a), and calculate the slopes as defined in Section 4.2.3. The profiles can be well fitted with a linear line (Eq. 4.6) at  $r < R_e$  and  $r = 1 - 2R_e$  separately, as shown with the faint dotted lines. For all feedback models, the luminosity-weighted and mass-weighted stellar metallicity give almost the same inner gradients  $\alpha_{*,in}$ . The luminosity-weighted gradients are steeper by  $\sim 0.01$  than the mass-weighted ones for the outer and total gradients ( $\alpha_{*,out}$  and  $\alpha_*$ , respectively) due to slight positive age gradients. For luminosity-weighted stellar metallicities, the total gradients  $\alpha_*$  for this massive galaxy are not so much affected by the supernova feedback model. The gradient is only slightly flatter in the thermal (blue) case by  $0.03 \pm 0.013$  and  $0.03 \pm 0.014$  than in the stochastic (orange) and mechanical (red) models, respectively. The outer gradient  $\alpha_{*,out}$  is flatter in the stochastic case by  $0.03 \pm 0.008$  and  $0.04 \pm 0.006$  than in the mechanical and thermal cases, respectively. However, the inner gradient  $\alpha_{*,in}$  is significantly steeper with the thermal feedback by  $0.05 \pm 0.005$  than in the mechanical case. This means it is important to measure the inner and outer gradients separately to see the impact of stellar feedback on the stellar metallicity gradients. All the stellar gradients are negative independently from the feedback model or weighting, meaning that Galaxy A is more metal-rich in the central part, as already seen in the stellar histograms of Figure 4.1, which indicates an inside-out growth (e.g., Vincenzo and Kobayashi, 2020).

The SFR-weighted (solid lines) and mass-weighted (dashed lines) gas-phase oxygen abundance gradients,  $\alpha_{g,in}$ , are quantified in Figure 4.2(b), where the SFR-weighted profiles start at  $r > 2$  kpc (for mechanical) and  $r > 8$  kpc (for stochastic) due to the SFR-weighting as the central part of the galaxy has very few star-forming gas particles. The gas is not star-forming at all in the thermal case, resulting in the absence of the SFR-weighted metallicity profile. Although

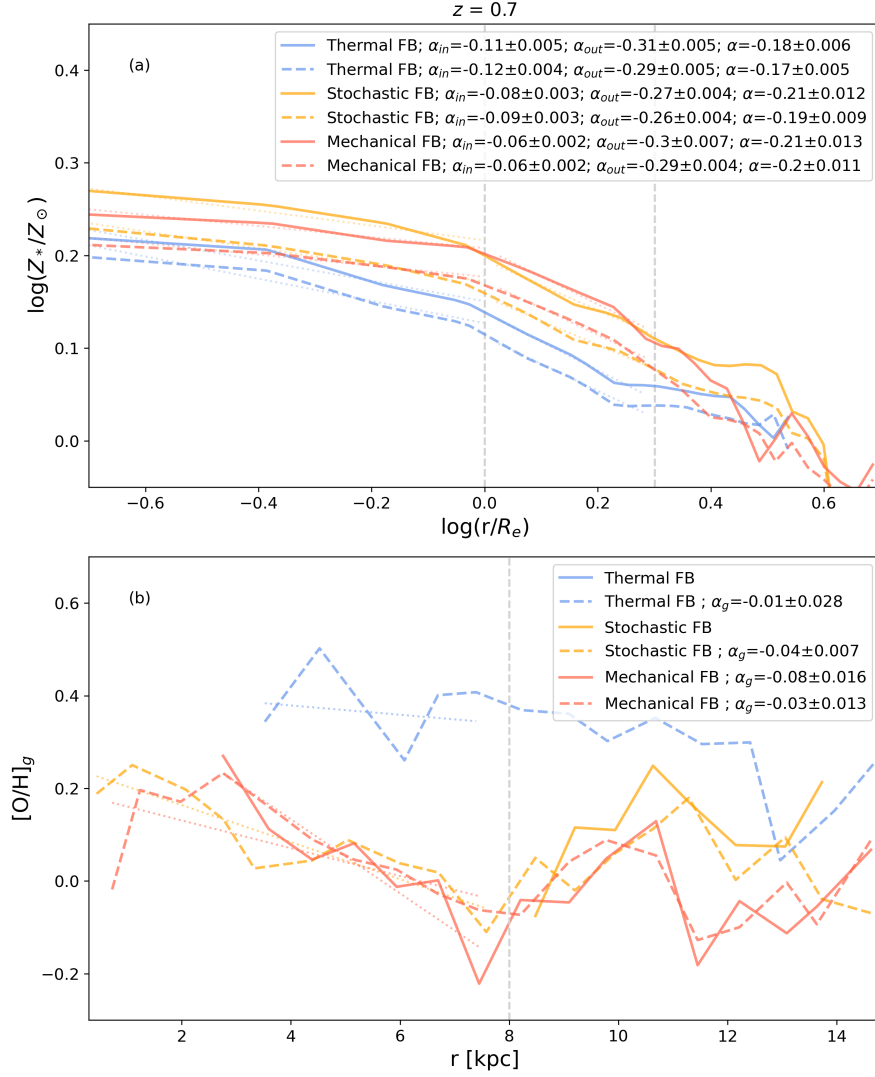


FIGURE 4.2: (a) V-band luminosity-weighted (solid lines) and mass-weighted (dashed lines) stellar metallicity profiles for Galaxy A at  $z = 0.7$  for the thermal (blue), stochastic (orange) and mechanical (red) feedback models. We show the profiles with measurable radius  $\alpha$ , the inner gradient  $\alpha_{*,in}$  within  $R_e = 4.59$  kpc, and the outer gradient  $\alpha_{*,out}$  between  $R_e$  and  $2R_e$  (vertical dashed grey lines). (b) SFR-weighted (solid lines) and mass-weighted (dashed lines) gas-phase metallicity profiles for Galaxy A at  $z = 0.7$  with measurable gradients  $\alpha_{g,in}$  in 8 kpc (vertical dashed grey lines). The dotted lines show the best linear regression fits.

some enhancement is seen in the outskirts with the stochastic and mechanical feedback, the gradients can be fitted with a linear line within 8 kpc as shown with the dotted line (Eq. 4.7). Considering the fitting error of the thermal model, we do not find a significant difference in the mass-weighted gradients. Within 8kpc, the SFR-weighted gradient for this galaxy is only available for the mechanical feedback and is  $\alpha_{g,in} = -0.08 \pm 0.016$  dex/kpc, which is steeper than the mass-weighted one by  $0.05 \pm 0.021$  dex/kpc.

To understand the impact of stellar feedback on the gas distribution further, we study the kinematics of this galaxy in Appendix B.1 using velocity maps. Galaxy A shows no significant rotation for

stars and gas. The stellar feedback models do not seem to impact the kinematics so much either for this massive galaxy.

## Galaxy B

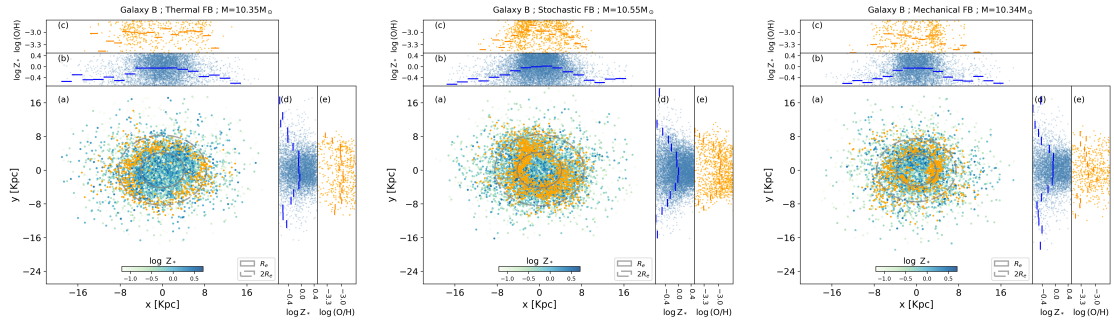
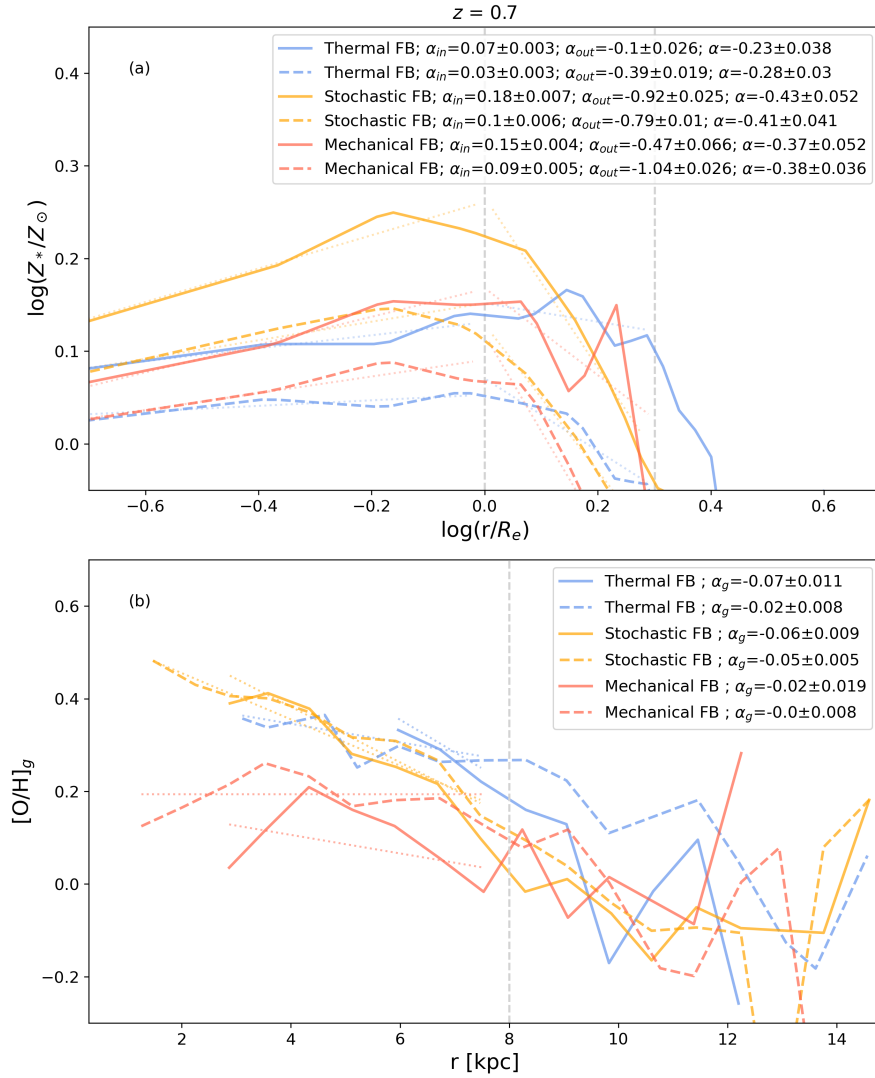


FIGURE 4.3: Same as Fig. 4.1 but for an intermediate-mass galaxy B ( $M_* \sim 10^{10} M_\odot$ ).

Figure 4.3 is the same as Figure 4.1 but for an example intermediate-mass galaxy ( $M_* \sim 10^{10} M_\odot$ ), that we will refer to as Galaxy B. The stellar distribution is similar for all feedback models, although it is slightly more elongated with the stochastic feedback and more concentrated in the galactic centre with the mechanical feedback. Supernova feedback has a larger impact on gas-phase distributions for intermediate-mass galaxies than for massive galaxies. In this example, the gas particles are pushed away from the centre of the galaxy mainly due to AGN feedback, leading to the absence of gas particles in the centre. This “hole” feature is most clearly seen in the thermal feedback at  $r \sim 6$  kpc, while the feature is less visible with the mechanical feedback.

The stellar and gas-phase metallicity gradients for this galaxy are shown in Figure 4.4(a) and 4.4(b), respectively, for the thermal (blue), stochastic (orange), and mechanical (red) feedback. The stellar metallicity profiles change around  $1R_e$ , so we also measure inner and outer gradients. The luminosity-weighted (solid) and mass-weighted (dashed) stellar gradients are similar for the total gradients  $\alpha_*$ . However, the inner gradients  $\alpha_{*,in}$  are positive and steeper by  $\sim 0.04$ - $0.08$  with luminosity-weighted, possibly due to negative age gradients of inside-out quenching. The outer gradients  $\alpha_{*,out}$  significantly depend on the weighting, where the luminosity-weighted gradients are steeper by  $0.57 \pm 0.07$  for the mechanical, and flatter by  $0.13 \pm 0.02$  for the stochastic model. For luminosity-weighted stellar metallicities, the total gradient  $\alpha_*$  is steeper for the stochastic feedback by  $0.20 \pm 0.064$  and  $0.06 \pm 0.07$  than the thermal and mechanical, respectively. The outer gradients  $\alpha_{*,out}$  are considerably steeper in the stochastic models ( $\alpha_{*,out} = -0.92 \pm 0.03$ ) than in the thermal and mechanical feedbacks ( $\alpha_{*,out} = -0.10 \pm 0.03$  and  $\alpha_{*,out} = -0.47 \pm 0.06$ , respectively), this may be caused by the limited number of particles at the outskirts (Fig. 4.3). With all feedback models, the inner gradients  $\alpha_{*,in}$  for Galaxy B is *positive* (inverted), meaning the star particles in the galactic centre are more metal-poor. As shown in the following sections, the inverse metallicity gradients are unusual, which might be because this example galaxy was selected from the unique ring structure of the gas.

FIGURE 4.4: Same as Figure 4.2, but for Galaxy B with  $R_e = 3.74$  kpc.

In Figure 4.4(b) we compare the SFR-weighted (solid) and mass-weighted (dashed) gas-phase oxygen abundance gradients,  $\alpha_{g,in}$ , again within 8 kpc. The SFR-weighted gradient is steeper than the mass-weighted one by  $0.05 \pm 0.01$  and  $0.01 \pm 0.01$  dex/kpc for the thermal and stochastic feedback models, respectively. The SFR-weighted gas-phase metallicity profile of this galaxy in the thermal case starts at  $r > 6$  kpc because the gas particles are not star-forming at  $r < 6$  kpc, which may cause the steepness of the gradient by  $\sim 0.05$  dex/kpc compared the mass-weighted one.

We study the kinematics of Galaxy B in Appendix B.1 and find stellar rotation in the  $x - y$  plane. The gas phase particles are also rotating but on a perpendicular angle. The rotation seems stronger with the stochastic feedback.

### 4.3.2 Radial stellar metallicity profiles

We extend our analysis of radial metallicity gradients to all galaxies in our simulations. We find it interesting to show the metallicity profiles of massive and lower-mass galaxies separately at the threshold stellar mass  $M_* \sim 10^{10} M_\odot$ . The metallicity profiles for lower-mass galaxies ( $M_* < 10^{10} M_\odot$ ) in our simulations at  $z = 0.7$  are shown in Figure 4.5 for V-band luminosity-weighted stellar metallicities (the upper panel a) and SFR-weighted gas-phase oxygen abundances (the lower panel b).

For stars, the solid lines are the medians calculated for 20 bins along the projected radius  $\log(r/R_e)$  of 631, 794, and 434 lower-mass galaxies respectively for the thermal (blue), stochastic (orange), and mechanical (red) feedback models. The shaded areas are for  $1\sigma$  scatter. The dotted lines show the best linear regression fits of these medians. As in Figs. 4.2(a) and 4.4(a), we fit with a broken power-law to calculate the inner gradient  $\alpha_{*,in}$  between 0.73 kpc (which corresponds to our spatial resolution limit at  $z = 0.7$ ) and  $1R_e$ , and the outer gradient  $\alpha_{*,out}$  between  $1R_e$  and  $2R_e$ . The vertical grey solid lines represent the fitting range. We also fit with a single slope  $\alpha_*$  along the total radius. These slope values are presented on each figure for each model.

As shown in Ibrahim and Kobayashi (2024), the mechanical feedback produces a lower stellar metallicity. Here, we find that all median gradients are negative independent of the feedback models. The single-slope gradient  $\alpha_*$  for the mechanical feedback model is  $\alpha_* = -0.45 \pm 0.041$ , which is significantly flatter by  $\sim 0.3$  than for the other models; the stochastic feedback gives slightly steeper gradient than the thermal feedback. Also, with the broken power-law fit, both the inner and outer gradients are flatter with the mechanical feedback. For all feedback models, the inner gradients are much flatter than the outer gradients.

Figure 4.6(a) is the same as Figure 4.5(a), but for massive galaxies ( $M_* > 10^{10} M_\odot$ ) in our simulations, which have 207, 325, and 157 massive galaxies for the thermal (blue), stochastic (orange), and mechanical (red) feedback models, respectively. The inner gradients are considerably flatter than the outer gradients. Unlike for lower-mass galaxies, the median stellar metallicity gradient of massive galaxies in our simulations is not highly impacted by the stellar feedback for both the total and outer gradients. Nevertheless, the inner gradient  $\alpha_{*,in} = 0.05 \pm 0.03$  is flatter with the thermal model by  $0.17 \pm 0.03$  than in the stochastic model, and by  $0.09 \pm 0.04$  than in the mechanical model.

For all mass ranges, we find that the median stellar gradient in our simulations is always negative, making most galaxies more metal-rich in the central regions. For massive galaxies, the impact of stellar feedback on the gradients is subtle; the thermal feedback results in a flatter inner gradient for the median but not for Galaxy A (§4.3.1). For lower-mass galaxies, however, both the inner and outer gradients are flatter with the mechanical feedback, which can be explained by the suppression of star formation at the centre and the ejection of metals to the outskirts.

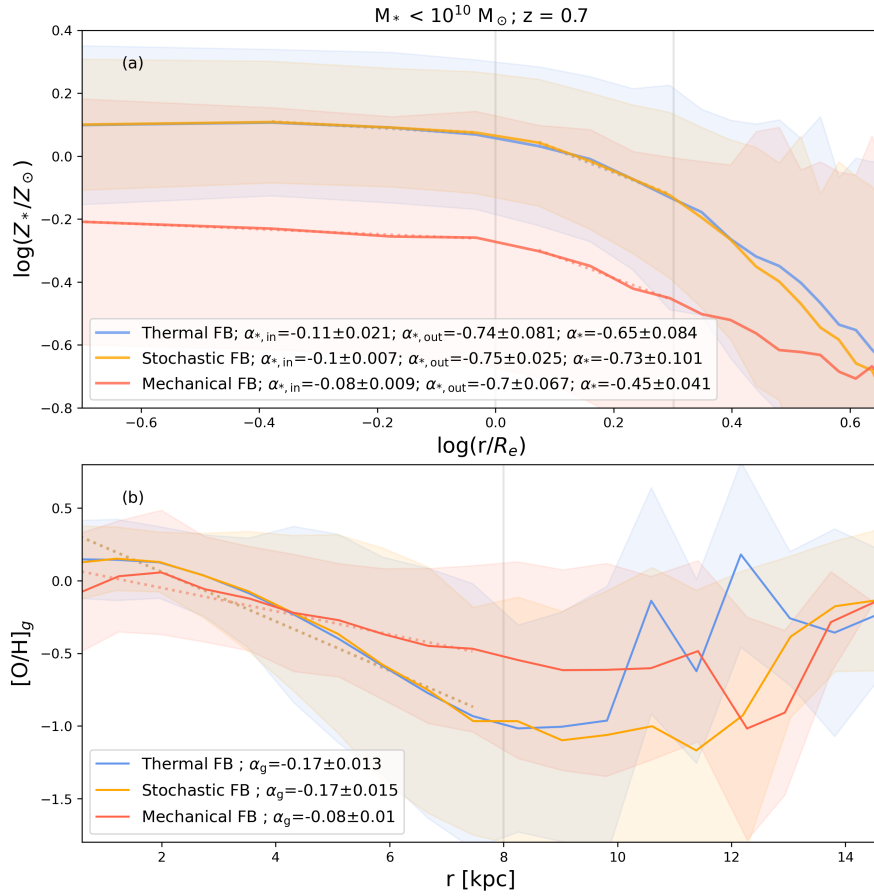


FIGURE 4.5: (a) V-band luminosity-weighted stellar metallicity profiles for lower-mass galaxies ( $M_* < 10^{10} M_\odot$ ) with measurable gradients at  $z = 0.7$  in our simulations. The solid lines are the median for the thermal (blue), stochastic (orange), and mechanical (red) feedback models. The shaded areas are  $1\sigma$  scatter. The dotted lines are the best linear fit of the medians for a single slope  $\alpha_*$ , the inner gradient  $\alpha_{*,in}$  within  $1R_e$ , and the outer gradient  $\alpha_{*,out}$  between  $1R_e$  and  $2R_e$ . The vertical grey solid lines represent  $1R_e$  and  $2R_e$ . (b) The same as (a), but for SFR-weighted gas-phase oxygen abundance profiles. The medians are fitted with a single slope  $\alpha_{g,in}$  (dotted line) within  $8$  kpc, indicated by the vertical grey solid line.

### 4.3.3 Radial gas-phase metallicity profiles

Figures 4.5(b) and 4.6(b) show the SFR-weighted gas-phase oxygen abundance profiles for our lower-mass ( $M_* < 10^{10} M_\odot$ ) and massive ( $M_* > 10^{10} M_\odot$ ) galaxies, respectively. The blue, orange, and red solid lines are the best linear fits of medians for galaxies obtained with the thermal, stochastic and mechanical feedback models, respectively. The shaded area is for  $1\sigma$  scatter. As in Figs. 4.2(b) and 4.4(b), the gas-phase metallicity gradients  $\alpha_{g,in}$  are calculated within  $8$  kpc, represented by the vertical grey solid line, which approximately corresponds to  $2R_e$  (Sánchez et al., 2014).

Figure 4.5(b) shows that the stellar feedback significantly impacts the gas-phase metallicity gradients for lower-mass galaxies; although the central gas-phase metallicities are not so different, a clear difference is seen at  $r > 5$  kpc. The gradient is flatter for the mechanical case by  $\sim 0.1$

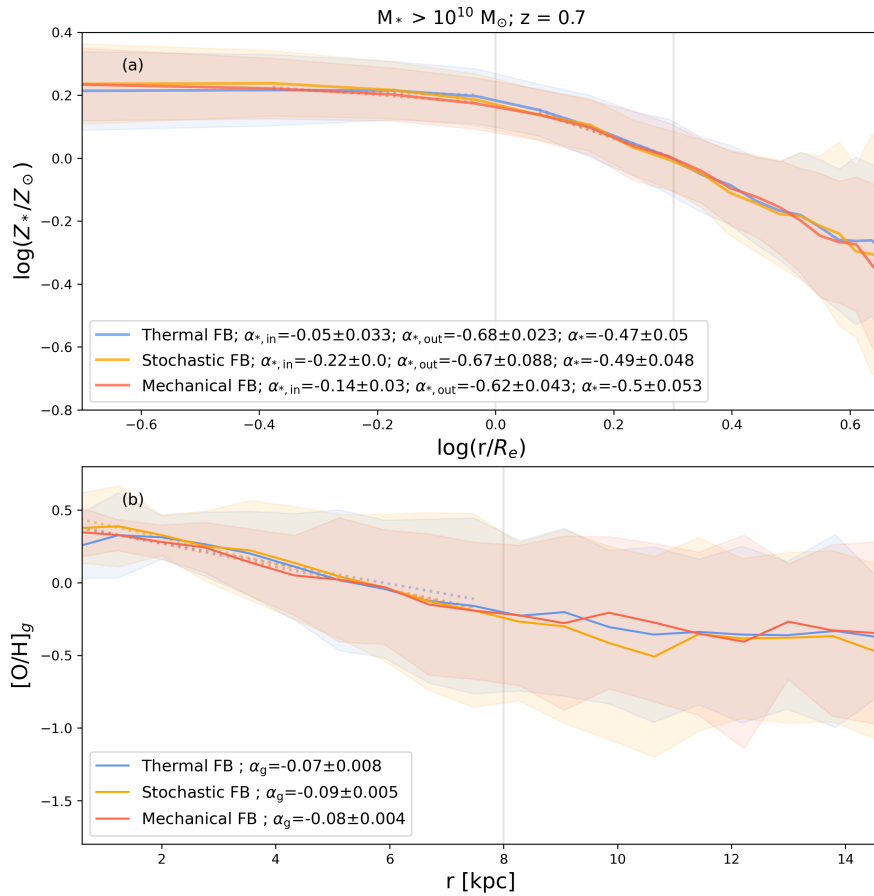


FIGURE 4.6: Same as Figure 4.5, but for massive galaxies with  $M_* > 10^{10} M_\odot$ .

dex/kpc than for the other models. We note an interesting divergence between the stellar and gas-phase metallicity profiles in the mechanical-feedback run: stellar metallicities are lower than in the other models, while the gas-phase O/H is higher at intermediate radii. A plausible explanation is that the mechanical scheme more efficiently ejects and redistributes recent SN metals into the outskirts (raising gas-phase O/H at  $r \sim 1\text{--}2R_e$ ) while simultaneously suppressing late star formation. As a result, a larger fraction of the stellar mass formed earlier from less-enriched gas, lowering the V-band-weighted stellar metallicity. Consistent with this picture, we find that the young-star ( $<100\text{--}200$  Myr) metallicity profile more closely tracks the gas-phase profile than the total stellar one. For massive galaxies, however, we do not see a significant difference for gas-phase metallicity gradients, as shown in Figure 4.6(b), which is also the case for stellar gradients in Figure 4.6(a).

For all mass ranges of galaxies, the median gas-phase metallicity gradient is always negative. This could be due to the inflow of metal-rich gas, but for galaxies with low gas density at the centre (§4.3.1), it is more likely to be caused by stellar mass-loss (§4.3.2). For lower-mass galaxies, the median gradient is flatter with the mechanical feedback, possibly due to outflows driving metal-rich gas to the outer regions of the galaxies. As for stellar gradients, the supernova feedback model has no significant impact on the gradient of massive galaxies.

#### 4.3.4 Present-day gradients vs mass

In Figure 4.7, we show the dependence of the metallicity gradients on stellar mass at  $z = 0$  specifically with the mechanical feedback model, which gave the best matches to the observed MZR in Ibrahim and Kobayashi (2024). The upper panel is for V-band luminosity-weighted stellar metallicity gradients for all galaxies in our simulation. The red circles represent the gradients of individual galaxies, here within  $1.23 \text{ kpc} < r < 1.5R_e$  to compare with the observational data (black symbols and lines, and grey shading). The red solid line connects the median values at a given stellar mass of our simulated galaxies. The median stellar metallicity gradient is steeper for intermediate-mass galaxies ( $M_* \sim 10^{10}M_\odot$ ) by  $\sim 0.2$  dex than for massive galaxies, which is in excellent agreement with observational data from the CALIFA sample of 62 nearly face-on, spiral galaxies (Sánchez-Blázquez et al., 2014, black triangles with errorbars, measured in  $1.5R_e$ ), the CALIFA sample of 300 from spheroids to spiral galaxies (González Delgado et al., 2015, dashed black line, measured in  $\sim 1R_e$ ), the SAURON sample of 48 early-type galaxies (Kuntschner et al., 2010, black squares with errorbars), and the ATLAS3D sample of 253 galaxies (grey shading, Kuntschner et al., priv. comm.).

This flattening of gradients toward the massive end is found to be due to major mergers in Kobayashi (2004) and Taylor and Kobayashi (2017). Then our gradients become flatter again toward the low-mass end, which is possibly due to supernova feedback (Fig. 4.5(a)). A similar V-shape trend (against the central velocity dispersion) is found in the observations by Spolaor et al. (2010).

The lower panel is the same but for SFR-weighted gas-phase oxygen abundance gradients within 8 kpc; the fitting range does not change the results due to the SFR weighting (see also Figs. 4.9 and 4.10). To compare with observational data, we convert our gradients such that our units become [dex/ $R_e$ ]. Galaxies around  $M_* \sim 10^{10}M_\odot$  have steepest gradients by  $\sim 0.15$  dex/ $R_e$ . This is also in excellent agreement with recent observational data from direct method abundances of stacked spectra of 4140 star-forming galaxies from the MaNGA survey (Khoram and Belfiore 2024, black line) and from 25 star-forming face-on spiral galaxies from the SAMI survey (Poetrodjojo et al. 2018, black points with tiny errorbars).

Poetrodjojo et al. (2018) originally measured metallicity gradients in SAMI galaxies using the  $R_{23}$  diagnostic, but later noted that the weak [OII] emission line limited the reliability of those measurements. In Poetrodjojo et al. (2021), they improved upon this analysis by using more robust diagnostics. They concluded that their ‘Rcal’ calibration provides the most robust and consistent metallicity gradients and recommended it for comparisons with theoretical predictions. Using this method, they found a clear correlation between stellar mass and metallicity gradient: more massive galaxies tend to have shallower gradients, while lower-mass systems show steeper and more scattered gradients. Our gradients seem to have comparable scatter to this observation with Rcal metallicity diagnostics, but larger scatter than the Scal one.

The steep gradients at intermediate stellar masses are also seen in [Sharda et al. \(2021\)](#), who used semi-analytic scaling models to reproduce observed trends. Their models also predict the steepest gradients at  $M_* \sim 10^{10} - 10^{10.5} M_\odot$ , with a flattening at both lower and higher masses. This curvature is interpreted as a transition from advection-dominated to accretion-dominated regimes in galaxy evolution. Our simulations indicate that their effective yield reduction factor,  $\phi$ , varies with stellar mass:  $\phi = 0.4$  at  $M_* = 10^{10} M_\odot$ ,  $\phi = 0.2$  at  $10^{11} M_\odot$ . Our gradients are quantitatively flatter than those predicted by the two empirical scalings adopted in their models. However, the qualitative shape of the relation remains similar, and our results fall within the range spanned by their model predictions for different  $\phi$  values.

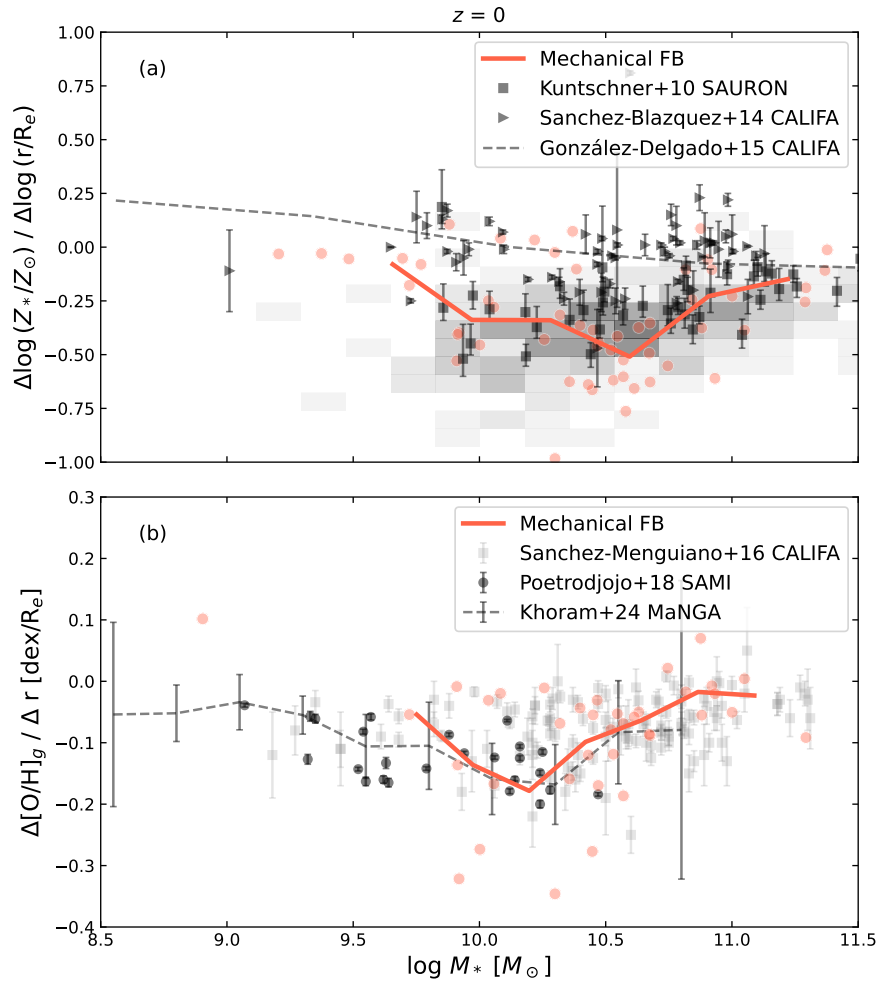


FIGURE 4.7: *Top panel:* V-band luminosity weighted stellar metallicity gradients measured within  $1.5 R_e$  as a function of the galaxy’s total stellar mass at  $z = 0$  in our simulation with the mechanical feedback model (red circles). The red line shows the median value at a given mass. Observational data are taken from the SAURON survey ([Kuntschner et al. 2010](#), black squares), the CALIFA survey ([Sánchez-Blázquez et al. 2014](#), black triangles; and [González Delgado et al. 2015](#), black dashed line), and from the ATLAS<sup>3D</sup> survey (grey shading, [Kuntschner et al.](#), priv. comm.). *Bottom panel:* Same, but for the SFR-weighted gas-phase oxygen abundance gradients measured within 8 kpc. Observational data are taken from [Sánchez-Menguiano et al. \(2016, CALIFA](#), black square), [Poetrodjojo et al. \(2018, SAMI](#), black circle) and [Khoram and Belfiore \(2024, MaNGA](#), black line).

## 4.4 Redshift Evolution

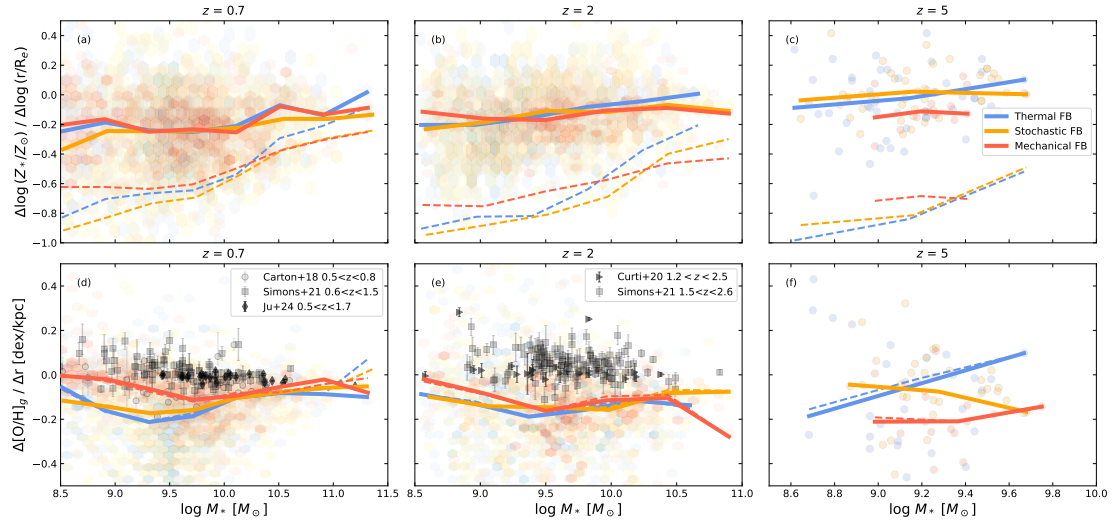


FIGURE 4.8: Upper panels: The V-band luminosity weighted stellar metallicity inner gradients  $\alpha_{*,\text{in}}$  within  $1.5 R_e$  as a function of the galaxy total stellar mass at  $z = 0.7$  (a),  $z = 2$  (b), and  $z = 5$  (c) for all galaxies in our simulations with the thermal (blue), stochastic (orange), and mechanical (red) feedback models (see main text). The solid lines are the median at a given mass. The dashed lines are the metallicity gradients  $\alpha_*$  along the total projected radius. The lower panels (d, e, and f) are the same, but for the SFR-weighted gas-phase oxygen abundance gradients  $\alpha_g$  within 8 kpc (solid lines) and total gradients (dashed lines). The distributions of simulated galaxies are shown with hexagonally binned density maps at  $z = 0.7$  and 2, while with scattered points at  $z = 5$ , with the same colour. The black/gray symbols are observational data from [Carton et al. \(2018\)](#) at  $0.5 < z < 0.8$  (circles), [Simons et al. \(2021\)](#) at  $0.6 < z < 1.5$  and  $1.2 < z < 2.6$  (squares), [Curti et al. \(2020b\)](#) at  $1.2 < z < 2.5$  (triangles), and [Ju et al. \(2024\)](#) at  $0.5 < z < 1.7$  (diamonds).

### 4.4.1 Stellar Gradients vs Mass

The top panels in Figure 4.8 show the V-band luminosity-weighted stellar metallicity gradients with respect to galaxy total stellar mass at  $z = 0.7$  (panel a),  $z = 2$  (b), and  $z = 5$  (c) in our simulations, with the thermal (blue triangles), stochastic (orange diamonds), and mechanical (red circles) feedback models. As in Fig. 4.7, these symbols represent the inner gradients  $\alpha_{*,\text{in}}$  within  $1.5 R_e$  for individual galaxies, and the solid lines represent the median metallicity gradients at a given mass in each simulation. As already shown in Figs. 4.5(a) and 4.6(a), the medians of inner gradients are much flatter than the medians of the total metallicity gradients ( $\alpha_*$ , dashed lines) along the total radius. The distribution of simulated galaxies are also shown. To reduce overcrowding from individual data points at  $z = 0.7$  and 2 (a and b), we use hexagonally binned density maps in the background with a consistent color scheme. This hexbin visualization highlights the data distribution, especially in regions of high density points. At  $z = 5$  (panel c), we plot all individual galaxy points (circles) for the thermal (blue), stochastic (orange), and mechanical (red) feedback models. Some points lie outside the gradient range shown, which

explains why, for example, the blue fit at the low-mass end in the bottom panel does not align with the displayed blue points.

At  $z = 0.7$ , the inner gradients of individual galaxies (points) are clustered between  $\alpha_{*,\text{in}} \sim -0.5$  and  $\sim 0.0$  for all models. At the low-mass end ( $M_* < 10^9 M_\odot$ ), a significant fraction of galaxies with the mechanical (22%) and thermal (24%) and stochastic (14%) feedback show inverted inner gradients ( $> 0$ ). At the intermediate mass ( $M_* \sim 10^{10} M_\odot$ ) quite a few individual galaxies with the stochastic feedback have very steep gradients ( $\sim -0.9$ ). At the massive end ( $M_* > 10^{11} M_\odot$ ) the gradients are close to 0 dex (i.e. flat). This flattening of stellar metallicity gradients for massive galaxies was explained by the occurrence of major mergers (Kobayashi, 2004; Taylor and Kobayashi, 2017), which perturb the spatial distribution of stars (see Fig.12 of Kobayashi 2004). Hence, we do not expect to see a significant difference among feedback models, as in Figure 4.6(a). The medians (solid lines) show only a small ( $\sim 0.1$ ) difference among the feedback models depending on the mass. Mechanical feedback gives slightly flatter gradients for lower-mass galaxies and shows no significant difference at higher-mass galaxies compared with the other feedback models. These are consistent with what we find in Section 4.3.2. From low-mass to high-mass galaxies, the median inner gradient becomes flatter, with a maximum difference of  $\sim 0.2$  in the plotted mass range. On the other hand, the median total gradient  $\alpha_*$  (dashed lines) becomes much flatter by  $\sim 0.4$  and  $\sim 0.8$  for the mechanical and thermal feedback models, respectively. This stronger mass dependence should be caused by outer gradients.

At  $z = 2$  (panel b), the median of inner gradients  $\alpha_{*,\text{in}}$  (solid lines) is not so much impacted by the stellar feedback models, while at  $M_* < 10^{9.5} M_\odot$  it is flatter with the mechanical model by  $\sim 0.1$ , and at  $M_* > 10^{9.5} M_\odot$  it is flatter with the thermal model by  $\sim 0.1$ , than the other models. The median total gradients  $\alpha_*$ , however, greatly depend on the feedback model at all mass ranges. At  $M_* < 10^{10} M_\odot$ , the mechanical gradient is flatter by  $\sim 0.2$  than the stochastic one, while at  $M_* > 10^{9.7} M_\odot$ , the thermal one is flatter by  $\sim 0.3$ .

We find a similar gradient–mass relation and feedback dependence at  $z = 4$ . However, we find an interesting transition at  $z = 5$ . At  $z = 5$  (panel c), the inner gradient becomes much steeper ( $\alpha_{*,\text{in}} \sim -0.2$ ) with the mechanical feedback than for the other models. There is no clear mass dependence of gradients with the stochastic and mechanical models, although there is with the thermal feedback model.

This feedback dependence for the total gradient (including  $> 1.5 R_e$ ) is remarkable, and it would be very useful if stellar gradient evolution could be measured for a wide range of galaxy mass. For all shown redshifts and with all feedback models, the stellar metallicity total gradient is steeper for lower stellar mass, on average. However, the gradients increase from the low-mass to high-mass end is larger for the stochastic and thermal feedback models and smallest for the mechanical one, which tends to give flatter gradients at  $M_* < 10^{10} M_\odot$ . This mass dependence is not as much retrieved for the inner gradients.

#### 4.4.2 Gas-phase Gradients vs Mass

The bottom panels in Figure 4.8 are the same as the top panels, but for the SFR-weighted gas-phase oxygen abundance gradients at  $z = 0.7$ ,  $z = 2$ , and  $z = 5$  (in panels (d), (e), and (f), respectively) for the three difference feedback models. The solid lines represent the medians inner gradients  $\alpha_{g,in}$  (within 8 kpc) at a given mass of simulated galaxies (hexbin or points). The dashed lines are the total gradients along the total radius, which are very similar to the inner gradients except for the massive end.

At  $z = 0.7$ , the median gradient is significantly flatter with the mechanical feedback for low-mass galaxies ( $M_* < 10^{10} M_\odot$ ). It is less impacted by the supernova feedback for massive galaxies ( $M_* > 10^{10} M_\odot$ ), as previously discussed in Section 4.3.3. By looking at individual galaxies (points) in all feedback models, most galaxies have gas-phase gradients clustered between  $\alpha_{g,in} \sim -0.3$  and  $\sim 0$  dex/kpc. However, certain galaxies with  $M_* \sim 10^{9.5} M_\odot$  in the thermal and stochastic models have very steep gradients reaching  $\alpha_{g,in} \sim -0.5$  dex/kpc. Massive galaxies ( $M_* > 10^{10} M_\odot$ ) have gradients  $\alpha_{g,in} \sim -0.1$  dex/kpc for all feedback models. At the low-mass end, the galaxies with the mechanical feedback (red) are clustered around  $\alpha_{g,in} = 0$  dex/kpc, again showing flatter gradients in this model. This is likely due to outflows driving metal-rich gas to the outer regions of the galaxies (§4.3.3). In addition, 46% (mechanical), 22.5% (thermal), and 15.8% (stochastic) of low-mass galaxies with  $M_* < 10^9 M_\odot$  show a positive gradient in the three models, meaning they have more metal-rich gas in the outskirts. This requires an additional effect, such as the inflow of pristine gas. The mechanical feedback gradients are closer to observational data from MUSE/VLT (Carton et al., 2018, light gray circles) at  $0.5 < z < 0.8$ , the CANDELS CLEAR survey with HST (Simons et al., 2021, gray squares) at  $0.6 < z < 1.5$ , and the MSA-3D survey with JWST/NIRSpec of 26 galaxies at  $0.5 < z < 1.7$  (Ju et al., 2024, black diamonds), as well as other observational datasets (e.g., Stott et al., 2014b; Förster Schreiber et al., 2018), that are not included in the figure to avoid overcrowding.

At  $z = 2$  (panel e), the median gradient with the mechanical feedback is slightly steeper than at  $z = 0.7$ . We can also see the feedback dependence of the gradients here. The stochastic and thermal gradients are clustered near  $\sim -0.1$  dex/kpc at  $M_* < 10^{10} M_\odot$ , while the mechanical feedback gives slightly flatter gradients. At  $M_* > 10^{10} M_\odot$ , the mechanical feedback gives steeper gradients reaching  $\alpha_{g,in} \sim -0.2$  dex/kpc, however, this may be due to the small number of massive galaxies at this redshift. All feedback models give gradients steeper by  $\sim 0.1$  dex/kpc compared to observational data from the KLEVER survey with KMOS at  $1.2 < z < 2.5$  (Curti et al., 2020b, black triangles) and from the CLEAR survey at  $1.5 < z < 2.6$  (Simons et al., 2021, gray squares).

As for stellar gradients, the evolutionary transition is seen not at  $z = 4$  but at  $z = 5$ . At  $z = 5$  (panel f), the mechanical model gives much steeper median gradients ( $\alpha_{g,in} \sim -0.2$  dex/kpc) with no clear mass dependence. Note that at this redshift, our galaxy sample may be limited. In our future work, we will extend this study for  $z > 5$ , to have a more complete sample of gas-phase oxygen

abundance gradients in our hydrodynamical simulations at high redshift.

Up to  $z = 4$ , the gas-phase oxygen abundance gradients tend to become flat at the low-mass end, specifically with the mechanical feedback, which is consistent with recent observational data (e.g. Belfiore et al. 2017; Simons et al. 2021; Ju et al. 2024). At  $10^9 M_\odot < M_* < 10^{10} M_\odot$ , the predicted gradients are steeper than observed, which might indicate that metal outflow, pristine gas inflow, and/or gas mixing is inefficient in our simulations.

### 4.4.3 Time evolution of metallicity gradient

At high redshifts, available observational data are for gas-phase oxygen abundances only (e.g. Cresci et al. 2010; Jones et al. 2010; Yuan et al. 2011; Curti et al. 2020a), thus we focus on gas-phase gradients, but we also show our predictions of stellar metallicity gradients for future. The medians and one sigma scatter are also listed as a function of redshift in Table 4.1.

The top panel of Figure 4.9 shows the redshift evolution of the SFR-weighted gas-phase oxygen abundance gradients for all galaxies in our simulations with the thermal (blue), stochastic (orange), and mechanical (red) feedback models. The gradients are measured along the projected radius for each galaxy, in a fixed range  $r < 8$  kpc, and then the medians at a given redshift are calculated (solid lines). The shaded areas are  $1\sigma$  scatter. Note that we show our simulations wherever available, i.e., down to  $z = 0.7$  for the stochastic and thermal models and down to  $z = 0$  for the mechanical model. This is due to overheating in the feedback runs at  $z < 0.7$ , which leads to suppressed star formation and unrealistic galaxy properties. These effects are discussed in detail in Ibrahim and Kobayashi (2024). For  $z = 0$ , our main conclusions rely on the mechanical feedback model, which remains consistent with observations down to  $z = 0$ .

There is only a mild evolution in the metallicity gradients from  $z = 0$  to  $z = 4$  for all feedback models. The mechanical feedback has the flattest gradient ( $\alpha_{\text{g,in}} = -0.07 \pm 0.12$  dex/kpc at  $z = 0.7$ ) up to  $z = 4$ , as already shown in Fig. 4.8. The thermal and stochastic models produce similar gradients up to  $z = 4$ , where the gradient becomes steeper in the thermal case ( $-0.12 \pm 0.15$  dex/kpc at  $z = 4$ ). With all three supernova feedback models, the gradients always remain negative at all redshifts, making it steeper than observational data (e.g., Curti et al. 2020a, Ju et al. 2024).

Since there is a gradient–mass relation (Fig. 4.8), this figure looks different depending on the galaxy mass. The bottom panel of Figure 4.9 is the same as the top panel, but only for the massive galaxies ( $M_* \geq 10^{10} M_\odot$ ) in our simulations. This figure shows a clear impact of the feedback models on the gradients at  $z > 2$ , where the mechanical feedback gives significantly flatter gradients, although there is no impact at  $z < 2$  for these massive galaxies. Even so, our predicted gradients are still steeper than observed.

As galaxy sizes evolve with redshift, one might think that it would be preferable to measure the gradients differently. Figure 4.10 is the same as Figure 4.9 but with units of dex/ $R_e$  and measured

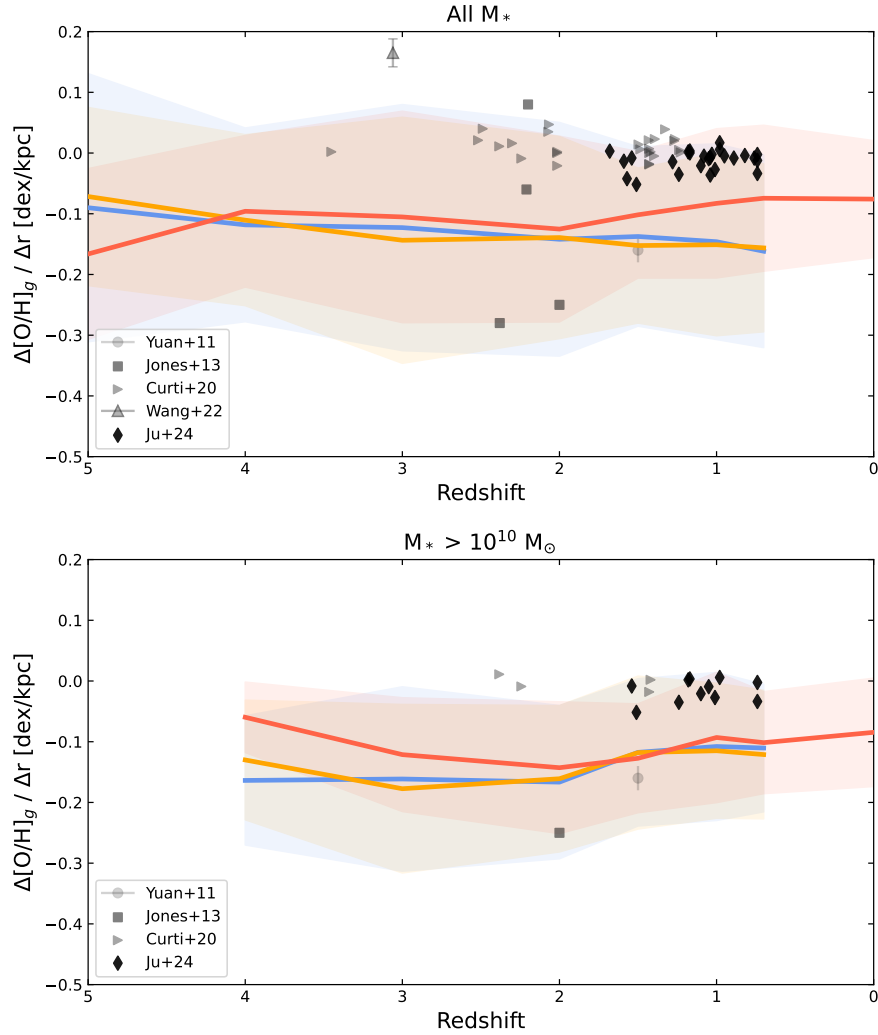


FIGURE 4.9: *Top panel:* SFR-weighted gas-phase metallicity gradient in [dex/kpc] as a function of redshift for all galaxies in our simulations with the thermal (blue solid line), stochastic (orange), and mechanical (red) feedback models. The shaded areas are  $1\sigma$  scatter. The black/gray symbols are observational data from Yuan et al. (2011, circle) using AO-assisted spectroscopy OSIRIS on Keck II on a face-on spiral galaxy at  $z \sim 1.5$ , Jones et al. (2013, Square) using AO-assisted spectroscopy OSIRIS on Keck on gravitationally lensed systems, Curti et al. (2020a, right-pointing triangles) using KMOS KLEVER survey on 42 gravitationally lensed galaxies, Wang et al. (2022, upward-pointing triangle) with NIRISS, early result from GLASS-JWST and Ju et al. (2024, diamonds) with the JWST/NIRSpec Slit-stepping Spectroscopy. *Bottom panel:* Same as the top panel but for massive galaxies ( $M_* > 10^{10} M_\odot$ ) only.

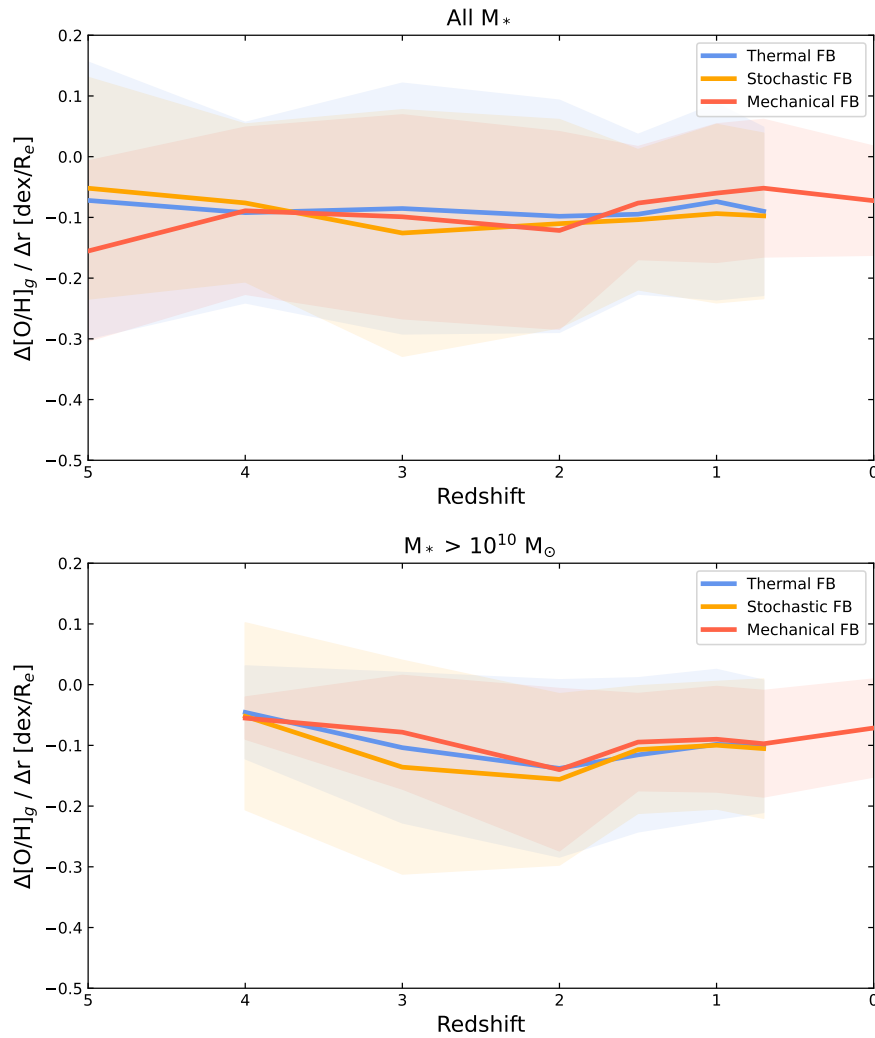


FIGURE 4.10: Same as Figure 4.9, but in  $[\text{dex}/R_e]$  measured within  $2.5 R_e$ .

in  $2.5 R_e$  instead of 8 kpc using the effective radius  $R_e$  of each galaxy. Since these metallicities are weighted by the SFR, the fitting range is not so important, as long as a sufficiently large range is covered. While the gradient in dex/kpc is more straightforward to measure observationally, this scale does not account for galaxy size evolution and can be misleading when comparing across redshifts. Galaxies at high redshifts are typically more compact for a given stellar mass than their low-redshift counterparts. This size growth is particularly pronounced for massive galaxies, which experience stronger inside-out growth and feedback driven expansion of their stellar and gas distributions. This normalization by effective radius provides a comparison of metallicity gradients across galaxies taking account of their size evolution. The trend in Figure 4.10 is very similar to that in Figure 4.9, and both show that the metallicity gradients remain relatively flat across cosmic time, with mild fluctuations. For the massive galaxies, however, the unit change tends to flatten the gradients, and there is no significant difference among feedback models at  $z = 4$ .

Figure 4.11 is the same as Figure 4.9 but for the V-band luminosity weighted stellar metallicity

gradients along the projected radius within  $1.5R_e$ . Gradients are measured against  $\log(r/R_e)$  of each galaxy, then medians are calculated at a given redshift (solid lines). The top panel includes all galaxies in our simulations and shows that the stellar metallicity gradient is not highly impacted by supernova feedback models, although the stochastic model gives flatter gradients (by  $\sim 0.1$  than the mechanical model) at  $z > 2$ .

As seen in the gradient–mass relations (Fig. 4.6), massive galaxies show a clear impact of the feedback models. The bottom panel shows that, for massive galaxies ( $M_* \geq 10^{10} M_\odot$ ), the stellar gradients are more impacted by the feedback model at  $z > 2$ , where the mechanical feedback also gives flatter gradients (by  $\sim 0.2$  than the thermal feedback at  $z = 4$ ). The *positive* gradients are caused by slower chemical enrichment at the centre, which is surprising and could be due to inflow of low-metal gas and/or outflow of metal-rich gas (see Section 4.6 for more discussion).

Although there are no observational data at high redshifts, at  $z = 0$ , we find that our gradient with the mechanical feedback shows a great match with observational data of nearby galaxies (e.g. Kobayashi and Arimoto, 1999; Kuntschner et al., 2010).

$z$	Thermal	Stochastic	Mechanical
$\alpha_{g,in} \equiv \Delta[\text{O}/\text{H}]_g / \Delta r$ [dex/kpc]			
0	---	---	$-0.07 \pm 0.09$
0.7	$-0.16 \pm 0.16$	$-0.16 \pm 0.13$	$-0.07 \pm 0.12$
1	$-0.15 \pm 0.16$	$-0.15 \pm 0.15$	$-0.08 \pm 0.12$
1.5	$0.14 \pm 0.15$	$-0.15 \pm 0.13$	$-0.10 \pm 0.10$
2	$-0.14 \pm 0.19$	$-0.14 \pm 0.17$	$-0.13 \pm 0.15$
3	$-0.12 \pm 0.20$	$-0.14 \pm 0.20$	$-0.11 \pm 0.17$
4	$-0.12 \pm 0.15$	$-0.11 \pm 0.14$	$-0.10 \pm 0.12$
5	$-0.09 \pm 0.22$	$-0.07 \pm 0.15$	$-0.17 \pm -0.14$
$\Delta[\text{O}/\text{H}]_g / \Delta r$ [dex/ $R_e$ ]			
0	---	---	$-0.07 \pm 0.06$
0.7	$-0.09 \pm 0.14$	$-0.10 \pm 0.13$	$-0.05 \pm 0.11$
1	$-0.07 \pm 0.16$	$-0.9 \pm 0.14$	$-0.06 \pm 0.11$
1.5	$-0.09 \pm 0.13$	$-0.10 \pm 0.11$	$-0.08 \pm 0.09$
2	$-0.10 \pm 0.19$	$-0.11 \pm 0.17$	$-0.12 \pm 0.16$
3	$-0.09 \pm 0.20$	$-0.13 \pm 0.20$	$-0.09 \pm 0.17$
4	$-0.09 \pm 0.15$	$-0.07 \pm 0.12$	$-0.08 \pm 0.13$
5	$-0.07 \pm 0.22$	$-0.05 \pm 0.18$	$-0.16 \pm 0.15$
$\alpha_{*,in} \equiv \Delta \log(Z_*/Z_\odot) / \Delta \log(r/R_e)$			
0	---	---	$-0.25 \pm 0.23$
0.7	$-0.19 \pm 0.20$	$-0.19 \pm 0.20$	$-0.17 \pm 0.18$
1	$-0.18 \pm 0.23$	$-0.18 \pm 0.22$	$-0.16 \pm 0.18$
1.5	$-0.15 \pm 0.22$	$-0.13 \pm 0.28$	$-0.16 \pm 0.18$
2	$-0.10 \pm 0.23$	$-0.08 \pm 0.23$	$-0.11 \pm 0.15$
3	$-0.05 \pm 0.25$	$-0.006 \pm 0.32$	$-0.05 \pm 0.25$
4	$0.02 \pm 0.22$	$0.01 \pm 0.28$	$-0.05 \pm 0.14$
5	$-0.05 \pm 0.23$	$0.03 \pm 0.17$	$-0.10 \pm 0.11$

TABLE 4.1: The median of the SFR-weighted gas-phase oxygen abundance gradients in dex/kpc (upper table) and dex/ $R_e$  (middle table), and the V-band luminosity-weighted stellar metallicity gradients (bottom table), as a function of redshift  $z$  for all galaxies in our simulations with the thermal, stochastic, and mechanical feedback models. The  $1\sigma$  scatters are also given.

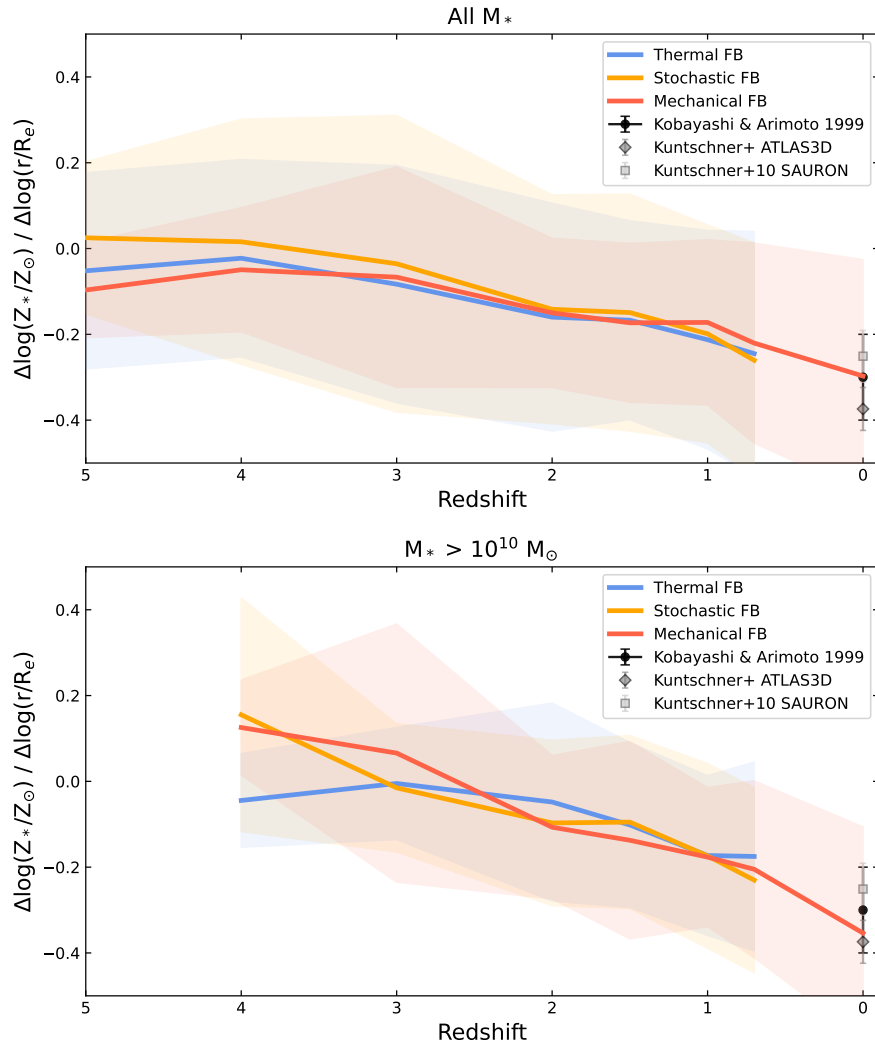


FIGURE 4.11: *Top panel:* V-band luminosity weighted stellar metallicity gradients measured within  $1.5 R_e$  as a function of redshift for all galaxies in our simulations with the thermal (blue), stochastic (orange), and mechanical (red) feedback models. Gradients are measured for each galaxy, normalized by the effective radius  $R_e$ , and then the median is calculated at a given redshift (solid lines). The shaded areas are  $1\sigma$  scatter. Observational data are taken from Kobayashi and Arimoto (1999, black point with error bar), the SAURON survey (Kuntschner et al. (2010, light gray square with error bar); and the ATLAS<sup>3D</sup> survey (Kuntschner et al., priv. comm; gray diamond with error bar). *Bottom panel:* Same as top panel but for massive galaxies with  $M_* > 10^{10} M_\odot$ .

## 4.5 Galaxy type dependence

To understand the offset between the simulations and observations, one may ask if observational data are biased toward star-forming galaxies. In this section, we study the dependence of the metallicity gradient on the galaxy “type”. All simulated galaxies for which we measured gas-phase metallicity gradients are star-forming. Thus, we split our sample into lower star formation earlier-type galaxies (ETGs) and higher star formation later-type galaxies (LTGs), using the star-formation main sequence (SFMS) of galaxies that are commonly used in observations (e.g. [Renzini and Peng 2015](#)) and in simulations (e.g. [Taylor and Kobayashi 2016](#)).

The SFMS of our simulated galaxies are shown in Figure B.5 in Appendix B.2. To select “ETGs” and “LTGs”, we use the same method as in [Taylor and Kobayashi \(2017\)](#), where we take the best linear fit of our simulated SFMS and calculate the perpendicular distance ( $\Delta$ SFMS) of this fit from the data. We then use this quantity to define the galaxies such that “ETGs” have  $\Delta$ SFMS  $< -0.5$ , and “LTGs” have  $\Delta$ SFMS  $\geq -0.5$ .

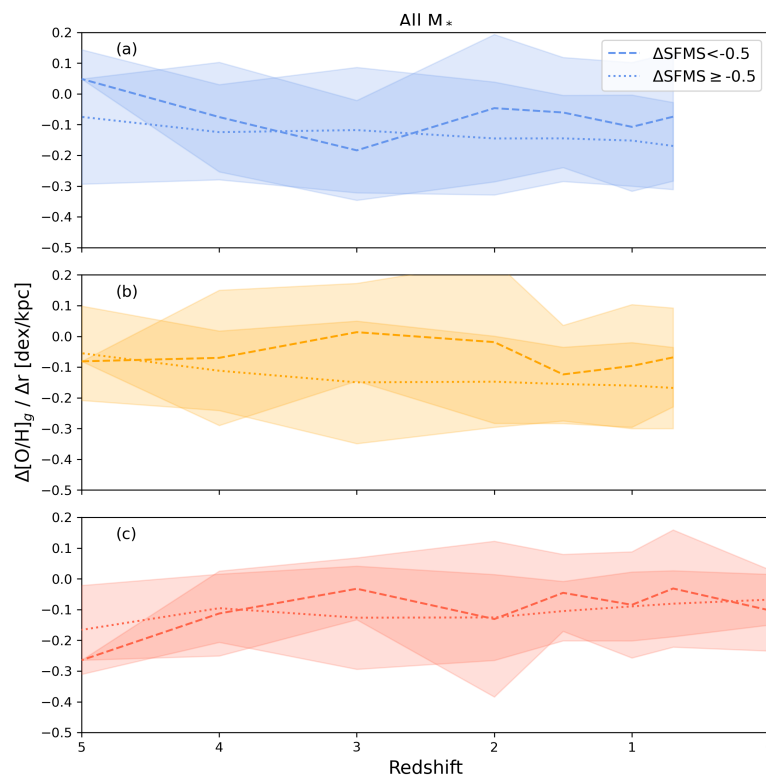


FIGURE 4.12: The SFR-weighted gas-phase oxygen abundance gradients as a function of redshift for all galaxies in our simulations with the thermal (blue, top panel), stochastic (orange, middle panel), and mechanical (red, bottom panel) feedback models. The dashed and dotted lines show the medians of earlier-type galaxies ( $\Delta$ SFMS  $< -0.5$ ) and later-type galaxies ( $\Delta$ SFMS  $\geq -0.5$ ), respectively. The shaded areas are  $1\sigma$  scatter.

Figure 4.12 shows the redshift evolution of the SFR-weighted gas-phase metallicity gradients for ETGs (dashed lines) and LTGs (dotted lines) for thermal (blue top panel), stochastic (orange,

middle panel), and mechanical (red, bottom panel) feedback models. Overall, ETGs have a flatter gradient at all redshifts with all feedback models. Hence, the offset between observations and simulations is not due to the selection bias. At  $z \sim 5$ , ETGs seem to show a steep gradient with mechanical feedback.

## 4.6 Discussion

In hydrodynamical simulations, metallicity gradients are affected by several physical processes: inside-out growth, metal flows, stellar migration, and galaxy mergers. These processes interact with one another, and it is beyond the scope of this work to disentangle their individual impacts. However, we wish to discuss our findings in relation to previous studies.

### 4.6.1 Present-day gradients

At  $z = 0$ , both observations and theory consistently find that gas-phase metallicity gradients are predominantly negative. Surveys such as CALIFA, MaNGA, and SAMI measure typical slopes of  $-0.05$  to  $-0.1$  dex/ $R_e$  (Sánchez et al., 2014; Belfiore et al., 2017; Poetrodjojo et al., 2021), while cosmological simulations (Illustris/TNG50, EAGLE, FIRE, SIMBA) predict similarly mild negative values of  $-0.01$  to  $-0.06$  dex/kpc (Hemler et al., 2021; Ma et al., 2017; Davé et al., 2019; Garcia et al., 2025). Analytic inside-out and “bathtub” models can create negative gradients, depending on the assumed gas accretion and star-formation efficiencies (e.g. Chiappini et al., 2001; Mollá and Díaz, 2005; Sharda et al., 2021). We find  $\sim -0.07$  both for dex/kpc and dex/ $R_e$  (Table 4.1) for gas with our preferred, mechanical feedback model.

Moreover, both for observations and simulations, there is a galaxy mass dependence (Fig. 4.7b), where massive galaxies ( $M_* \gtrsim 10^{10.5} M_\odot$ ) exhibit flatter gradients ( $-0.06$  to  $-0.03$  dex/ $R_e$ ). This could be due to ‘equilibrium’ reached with low gas density at the centre (Belfiore et al., 2017). It is also important to note that we find a similar trend also for stellar gradients (Fig. 4.7a), which is predominantly caused by galaxy mergers (Kobayashi, 2004). This leads to a radial gradient of metals in stellar mass-loss, which keep supplying metals in the ISM. Therefore, the flattening of gas gradients at the massive end is also due to galaxy mergers. On the other hand, intermediate-mass systems ( $M_* \sim 10^{10.5} M_\odot$ ) show steeper gas-phase gradients (down to  $-0.3$  dex/ $R_e$ ), which we also see in stellar gradients. We find that the steep gas-phase gradients are caused by on-going star formation and higher gas density at the centre (Figs. 4.13 and 4.14). However, lower-mass galaxies ( $M_* \sim 10^9 M_\odot$ ) show flat gradients, which could be explained by enhanced radial mixing likely driven by feedback in shallow potentials. This is supported as we find this flattening at the low-mass end weaker with the other feedback models (Fig. 4.8).

To better understand the physical origin of the *steep* metallicity gradients in our simulated galaxies, we examined the radial profiles of gas surface density (Figure 4.13) and star formation rate (Figure

4.14) for the mechanical feedback model at  $z = 0$ . We compute the radial hydrogen number density profiles (in 3D) by binning the gas particles in concentric spherical shells centred on each galaxy. For each shell between inner radius  $R_1$  and outer radius  $R_2$ , the gas mass is measured by summing the masses of all particles whose radii satisfied  $R_1 \leq r < R_2$ . The shell volume was computed as  $V = \frac{4}{3}\pi(R_2^3 - R_1^3)$ , yielding a mass density  $n_{\text{gas}} = M_{\text{gas}}/V$  in units of  $M_{\odot} \text{ kpc}^{-3}$ . We then converted this to a number density in  $\text{cm}^{-3}$  and dividing by the mean particle mass  $\mu m_{\text{H}}$ . We adopted  $\mu = 1.4$  to account for the presence of helium in addition to hydrogen. The resulting profile therefore represents the median hydrogen number density of gas as a function of radius. We also compute the radial SFR profiles (in 3D) using the same concentric spherical shells defined for the gas density profiles. For each shell between inner radius  $R_1$  and outer radius  $R_2$ , the SFRs of all gas particles are added, then divided by the shell volume to obtain the SFR volume density in units of  $M_{\odot} \text{ yr}^{-1} \text{ kpc}^{-3}$ . This approach yields the SFR density profiles of individual galaxies, which were then stacked to compute the median profiles for each subsample.

Figure 4.13 shows the hydrogen number density profiles for different bins of gas-phase metallicity gradients, defined such that each bin contains the same number of galaxies. Galaxies with steeper metallicity gradients tend to have more centrally concentrated gas distributions. In the steepest-gradient bin ( $-0.35$  to  $-0.05$  dex/kpc; purple), the gas density peaks sharply at  $r < 1$  kpc with values around  $3 \text{ cm}^{-3}$  and declines rapidly beyond  $\sim 1.5$  kpc. Galaxies with intermediate gradients ( $-0.05$  to  $-0.02$  dex/kpc; orange) show a similar but less pronounced central concentration with lower maximum densities. Meanwhile, galaxies with flatter or inverted gradients ( $-0.02$  to  $+0.10$  dex/kpc; yellow) have the most diffuse central gas, with comparatively low central densities  $\sim 1 \text{ cm}^{-3}$ .

Similarly, Figure 4.14 shows that steep-gradient galaxies ( $-0.35$  to  $-0.05$  dex/kpc; purple) exhibit a SFR peak ( $\sim 0.013 M_{\odot} \text{ yr}^{-1} \text{ kpc}^{-3}$ ) at  $r < 1$  kpc followed by a rapid decline beyond  $r \approx 1.5$  kpc, indicating highly concentrated star formation. Galaxies with flatter or positive gradients have lower SFRs with a broad maximum of  $\sim 0.004 M_{\odot} \text{ yr}^{-1} \text{ kpc}^{-3}$  that falls off at  $r \sim 1.5$ – $2$  kpc and sustains activity out to  $\sim 3.5$  kpc. These profiles show that the radial distribution of star formation is a driver of the overall metallicity gradient.

From these two figures, we can conclude that steeper metallicity gradients are caused in galaxies that are more centrally concentrated in both gas density and star formation, and thus there is a small, dense star-forming core that rapidly enriches its inner few kpc. On the other hand, flatter (or inverted) gradients arise in systems where the gas reservoir and star formation is spread out to larger radii, diluting any strong inner metallicity peak.

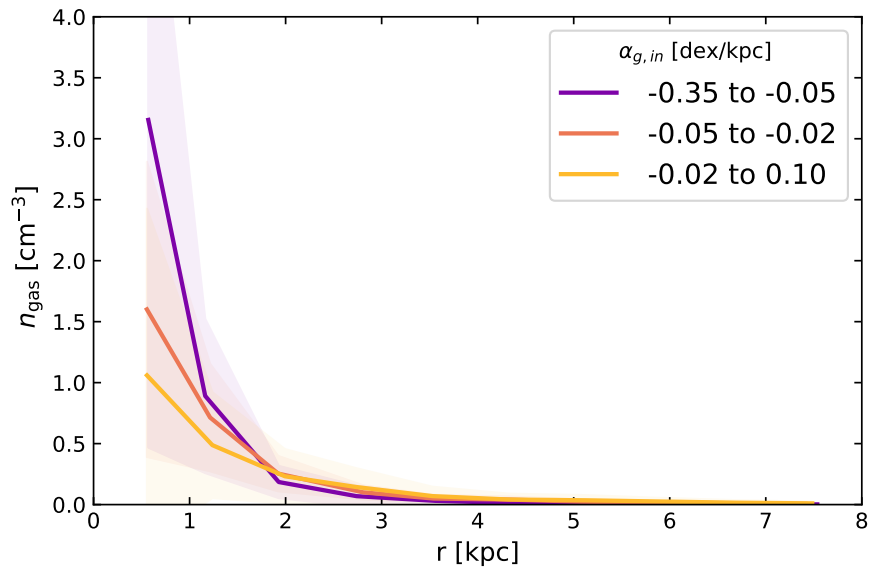


FIGURE 4.13: Radial gas number density profiles for galaxies grouped by different bins of gas-phase metallicity gradients  $\alpha_{g,in}$  within 8 kpc. Each line represents the median profile within a given gradient range. The shaded area is the 1  $\sigma$  scatter. Results are shown for  $z = 0$  with the mechanical feedback.

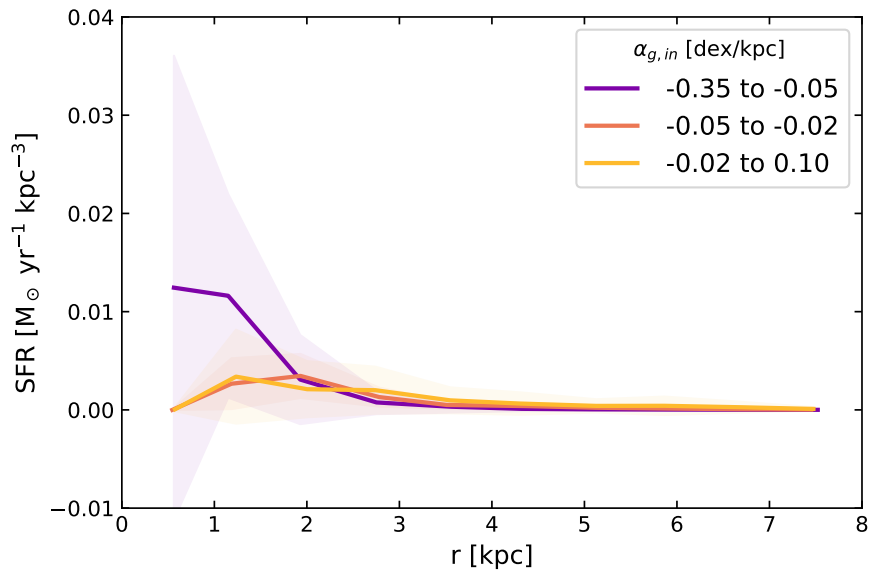


FIGURE 4.14: Same as Fig. 4.13, but for radial star formation rate profiles.

### 4.6.2 Overall evolution of gradients

At high redshifts ( $z \gtrsim 1$ ), the picture of gas-phase metallicity-gradient evolution becomes notably more complex, with some studies finding significantly steeper gradients while others report flat or even inverted profiles. Early, small-sample AO observations of lensed galaxies (e.g. Jones et al. 2010, 2013; Yuan et al. 2011) predict that gradients steepen with redshift, which were in excellent agreement with zoom-in simulations of a Milky-Way type galaxy (Kobayashi and Nakasato, 2011b; Pilkington et al., 2012) and some cosmological simulations (e.g. TNG50, with a steepening rate of  $\sim 0.02$  dex/kpc per  $z$ ; Hemler et al. 2021; MUGS with “normal” feedback; Gibson et al. 2013). Our mechanical feedback (Fig. 4.9) runs likewise steepen by  $\sim 0.1$  dex/kpc from  $z = 0$  to 5, although for  $M_* > 10^{10} M_\odot$  systems the gradient peaks around  $z \approx 2$  before flattening again by  $z \sim 4$  (see below for more discussion).

In contrast, other works, both observational (e.g. Swinbank et al. 2012; Cresci et al. 2010; Leethochawalit et al. 2016; Wuyts et al. 2016; Wang et al. 2017; Förster Schreiber et al. 2018; Curti et al. 2020a) and theoretical (enhanced-feedback MaGICC; Gibson et al. 2013; FIRE; Ma et al. 2017; EAGLE; Tissera et al. 2022; analytic Milky Way models; Mott et al. 2013; Sharda et al. 2021), find no evolution or flatter (or inverted) gradients at  $z > 1$  than  $z = 0$ , often with large scatter. Our stochastic and thermal feedback models also produce flatter (or inverted) gradients in some galaxies (Fig. 4.8).

As galaxies evolve, mergers tend to flatten metallicity gradients (Kobayashi, 2004; Taylor and Kobayashi, 2017), as does inside-out growth (Vincenzo and Kobayashi, 2020). On the other hand, dilution and mixing of metals driven by strong feedback can produce flat gradients at any stage of a galaxy’s history. In addition to these gas-phase processes, physical mechanisms such as stellar migration can also influence the evolution of metallicity gradients, particularly in the stellar component. Radial migration flattens the stellar metallicity gradient over time by redistributing older stars outward from the chemically enriched inner regions (Vincenzo and Kobayashi, 2020). This process is expected to be especially important in massive, well-structured disks. However, for massive galaxies, we find stellar gradients becoming steeper as time (Fig. 4.11). We do not see the impact of stellar migration, although this could be due to the insufficient resolution.

Instead, we find that the inverse stellar gradients of massive galaxies are caused by off-center star formation (in a similar SFR profile as in Fig. 4.14). In these galaxies, early central star formation occurred from relatively metal-poor gas, while later star formation in the outskirts used gas that had already been enriched. This combination can explain the positive stellar gradients at early times, even in systems whose gas-phase metallicity decreases with radius. We have seen this in Galaxy B at  $z = 0$  with a comparable stellar mass (Fig. 4.3), and the stellar gradient was indeed positive (Fig. 4.4).

It is important to acknowledge other small-scale mixing processes such as turbulence driven diffusion and superbubble evolution, which can impact metallicity gradients (e.g. Sharda et al.

2021), are not explicitly captured. This may affect the fine structure of metallicity gradients, but we expect the global trends with mass and redshift to remain robust. Future work with higher-resolution simulations and explicit mixing models will help quantify these effects.

### 4.6.3 Gradient evolution in an individual galaxy

In cosmological simulations, tracing the detailed evolutionary history of individual galaxies is challenging. Here, we present the redshift evolution of gas-phase and stellar metallicity gradients for a representative system, Galaxy A. We track Galaxy A across snapshots using its unique catalog ID to link the same system between redshifts. At each snapshot all candidate star particles associated with that ID (including post mergers fragments; see Figure B.9) are collected to assign the most massive bound system as the descendant for that epoch. We then re-center the galaxy by recomputing the center of mass. Gas-phase metallicity profiles and gradients are measured as described in Section 4.2. This procedure ensures a consistent descendant choice and robust centering at every redshift before estimating the metallicity gradients.

Figure 4.15 shows the evolution of SFR-weighted gas-phase metallicity profile of Galaxy A across five redshifts:  $z = 5$  (red), 3 (orange), 2 (light green), 0.7 (cyan), and 0.5 (purple). The metallicity gradient  $\alpha_{g,in}$  is computed via a linear fit within 8 kpc at each redshift. The figure clearly shows the flattening of the gradient as a function of time. In other words, the metallicity evolves more rapidly in the outskirts than in the centre. The slope is steep from  $\alpha_{g,in} = -0.20 \pm 0.103$  dex/kpc at  $z = 5$  to a maximum of  $-0.31 \pm 0.043$  at  $z = 3$ , and then gradually flattens, reaching  $\alpha_{g,in} = 0.00 \pm 0.034$  at  $z = 0.5$ . This progression is consistent with inside-out growth and the increasing impact of stellar feedback, which redistributes metals over time, as well as the flattenings due to mergers (see Figure B.9). Figure 4.16 shows the evolution of stellar metallicity gradients, which remain negative at all times. Note that this is not the same massive galaxy that showed a positive gradient at  $z = 4$  in Figure 4.11.

Between  $z = 0.5$  and  $z = 0.7$  our measured  $\alpha$ -slopes indicate small flattening of the gradients both for gas and stars; however, the difference is comparable to the temporal variation observed in individual systems (e.g.,  $\sim 0.05$ – $0.2$  dex/kpc in Fig. 12 of Taylor and Kobayashi 2017) and therefore may not be significant. In other words, selecting a snapshot slightly earlier or later near  $z \approx 0.7$  could yield a slightly different  $\alpha$  value. It is also possible that the galaxy is already in a steady state. By contrast, from  $z \approx 0.7$  to  $z \approx 2$  the gradient change is much larger but the intrinsic variability is also expected to be large around  $z \sim 2$ , where mergers and bursty episodes drive “zig-zag” evolution in single-galaxy tracks (Taylor and Kobayashi, 2017). These temporal fluctuations are troublesome when following individual galaxies, and are not included in the gradients values shown in Figures 4.2 and 4.4; however, they can be neglected in our main figures, where the results are averaged over many systems.

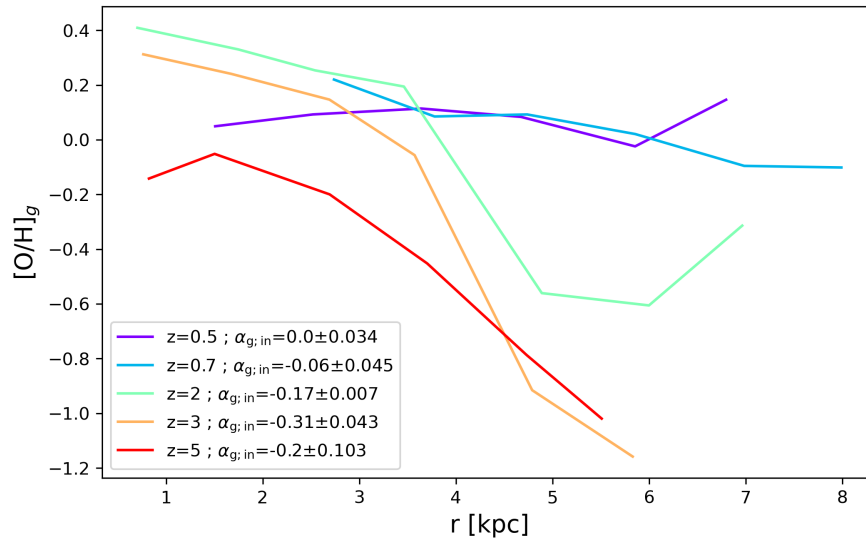


FIGURE 4.15: Evolution of the SFR-weighted gas-phase metallicity profile of Galaxy A with the mechanical feedback, at redshifts  $z = 0.7, 2, 3,$  and  $5$ . The slope of each profile,  $\alpha_{g,in}$  [dex/kpc], is obtained within 8 kpc and is listed in the legend.

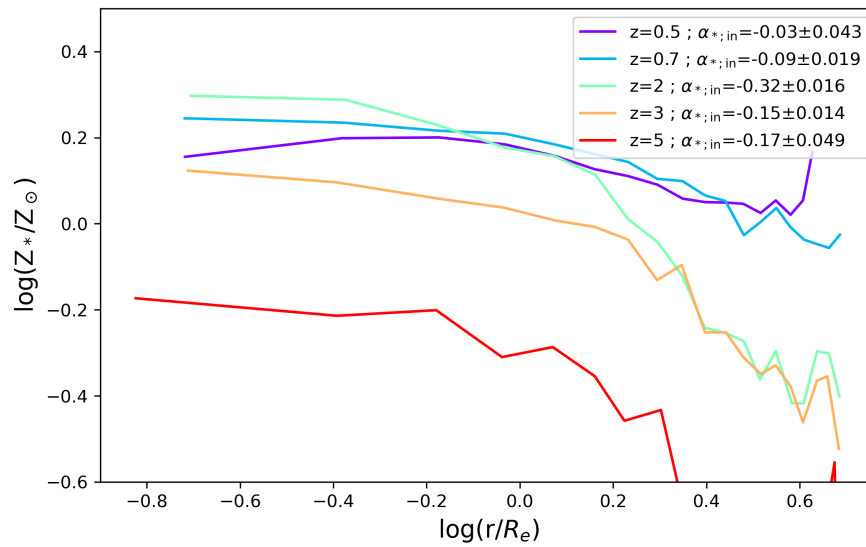


FIGURE 4.16: Same as Fig. 4.15 but for the luminosity-weighted stellar metallicity profile of Galaxy A. The slope of each profile  $\alpha_{*,in}$  [dex/kpc], is obtained within  $1.5 R_e$  (at each redshift) and is listed in the legend.

## 4.7 Conclusions

We predict the evolution of stellar and gas-phase radial metallicity gradients across cosmic time, using our cosmological hydrodynamical simulations with the latest nucleosynthesis yields. Namely we show the dependence of the gradients on the stellar feedback models: thermal, stochastic and mechanical supernovae feedback models described in [Ibrahim and Kobayashi \(2024\)](#).

For the luminosity-weighted stellar metallicity, we find the radial profiles is best quantified with a logarithm fit (Eq.4.6) of the inner gradient  $\alpha_{*,in}$  ( $r < 1R_e$  and  $r < 1.5R_e$ ) and the outer gradient  $\alpha_{*,out}$  ( $r \in [1R_e \text{ and } 2R_e]$  or  $r \in [1.5R_e \text{ and } 2R_e]$ ), rather than the total gradient  $\alpha_*$  (along the total projected radius). For the SFR-weighted gas-phase oxygen abundance, we use a linear fit (Eq.4.7) to the inner gradient  $\alpha_{g,in}$  within  $r < 8\text{kpc}$ .

- At  $z = 0$ , our simulation with the mechanical feedback successfully reproduces the observed metallicity gradient vs mass relations of both stellar metallicity (Fig. 4.7). Gradients are the steepest at intermediate-mass ( $M_* \sim 10^{10}M_\odot$ ) and become flatter in massive galaxies probably by major mergers ([Kobayashi, 2004](#); [Taylor and Kobayashi, 2017](#)).and in low-mass galaxies due to efficient feedback (Section 4.6.1).
- Galaxies with steep negative gradients tend to have centrally concentrated gas and star formation (Figs. 4.15 and 4.16), resulting in strong inner enrichment and limited metal transport to the outer regions. In contrast, galaxies with flatter or inverted gradients show more extended radial gas distributions and star formation, indicating efficient radial mixing likely driven by feedback.
- For massive galaxies ( $M_* > 10^{10}M_\odot$ ) at  $z = 0.7$ , inner stellar gradients ( $\alpha_{*,in} \sim -0.1$ ) are much flatter than outer ( $\alpha_{*,out} \sim -0.7$ ) and total gradients. Gas-phase oxygen abundance gradients are also negative ( $\alpha_{g,in} \sim -0.1 \text{ dex/kpc}$ ). The impact of stellar feedback on these gradients are subtle (Fig. 4.6), which is expected due to their deep potential well.
- For lower-mass galaxies ( $M_* < 10^{10}M_\odot$ ) at  $z = 0.7$ , the feedback models have a significant impact on the gradients. Stellar total gradients  $\alpha_*$  are significantly flatter with the mechanical feedback by  $\sim 0.2\text{--}0.3$ . Inner gradients  $\alpha_{*,in}$  are slightly flatter for the mechanical feedback by  $\sim 0.02\text{--}0.03$ . Gas-phase gradient  $\alpha_{g,in}$  is also flatter with the mechanical feedback by  $\sim 0.1 \text{ dex/kpc}$  than the thermal and stochastic cases (Fig. 4.5). These can be explained by the suppression of star formation at the centre and ejection of metals to the outskirts.
- The galaxy stellar mass dependence of the stellar and gas-phase metallicity gradients with the three feedback models are shown up to  $z = 5$  (Fig. 4.8). From  $z = 0.7$  to  $z = 4$ , we retrieve a relation between stellar mass and stellar metallicity gradient, where the gradient is

steeper for lower-mass galaxies. This relation is stronger with the total gradients  $\alpha_*$  than for the inner gradients  $\alpha_{*,\text{in}}$ . Stellar outer gradients would be more informative, although these are very difficult to measure with high-redshifts observations. For gas-phase, gradients are steepest at the intermediate mass, and become flatter toward lower and higher masses. While the mechanical feedback results in gradients closest to observational data at  $z = 0.2$ , the gradients are still steeper than observed at  $z = 2$  over  $10^9\text{--}10^{10}M_\odot$ .

- To explain recent and ongoing observational IFU data, the redshift evolution of the gas-phase oxygen abundance metallicity gradients up to  $z = 5$  is presented (Fig. 4.9). At all redshifts and with all three models, the gradient of the majority of galaxies in our simulations have negative gradients. With the mechanical feedback, lower-mass galaxies have significantly flatter gradients up to  $z = 2$ , whereas massive galaxies have flatter gradients at  $z > 2$ . These gradients are still steeper than recent IFU observations (e.g. Curti et al., 2020b; Wang et al., 2022; Ju et al., 2024), although our results are in reasonably good agreement with observations in Yuan et al. (2011); Jones et al. (2013).
- The discrepancy of the gas-phase gradients at high-redshifts are unlikely due to the selection bias as shown with the the dependence on galaxy type (Fig. 4.12). Earlier type galaxies tend to have a gradient flatter by  $\sim 0.1$  dex/kpc compared to later type galaxies.
- For future observations, the evolution of stellar metallicity gradients up to  $z = 5$  is also predicted (Fig. 4.11). The stellar gradients become flatter and flatter toward  $z \sim 4$ . Massive galaxies show inverse inner stellar gradients at  $z \sim 4$ , possibly because their centres formed most of their stars early from metal-poor gas, while later star formation in the outer regions used gas that was already enriched (Section 4.6.2).
- We find an evolutionary transition at  $z \sim 5$  with the mechanical feedback, where both stellar and gas-phase metallicity gradients become steep. This can be tested with future JWST observations.

Note that the metallicity profiles vary from galaxy to galaxy, so it is important to apply a proper fitting method to quantify the gradients. Above, we summarized the averaged results of our sample of galaxies. Nevertheless, to demonstrate this case-by-case scenario, we analyzed an example of massive and intermediate-mass galaxies (Galaxies A and B, respectively) in detail, including their kinematics (Appendix). Galaxy A is a typical massive galaxy with negligible rotation. Even though different feedback models lead to a different gas distribution (Fig. 4.1), the metallicity gradients are largely unchanged (Fig.4.2). Galaxy B is a rotating intermediate-mass galaxy where inside-out quenching due to stellar feedback causes a *positive* inner gradient (Fig. 4.4) inside the gas ring (Fig. 4.3).

This detailed feature might not be well resolved in lower-mass galaxies of our simulations, which might be the reason for the discrepancy of metallicity gradients at high redshifts. We will study

this with a higher-resolution simulation in our future work. It is important to note that our simulation with the mechanical feedback is in excellent agreement with the observations at  $z = 0$  after the active star formation and feedback phase in the universe. Therefore, testing our model at very high redshifts is also important. Although the galaxy sample is limited, we predict the metallicity gradients become steeper at  $z = 5$  than at  $z = 4$ , which will be studied with a larger volume simulation in our future works.

## CHAPTER 5

# NUCLEOSYNTHESIS YIELDS FROM POPULATION III STARS

---

<b>5.1</b>	<b>INTRODUCTION</b>	<b>102</b>
<b>5.2</b>	<b>METHOD</b>	<b>103</b>
5.2.1	MODEL	104
5.2.2	POP III NUCLEOSYNTHESIS YIELDS	104
5.2.3	POP III IMF	105
<b>5.3</b>	<b>RESULTS</b>	<b>105</b>
5.3.1	N/O	105
5.3.2	OTHER ELEMENTAL ABUNDANCE RATIOS	107
5.3.3	POP III IMF DEPENDENCE	109
<b>5.4</b>	<b>CONCLUSIONS</b>	<b>115</b>

---

## 5.1 Introduction

Recent observational data from the JWST have significantly advanced our understanding of galaxy formation and chemical evolution in the early Universe. Spectroscopic observations have revealed unexpectedly strong emission lines in very high-redshift galaxies, including very elevated nitrogen-to-oxygen abundance ratios. For example, the galaxy GN-z11 at  $z = 10.6$  shows  $[N/O] \geq 0.5$ , which is more than four times the solar value (Bunker et al., 2023; Cameron et al., 2023). Other galaxies have since been observed with similarly enhanced nitrogen emission (e.g., Marques-Chaves et al. 2024,  $z = 8.68$ ; Isobe et al. 2023,  $z = 6.23$ ; Topping et al. 2024a,  $z = 6.1$ ; Topping et al. 2024b,  $z = 7.04$ ; Castellano et al. 2024b,  $z = 12.34$ ; Schaerer et al. 2024b,  $z = 9.3$ ). The properties of these nitrogen-rich systems are summarized in Table 5.1.

Galaxy	$z$	Survey	$\log(M_*/M_\odot)$	$\log(N/O)$	$12+\log(O/H)$	Reference	Type
GS-z9	9.43	JADES	$\sim 8.17$	$-0.93 \pm 0.24$	$7.49 \pm 0.11$	Curti et al. (2024a)	AGN?
GN-z11	10.6	JADES	$\sim 8.73$	$> -0.25$	$\approx 7.82$	Bunker et al. (2023) Cameron et al. (2023)	AGN?
CEERS-01019	8.68	CEERS	$8.66 - 8.94$	$-0.18 \pm 0.11$ $> 0.28$	$7.70 \pm 0.18$ $\sim 7.94$	Marques-Chaves et al. (2024) Isobe et al. (2023)	SF-galaxy
GLASS_150008	6.23	GLASS		$\sim -0.40$	$\sim 7.65$	Isobe et al. (2023)	
A1703-zd6 (lensed)	7.04		$7.70 \pm 0.24$	$-0.6$	$7.47 \pm 0.19$	Topping et al. (2024b)	SF
RXCJ2248-ID (lensed)	6.1		$\sim 8.05$	$-0.39 \pm 0.1$	$\sim 7.43$	Topping et al. (2024a)	
GN-z9p4	9.38	GOODS-N	$8.7 \pm 0.2$	$-0.59 \pm 0.24$	$7.37 \pm 0.15$	Schaerer et al. (2024a)	SF
GHZ2	12.3	GLASS	$\sim 9.05$	$-0.29 - -0.2$	$\sim 7.26$	Castellano et al. (2024a)	SF

TABLE 5.1: Table summarizing properties of JWST observed galaxies with high nitrogen-to-oxygen ratios at  $z > 6$ .

Several scenarios have been proposed to explain these extreme N/O ratios. For example, using a correlation with stars in globular clusters (e.g. Charbonnel et al. 2023; Senchyna et al. 2024), while others suggest enrichment by supermassive stars (SMSs) (Nagele and Umeda 2023; Nandal et al. 2024) and very massive stars (VMSs) (Vink, 2022). In the early Universe, the properties of the first stars may be very different from local stellar populations, including a top-heavy IMF and enhanced yields from massive stars instead. Kobayashi and Ferrara (2024) introduced chemical evolution models incorporating WR stars and intermittent star formation which can explain these observations. Additional studies have emphasized the role of rotating WR stars, which can enrich nitrogen rapidly via strong stellar winds (Watanabe et al., 2024; Fukushima and Yajima, 2024). However, GN-z11 is already a relatively evolved system, with a stellar mass of  $\sim 10^9 M_\odot$ , raising key questions about how such galaxies form and chemically mature so early. To investigate this, it is important to model their evolution within a cosmological context. In this work, we present the first attempt to incorporate these exotic chemical enrichment sources, including WR stars and potentially PISNe, self-consistently in cosmological hydrodynamical simulations, offering a new framework to interpret the chemical signatures of early galaxies.

## 5.2 Method

To predict the abundances of the first galaxies, we include nucleosynthesis yields from Pop III stars up to  $300M_\odot$ , including faint supernovae, WR stars and PISN into our simulations. The simulations shown in the previous Chapters include the same nucleosynthesis yields as Kobayashi et al. 2020a, which we refer to as C5 (for Chem5). C5 is also used in other simulations such as SIMBA-C (Hough et al., 2023; Padawer-Blatt et al., 2025). In the following sections, we present our new simulation, C6, including yields from Pop III stars.

### 5.2.1 Model

We use chemodynamical simulations with our same code based on GADGET-3 (Springel et al., 2005) including the same baryon physics described in previous chapters (Ibrahim and Kobayashi, 2024, 2025).

In this Chapter, the simulations are run with the same initial conditions and resolution in a  $10h^{-1}\text{Mpc}$  cubic box, with periodic boundary conditions. The number of gas and dark matter particles is  $N_{\text{gas}} = N_{\text{DM}} = 96^3$ , with mass  $M_{\text{gas}} = 2.2 \times 10^7 h^{-1} M_{\odot}$  and  $M_{\text{DM}} = 1.2 \times 10^8 h^{-1} M_{\odot}$ . We use the same cosmological parameters as in Ibrahim and Kobayashi (2024):  $\Lambda\text{CDM}$  cosmology with  $h = 0.68$ ,  $\Omega_m = 0.31$ ,  $\Omega_{\Lambda} = 0.69$  and  $\Omega_b = 0.048$  (Planck Collaboration, 2020). The gravitational softening lengths are  $\epsilon_{\text{gas}} = 0.84375 h^{-1} \text{kpc}$  and  $\epsilon_{\text{DM}} = 1.6875 h^{-1} \text{kpc}$  for gas and dark matter/stars, respectively.

We include various physical processes: metallicity-dependent radiative cooling (Kobayashi, 2004), star formation (Kobayashi et al., 2007), black hole physics (Taylor and Kobayashi, 2014), and element and energy production from AGBs, Type Ia, Type II supernovae (Kobayashi, 2004) and hypernovae (Kobayashi and Nakasato, 2011b). In this Chapter we use the thermal supernovae feedback model described in Ibrahim and Kobayashi (2024), but we aim to switch to the mechanical feedback model in our future work.

The main new ingredients in C6 are the inclusion of yields from WR stars and PISNe, which provide additional enrichment channels beyond those already present in C5. The energetic contributions of different stellar types have been investigated in earlier studies; for example, Kobayashi et al. (2007) examined HNe and showed that their feedback can significantly enhance metal-rich outflows in low-mass galaxies and strongly affect chemical enrichment patterns. A detailed quantitative breakdown of the energy budget by different stellar sources (e.g. ccSNe, HNe, WR winds, and PISNe) will be presented in forthcoming work that directly compares C5 and C6.

### 5.2.2 Pop III nucleosynthesis yields

For nucleosynthesis yields from PISNe, we use the rotating model from Takahashi et al. (2018) from 170 to 300  $M_{\odot}$ , as presented in Chapter 2.

For nucleosynthesis yields from WR stars, we use a combination of the CO core yields from Kobayashi et al. (2020a) with the contributions of C and N from rotating stellar envelopes and winds from Limongi and Chieffi (2018b) from 40 to 120  $M_{\odot}$ . This integration is necessary because the Limongi and Chieffi (2018b) yields alone do not reproduce observations of iron-peak elements due to their simplified supernova explosions and the lack of hypernovae. This WR yields calibration is implemented to match the observed  $[(\text{C,N,O})/\text{Fe}]$  abundances in the Milky

Way (Kobayashi, 2022). We also use nucleosynthesis yields from faint supernovae from 15 to 40  $M_{\odot}$  (Ishigaki et al., 2018).

### 5.2.3 Pop III IMF

The Pop III IMF describes the mass distribution of the first generation of stars that formed in a metal-free environment during the early universe. Due to the lack of metals ( $Z = 0$ ), cooling mechanisms were inefficient, leading to the formation of predominantly massive stars ( $M_* \sim 10\text{-}300M_{\odot}$ ). The slope of the Pop III IMF, denoted as  $x_{imf3}$ , determines how mass is distributed among these stars: a lower  $x_{imf3}$  (flatter IMF) produces more massive stars, while a higher  $x_{imf3}$  (steeper IMF) results in a more significant fraction of lower-mass stars. Pop III stars evolve rapidly, with most ending their lives as SNe, HNe, or PISNe, significantly enriching the ISM with the first metals.

The transition to Population II stars occurs when the gas becomes metal-enriched, a shift regulated by the metallicity threshold  $Z_{max3}$ , which sets the maximum metallicity at which Pop III stars can form.  $Z_{max3}=0$  means only star particles with zero metallicity are considered Pop III stars. A lower  $Z_{max3}$  allows Pop III stars to last longer, while a higher  $Z_{max3}$  leads to an earlier transition to Pop II, where star formation follows a more bottom-heavy IMF, producing a greater fraction of low- and intermediate-mass stars ( $M_* \sim 0.1\text{-}100M_{\odot}$ ). While Pop III stars form in large and hot gas clouds, Pop II stars benefit from enhanced cooling due to metals, leading to smaller, fragmented clouds.

## 5.3 Results

### 5.3.1 N/O

Recent observational data from JWST/NIRSpec have shown bright nitrogen emission NIV]  $\lambda 1486$  and NIII]  $\lambda 1748$  in the GN-z11 galaxy (Bunker et al., 2023). This galaxy also shows a high nitrogen-to-oxygen abundance ratio of  $[N/O] \geq 0.5$  (Cameron et al., 2023). In the ISM, nitrogen is primarily produced via the CNO cycle in massive stars (a process that is enhanced by stellar rotation), then from AGB stars through the primary process, and in metal-rich massive stars via the secondary process. However, the extremely high N/O ratio observed at redshift  $z = 10.6$  remains difficult to explain, as AGB stars evolve on longer timescales than the rapid oxygen enrichment from supernovae. An alternative explanation involves stellar rotation in intermediate-mass stars, which can significantly accelerate nitrogen production ( $\sim 3$  Myr). Stellar rotation enhances the mixing of H and He layers, enhancing the CNO cycle and leading to early nitrogen enrichment (Limongi and Chieffi 2018b).

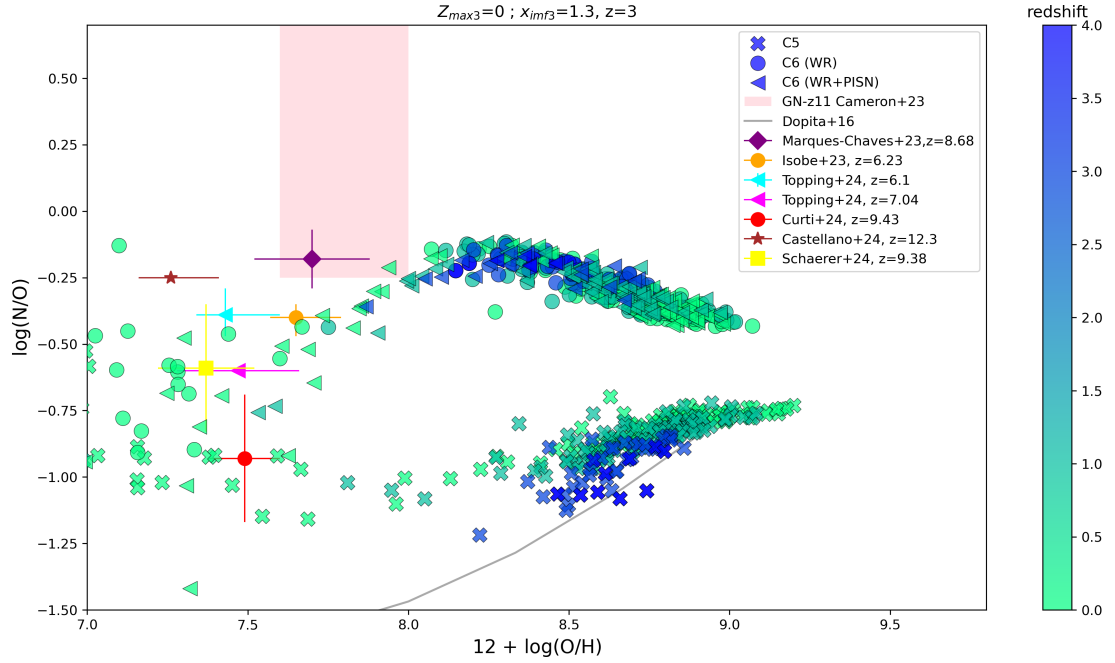


FIGURE 5.1: The evolution of SFR-weighted gas-phase N/O abundance ratios compared to oxygen abundances with Pop III nucleosynthesis yields from WR (circles), WR and PISN (triangles) and without (cross), including faint supernovae. We compare with observational data of from Cameron et al. (2023, GNz-11 ( $z = 10.6$ ); pink area), Isobe et al. (2023, orange circle), Marques-Chaves et al. (2024, purple diamond), Topping et al. (2024a, cyan triangle), Topping et al. (2024b, magenta triangle), Curti et al. (2024a, red circle), Castellano et al. (2024a, brown star), Schaerer et al. (2024a, yellow square), and Dopita et al. (2016, gray line).

To investigate the chemical origin of this early nitrogen enrichment, we use the latest nucleosynthesis yields from Kobayashi et al. 2020a, including rotating WR envelopes (Limongi and Chieffi 2018a; see details in Section 5.2), faint supernovae and rotating PISNe for Pop III stars (Takahashi et al., 2018). Similar yields are used in Kobayashi and Ferrara (2024), but excluding faint supernovae.

We explore the impact of different parameters for Pop III star contributions (see Section 5.3.3), but in this section we show the abundance ratios with three different models while keeping the constant Kroupa IMF slopes (Kroupa, 2008) as for Pop II stars between the lower and upper stellar mass limits ( $[m_\ell, m_u]$ ). For consistency with earlier “C5” simulations, we use thermal feedback only.

Figure 5.1 presents the N/O versus O/H relation from our simulations. The C5 model (cross symbols) includes nucleosynthesis yields from Kobayashi et al. (2020a,b) from  $z = 0$  (green), to  $z = 4$  (blue), which agrees well with the compilation of local observational data (solid line) from Dopita et al. (2016). This observed local relation has been explained as follows. (i) The plateau at low metallicities caused by rotating massive stars in one-zone galactic chemical evolution models (Chiappini et al., 2006), or inhomogeneous enrichment from AGB stars in cosmological simulations as explained in Vincenzo and Kobayashi (2018). (ii) The increasing trend toward higher metallicities is caused by the metallicity dependence of N yields in all mass range of stars

and the delayed enrichment from AGB stars. The stellar population ages of our simulated galaxies at  $z \sim 3\text{--}4$  have a median of  $\sim 0.3$  Gyr. These ages are comparable to those inferred for many galaxies observed at  $z > 6$  (e.g. Laporte et al. 2017; Tacchella et al. 2022; Carnall et al. 2023). This supports our approach of comparing abundance patterns across these different redshifts, since the underlying stellar populations are of similar age even though the galaxies are observed at different epochs.

We also show results from our new simulations: C6 (WR), which includes rotating WR stars (circles) with initial masses  $M_*=[0.01, 120] M_\odot$ , and C6 (WR+PISN), which includes both rotating WR stars and rotating PISNe (triangles; with  $M_*=[15, 300] M_\odot$ ). In C5, the N/O ratio exhibits a clear evolution with redshift, increasing over time, whereas this is less apparent in C6. Both C6 models significantly enhance the N/O ratio across all metallicities and redshifts compared to C5. This enhancement is primarily driven by stellar rotation, which increases mass loss through stellar winds, promoting WR formation and ejecting nitrogen and carbon into the ISM (Limongi and Chieffi, 2018a). PISNe have a relatively minor effect, probably because of their small contribution with  $x_{imf3} = 1.3$ , which may be enhanced with lower  $x_{imf3}$ , higher redshifts, and higher  $Z_{max3}$ . The presence of rotating WR stars leads to higher N/O ratios, particularly at early times, providing a promising explanation for the extreme nitrogen enrichment seen in high-redshift galaxies like GN-z11.

However, while the C6 models match high- $z$  observations (blue), they overproduce local N/O values (green). In contrast, the C5 model fits the local relation but underproduces nitrogen at high redshifts. To resolve this tension, we propose a hybrid model that combines the strengths of both C5 and C6 and incorporates metallicity-dependent WR yields, which we aim to explore in future work. Specifically, we plan to investigate dependence of the yields on stellar rotation within the C6 model. If suppressing rotation at low metallicity reduces the N/O excess at  $z = 0$ , this would naturally reconcile the models. If, however, enhanced N/O persists even without rotation, we would then introduce a metallicity dependence on the WR yield prescription, transitioning from C6-like yields at low metallicity (where rapid rotation is more likely) to C5-like yields at high metallicity (where stronger mass loss reduces angular momentum and limits rotational mixing). Such a metallicity dependence would be physically motivated, as stellar rotation rates are expected to decrease with increasing metallicity due to stronger mass loss in metal-rich stars, although other factors such as magnetic fields or environment may also play a role.

### 5.3.2 Other elemental abundance ratios

Recent JWST data have also expanded the high redshift observations of other elemental abundances such as Carbon and Neon. In this section we analyze the impact of the PoP III yields on C/O, Ne/O, Ar/O, and S/O. In this work, we present the redshift evolution up to  $z = 4$ , but the aim of

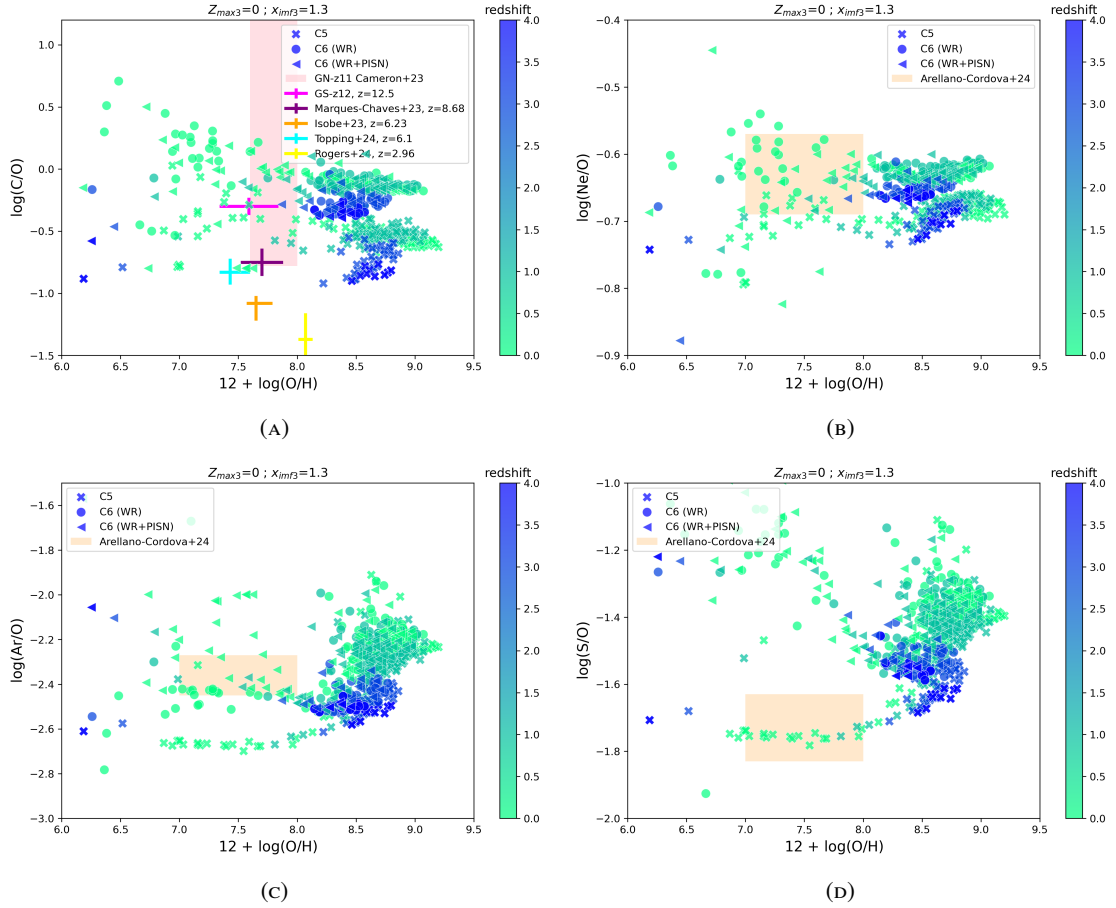


FIGURE 5.2: Same as Figure 5.1, but for (A): carbon to oxygen ratio, (B): neon to oxygen ratio, (C): argon to oxygen ratio, (D): sulfur to oxygen ratio. Observational data are from Marques-Chaves et al. (2024, purple), Isobe et al. (2023, orange), Topping et al. (2024a, cyan), Rogers et al. (2024, yellow), D’Eugenio et al. (2024, magenta symbol), Cameron et al. (2023, pink area), and Arellano-Córdova et al. (2024, orange area;  $0.02 < z < 0.18$ ).

this study is to use these higher redshift observational data for further constrains, which will be presented in our future work.

Figure 5.2a is the same as Figure 5.1 but for the carbon-to-oxygen ratio as a function of gas-phase oxygen abundance. With all models, the simulated galaxies evolve toward higher O/H as expected. C6 produces higher C/O than C5 at all redshifts. At high redshifts ( $z = 4$ ), C6 produces higher C/O ( $\log(C/O) \sim -0.3$  to  $-0.1$ ), approaching the GN-z11 band (pink area, Cameron et al. 2023) and the carbon enhanced GS-z12 (magenta symbol, D’Eugenio et al. 2024), suggesting that WR and PISN yields are needed to explain the high- $z$  C/O ratios, as seen for N/O ratios. At low redshifts, C6 overpredicts C/O, which suggests that C6 models might need redshift-dependent yields or feedback regulation to suppress late carbon production (or enhance carbon ejection).

Figure 5.2c is the same but for neon-to-oxygen ratio as a function of oxygen abundance. The Ne/O ratio remains relatively constant across metallicities, which is expected as neon and oxygen are both  $\alpha$ -elements produced in similar stellar environments (mainly cc-SN). Ne/O is enhanced in C6, where most points lie within the shaded orange region (observed range from Arellano-Córdova

et al. 2024), suggesting that the new simulations with Pop III yields better reproduce the observed Ne/O ratios. The scatter at low metallicities is slightly larger, possibly due to variations in stellar population contributions at early epochs. In C6, the Ne/O ratio slightly decreases at higher redshifts. However, it remains higher than in C5. Combining both simulations in our future work should regulate this pattern.

Figure 5.2b is the same but for argon-to-oxygen ratio as a function of oxygen abundance. At  $z = 0$  (green) and  $(12 + \log(\text{O}/\text{H}) < 8.5)$ ,  $\log(\text{Ar}/\text{O})$  with C5 shows a significant number of points lying below the observed range (shaded orange region from Arellano-Córdova et al. 2024). The C6 WR+PISN model (triangles) produces significantly enhanced Ar/O at low metallicities, suggesting that PISNe might contribute more argon at early times (Bhattacharya et al., 2024). At higher metallicities ( $12 + \log(\text{O}/\text{H}) > 8.5$ ), the different simulation setups (C5, C6) converge towards a relatively stable Ar/O ratio, aligning well with observations. The increasing trend with metallicity in the high-metallicity regime may indicate enrichment from Type Ia supernovae at later epochs.

Figure 5.2d is the same but for sulfur-to-oxygen ratio as a function of oxygen abundance. At low metallicities, there is a clear bimodal distribution in S/O, with C5 lying in the observed orange region also consistent with Arellano-Córdova et al. 2024 at  $z = 0$ , and C6 clustered above it at  $\log(\text{S}/\text{O}) \sim -1.2$ . This suggests that WR stars and PISNe enhance sulfur relative to oxygen, supporting the idea that massive stars at early times produce significant sulfur. The scatter is more significant at low metallicities, suggesting that sulfur evolution is more sensitive to the IMF or nucleosynthesis sources than Ne/O and Ar/O. At high metallicity ( $12 + \log(\text{O}/\text{H}) > 8.5$ ), the low redshifts S/O ratio plateaus but remains consistently above the observed range. The overproduction of sulfur is particularly evident in the C6 simulations, where the current WR and PISN yields might be too aggressive, especially at early times. The absence of observational S/O constraints at high- $z$  makes this a predictive signature, which should be tested by future JWST observations.

### 5.3.3 Pop III IMF dependence

As shown in previous section, including nucleosynthesis yields from Pop III stars in our cosmological hydrodynamical simulations has a significant impact on the predicted elemental abundance ratios, particularly enhancing both N/O and C/O. To identify which types of Pop III stars are primarily responsible for this enrichment, and to determine the epochs at which they contribute most effectively, we perform a detailed parameter study of the Pop III IMF in the following section.

We investigate the influence of Pop III IMF on SFRs and MZR, and present the results highlighting how different Pop III IMF slopes  $x_{imf3}$  and Pop III metallicity thresholds  $Z_{max3}$  affect the results (SFR and MZR) within different mass ranges, allowing us to study how the fraction of low- and high-mass Pop III stars influence the buildup of metals in both stars and the ISM.

## SFR

### $x_{imf3}$ dependence

Figure 5.3 presents the SFR from our cosmological simulations with the thermal feedback, where we conduct a parameter study by varying the slope of the Pop III IMF ( $x_{imf3}=0.3; 1.3; 2.3$ , dark blue, pink, yellow, respectively) within a mass range of  $M_*=[0.01-120]M_\odot$  (left panel) and  $M_*=[15-300]M_\odot$  (right panel) with our previous simulations C5 (dashed lines) and the updated versions C6 (solid lines).

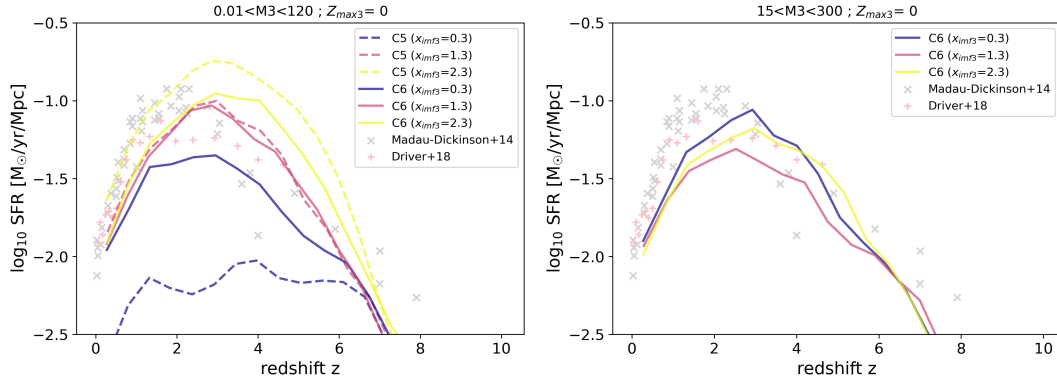


FIGURE 5.3: Redshift evolution of the SFR in our cosmological simulations with thermal FB in a  $(10h^{-1} \text{ Mpc})^3$  box. We compare SFRs with various Pop III IMF slopes ( $x_{imf3} = 0.3, 1.3, 2.3$ ; shown in blue, pink, yellow, respectively) with yields from WR and PISN (C6; solid lines) and without (C5; dashed lines). The left panel corresponds to the Pop III IMF mass range  $M_*=[0.01, 120]M_\odot$ , and the right panel to  $M_*=[15, 300]M_\odot$ . Observational data are taken from Madau and Dickinson (2014, gray cross symbols) and Driver et al. (2018, pink plus symbols).

In the left panel of Figure 5.3, with both C5 and C6, the top-heavy (flatter) IMF ( $x_{imf3}=0.3$ , blue) increases the formation of massive stars, leading to enhanced stellar feedback, which suppresses star formation producing lower SFRs. C6 (solid blue line) produces a higher SFR than C5 in the top-heavy IMF case, where metal enrichment from massive stars dominate. This is expected since C6 includes WR stars and PISN, which inject metals earlier, enhancing star formation.

In contrast, the bottom-heavy, steeper IMF ( $x_{imf3}=2.3$ , yellow) promotes the formation of low-mass stars, which contribute less feedback energy, resulting in a higher SFR at later epochs due to sustained star formation. As expected, we observe no significant differences between C5 and C6 with  $x_{imf3}=1.3$  (pink) confirming the robustness of our simulations.

The right panel is the same but for the higher mass range ( $M_*=[15-300]M_\odot$ ) with C6, where low-mass Pop III stars are entirely excluded. As a result, the flatter IMF ( $x_{imf3}=0.3$ , blue) produces slightly more stars overall than  $x_{imf3}=2.3$  (yellow), suggesting that cooling from metal production outweighs heating from stellar feedback. While feedback can remain strong for  $x_{imf3}=0.3$ , the dominance of massive stars in this mass range ensures a higher SFR, as there are no competing low-mass stars to reduce the overall SFR. This indicates a delicate balance between negative thermal feedback and positive feedback (metal-driven cooling). For a deeper

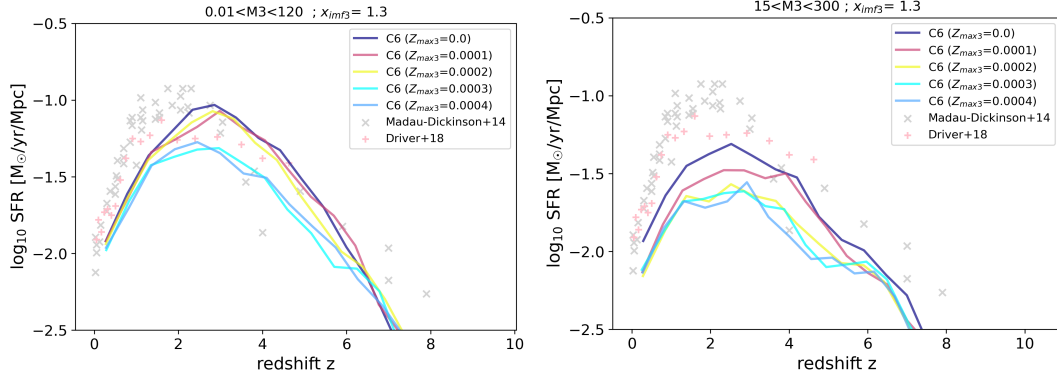


FIGURE 5.4: Same as Figure 5.3, but showing the impact of the Pop III initial metallicity threshold  $Z_{max3}$  on the cosmic SFR for C6, with a fixed Pop III IMF slope of  $x_{imf3} = 1.3$ .

understanding of these effects, we aim to analyze the evolution of cold gas and cosmic metallicity in upcoming studies.

#### $Z_{max3}$ dependence

Figure 5.4 shows the impact of  $Z_{max3}$  on the cosmic SFR for C6, with a fixed IMF slope ( $x_{imf3} = 1.3$ ). In the left panel ( $0.01 < M_* < 120 M_\odot$ ), a lower  $Z_{max3}$  results in a higher early SFR, as Pop III stars transition to Pop II earlier. As  $Z_{max3}$  increases, this transition is delayed, allowing Pop III stars to persist longer. This results in a suppressed SFR at high redshifts ( $z > 4$ ), due to the stronger feedback effects associated with the more massive and energetic Pop III population.

In the massive range (right panel,  $15 < M_* < 300 M_\odot$ ), the SFR is lower for all  $Z_{max3}$ , primarily due to the larger number of supernovae produced by massive stars, which enhance feedback and suppress star formation. The suppression becomes even more pronounced at higher  $Z_{max3}$ , as Pop III stars including PISNe persist slightly longer before transitioning. While supernovae and PISNe contribute to metal enrichment, which can promote cooling and lead to positive feedback, this effect is not dominant here, and the net result is still a stronger suppression of the SFR.

## MZR

Top panels of Figure 5.5 show the luminosity-weighted stellar MZR at  $z = 0$  with thermal feedback, comparing different Pop III IMF slopes ( $x_{imf3}$ ) in two different mass ranges:  $0.01 < M < 120M_{\odot}$  (upper left panel) and  $15 < M < 300M_{\odot}$  (upper right panel). Observational data are from (Zahid et al., 2017) (dashed gray line) with  $1\sigma$  scatter.

In the upper left panel, where lower-mass Pop III stars ( $0.01-120M_{\odot}$ ) contribute, the steep IMF ( $x_{imf3}=2.3$ , yellow) results in much lower metallicities with C5 (dashed lines) than C6 (solid line), where the additional metal enrichment from WR and PISN in C6 enhances the overall metallicity. However, for flatter IMFs ( $x_{imf3}=0.3$ , blue), the metallicity in C6 is actually lower than in C5. This suggests that in a scenario dominated by massive stars, strong feedback from PISN in C6 actually suppress subsequent star formation, limiting continued metal production.

Note that at  $x_{imf3}=1.3$  (pink), C5 and C6 produce similar metallicities, higher than the observational trend from Zahid et al. (2017) due to the current thermal feedback in a  $10h^{-1}\text{Mpc}$  box. This will be improved when we combine the C6 simulation with the mechanical feedback model described in previous Chapters in a larger volume box.

In the upper right panel, the MZR in the massive range are fairly similar to the left panel. Although with the steeper IMF (yellow), the metallicity is slightly lower possibly because of the feedback from the massive stars suppressing star formation.

In conclusion, Pop III IMF does not impact stellar MZR because of the combination of negative and positive feedback.

The bottom panels of Figure 5.6 present the SFR-weighted gas-phase MZR at  $z = 0$ , comparing different Pop III IMF slopes ( $x_{imf3}$ ) in the C5 (dashed lines) and C6 (solid lines) simulations in two different mass ranges:  $0.01 < M < 120M_{\odot}$  (bottom left panel) and  $15 < M_{*} < 300M_{\odot}$  (bottom right panel). Gas-phase MZR is more complicated as feedback affects gas flows and SFR-weighting.

In the bottom left panel, C5 predicts higher gas-phase metallicities than C6 with the flatter IMF ( $x_{imf3}=0.3$ , blue), where enriched gas is probably more efficiently removed from the ISM in C6. In contrast, C5 shows lower metallicity for steeper IMFs ( $x_{imf3}=2.3$ , yellow) than C6; despite the steep IMF favoring low-mass stars, the limited but metal-rich high-mass end in C6 leads to more efficient early oxygen enrichment, while the extended low-mass range in C5 dilutes the enrichment with a larger number of stars that seem to contribute little to the ISM metallicity. The non-monotonic behavior at lower stellar masses is also due to the limited sample of galaxies with this resolution.

The bottom right panel extends the analysis to higher-mass Pop III stars ( $15 < M_{*} < 300M_{\odot}$ ), which undergo PISN and can contribute to strong metal outflows. The results show that at  $\log M_{*} > 10M_{\odot}$ , flatter IMFs ( $x_{imf3}=0.3$ , blue line) produce lower gas-phase metallicities, indicating that more

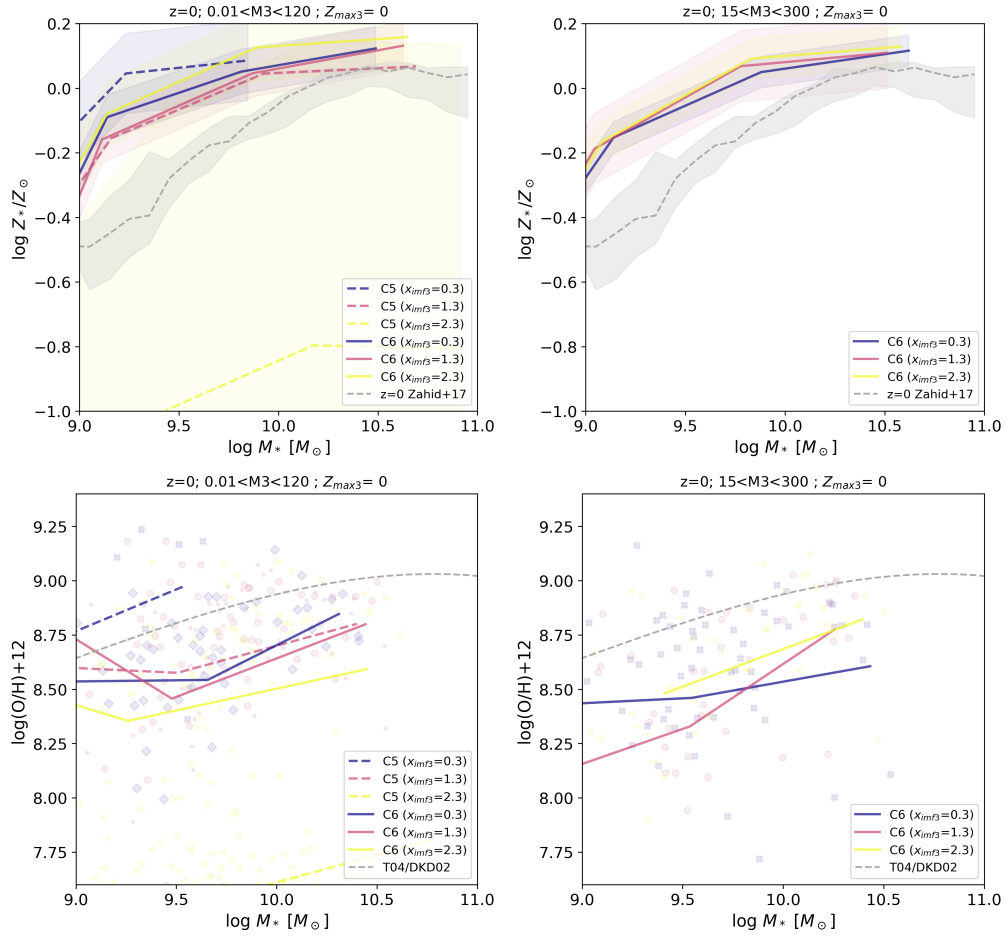


FIGURE 5.5: Upper panels: Luminosity-weighted stellar MZR in our cosmological simulations at  $z = 0$ , within a  $(10h^{-1} \text{ Mpc})^3$  box. We compare MZR for different Pop III IMF slopes ( $x_{imf3} = 0.3, 1.3, 2.3$ , in blue, pink, and yellow, respectively) with C5 (dashed lines) and C6 (solid lines) models. The left panel corresponds to an initial mass range of  $M_* = [0.01, 120]M_\odot$ , and the right panel to  $M_* = [15, 300]M_\odot$ . Observational data are taken from [Zahid et al. \(2017\)](#), gray line). Bottom panels: Same as the upper panels, but for SFR-weighted gas-phase MZR.

massive stars drive stronger feedback, expelling metals from the ISM more efficiently. In contrast, steeper IMFs ( $x_{imf3}=2.3$ , yellow line) result in higher gas-phase metallicities, suggesting that a greater fraction of lower-mass stars allows for more gradual chemical enrichment with less metal loss. As with the bottom left panel, both models underpredict the observed metallicities at higher stellar masses, which can be improved with the mechanical feedback model in a larger box volume as discussed in 3.

### $Z_{max3}$ dependence

The upper panels of Figure 5.6 display the luminosity-weighted stellar MZR at  $z = 0$  for different maximum metallicity thresholds for Pop III stars ( $Z_{max3}$ ), with a fixed IMF slope ( $x_{imf3}=1.3$ ). We present two different Pop III mass ranges:  $0.01 < M_* < 120M_\odot$  (left panel) and  $15 < M_* < 300M_\odot$  (right panel). In all cases, the stellar metallicity increases with stellar mass, following the expected

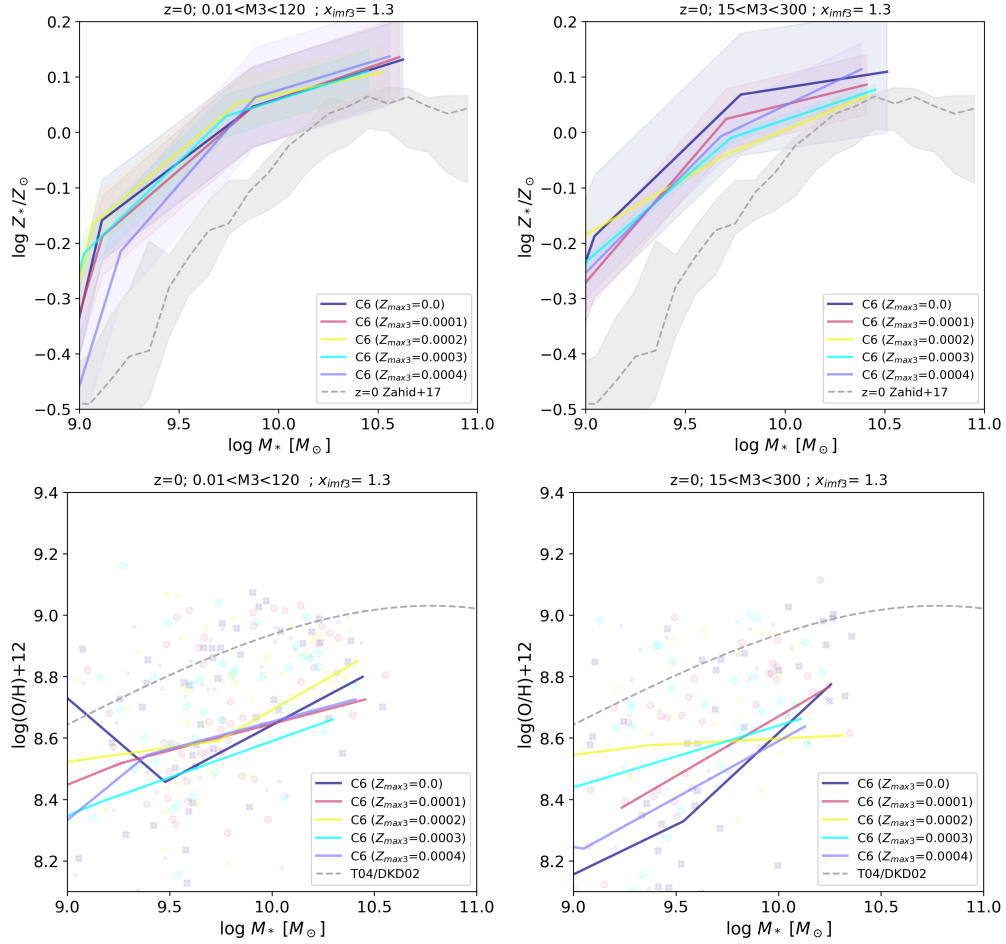


FIGURE 5.6: Same as Figure 5.5, but with a fixed  $x_{\text{imf}3} = 1.3$ , for various  $Z_{\text{max}3}$ .

MZR, where higher-mass galaxies are more metal-rich. The right panel shows that the lowest metallicity threshold ( $Z_{\text{max}3}=0.0$ , dark blue line) results in slightly higher stellar metallicities, while higher  $Z_{\text{max}3}$  values show lower metallicities, suggesting that a later transition to Pop II stars may lead to reduced overall metal production.

The bottom panels of Figure 5.6 are the same as the upper panels but for the SFR-weighted gas-phase metallicity at  $z = 0$ . In the left bottom panel ( $0.01 < M_* < 120 M_\odot$ ), varying  $Z_{\text{max}3}$  has no significant impact on the gas-phase metallicity, suggesting that metal enrichment in this mass range is largely dominated by Pop II star formation and subsequent metal feedback rather than the precise transition point from Pop III to Pop II.

In the right panel ( $15 < M_* < 300 M_\odot$ ), a clear dependence on  $Z_{\text{max}3}$  appears at lower stellar masses ( $\log M_* < 9.5 M_\odot$ ), where overall lower  $Z_{\text{max}3}$  leads to lower gas-phase metallicities, likely due to the brief duration of Pop III star formation producing less metals. However, at higher stellar masses ( $\log M_* > 9.5 M_\odot$ ), the impact of  $Z_{\text{max}3}$  lowers, suggesting that in massive galaxies, metal enrichment becomes dominated by sustained Pop II star formation rather than the early enrichment history set by Pop III stars. This highlights that the transition metallicity

for Pop III stars primarily affects low-mass systems, where the competition between early metal production and metal loss via feedback is more significant, while more massive galaxies allow for better metal production, making the details of early Pop III enrichment less crucial to present-day gas-phase metallicities.

## 5.4 Conclusions

In this chapter, we presented a new generation of cosmological hydrodynamical simulations (C6) that include updated nucleosynthesis yields from Population III stars, incorporating rotating WR stars, faint supernovae, and PISNe. These models were developed in response to recent JWST observations that revealed unexpectedly high elemental abundance ratios, particularly nitrogen and carbon, in galaxies at redshifts  $z > 6$ , such as GN-z11.

Our results demonstrate that rotating massive stars, especially WR stars, significantly enhance nitrogen and carbon production in the early Universe, improving agreement with high-redshift observations. While these updated yields help reproduce observed N/O and C/O ratios, they tend to overpredict abundances at lower redshifts, suggesting that a metallicity-dependent treatment of stellar rotation may be necessary, which we plan to explore in future work.

The updated C6 yields lead to significantly enhanced S/O at low metallicity, while Ne/O is consistently enhanced across all metallicities. Ar/O also shows moderate enhancement with C6, particularly due to PISNe, highlighting its potential as a tracer of rare, energetic enrichment events.

We also explored how different Pop III IMFs and metallicity thresholds affect star formation histories and metal enrichment. We find that Pop III enrichment is more important in low-mass galaxies, while higher-mass systems are more influenced by sustained Pop II star formation.

This work presents a self-consistent approach for connecting the first stars to the chemical signatures observed in early galaxies. It improves our understanding of early chemical enrichment and lays the groundwork for future studies using mechanical feedback and larger simulation volumes.

## CHAPTER 6

# CONCLUSIONS

---

The motivation for this thesis is to understand the origin of the first metals in the Universe — how they were produced and distributed in the earliest galaxies. This broad question is deeply connected to the physics of galaxy formation, and as our work progressed, it became increasingly clear that stellar feedback plays a central role in shaping the chemical evolution of galaxies. As a result, a major focus of this thesis is exploring how different supernova feedback mechanisms influence metal production and distribution using state-of-the-art cosmological hydrodynamical simulations. I explore how stellar feedback and nucleosynthesis shape the mass–metallicity relation, metallicity gradients, and elemental abundance patterns across cosmic time, from the early Universe to the present day.

I began with a detailed overview of the origin of elements, including the roles of Big Bang and stellar nucleosynthesis in Chapter 1, briefly summarizing the theory of galaxy formation and evolution

In Chapter 2, I introduced the cosmological simulation framework used in this thesis and described the key physical processes included in our model. This includes star formation, stellar lifetimes, and stellar feedback. I also provided an overview of the nucleosynthesis yield sets adopted in this work for both Population II and Population III stars, detailing the sources and assumptions behind each yield set. A full set is included for the first time in this thesis, and is presented in Chapter 5.

Another major contribution of this work is the implementation and comparison of four feedback models: thermal, stochastic, kinetic, and mechanical. These are integrated into our simulations and tested based on their impact on chemical properties. Mechanical feedback consistently stood out as the most physically realistic model, both in its ability to regulate star formation and in reproducing observed chemical trends. In Chapter 3, we examined the mass-metallicity relation (MZR) of stars and gas, consistently, up to redshift  $z = 5$ . This includes a detailed analysis of the redshift evolution of the MZRs. While kinetic feedback performs reasonably well at  $z > 2$ , we conclude that it is too strong, leading to excessive suppression of star formation and unrealistically low metallicities compared to local observations. Our findings showed that the mechanical feedback model, which incorporates a more detailed and realistic treatment of energy

and momentum transfer, provides the best match overall to local observational data. Our initial expectation was that a model with more realistic physics would yield more reliable results, and indeed the simulations confirmed this: the mechanical feedback model not only reproduced chemical enrichment patterns more accurately but also matched observed scaling relations better than purely thermal feedback. This demonstrates that using more realistic subgrid physics directly enhances the predictive power of cosmological simulations.

Chapter 4 extended the analysis to metallicity gradients within galaxies. Once again, the mechanical model outperformed others, producing realistic radial stellar and gas-phase gradients that evolved consistently with galaxy mass, particularly at  $z = 0$ . These results emphasize that feedback not only regulates how much metal is produced but also how metals are distributed within galaxies. At high redshift, the gas-phase metallicity gradients from the mechanical model in our simulations are in better agreement with observations, although the gradients remain negative across all models.

In Chapter 5 we focus on elemental abundance ratios in the early Universe. Recent findings from the James Webb Space Telescope, including the unexpectedly high nitrogen abundances in galaxies like GN-z11, have required further updates to our nucleosynthesis yields models to better explain these observations. To investigate this, we implemented Population III yields – specifically from rotating Wolf-Rayet (WR) stars and Pair Instability Supernovae (PISNe) – into our simulations. The results presented in this thesis extend up to redshift  $z = 4$ , where the chemical signatures of short-lived Population III stars are expected to persist. The results suggest that rotating WR stars may significantly contribute to the elevated nitrogen and carbon abundances, and may be necessary to provide a plausible explanation for the observed high N/O and C/O ratios (Cameron et al., 2023; D’Eugenio et al., 2024) at high redshift. Our future work will extend the analysis to  $z > 10$  to enable more direct comparisons with enhanced ratios in early galaxies. In addition, the updated C6 yields result in consistently enhanced Ne/O across all metallicities and redshifts, improving agreement with recent local observations. S/O is significantly elevated at low metallicity and low redshift, while Ar/O shows moderate enhancement due to PISNe, making it a potential tracer of rare enrichment events.

Throughout this work, I also examined the roles of stellar lifetimes, cumulative yield functions, and Population III initial mass functions, all of which are critical for modeling the chemical evolution of galaxies. Our results show that even small differences in feedback or yield assumptions can affect simulated chemical properties of galaxies.

In this thesis, I used both the UH High Performance Computing (UHHPC) cluster and the DiRAC HPC facility to run cosmological simulations across a range of volumes and resolutions. I explored how to optimize performance by balancing computational cost, CPU usage, and run time. To support this, I carried out a dedicated performance test, which is presented in Chapter C, comparing the efficiency of different configurations and identifying the most effective setup for

large-scale simulations.

In conclusion, while the original question guiding this thesis was the origin of the first elements, our results make clear that a full understanding of this topic requires an accurate treatment of stellar feedback. By systematically testing feedback models and incorporating early stellar populations, this thesis contributes to bridging simulations with observations in the high-redshift Universe. Future work — outlined in the next section — will help further uncover the chemical history of galaxies from the earliest stars to the present day.

## 6.1 Future work

Future progress in the study of the first chemical elements will depend equally on observational and theoretical advances. On the observational side, JWST has already begun to transform the field by revealing unexpectedly high nitrogen and carbon abundances in galaxies at  $z > 10$  (Cameron et al., 2023; D'Eugenio et al., 2024). Upcoming deep spectroscopic campaigns with JWST will expand the sample of high- $z$  galaxies with reliable metallicity determinations. Future instruments such as MICADO, HARMONI, and MOSAIC on the 39-m Extremely Large Telescope (ELT), equipped with advanced adaptive optics, will provide unprecedented light-collecting power and resolution. Together, these facilities will deliver critical data to test stellar yield models, particularly for Population III stars, and help constrain feedback processes that regulate early star formation. Complementary ground-based efforts, such as 4MOST on ESO/VISTA, MOONS on the VLT, and PFS on Subaru telescope, will provide millions of spectra across billion years of cosmic history, enabling SDSS-like studies at Cosmic Noon and clarifying the role of environment in shaping chemical enrichment. On the theoretical side, simulations face significant challenges: current uncertainties in nucleosynthetic yields (especially from rotating massive stars and PISNe), limited resolution to model turbulent metal mixing, and the computational cost of coupling chemodynamics with radiative transfer. Overcoming these limitations will require a combination of larger-volume simulations, higher-resolution zoom-ins, and hybrid yield prescriptions.

The future study of chemical enrichment from Pop III stars will require progress in both theory and observations. A major theoretical uncertainty lies in how feedback regulates enrichment, directly affect the mixing of metals into the interstellar and intergalactic medium and hence the abundance signatures left behind. Observationally, no genuine low-mass Pop III survivors have yet been identified in stellar archaeology surveys, but expanding samples of extremely metal-poor stars will either confirm or rule out their contribution, placing strong constraints on enrichment channels. At high redshift, detecting Pop III halos directly with JWST is challenging without strong lensing, but Pop III supernovae, although rare, remain one of the most promising probes of their metal yields. Finally, the discovery of gravitational wave events in the pair-instability mass gap may point to dense Pop III clusters where collisions and subsequent enrichment play a role.

Together, these approaches will sharpen constraints on how Pop III stars seeded the first chemical elements in galaxies and shaped the abundance patterns observed at later epochs.

A critical future step will also be to link cosmological enrichment models with the growing body of stellar archaeology data from extremely metal-poor stars in the local Universe.

Based on the findings of this thesis, several directions are planned for future research:

- Incorporate a stronger metallicity dependence in stellar rotation models. Current results show that stellar rotation plays a major role in shaping the yields of nitrogen and carbon from massive stars, but the adopted models lack a detailed treatment of metallicity dependence. Implementing metallicity-sensitive prescriptions for rotation and mass loss will be essential for improving predictions of abundance ratios such as N/O and C/O across different redshifts. This will also allow more accurate comparisons with recent JWST measurements of chemically enriched galaxies at  $z > 6$ .
- The C6 yield set, which includes rotating Wolf–Rayet stars and pair-instability supernovae, has shown promise in explaining the enhanced nitrogen and carbon abundances observed at high redshift. However, in the present thesis these yields were tested independently of the mechanical feedback scheme, which was identified as the most physically realistic feedback model. A natural next step is to couple both approaches, enabling a more self-consistent framework for predicting the joint evolution of metallicity and star formation.
- The current simulations extend to  $z \sim 4\text{--}6$ , but the persistence of Population III signatures is expected at even earlier epochs ( $z > 10$ ). Running larger-volume, higher-redshift simulations will make it possible to capture rare systems such as GN-z11 like galaxies and to provide predictions directly comparable to JWST observations. This will also help assess the relative role of Pop III and Pop II stars in shaping the first abundance ratios.
- The fundamental metallicity relation (FMR) has been well studied in the local Universe, but its behaviour at  $z > 6$  remains poorly constrained. Using the enriched simulation framework developed in this thesis, it will be possible to test how the first generations of massive stars influence the correlation between stellar mass growth, gas accretion, and chemical enrichment.
- Higher-resolution simulations will enable a more accurate investigation of how radial abundance gradients evolve in the early Universe, and how these are affected by feedback and inflows. This will provide a direct theoretical counterpart to spatially resolved spectroscopy of galaxies, soon to be expanded by JWST and ELT observations.

## CHAPTER A

# APPENDIX – MZR

### A.1 Star formation rates

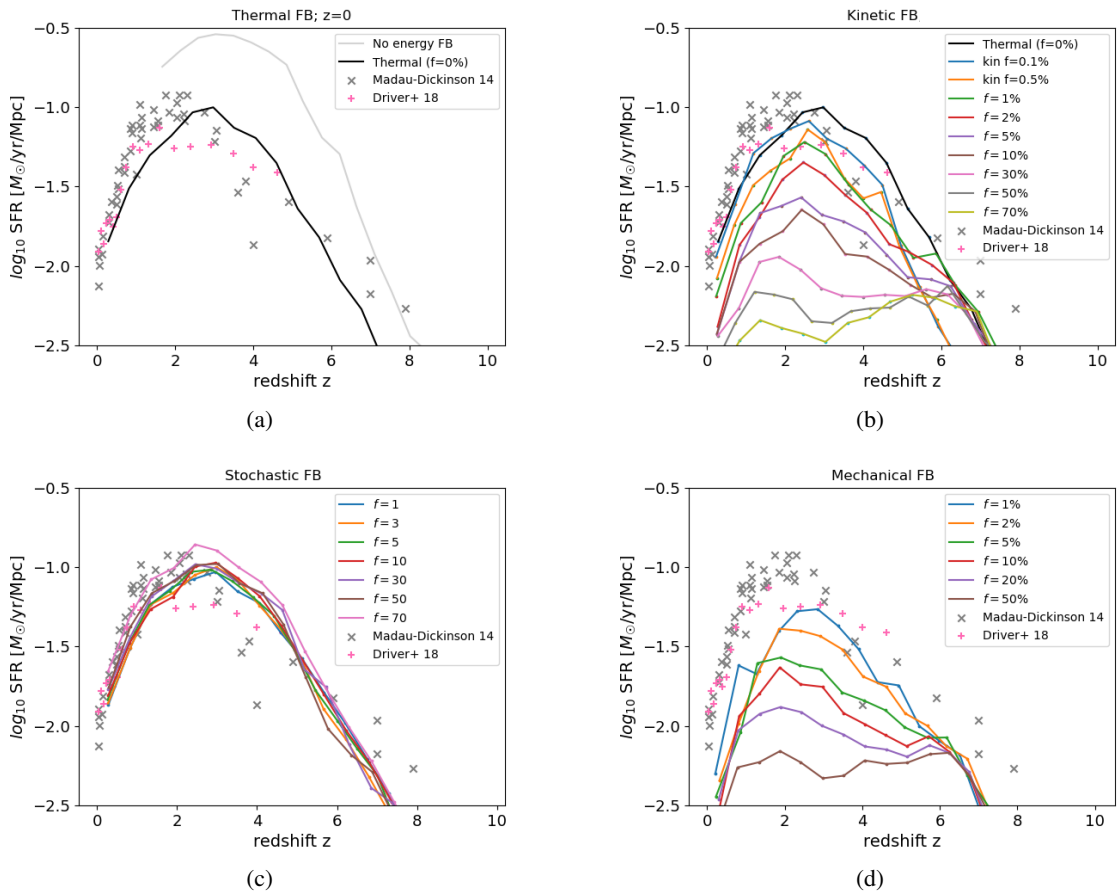


FIGURE A.1: Cosmic SFRs for thermal, kinetic, stochastic and mechanical feedback models in panels (a), (b), (c) and (d) respectively. For each model we explore a wide range of feedback parameter  $f$ . The grey line in panel (a) shows a run where supernova energy feedback is completely switched off (while retaining chemical feedback). The grey cross and magenta plus are observational data taken from [Madau and Dickinson \(2014\)](#) and [Driver et al. \(2018\)](#), respectively, from far UV to mid IR.

The fiducial model parameters were chosen to reproduce the observed cosmic star SFR history. Fig. A.1 shows the SFRs as a function of redshift for different values of the feedback parameter  $f$  as obtained for thermal, kinetic, stochastic and mechanical feedback models, in panels (a),(b), (c), and (d), respectively. For this figure we use a resolution of  $N_{\text{gas}}=N_{\text{DM}}=96^3$ . All curves show a peak in the SFRs at  $z \sim 3$ . The box size in our simulation is limited due to the computation time. As a result, it does not include the formation of very massive galaxies and galaxy clusters at low redshifts. This explains the observed SFR peaks around  $z \sim 2 - 3$ , which are expected to be more consistent with observations for a larger simulation volume. For the kinetic and mechanical models, a larger  $f$  results in a more efficient formation across cosmic time, but not for the stochastic model. The results of our parameter study can be summarised as follows.

- Figure A.1a shows the SFR for the thermal feedback (black line) case ( $f = 0\%$  means pure thermal energy with no kinetic energy) compared with a an additional run where supernova energy feedback is switched off (grey line). For the no-feedback case, we switch off the supernova energy (heating) feedback but keep the chemical feedback so that metallicity maps remain comparable; the run is shown up to  $z = 2$  because the calculation becomes very slow once large numbers of stars form. In this run the SFR is dramatically higher at all redshifts, exceeding observational constraints by more than an order of magnitude at late times, which highlights the crucial role of SN feedback in regulating galaxy growth. In the fiducial thermal feedback case, the SFR increases from  $z \sim 10$  to  $z \sim 3$ , and then decreases towards the present day because: (1) more gas has already turned into stars, (2) stronger supernova feedback suppresses further star formation, and (3) AGN feedback becomes increasingly important.
- Figure A.1b shows the cosmic SFR with the kinetic feedback for different parameter values  $f$ . It shows that at high redshifts, the slope is the same for all parameters, as stars have not formed yet in these simulations. The feedback impact can only be seen after sufficient star formation has occurred, i.e. around redshift  $z = 6$ . At redshift  $z \leq 6$ , star formation is suppressed too much for  $f > 30\%$ . Then, the SFR slightly increases around  $z = 3$ . This wave-shaped SFR history is explained independently of the feedback method by self-regulation: strong feedback suppresses star formation, resulting in less stellar feedback, which will, in return, increase star formation. (starting roughly at  $z \sim 4$  depending on the parameters). For a small parameter  $f < 30\%$ , the SFR increases from  $z \sim 6$  to  $z \sim 2$ , where the feedback starts suppressing star formation. The kinetic model with  $f = 0.1\%$  gives similar results to the thermal feedback. In order to demonstrate the impact of the kinetic part, we choose to use  $f = 1\%$  as our fiducial parameter. Overall, the kinetic feedback in our simulation is too strong and suppresses star formation too much, as even with  $f = 1\%$ , the SFR peak remains too low compared to the observations.

- Figure A.1c shows the cosmic SFR applying the stochastic feedback with different parameter values  $f$ . The SFR is larger for a larger  $f$ . This may be explained using Equation 3.3 where the energy increase  $\Delta e$  is proportional to  $f$ . Thus a large  $f$  results in a large  $\Delta e$ , which yields the right-hand side of Equation 3.4 to be small. Therefore, for a large  $f$ , Equation 3.4 is rarely satisfied. Hence only a small number of particles receive the energy increase and are impacted by the feedback. When the condition is not satisfied, feedback does not impact the gas particles, which do not receive heating energy. The particles keep getting cool by following the cooling function until their temperature reaches  $10^4\text{K}$ . Once the particles are cool, the pressure is lost, the matter collapses toward the cooling particles where the density increases, and then the cooling rate becomes high (i.e. it accelerates the cooling). These features are shown in the star-forming region (low temperature, high density) of the gas-phase space diagram (Fig. 3.4).
- Finally, mechanical feedback SFR is shown in Figure A.1d, where we retrieve a similar behaviour as for the kinetic feedback, but slightly less efficient. We also find that this method is more affected by numerical resolutions than the other models, and have presented higher resolution results only in the previous sections.

For each method, we select the following fiducial parameters:  $f = 1\%$  (kinetic feedback),  $f = 50$  (stochastic feedback), and  $f = 1\%$  (mechanical feedback).

## A.2 Stellar Metallicities

In what follows, we compare the impact of the feedback parameter  $f$  on the stellar MZR at  $z = 0$  for each model.

- The MZR for thermal feedback is shown in Figure A.2a, comparing the luminosity-weighted metallicity (blue) with the mass-weighted metallicity (orange). There is a 0.2dex offset; the luminosity-weighted metallicity is higher because it is weighted for young and metal-rich stars.
- Figure A.2b shows the MZRs using the kinetic feedback model with different parameter values  $f$ . It shows that overall the metallicity is always lower than the observed MZR. The metallicity is lower for stronger kinetic feedback (larger  $f$ ) because a large kinetic velocity ejects more outflows, driving the metal-enriched gas out of the galaxy. As explained above, this difference is more visible in low-mass galaxies.
- Figure A.2c shows the MZRs with the stochastic feedback. At the high-mass end, the MZR is not impacted by the parameter  $f$  and the metallicities are always higher than observed. Lower mass galaxies ( $M < 10^9 M_\odot$ ) have higher metallicities with a larger  $f$ . This agrees

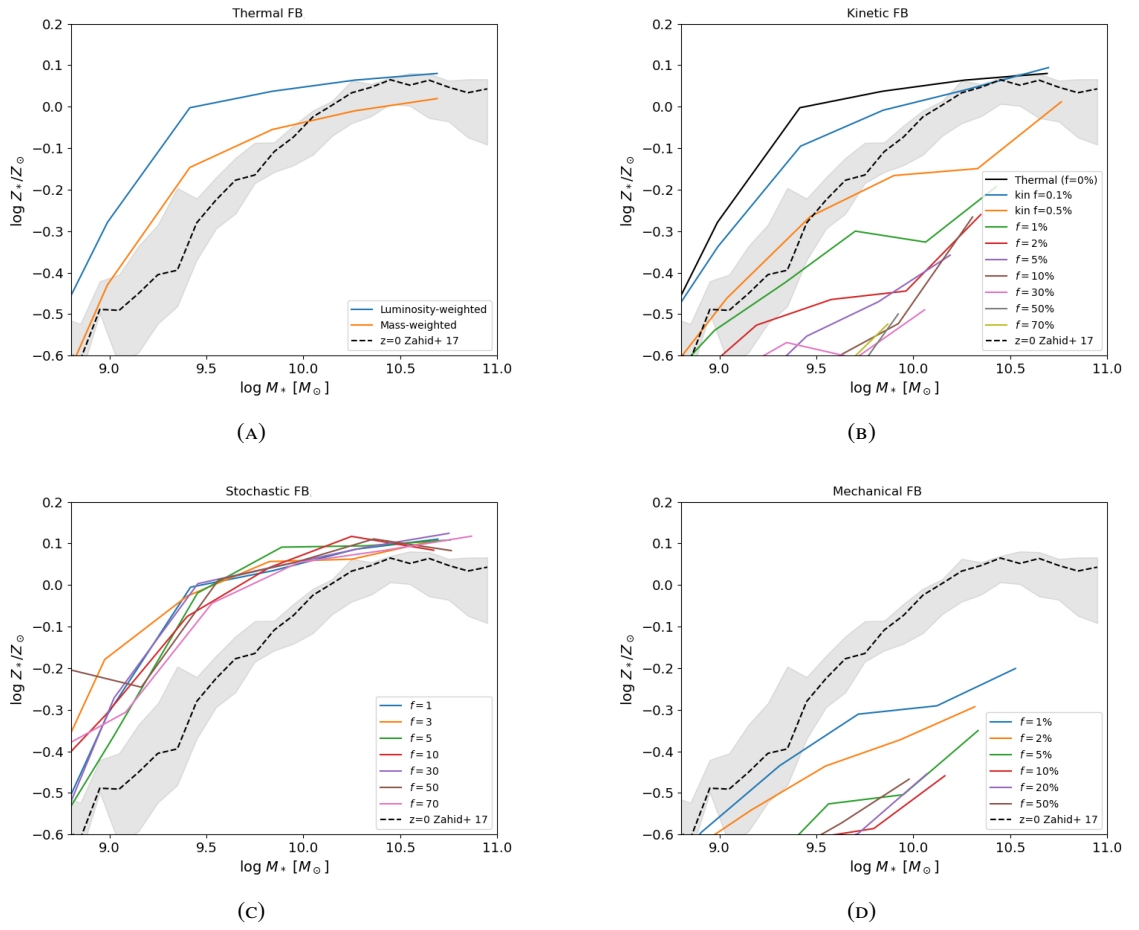


FIGURE A.2: Stellar MZR for thermal, kinetic, stochastic and mechanical feedback models are shown in panels (a), (b), (c) and (d), respectively. For the thermal feedback (panel (a)), we compare luminosity-weighted metallicity (blue) with mass-weighted metallicity (orange). For panels (b), (c) and (d), we explore a wide range of feedback parameters  $f$ , at  $z = 0$ . The black dashed line and shaded are optical observational data taken from [Zahid et al. \(2017\)](#) of star-forming galaxies in the SDSS at  $z = 0$ .

with what is discussed above for the SFR with the stochastic feedback where a larger  $f$  produces more star formation, enhancing the metallicities.

- Finally, the mechanical feedback MZR are shown in Figure A.2d where we retrieve a similar behaviour as for the kinetic feedback. The metallicities are higher for a smaller  $f$ .

### A.3 Age dependence of the stellar MZR

In Section 3.3.5.4, we have shown that young stellar MZR is roughly consistent with gas-phase MZR at  $z = 0$ . Here, we show the MZR dependence on the age-unfolding at various redshifts, which might indicate when the stellar MZR is established.

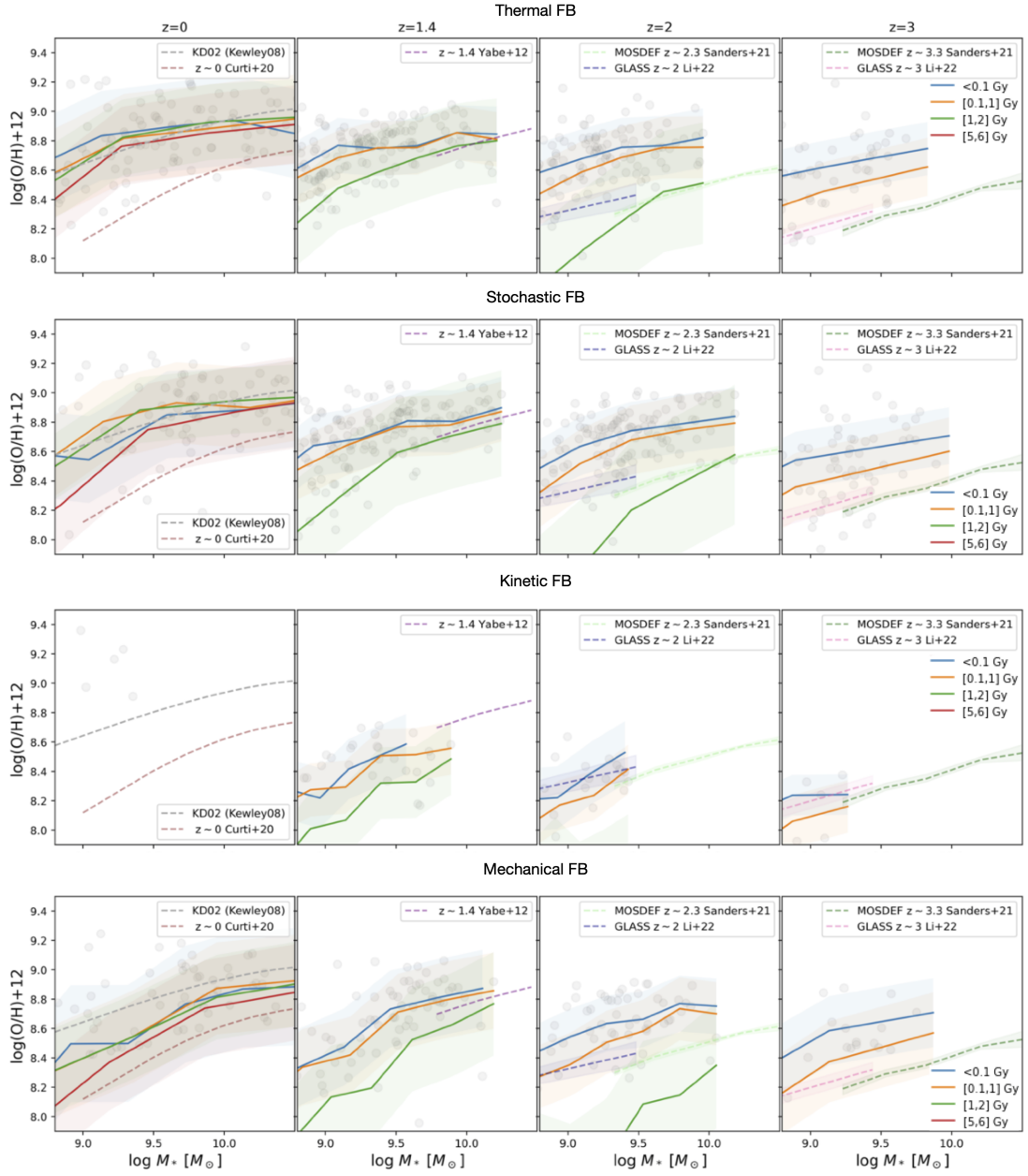


FIGURE A.3: Evolution of luminosity-weighted stellar MZR of galaxies with different ages of star particles:  $< 0.1$  (blue),  $0.1\text{--}1$  (orange),  $1\text{--}2$  (green), and  $5\text{--}6$  Gyr (red), comparing to the gas-phase metallicities of galaxies (grey points). From top panel to bottom, the figure shows thermal, stochastic, kinetic and mechanical feedback models. The solid lines are for medians, and the shaded areas show the  $1\sigma$  scatter. The dashed lines represent the same observational data for the gas-phase MZR as in Fig. 3.11.

Figure A.3 compares the stellar MZR with different stellar ages (ages of star particles) for the four feedback models. A clear time evolution is seen; younger stars tend to have higher metallicities. Stars  $< 0.1$  Gyr (blue line) look less metal-rich than green and orange lines at the massive end because of the small sample. The MZR of stars younger than  $\sim 1$  Gyr are consistent with simulated gas-phase metallicities (grey points) at all redshifts. At  $z \sim 3$ , MZR with 0.1–1 Gyr old stars (orange line) show a similar slope as the other MZR plotted in this figure; these stars have formed around  $z \sim 5$ . At  $z \sim 2$ , MZR with 1–2 Gyr old stars (green line) show significantly lower metallicities with a larger scatter; these stars have formed around  $z \sim 5$ . These might mean that MZR are established at  $z \sim 5$ , which might be consistent with the lack of a clear MZR in the recent JWST observations of  $z \sim 8$  galaxies (Curti et al., 2023). Better statistics would be required to investigate this further.

## CHAPTER B

# APPENDIX – METALLICITY GRADIENTS

---

### B.1 Kinematics

Figure B.1 shows the stellar projection map for the line of sight velocity  $\langle V_z \rangle$  (first column) of galaxy A, the radial velocity  $V_{xy} = \sqrt{\langle V_x \rangle^2 + \langle V_y \rangle^2}$  (second column), the angle  $\phi = \tan^{-1}(\langle V_y \rangle / \langle V_x \rangle)$  (third column) indicating the direction of motion such that  $\phi = 0^\circ$  means pure orbital velocity, while  $\phi = 90^\circ$  means pure radial velocity, and anything in between means the combination of both. And finally, the line-of-sight velocity dispersion  $\sigma_z$  (fourth column). The line of sight velocity  $\langle V_z \rangle$  of stars for Galaxy A is close to zero near the centre,  $V_{xy}$  is radially increasing from the centre and shows a higher velocity toward the north and south poles, and  $\phi$  shows the direction of motion of the particles in the plane and shows no particular rotation for this galaxy. These maps are obtained for galaxies observed through the  $z$  axis of our simulation box, and a sphere of 20 kpc radius is projected on the  $x - y$  plane. We tried a cylindrical selection (circle of 20 kpc radius on the  $xy$  plan with  $\pm 20$  kpc along the  $z$  axis) to mimic observations, but we found no significant difference. In this particular example, the feedback model does not appear to strongly affect the stellar kinematics, though this may reflect the specific mass and gas content of Galaxy A. Although, the stellar velocity dispersion is higher at the centre with the stochastic and mechanical feedback.

Figure B.2 is the same as Figure B.1, but for gas-phase. There is no significant rotation for stars and gas with all feedback models. The different distribution of gas among different feedback models does not affect the kinematics of stars either.

Figures B.3 and B.4 are the same as B.1 and B.2, respectively, but for an intermediate-mass galaxy B. This galaxy is viewed almost face-on, which makes  $\langle V_z \rangle$  close to zero along the disk, and  $V_{xy}$  radially increasing from the centre.  $\phi$  shows the direction of motion of stars and gas particles in the plane, suggesting that this galaxy is rotating. Inside the ring structure of gas, there is a non-rotating stellar core with all feedback models. The velocity maps presented in this appendix are intended as illustrative examples of how stellar and gas kinematics vary across feedback models for two representative galaxies. While these cases provide useful insights into

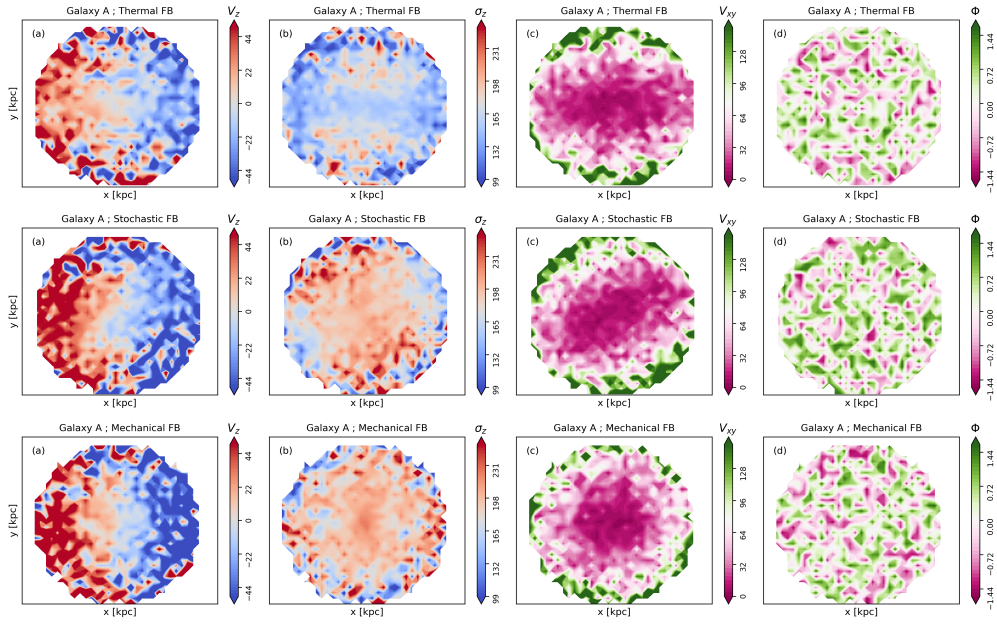


FIGURE B.1: Stellar kinematic maps of a massive galaxy A with the thermal, stochastic, and mechanical feedback simulations in the top, middle, and bottom rows, respectively. Each panel shows a projection along 20 kpc in the x and y axis for a map of the line of sight velocity  $\langle V_z \rangle$  (first column), velocity dispersion  $\sigma_z$  (second column), radial velocity  $V_{xy} = \sqrt{\langle V_x \rangle^2 + \langle V_y \rangle^2}$  (third column), the angle  $\phi = \tan^{-1}(\langle V_y \rangle / \langle V_x \rangle)$  showing the direction of motion in the plane (fourth column).

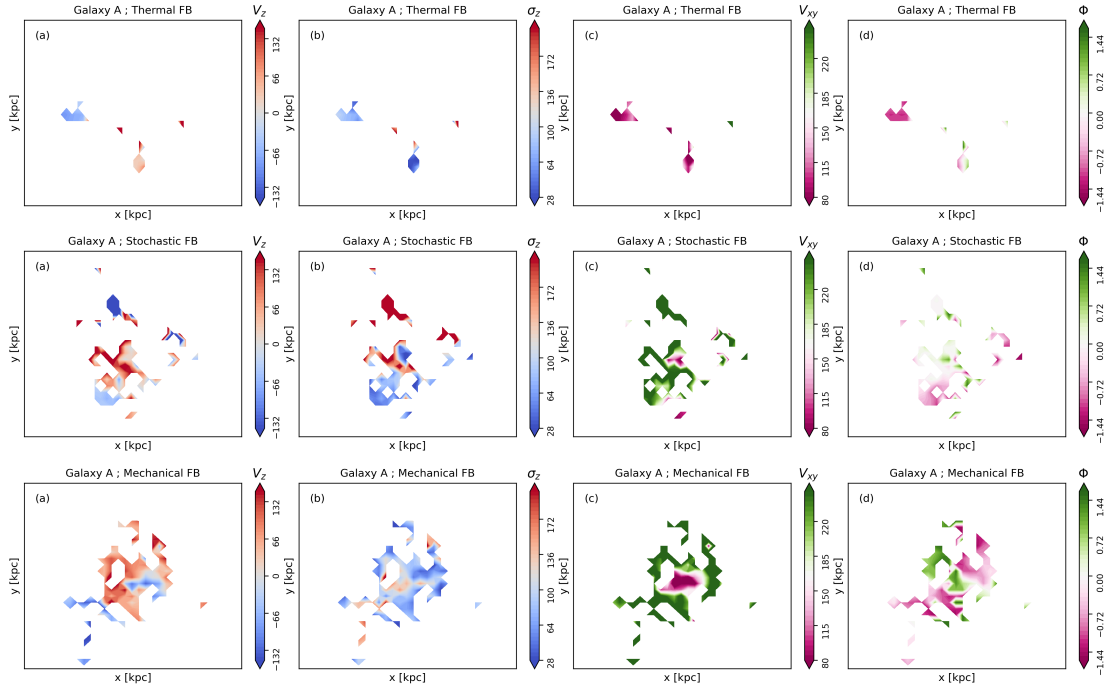


FIGURE B.2: Same as Figure B.1 but for gas kinematic maps of Galaxy A.

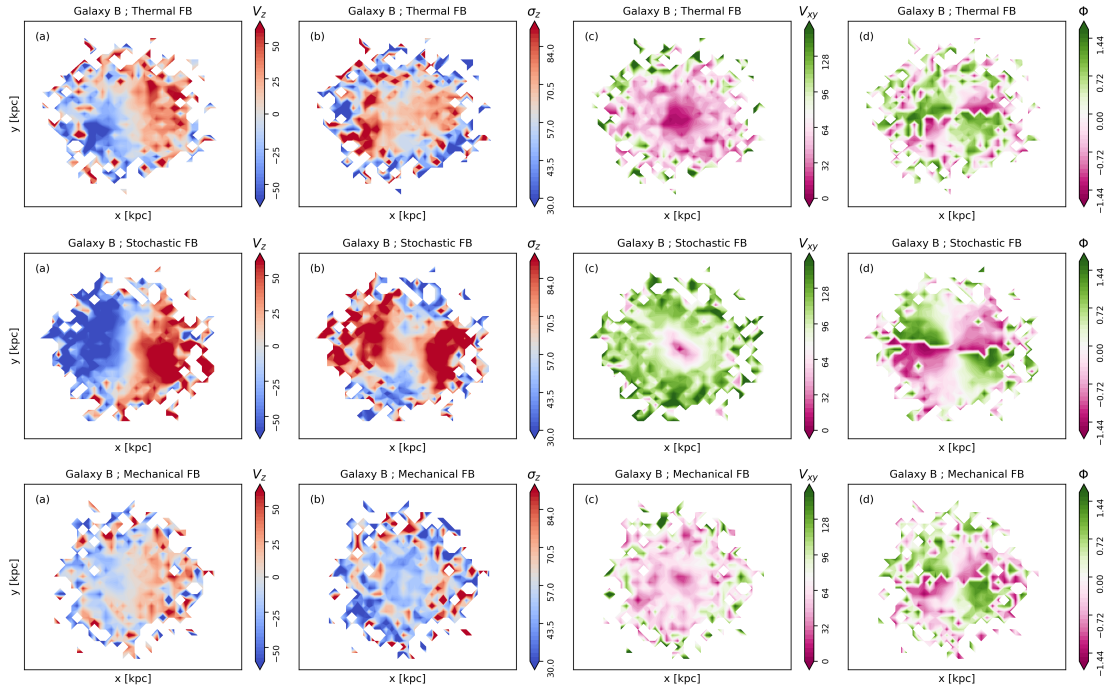


FIGURE B.3: The same stellar kinematic maps as Figure B.1 but for an intermediate-mass galaxy B.

the diversity of kinematic structures in our simulations, they are not intended to draw general conclusions about the relationship between feedback, kinematics, and metallicity gradients based on these two cases alone. In particular, the limited gas content in some feedback models (e.g., mechanical feedback for Galaxy A) reduces the interpretability of the gas velocity fields. A more comprehensive, quantitative analysis of the role of kinematics in shaping metallicity gradients across our full galaxy sample will be explored in future work.

## B.2 Star Formation Main Sequence

All simulations with three different feedback models have a well-defined SFMS and a small number of ETGs below the SFMS. The left panel in Figure B.5 shows the SFMS for the thermal (blue), stochastic (orange), and mechanical (red) feedback models. The points show individual galaxies, and the solid lines are the linear fits of these points. The dashed lines are parallel to the solid lines shifted down by 0.5 dex/kpc, which defines our delimitation for ETGs and LTGs (Section 4.5). The diamond and square symbols represent galaxy A and B, respectively in each model. The right panel in Figure B.5 is the distribution of the perpendicular distances  $\Delta$ SFMS. The grey dashed line shows the division between ETGs/LTGs at  $\Delta$ SFMS =  $-0.5$ . Although the simulation with the stochastic model has a larger number of galaxies, the fraction of ETGs is not so different and is 20, 14, and 12% for thermal, stochastic, and mechanical feedback, respectively.

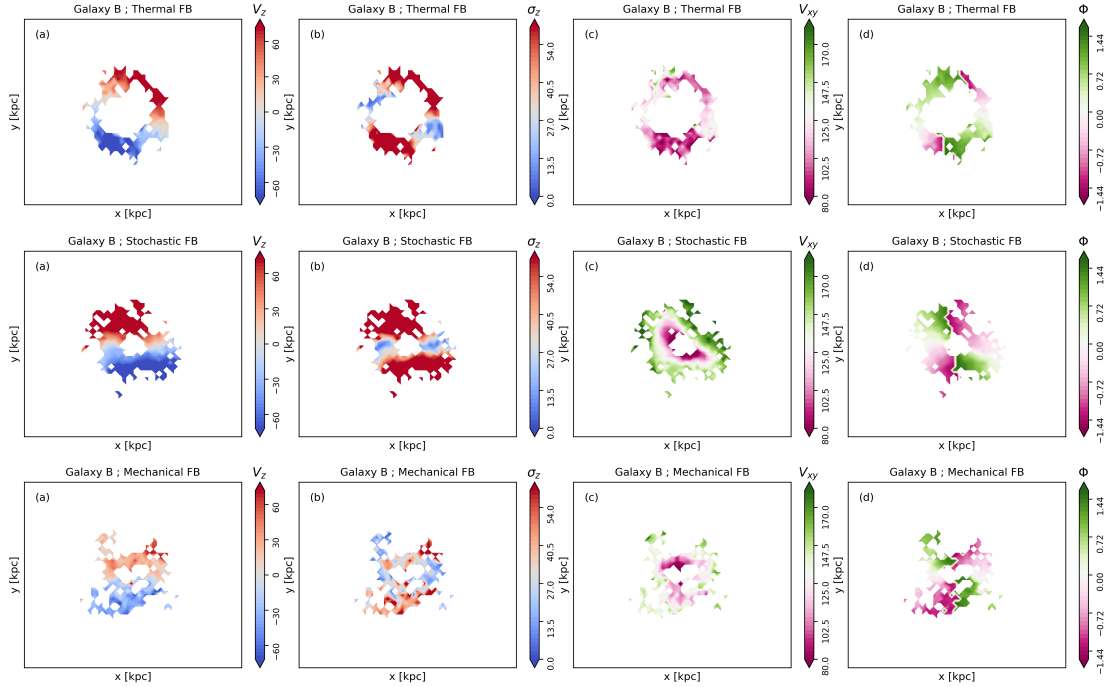


FIGURE B.4: The same gas kinematic maps as Figure B.1 but for Galaxy B.

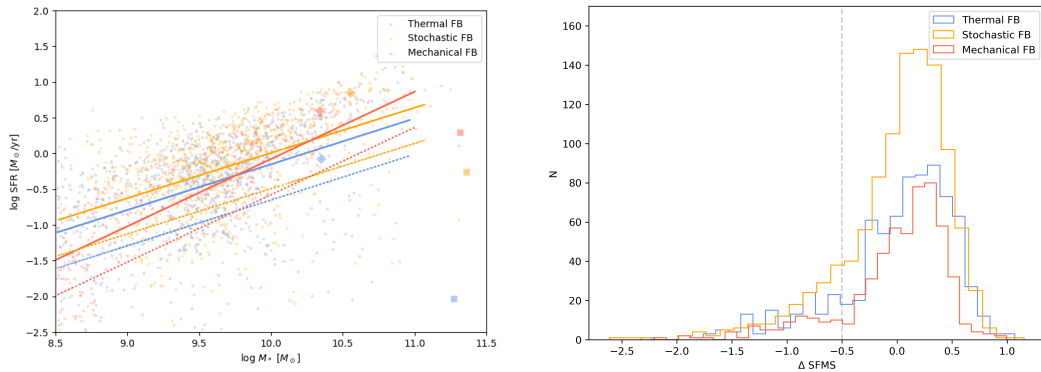


FIGURE B.5: *Left*: SFMS for all galaxies in our simulations with the thermal (blue), stochastic (orange), and mechanical (red) feedback models at  $z = 0.7$ . The solid lines show the best fit to the data. The dotted lines are the perpendicular shift of the solid lines by  $-0.5$  dex. The square and diamond symbols represent galaxy A and B in each model. *Right*: Distribution of the perpendicular distances from the SFMS ( $\Delta$ SFMS) in our simulations with the thermal (blue), stochastic (orange), and mechanical (red) feedback models.

Figure B.6 is similar to Figure 4.8, where we show the stellar (top panels) and gas-phase (bottom panels) metallicity gradients as a function of galaxy stellar mass at  $z = 0.7$ ,  $z = 2$ , and  $z = 4$  (first, second, and third columns, respectively) for our simulation with the thermal feedback. Each symbol is an individual galaxy, and the data is colour-coded by SFMS. The solid lines are the linear fits median of the galaxies with  $\Delta$ SFMS  $\geq -0.5$  (blue line) and  $\Delta$ SFMS  $< 0.5$  (red line). As we have already seen, there is a weak correlation between stellar gradients and mass, where more massive galaxies tend to have flatter gradients. This is also the case if we split our sample into LTGs (blue triangles) and ETGs (red triangles). Overall, ETGs (the red lines) have flatter

gradients than LTGs (blue lines) at all mass ranges and at all redshifts plotted here. The gas-phase metallicity gradients are significantly flatter for ETGs (red), notably at the low mass end with a  $\sim 0.1$  dex/kpc difference. The difference becomes small at  $\log M_*/M_\odot > 10.5$ . The range of gas-phase gradients for ETG is wider at  $z = 2$ , with galaxies reaching 0.3 dex/kpc. This continues at  $z = 4$ , where ETGs seem to have flatter gas-phase gradients than LTGs.

Figure B.7 and B.8 are the same as B.6 with the stochastic and mechanical feedback models, respectively. The stochastic feedback shows that massive ( $\log M_* > 10M_\odot$ ) LTGs have gradients flatter than massive LTGs at all shown redshifts, which is not the case in thermal and mechanical models. The gas-phase metallicity gradient for ETGs at  $z = 2$  becomes much steeper toward low-mass galaxies, which may be due to the ejection of metals from the centre and could be a clear signature to test this feedback model. The galaxy-type dependence of the metallicity gradients with mechanical feedback is, overall, similar to thermal feedback but with a slightly smaller difference between ETGs and LTGs. Overall, at all mass ranges, ETGs tend to show a flatter gradient than LTGs, which is expected and can be explained by the merging history of these galaxies.

### B.3 Tracking individual galaxies

Figure B.9 shows the formation history of Galaxy A from  $z = 5$  (top left panel) to  $z = 0$  (bottom right panel) with the mechanical feedback. Each panel shows the cosmic map with gas particles (orange), star particles (blue), and the central Friends-of-Friends group (black cross).

The galaxy member star particles are selected at  $z = 0$ , and traced using their ID numbers across redshift. Each panel has a physical side length of  $4 \times 3 \text{ Mpc}^2$ . We adopt a fixed centre chosen to include all member particles of Galaxy A at  $z = 0.7$ . All gas particles in the frame are also plotted in the background. The selected descendant is marked with a black cross surrounded by a white circle. This ‘merging tree’ is used for making the metallicity gradient evolution in Figures 4.15 and 4.16.

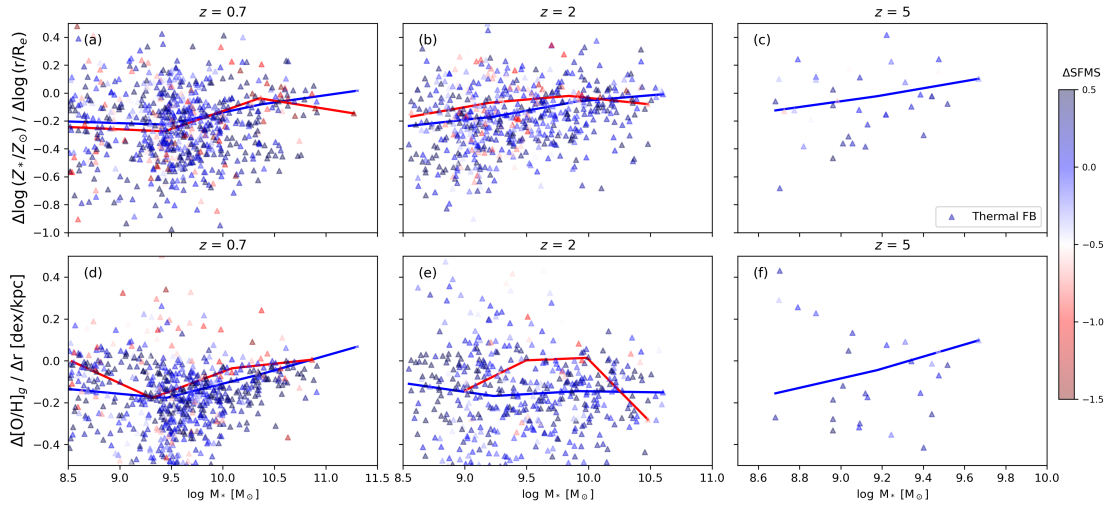


FIGURE B.6: Same as Figure 4.8, but for the thermal feedback only, colour-mapped by  $\Delta \text{SFMS}$  for ETGs (red) and LTGs (blue).

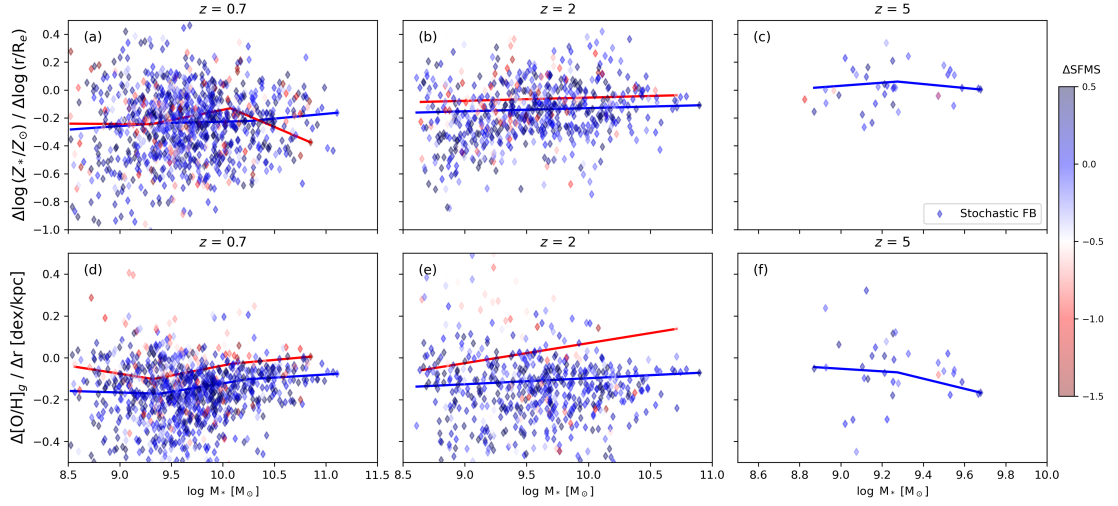


FIGURE B.7: Same as Figure B.6, but for the stochastic feedback.

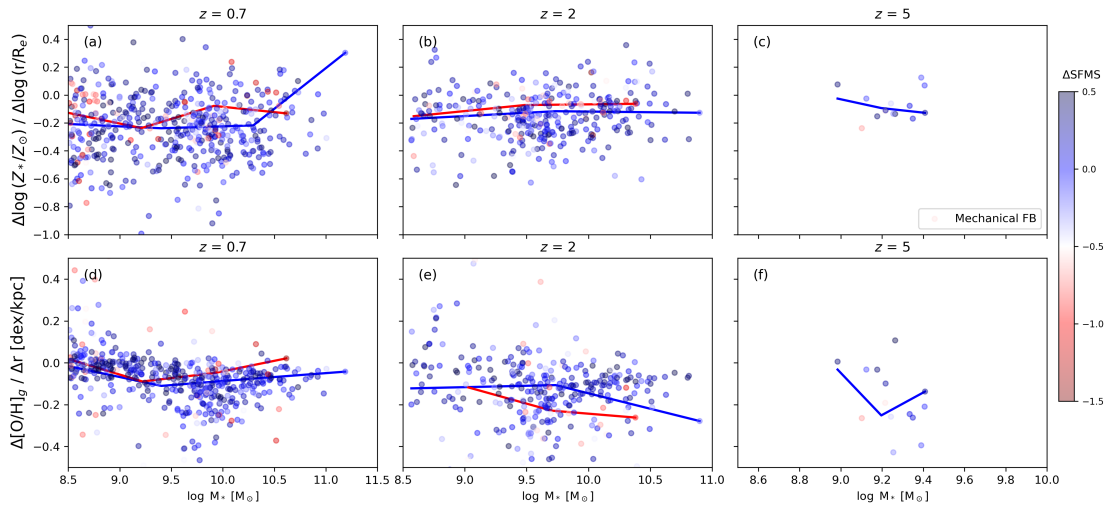


FIGURE B.8: Same as Figure B.6, but for the mechanical feedback.

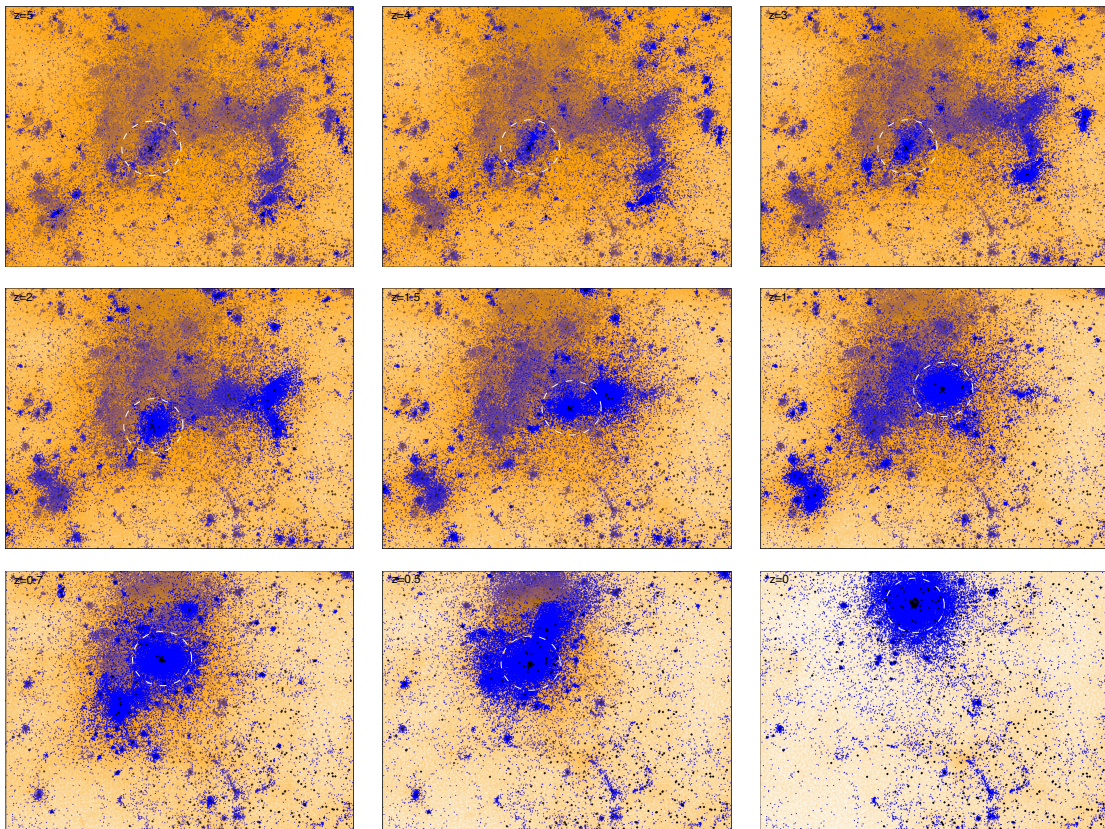


FIGURE B.9: Formation history of Galaxy A across cosmic time with the mechanical feedback. Each panel shows a projected view of the simulation volume in a box of  $4 \times 3 \text{ Mpc}^2$  in side, with gas particles in orange, star particles in blue, and the central Friends-of-Friends group marked with a black cross. The white circle shows the selected descendant of Galaxy A. The panels are ordered chronologically from top left ( $z = 5$ ) to bottom right ( $z = 0$ ).

## CHAPTER C

# APPENDIX – COMPUTATION TIME

This section presents the results of a simple performance test of the simulation using the mechanical feedback model, run on different compute nodes with varying box sizes and resolutions on the UH and DiRAC high-performance computing (HPC) systems.

In all cases, we use the 400th snapshot of each simulation ( $z \sim 9$ ) as the initial condition, and the simulation was run until snapshot 500 ( $z \sim 6$ ). This redshift range was chosen to capture the onset of star formation in the simulations.

Figure C.1 shows the runtime (in minutes) as a function of the number of CPU cores used. Solid lines represent simulations run on UHHPC, while dashed lines represent those run on DiRAC HPC. The pink and green lines correspond to the 10mpc96 and 10mpc128 simulations, respectively, indicating different resolutions within a 10 Mpc box.

As expected, simulations with higher resolution (i.e., more particles) require more computation

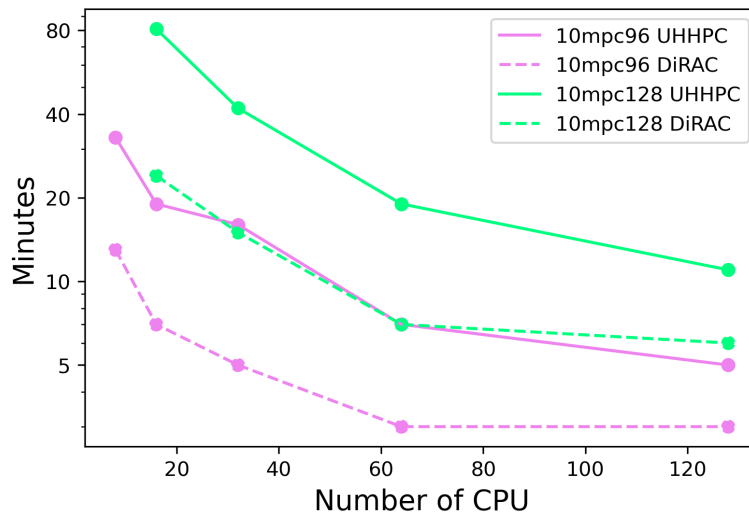


FIGURE C.1: Time taken (in minutes) to complete simulation runs as a function of the number of CPU cores, for different box sizes and resolutions on UHHPC (solid lines) and DiRAC HPC (dashed lines) systems. The 10mpc96 and 10mpc128 labels indicate the simulation box size (10 Mpc) and grid resolution ( $96^3$  and  $128^3$  particles, respectively).

time for a given number of cores. Additionally, runs on UHHPC nodes generally take longer than equivalent runs on DiRAC HPC, highlighting the differences in hardware and performance between the two systems.

## C.1 Resolution convergence tests

To test the numerical convergence of our simulations, we carried out resolution studies using 10 Mpc boxes run at three different particle resolutions ( $96^3$ ,  $128^3$ , and  $192^3$ ). The left panel of Figure C.2 shows the cosmic star-formation history. All runs broadly reproduce the observed shape and normalization of the SFR (Madau and Dickinson, 2014; Driver et al., 2018), with differences between the  $128^3$  and  $192^3$  runs remaining within  $\sim 0.1$  dex over most of cosmic time. At  $z \sim 7-8$ , the higher-resolution runs are able to resolve more small-scale star-forming clumps, which leads to an enhanced SFR. However, the two highest-resolution runs (cyan and green) converge after  $z < 2$ , resulting in a similar present-day MZR (right panel). By contrast, the lowest-resolution run ( $96^3$ ; magenta) underpredicts the SFR density at  $z \sim 2-3$  and does not converge, indicating that the 10 Mpc  $96^3$  run is insufficient for this analysis, while the 10 Mpc  $128^3$  run provides a reasonable compromise.

The right panel of Figure C.2 shows the luminosity-weighted stellar MZR at  $z = 0$ . Here again, the  $128^3$  and  $192^3$  runs are in good agreement with each other and with the observed relation (Zahid et al., 2017), differing by less than 0.05 dex over the mass range  $\log M_\star/M_\odot \gtrsim 9.5$ . The  $96^3$  run, however, systematically underpredicts metallicities by  $\sim 0.2-0.3$  dex, highlighting the need for sufficient resolution to capture enrichment and recycling processes in low-mass galaxies. Overall, these tests confirm that the key results presented in this thesis are not driven by numerical resolution effects.

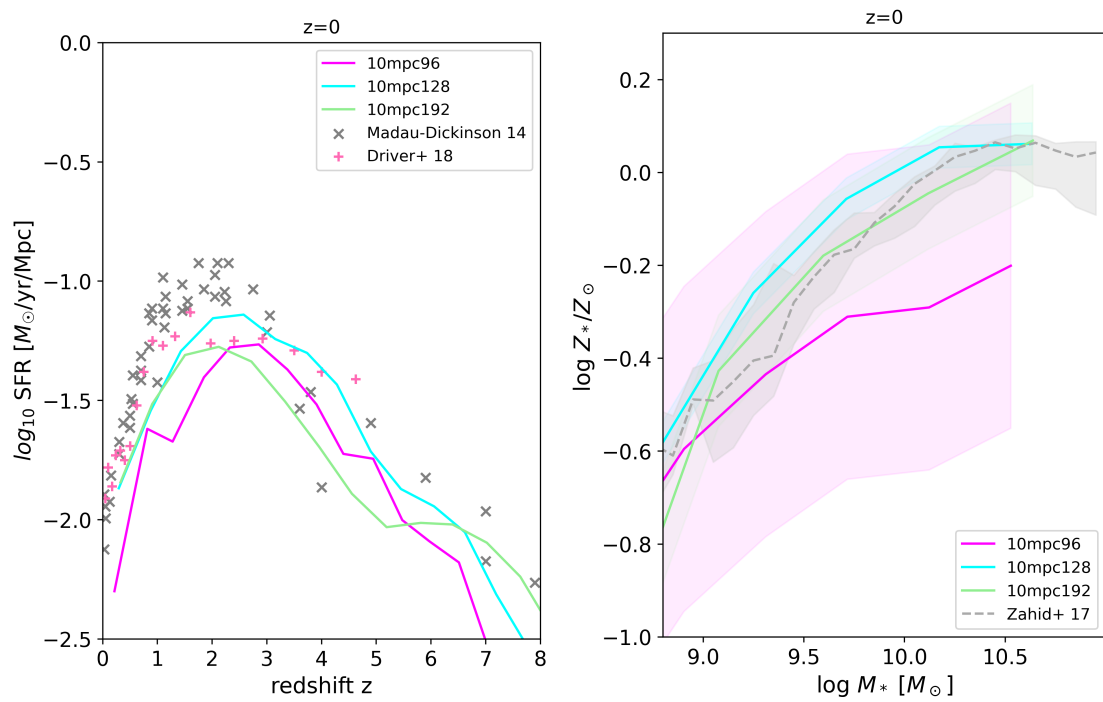


FIGURE C.2: Resolution convergence tests. **Left:** Cosmic star-formation history for 10 Mpc boxes at three resolutions ( $96^3$ ,  $128^3$ , and  $192^3$ ) compared with observational compilations (Madau and Dickinson, 2014; Driver et al., 2018). **Right:** Stellar mass–metallicity relation for the same runs at  $z = 0$ , compared with Zahid et al. (2017).

# BIBLIOGRAPHY

---

- Abel, T., Bryan, G.L., and Norman, M.L., 2000. The Formation and Fragmentation of Primordial Molecular Clouds. *ApJ*, 540(1):39.
- Abel, T., Bryan, G.L., and Norman, M.L., 2002. The Formation of the First Star in the Universe. *Science*, 295(5552):93.
- Acharyya, A., Peeples, M.S., Tumlinson, J., et al., 2025. Figuring Out Gas and Galaxies In Enzo (FOGGIE). VIII. Complex and Stochastic Metallicity Gradients at  $z > 2$ . *ApJ*, 979(2):129.
- Agertz, O., Moore, B., Stadel, J., et al., 2007. Fundamental differences between SPH and grid methods. *MNRAS*, 380(3):963.
- Alpher, R.A., Bethe, H., and Gamow, G., 1948. The Origin of Chemical Elements. *Physical Review*, 73(7):803.
- Angulo, R.E., Springel, V., White, S.D.M., et al., 2012. Scaling relations for galaxy clusters in the Millennium-XXL simulation. *MNRAS*, 426(3):2046.
- Arellano-Córdova, K.Z., Berg, D.A., Mingozzi, M., et al., 2024. CLASSY. IX. The Chemical Evolution of the Ne, S, Cl, and Ar Elements. *ApJ*, 968(2):98.
- Asplund, M., Grevesse, N., Sauval, A.J., et al., 2009. The Chemical Composition of the Sun. *Annual Review of Astronomy and Astrophysics*, 47(1):481.
- Baade, W., 1944. The Resolution of Messier 32, NGC 205, and the Central Region of the Andromeda Nebula. *ApJ*, 100:137.
- Bacon, R., Accardo, M., Adjali, L., et al., 2010. The MUSE second-generation VLT instrument. In I.S. McLean, S.K. Ramsay, and H. Takami, editors, *Ground-based and Airborne Instrumentation for Astronomy III*, volume 7735 of *Society of Photo-Optical Instrumentation Engineers (SPIE) Conference Series*, page 773508.
- Bagla, J., 2002. Treepm: A code for cosmological n-body simulations. *Journal of Astrophysics and Astronomy*, 23:185.

- Bahcall, J.N., Pinsonneault, M.H., and Wasserburg, G.J., 1995. Solar models with helium and heavy-element diffusion. *Reviews of Modern Physics*, 67(4):781.
- Baldry, I.K., Driver, S.P., Loveday, J., et al., 2012. Galaxy And Mass Assembly (GAMA): the galaxy stellar mass function at  $z < 0.06$ . *MNRAS*, 421(1):621.
- Barkat, Z., Rakavy, G., and Sack, N., 1967. Dynamics of Supernova Explosion Resulting from Pair Formation. *Physical Review Letters*, 18(10):379.
- Behling, T., Hazlett, R., Kulkarni, M., et al., 2025. Evaluating the Accuracy of Reionization Prescriptions in Semi-analytic Models of the First Stars and Galaxies. *arXiv e-prints*, arXiv:2508.04808.
- Belfiore, F., Maiolino, R., and Bothwell, M., 2016. Galaxy gas flows inferred from a detailed, spatially resolved metal budget. *MNRAS*, 455(2):1218.
- Belfiore, F., Maiolino, R., Tremonti, C., et al., 2017. SDSS IV MaNGA - metallicity and nitrogen abundance gradients in local galaxies. *MNRAS*, 469(1):151.
- Belfiore, F., Vincenzo, F., Maiolino, R., et al., 2019. From ‘bathtub’ galaxy evolution models to metallicity gradients. *MNRAS*, 487(1):456.
- Berg, D.A., Skillman, E.D., Croxall, K.V., et al., 2015. CHAOS I. Direct Chemical Abundances for H II Regions in NGC 628. *ApJ*, 806(1):16.
- Bhattacharya, S., Arnaboldi, M., Gerhard, O., et al., 2024. Unveiling galaxy chemical enrichment mechanisms out to cosmic dawn from direct determination of O & Ar abundances from JWST/NIRSPEC spectroscopy. *arXiv e-prints*, arXiv:2408.13396.
- Bland-Hawthorn, J., 2015. The Hector Survey: integral field spectroscopy of 100,000 galaxies. In B.L. Ziegler, F. Combes, H. Dannerbauer, and M. Verdugo, editors, *Galaxies in 3D across the Universe*, volume 309 of *IAU Symposium*, pages 21–28.
- Bond, H.E., 1981. Where is population III ? *ApJ*, 248:606.
- Boylan-Kolchin, M., Springel, V., White, S.D.M., et al., 2009. Resolving cosmic structure formation with the Millennium-II Simulation. *MNRAS*, 398(3):1150.
- Bresolin, F., 2011. The Abundance Scatter in M33 from H II Regions: Is There Any Evidence for Azimuthal Metallicity Variations? *ApJ*, 730(2):129.
- Bresolin, F., Kennicutt, R.C., and Ryan-Weber, E., 2012. Gas Metallicities in the Extended Disks of NGC 1512 and NGC 3621. Chemical Signatures of Metal Mixing or Enriched Gas Accretion? *ApJ*, 750(2):122.

- Bromm, V., Coppi, P.S., and Larson, R.B., 1999. Forming the First Stars in the Universe: The Fragmentation of Primordial Gas. *ApJ*, 527(1):L5.
- Bromm, V. and Larson, R.B., 2004. The First Stars. *Annual Review of Astronomy and Astrophysics*, 42(1):79.
- Bromm, V. and Yoshida, N., 2011. The First Galaxies. *Annual Review of Astronomy and Astrophysics*, 49(1):373.
- Bundy, K., Bershady, M.A., Law, D.R., et al., 2015. Overview of the SDSS-IV MaNGA Survey: Mapping nearby Galaxies at Apache Point Observatory. *ApJ*, 798(1):7.
- Bunker, A.J. et al., 2023. . *A&A*, 677:A88.
- Burbidge, E.M., Burbidge, G.R., Fowler, W.A., et al., 1957. Synthesis of the Elements in Stars. *Reviews of Modern Physics*, 29(4):547.
- Cameron, A.G.W., 1957. Nuclear Reactions in Stars and Nucleogenesis. *PASP*, 69(408):201.
- Cameron, A.G.W., 2001. Some Properties of r-Process Accretion Disks and Jets. *ApJ*, 562(1):456.
- Cameron, A.J., Katz, H., Rey, M.P., et al., 2023. Nitrogen enhancements 440 Myr after the big bang: supersolar N/O, a tidal disruption event, or a dense stellar cluster in GN-z11? *MNRAS*, 523(3):3516.
- Campbell, S.W. and Lattanzio, J.C., 2008. Evolution and nucleosynthesis of extremely metal-poor and metal-free low- and intermediate-mass stars. I. Stellar yield tables and the CEMPs. *A&A*, 490(2):769.
- Carnall, A.C., McLure, R.J., Dunlop, J.S., et al., 2023. A massive quiescent galaxy at redshift 4.658. *Nature*, 619(7971):716.
- Carr, B.J. and Hawking, S.W., 1974. Black holes in the early Universe. *MNRAS*, 168:399.
- Carton, D., Brinchmann, J., Contini, T., et al., 2018. First gas-phase metallicity gradients of  $0.1 \lesssim z \lesssim 0.8$  galaxies with MUSE. *MNRAS*, 478(4):4293.
- Castellano, M., Napolitano, L., Fontana, A., et al., 2024a. JWST NIRSpec Spectroscopy of the Remarkable Bright Galaxy GHZ2/GLASS-z12 at Redshift 12.34. *ApJ*, 972(2):143.
- Castellano, M. et al., 2024b. . *ApJ*, 972(2):143.
- Cen, R. and Ostriker, J.P., 1999. Where Are the Baryons? *ApJ*, 514(1):1.
- Chaikin, E., Schaye, J., Schaller, M., et al., 2022. The importance of the way in which supernova energy is distributed around young stellar populations in simulations of galaxies. *MNRAS*, 514(1):249.

- Charbonnel, C. et al., 2023. . *A&A*, 673:L7.
- Chiappini, C., Matteucci, F., and Romano, D., 2001. Abundance Gradients and the Formation of the Milky Way. *ApJ*, 554(2):1044.
- Chiappini, C. et al., 2006. . *A&A*, 449(2):L27.
- Clarke, L., Shapley, A.E., Sanders, R.L., et al., 2024. The Star-forming Main Sequence in JADES and CEERS at  $z > 1.4$ : Investigating the Burstiness of Star Formation. *ApJ*, 977(1):133.
- Coc, A., Uzan, J.P., and Vangioni, E., 2013. Standard Big-Bang Nucleosynthesis after Planck. *arXiv e-prints*, arXiv:1307.6955.
- Cole, S., Aragon-Salamanca, A., Frenk, C.S., et al., 1994. A recipe for galaxy formation. *MNRAS*, 271:781.
- Conroy, C., 2013. Modeling the Panchromatic Spectral Energy Distributions of Galaxies. *Annual Review of Astronomy and Astrophysics*, 51(1):393.
- Copi, C.J., Schramm, D.N., and Turner, M.S., 1995. Big-Bang Nucleosynthesis and the Baryon Density of the Universe. *Science*, 267(5195):192.
- Costa, T., Sijacki, D., and Haehnelt, M.G., 2015. Fast cold gas in hot AGN outflows. *MNRAS*, 448:L30.
- Crain, R.A., Schaye, J., Bower, R.G., et al., 2015. The EAGLE simulations of galaxy formation: calibration of subgrid physics and model variations. *MNRAS*, 450(2):1937.
- Cresci, G., Mannucci, F., Maiolino, R., et al., 2010. Gas accretion as the origin of chemical abundance gradients in distant galaxies. *Nature*, 467(7317):811.
- Cullen, F., McLure, R.J., Dunlop, J.S., et al., 2019. The VANDELS survey: the stellar metallicities of star-forming galaxies at  $2.5 < z < 5.0$ . *MNRAS*, 487(2):2038.
- Curti, M., D'Eugenio, F., Carniani, S., et al., 2023. The chemical enrichment in the early Universe as probed by JWST via direct metallicity measurements at  $z \approx 8$ . *MNRAS*, 518(1):425.
- Curti, M., Maiolino, R., Cirasuolo, M., et al., 2020a. The KLEVER Survey: spatially resolved metallicity maps and gradients in a sample of  $1.2 < z < 2.5$  lensed galaxies. *MNRAS*, 492(1):821.
- Curti, M., Mannucci, F., Cresci, G., et al., 2020b. The mass-metallicity and the fundamental metallicity relation revisited on a fully  $T_e$ -based abundance scale for galaxies. *MNRAS*, 491(1):944.
- Curti, M., Witstok, J., Jakobsen, P., et al., 2024a. JADES: The star-formation and chemical enrichment history of a luminous galaxy at  $z \approx 9.43$  probed by ultra-deep JWST/NIRSpec spectroscopy. *arXiv e-prints*, arXiv:2407.02575.

- Curti, M. et al., 2024b. . *Astronomy and Astrophysics*, 684:A75.
- Curtis-Lake, E., Carniani, S., Cameron, A., et al., 2023. Spectroscopic confirmation of four metal-poor galaxies at  $z = 10.3$ - $13.2$ . *Nature Astronomy*, 7:622.
- Dalla Vecchia, C. and Schaye, J., 2012. Simulating galactic outflows with thermal supernova feedback. *MNRAS*, 426(1):140.
- Damian, B., Jose, J., Samal, M.R., et al., 2021. Testing the role of environmental effects on the initial mass function of low-mass stars. *MNRAS*, 504(2):2557.
- Davé, R., Anglés-Alcázar, D., Narayanan, D., et al., 2019. SIMBA: Cosmological simulations with black hole growth and feedback. *MNRAS*, 486(2):2827.
- Davé, R., Cen, R., Ostriker, J.P., et al., 2001. Baryons in the Warm-Hot Intergalactic Medium. *ApJ*, 552(2):473.
- Davé, R., Finlator, K., and Oppenheimer, B.D., 2011. Galaxy evolution in cosmological simulations with outflows - II. Metallicities and gas fractions. *MNRAS*, 416(2):1354.
- Davé, R., Rafieferantsoa, M.H., Thompson, R.J., et al., 2017. MUFASA: Galaxy star formation, gas, and metal properties across cosmic time. *MNRAS*, 467(1):115.
- Davé, R., Thompson, R., and Hopkins, P.F., 2016. MUFASA: galaxy formation simulations with meshless hydrodynamics. *MNRAS*, 462(3):3265.
- Davies, R.L., Sadler, E.M., and Peletier, R.F., 1993. Line-strength gradients in elliptical galaxies. *MNRAS*, 262:650.
- De Lucia, G., Poggianti, B.M., Aragón-Salamanca, A., et al., 2004. The Buildup of the Red Sequence in Galaxy Clusters since  $z \sim 0.8$ . *ApJ*, 610(2):L77.
- De Rossi, M.E., Bower, R.G., Font, A.S., et al., 2017. Galaxy metallicity scaling relations in the EAGLE simulations. *MNRAS*, 472(3):3354.
- Dekel, A. and Silk, J., 1986. The Origin of Dwarf Galaxies, Cold Dark Matter, and Biased Galaxy Formation. *ApJ*, 303:39.
- D'Eugenio, F. et al., 2024. . *A&A*, 689:A152.
- Doherty, C.L., Gil-Pons, P., Lau, H.H.B., et al., 2014. Super and massive AGB stars - II. Nucleosynthesis and yields -  $Z = 0.02, 0.008$  and  $0.004$ . *MNRAS*, 437(1):195.
- Donnan, C.T., McLeod, D.J., Dunlop, J.S., et al., 2023. The evolution of the galaxy UV luminosity function at redshifts  $z = 8 - 15$  from deep JWST and ground-based near-infrared imaging. *MNRAS*, 518(4):6011.

- Dopita, M.A. et al., 2016. . *Astrophysics and Space Science*, 361:61.
- Driver, S.P., Andrews, S.K., da Cunha, E., et al., 2018. GAMA/G10-COSMOS/3D-HST: the  $0 < z < 5$  cosmic star formation history, stellar-mass, and dust-mass densities. *MNRAS*, 475(3):2891.
- Dubois, Y., Peirani, S., Pichon, C., et al., 2016. The Horizon-AGN simulation: morphological diversity of galaxies promoted by AGN feedback. *Monthly Notices of the Royal Astronomical Society*, 463(4):3948.
- Dubois, Y., Pichon, C., Welker, C., et al., 2014. Dancing in the dark: galactic properties trace spin swings along the cosmic web. *MNRAS*, 444(2):1453.
- Estrada-Carpenter, V., Papovich, C., Momcheva, I., et al., 2019. CLEAR. I. Ages and Metallicities of Quiescent Galaxies at  $1.0 < z < 1.8$  Derived from Deep Hubble Space Telescope Grism Data. *ApJ*, 870(2):133.
- Fanidakis, N., Baugh, C.M., Benson, A.J., et al., 2011. Grand unification of AGN activity in the  $\Lambda$ CDM cosmology. *MNRAS*, 410(1):53.
- Ferlito, F., Springel, V., Davies, C.T., et al., 2023. The MillenniumTNG Project: the impact of baryons and massive neutrinos on high-resolution weak gravitational lensing convergence maps. *MNRAS*, 524(4):5591.
- Finkelstein, S.L., Bagley, M., Song, M., et al., 2022. A Census of the Bright  $z = 8.5$ -11 Universe with the Hubble and Spitzer Space Telescopes in the CANDELS Fields. *ApJ*, 928(1):52.
- Finkelstein, S.L., Papovich, C., Ryan, R.E., et al., 2012. CANDELS: The Contribution of the Observed Galaxy Population to Cosmic Reionization. *ApJ*, 758(2):93.
- Finlator, K. and Davé, R., 2008. The origin of the galaxy mass-metallicity relation and implications for galactic outflows. *MNRAS*, 385(4):2181.
- Förster Schreiber, N.M., Renzini, A., Mancini, C., et al., 2018. The SINS/zC-SINF Survey of  $z \sim 2$  Galaxy Kinematics: SINFONI Adaptive Optics-assisted Data and Kiloparsec-scale Emission-line Properties. *ApJ*, 238(2):21.
- Frenk, C.S., White, S.D.M., Bode, P., et al., 1999. The Santa Barbara Cluster Comparison Project: A Comparison of Cosmological Hydrodynamics Solutions. *ApJ*, 525(2):554.
- Fu, J., Kauffmann, G., Huang, M.I., et al., 2013. Star formation and metallicity gradients in semi-analytic models of disc galaxy formation. *MNRAS*, 434(2):1531.
- Fukushima, H. and Yajima, H., 2024. Impacts of stellar wind and supernovae on star cluster formation: Origins of extremely high N/O ratios and multiple stellar populations. *Publications of the Astronomical Society of Japan*, 76(5):1122.

- Furlanetto, S.R., Oh, S.P., and Briggs, F.H., 2006. Cosmology at low frequencies: The 21 cm transition and the high-redshift Universe. *Physics Reports*, 433(4-6):181.
- Gallazzi, A., Bell, E.F., Zibetti, S., et al., 2014. Charting the Evolution of the Ages and Metallicities of Massive Galaxies since  $z = 0.7$ . *ApJ*, 788(1):72.
- Gallazzi, A., Charlot, S., Brinchmann, J., et al., 2005. The ages and metallicities of galaxies in the local universe. *MNRAS*, 362(1):41.
- Gallazzi, A., Charlot, S., Brinchmann, J., et al., 2006. Ages and metallicities of early-type galaxies in the Sloan Digital Sky Survey: new insight into the physical origin of the colour-magnitude and the  $Mg_2 - \sigma_V$  relations. *MNRAS*, 370(3):1106.
- Garcia, A.M., Torrey, P., Bhagwat, A., et al., 2025. Metallicity Gradients in Modern Cosmological Simulations I: Tension Between Smooth Stellar Feedback Models and Observations. *arXiv e-prints*, arXiv:2503.03804.
- Garcia, A.M., Torrey, P., Hemler, Z.S., et al., 2023. Gas-phase metallicity break radii of star-forming galaxies in IllustrisTNG. *MNRAS*, 519(3):4716.
- Genel, S., Vogelsberger, M., Springel, V., et al., 2014. Introducing the Illustris project: the evolution of galaxy populations across cosmic time. *MNRAS*, 445(1):175.
- Gentry, E.S., Krumholz, M.R., Dekel, A., et al., 2017. Enhanced momentum feedback from clustered supernovae. *MNRAS*, 465(2):2471.
- Gibson, B.K., Pilkington, K., Brook, C.B., et al., 2013. Constraining sub-grid physics with high-redshift spatially-resolved metallicity distributions. *A&A*, 554:A47.
- Gingold, R.A. and Monaghan, J.J., 1977. Smoothed particle hydrodynamics: theory and application to non-spherical stars. *MNRAS*, 181:375.
- Goddard, D., Thomas, D., Maraston, C., et al., 2017. SDSS-IV MaNGA: Spatially resolved star formation histories in galaxies as a function of galaxy mass and type. *MNRAS*, 466(4):4731.
- González Delgado, R.M., García-Benito, R., Pérez, E., et al., 2015. The CALIFA survey across the Hubble sequence. Spatially resolved stellar population properties in galaxies. *A&A*, 581:A103.
- Grazian, A., Fontana, A., Santini, P., et al., 2015. The galaxy stellar mass function at  $3.5 \leq z \leq 7.5$  in the CANDELS/UDS, GOODS-South, and HUDF fields. *A&A*, 575:A96.
- Greif, T.H., Springel, V., White, S.D.M., et al., 2011. Simulations on a Moving Mesh: The Clustered Formation of Population III Protostars. *ApJ*, 737(2):75.
- Guo, Y., Koo, D.C., Lu, Y., et al., 2016. Stellar Mass-Gas-phase Metallicity Relation at  $0.5 \leq z \leq 0.7$ : A Power Law with Increasing Scatter toward the Low-mass Regime. *ApJ*, 822(2):103.

- Haardt, F. and Madau, P., 1996. Radiative Transfer in a Clumpy Universe. II. The Ultraviolet Extragalactic Background. *ApJ*, 461:20.
- Heger, A. and Woosley, S.E., 2002. The Nucleosynthetic Signature of Population III. *ApJ*, 567(1):532.
- Hemler, Z.S., Torrey, P., Qi, J., et al., 2021. Gas-phase metallicity gradients of TNG50 star-forming galaxies. *MNRAS*, 506(2):3024.
- Hernquist, L. and Katz, N., 1989. TREESPH: A Unification of SPH with the Hierarchical Tree Method. *ApJ*, 70:419.
- Heyl, J.S., Cole, S., Frenk, C.S., et al., 1995. Galaxy formation in a variety of hierarchical models. *MNRAS*, 274(3):755.
- Hirano, S., Hosokawa, T., Yoshida, N., et al., 2014. One Hundred First Stars: Protostellar Evolution and the Final Masses. *ApJ*, 781(2):60.
- Ho, I.T., Kewley, L.J., Dopita, M.A., et al., 2014. The SAMI Galaxy Survey: shocks and outflows in a normal star-forming galaxy. *Monthly Notices of the Royal Astronomical Society*, 444(4):3894.
- Hopkins, P.F., Cox, T.J., Dutta, S.N., et al., 2009. Dissipation and Extra Light in Galactic Nuclei. II. “Cusp” Ellipticals. *ApJ*, 181(1):135.
- Hopkins, P.F., Kereš, D., Oñorbe, J., et al., 2014. Galaxies on FIRE (Feedback In Realistic Environments): stellar feedback explains cosmologically inefficient star formation. *MNRAS*, 445(1):581.
- Hopkins, P.F., Wetzell, A., Kereš, D., et al., 2018. How to model supernovae in simulations of star and galaxy formation. *MNRAS*, 477(2):1578.
- Hough, R.T., Rennehan, D., Kobayashi, C., et al., 2023. SIMBA-C: an updated chemical enrichment model for galactic chemical evolution in the SIMBA simulation. *MNRAS*, 525(1):1061.
- Hsu, W.H., Hartmann, L., Allen, L., et al., 2013. Evidence for Environmental Dependence of the Upper Stellar Initial Mass Function in Orion A. *ApJ*, 764(2):114.
- Ibrahim, D. and Kobayashi, C., 2024. The impact of supernova feedback on the mass-metallicity relations. *MNRAS*, 527(2):3276.
- Ibrahim, D. and Kobayashi, C., 2025. The evolution of metallicity gradients in galaxies from cosmological simulations. *arXiv e-prints*, arXiv:2501.11209.
- Ishigaki, M.N., Tominaga, N., Kobayashi, C., et al., 2018. The Initial Mass Function of the First Stars Inferred from Extremely Metal-poor Stars. *ApJ*, 857(1):46.

- Isobe, Y. et al., 2023. . *ApJ*, 959(2):100.
- Jones, T., Ellis, R., Jullo, E., et al., 2010. Measurement of a Metallicity Gradient in a  $z = 2$  Galaxy: Implications for Inside-out Assembly Histories. *ApJ*, 725(2):L176.
- Jones, T., Ellis, R.S., Richard, J., et al., 2013. The Origin and Evolution of Metallicity Gradients: Probing the Mode of Mass Assembly at  $z \sim 2$ . *ApJ*, 765(1):48.
- Ju, M., Wang, X., Jones, T., et al., 2024. MSA-3D: Metallicity Gradients in Galaxies at  $z \sim 1$  with JWST/NIRSpec Slit-stepping Spectroscopy. *arXiv e-prints*, arXiv:2409.01616.
- Karakas, A.I., 2010. Updated stellar yields from asymptotic giant branch models. *MNRAS*, 403(3):1413.
- Karakas, A.I. and Lattanzio, J.C., 2014. The Dawes Review 2: Nucleosynthesis and Stellar Yields of Low- and Intermediate-Mass Single Stars. *Publications of the Astron. Soc. of Australia*, 31:e030.
- Karakas, A.I. and Lugaro, M., 2016. Stellar Yields from Metal-rich Asymptotic Giant Branch Models. *ApJ*, 825(1):26.
- Katz, H., Sijacki, D., and Haehnelt, M.G., 2015. Seeding high-redshift QSOs by collisional runaway in primordial star clusters. *MNRAS*, 451(3):2352.
- Katz, N., 1992. Dissipational Galaxy Formation. II. Effects of Star Formation. *ApJ*, 391:502.
- Kauffmann, G., White, S.D.M., and Guiderdoni, B., 1993. The formation and evolution of galaxies within merging dark matter haloes. *MNRAS*, 264:201.
- Kawata, D. and Gibson, B.K., 2003. GCD+: a new chemodynamical approach to modelling supernovae and chemical enrichment in elliptical galaxies. *MNRAS*, 340(3):908.
- Kay, S.T., Thomas, P.A., and Theuns, T., 2003. The impact of galaxy formation on X-ray groups. *MNRAS*, 343(2):608.
- Keller, S.C., Bessell, M.S., Frebel, A., et al., 2014. A single low-energy, iron-poor supernova as the source of metals in the star SMSS J031300.36-670839.3. *Nature*, 506(7489):463.
- Kewley, L.J. and Dopita, M.A., 2002. Using Strong Lines to Estimate Abundances in Extragalactic H II Regions and Starburst Galaxies. *ApJ*, 142(1):35.
- Kewley, L.J. and Ellison, S.L., 2008. Metallicity Calibrations and the Mass-Metallicity Relation for Star-forming Galaxies. *ApJ*, 681(2):1183.
- Kewley, L.J., Rupke, D., Zahid, H.J., et al., 2010. Metallicity Gradients and Gas Flows in Galaxy Pairs. *ApJ*, 721(1):L48.

- Khoram, A.H. and Belfiore, F., 2024. Direct-method metallicity gradients derived from spectral stacking with SDSS-IV MaNGA. *arXiv e-prints*, arXiv:2410.22407.
- Kimm, T., Cen, R., Devriendt, J., et al., 2015. Towards simulating star formation in turbulent high-z galaxies with mechanical supernova feedback. *MNRAS*, 451(3):2900.
- Kobayashi, C., 2004. GRAPE-SPH chemodynamical simulation of elliptical galaxies - I. Evolution of metallicity gradients. *MNRAS*, 347(3):740.
- Kobayashi, C., 2005. GRAPE-SPH chemodynamical simulation of elliptical galaxies - II. Scaling relations and the fundamental plane. *MNRAS*, 361(4):1216.
- Kobayashi, C., 2022. The role of mass loss in chemodynamical evolution of galaxies. In L. Decin, A. Zijlstra, and C. Gielen, editors, *The Origin of Outflows in Evolved Stars*, volume 366 of *IAU Symposium*, pages 63–82.
- Kobayashi, C. and Arimoto, N., 1999. Gradients of Absorption-Line Strengths in Elliptical Galaxies. *ApJ*, 527(2):573.
- Kobayashi, C. and Ferrara, A., 2024. . *ApJ*, 962(1):L6.
- Kobayashi, C., Karakas, A.I., and Lugaro, M., 2020a. The Origin of Elements from Carbon to Uranium. *ApJ*, 900(2):179.
- Kobayashi, C., Karakas, A.I., and Umeda, H., 2011a. The evolution of isotope ratios in the Milky Way Galaxy. *MNRAS*, 414(4):3231.
- Kobayashi, C., Karakas, A.I., and Umeda, H., 2011b. The evolution of isotope ratios in the Milky Way Galaxy. *MNRAS*, 414(4):3231.
- Kobayashi, C., Leung, S.C., and Nomoto, K., 2020b. New Type Ia Supernova Yields and the Manganese and Nickel Problems in the Milky Way and Dwarf Spheroidal Galaxies. *ApJ*, 895(2):138.
- Kobayashi, C. and Nakasato, N., 2011a. Chemodynamical Simulations of the Milky Way Galaxy. *ApJ*, 729(1):16.
- Kobayashi, C. and Nakasato, N., 2011b. Chemodynamical Simulations of the Milky Way Galaxy. *ApJ*, 729(1):16.
- Kobayashi, C., Springel, V., and White, S.D.M., 2007. Simulations of cosmic chemical enrichment. *Monthly Notices of the Royal Astronomical Society*, 376(4):1465.
- Kobayashi, C. and Taylor, P., 2023. Chemo-Dynamical Evolution of Galaxies. *arXiv e-prints*, arXiv:2302.07255.

- Kobayashi, C., Umeda, H., Nomoto, K., et al., 2006a. Galactic Chemical Evolution: Carbon through Zinc. *ApJ*, 653(2):1145.
- Kobayashi, C., Umeda, H., Nomoto, K., et al., 2006b. Galactic Chemical Evolution: Carbon through Zinc. *ApJ*, 653(2):1145.
- Kodama, T. and Arimoto, N., 1997. Origin of the colour-magnitude relation of elliptical galaxies. *A&A*, 320:41.
- Kormendy, J. and Bender, R., 1996. A Proposed Revision of the Hubble Sequence for Elliptical Galaxies. *ApJ*, 464:L119.
- Kroupa, P., 2008. Initial Conditions for Star Clusters. In S.J. Aarseth, C.A. Tout, and R.A. Mardling, editors, *The Cambridge N-Body Lectures*, volume 760, page 181.
- Kuntschner, H., Emsellem, E., Bacon, R., et al., 2010. The SAURON project – XVII. Stellar population analysis of the absorption line strength maps of 48 early-type galaxies. *Monthly Notices of the Royal Astronomical Society*, 408(1):97.
- Laporte, N., Ellis, R.S., Boone, F., et al., 2017. Dust in the Reionization Era: ALMA Observations of a  $z = 8.38$  Gravitationally Lensed Galaxy. *ApJ*, 837(2):L21.
- Larson, R.B., 1974. Effects of supernovae on the early evolution of galaxies. *MNRAS*, 169:229.
- Larson, R.B., 1976. Models for the formation of disc galaxies. *MNRAS*, 176:31.
- Lattimer, J.M. and Schramm, D.N., 1974. Black-Hole-Neutron-Star Collisions. *ApJ*, 192:L145.
- Leethochawalit, N., Jones, T.A., Ellis, R.S., et al., 2016. A Keck Adaptive Optics Survey of a Representative Sample of Gravitationally Lensed Star-forming Galaxies: High Spatial Resolution Studies of Kinematics and Metallicity Gradients. *ApJ*, 820(2):84.
- Lequeux, J., Peimbert, M., Rayo, J.F., et al., 1979. Chemical Composition and Evolution of Irregular and Blue Compact Galaxies. *A&A*, 80:155.
- Leroy, L., Elbaz, D., Magnelli, B., et al., 2024. The role of stellar mass in the cosmic history of star formation as seen by Herschel and ALMA. *A&A*, 691:A248.
- Li, M., Cai, Z., Bian, F., et al., 2022. The mass-metallicity relation of dwarf galaxies at the cosmic noon in the jwst era.
- Lian, J., Thomas, D., Maraston, C., et al., 2018. The mass-metallicity relations for gas and stars in star-forming galaxies: strong outflow versus variable IMF. *MNRAS*, 474(1):1143.
- Licquia, T.C. and Newman, J.A., 2015. Improved Estimates of the Milky Way's Stellar Mass and Star Formation Rate from Hierarchical Bayesian Meta-Analysis. *ApJ*, 806(1):96.

- Limongi, M. and Chieffi, A., 2018a. . *ApJ*, 237(1):13.
- Limongi, M. and Chieffi, A., 2018b. Presupernova Evolution and Explosive Nucleosynthesis of Rotating Massive Stars in the Metallicity Range  $-3 \leq [\text{Fe}/\text{H}] \leq 0$ . *ApJ*, 237(1):13.
- Lin, Y. and Zu, Y., 2023. Constraints on galactic outflows from the metallicity-stellar mass-SFR relation of EAGLE simulation and SDSS galaxies. *MNRAS*, 521(1):411.
- Lucy, L.B., 1977. A numerical approach to the testing of the fission hypothesis. *AJ*, 82:1013.
- Lugaro, M., Herwig, F., Lattanzio, J.C., et al., 2003. s-Process Nucleosynthesis in Asymptotic Giant Branch Stars: A Test for Stellar Evolution. *ApJ*, 586(2):1305.
- Ma, X., Hopkins, P.F., Faucher-Giguère, C.A., et al., 2016. The origin and evolution of the galaxy mass-metallicity relation. *MNRAS*, 456(2):2140.
- Ma, X., Hopkins, P.F., Feldmann, R., et al., 2017. Why do high-redshift galaxies show diverse gas-phase metallicity gradients? *MNRAS*, 466(4):4780.
- Madau, P. and Dickinson, M., 2014. Cosmic Star-Formation History. *Annual Review of Astronomy and Astrophysics*, 52:415.
- Magrini, L., Stanghellini, L., Corbelli, E., et al., 2010. Metal production in M 33: space and time variations. *A&A*, 512:A63.
- Maiolino, R. and Mannucci, F., 2019. De re metallica: the cosmic chemical evolution of galaxies. *Astronomy and Astrophysics Reviews*, 27(1):3.
- Maiolino, R., Nagao, T., Grazian, A., et al., 2008. AMAZE. I. The evolution of the mass-metallicity relation at  $z > 3$ . *A&A*, 488(2):463.
- Mannucci, F., Cresci, G., Maiolino, R., et al., 2010. A fundamental relation between mass, star formation rate and metallicity in local and high-redshift galaxies. *MNRAS*, 408(4):2115.
- Marchesini, D., Stefanon, M., Brammer, G.B., et al., 2012. The Evolution of the Rest-frame V-band Luminosity Function from  $z = 4$ : A Constant Faint-end Slope over the Last 12 Gyr of Cosmic History. *ApJ*, 748(2):126.
- Marques-Chaves, R. et al., 2024. . *A&A*, 681:A30.
- Martizzi, D., Faucher-Giguère, C.A., and Quataert, E., 2015. Supernova feedback in an inhomogeneous interstellar medium. *MNRAS*, 450(1):504.
- Matteucci, F. and Francois, P., 1989. Galactic chemical evolution : abundance gradients of individual elements. *MNRAS*, 239:885.

- McAlpine, S., Helly, J.C., Schaller, M., et al., 2016. The EAGLE simulations of galaxy formation: Public release of halo and galaxy catalogues. *Astronomy and Computing*, 15:72.
- McClure, R.D. and van den Bergh, S., 1968. Five-color intermediate-band photometry of stars, clusters, and galaxies. *AJ*, 73:313.
- McLeod, D.J., McLure, R.J., Dunlop, J.S., et al., 2021. The evolution of the galaxy stellar-mass function over the last 12 billion years from a combination of ground-based and HST surveys. *MNRAS*, 503(3):4413.
- Mihos, J.C. and Hernquist, L., 1994. Ultraluminous Starbursts in Major Mergers. *ApJ*, 431:L9.
- Mirabel, I.F., Dijkstra, M., Laurent, P., et al., 2011. Stellar black holes at the dawn of the universe. *A&A*, 528:A149.
- Mo, H.J., Mao, S., and White, S.D.M., 1998. The formation of galactic discs. *MNRAS*, 295(2):319.
- Mollá, M. and Díaz, A.I., 2005. A grid of chemical evolution models as a tool to interpret spiral and irregular galaxies data. *MNRAS*, 358(2):521.
- Monaghan, J.J., 2005. Smoothed particle hydrodynamics. *Reports on Progress in Physics*, 68(8):1703.
- Montero-Dorta, A.D. and Prada, F., 2009. The SDSS DR6 luminosity functions of galaxies. *MNRAS*, 399(3):1106.
- Mott, A., Spitoni, E., and Matteucci, F., 2013. Abundance gradients in spiral discs: is the gradient inversion at high redshift real? *MNRAS*, 435(4):2918.
- Mowla, L.A., van Dokkum, P., Brammer, G.B., et al., 2019. COSMOS-DASH: The Evolution of the Galaxy Size-Mass Relation since  $z \sim 3$  from New Wide-field WFC3 Imaging Combined with CANDELS/3D-HST. *ApJ*, 880(1):57.
- Murphy, G.G., Yates, R.M., and Mohamed, S.S., 2022. L-GALAXIES 2020: the formation and chemical evolution of stellar haloes in Milky Way analogues and galaxy clusters. *MNRAS*, 510(2):1945.
- Naab, T., Johansson, P.H., and Ostriker, J.P., 2009. Minor Mergers and the Size Evolution of Elliptical Galaxies. *ApJ*, 699(2):L178.
- Nagele, C. and Umeda, H., 2023. . *ApJ*, 949(1):L16.
- Naidu, R.P., Oesch, P.A., van Dokkum, P., et al., 2022. Two Remarkably Luminous Galaxy Candidates at  $z \approx 10$ -12 Revealed by JWST. *ApJ*, 940(1):L14.

- Nakamura, F. and Umemura, M., 2001. On the IMF of Population III Stars. In M. Umemura and H. Susa, editors, *The Physics of Galaxy Formation*, volume 222 of *Astronomical Society of the Pacific Conference Series*, page 39.
- Nandal, D. et al., 2024. . *A&A*, 683:A156.
- Narayan, R. and White, S.D.M., 1988. Gravitational lensing in a cold dark matter universe. *MNRAS*, 231:97p.
- Navarro, J.F. and White, S.D.M., 1993. Simulations of Dissipative Galaxy Formation in Hierarchically Clustering Universes - Part One - Tests of the Code. *MNRAS*, 265:271.
- Nishimura, N., Takiwaki, T., and Thielemann, F.K., 2015. The r-process Nucleosynthesis in the Various Jet-like Explosions of Magnetorotational Core-collapse Supernovae. *ApJ*, 810(2):109.
- Noeske, K.G., Weiner, B.J., Faber, S.M., et al., 2007. Star Formation in AEGIS Field Galaxies since  $z=1.1$ : The Dominance of Gradually Declining Star Formation, and the Main Sequence of Star-forming Galaxies. *ApJ*, 660(1):L43.
- Nomoto, K., Kobayashi, C., and Tominaga, N., 2013. Nucleosynthesis in Stars and the Chemical Enrichment of Galaxies. *Annual Review of Astronomy and Astrophysics*, 51(1):457.
- Nomoto, K., Tominaga, N., Umeda, H., et al., 2006. Nucleosynthesis yields of core-collapse supernovae and hypernovae, and galactic chemical evolution. *Nuclear Physics A*, 777:424.
- Nordlander, T., Amarsi, A.M., Lind, K., et al., 2017. 3D NLTE analysis of the most iron-deficient star, SMSS0313-6708. *A&A*, 597:A6.
- O'Shea, B.W., Nagamine, K., Springel, V., et al., 2005. Comparing AMR and SPH Cosmological Simulations. I. Dark Matter and Adiabatic Simulations. *ApJ*, 160(1):1.
- Padawer-Blatt, A., Shao, Z., Hough, R.T., et al., 2025. Core to Cosmic Edge: SIMBA-C's New Take on Abundance Profiles in the Intragroup Medium at  $z = 0$ . *Universe*, 11(2):47.
- Pallottini, A., Ferrara, A., Bovino, S., et al., 2017. The impact of chemistry on the structure of high- $z$  galaxies. *MNRAS*, 471(4):4128.
- Péroux, C. and Howk, J.C., 2020. The Cosmic Baryon and Metal Cycles. *Annual Review of Astronomy and Astrophysics*, 58:363.
- Pilkington, K., Few, C.G., Gibson, B.K., et al., 2012. Metallicity gradients in disks. Do galaxies form inside-out? *A&A*, 540:A56.
- Pillepich, A., Springel, V., Nelson, D., et al., 2018. Simulating galaxy formation with the IllustrisTNG model. *MNRAS*, 473(3):4077.

- Pitrou, C., Coc, A., Uzan, J.P., et al., 2018. Precision big bang nucleosynthesis with improved Helium-4 predictions. *Physics Reports*, 754:1.
- Planck Collaboration, 2020. Planck 2018 results: Vi. cosmological parameters. *Astronomy and Astrophysics*, 641.
- Planck Collaboration, Aghanim, N., Akrami, Y., et al., 2020. Planck 2018 results. VI. Cosmological parameters. *A&A*, 641:A6.
- Poetrodjojo, H., Groves, B., Kewley, L.J., et al., 2018. The SAMI Galaxy Survey: Spatially resolved metallicity and ionization mapping. *MNRAS*, 479(4):5235.
- Poetrodjojo, H., Groves, B., Kewley, L.J., et al., 2021. The SAMI Galaxy Survey: reconciling strong emission line metallicity diagnostics using metallicity gradients. *MNRAS*, 502(3):3357.
- Portinari, L. and Chiosi, C., 1999. On star formation and chemical evolution in the Galactic disc. *A&A*, 350:827.
- Prantzos, N. and Boissier, S., 2000. Chemo-spectrophotometric evolution of spiral galaxies - III. Abundance and colour gradients in discs. *MNRAS*, 313(2):338.
- Press, W.H. and Schechter, P., 1974. Formation of Galaxies and Clusters of Galaxies by Self-Similar Gravitational Condensation. *ApJ*, 187:425.
- Qian, Y.Z. and Wasserburg, G.J., 2007. Where, oh where has the r-process gone? *Physics Reports*, 442(1-6):237.
- Qian, Y.Z. and Woosley, S.E., 1996. Nucleosynthesis in Neutrino-driven Winds. I. The Physical Conditions. *Astrophysical Journal*, 471:331.
- Queyrel, J., Contini, T., Kissler-Patig, M., et al., 2012. MASSIV: Mass Assembly Survey with SINFONI in VVDS. III. Evidence for positive metallicity gradients in  $z \sim 1.2$  star-forming galaxies. *A&A*, 539:A93.
- Rees, M.J. and Ostriker, J.P., 1977. Cooling, dynamics and fragmentation of massive gas clouds: clues to the masses and radii of galaxies and clusters. *MNRAS*, 179:541.
- Renzini, A. and Peng, Y.j., 2015. An Objective Definition for the Main Sequence of Star-forming Galaxies. *ApJ*, 801(2):L29.
- Rich, J.A., Torrey, P., Kewley, L.J., et al., 2012. An Integral Field Study of Abundance Gradients in nearby Luminous Infrared Galaxies. *ApJ*, 753(1):5.
- Robertson, B.E., 2022. Galaxy Formation and Reionization: Key Unknowns and Expected Breakthroughs by the James Webb Space Telescope. *Annual Review of Astronomy and Astrophysics*, 60:121.

- Rogers, N.S.J., Strom, A.L., Rudie, G.C., et al., 2024. CECILIA: Direct O, N, S, and Ar Abundances in Q2343-D40, a Galaxy at  $z \sim 3$ . *ApJ*, 964(1):L12.
- Rossi, M., Salvadori, S., and Skúladóttir, Á., 2021. Ultra-faint dwarf galaxies: unveiling the minimum mass of the first stars. *MNRAS*, 503(4):6026.
- Samland, M., Hensler, G., and Theis, C., 1997. Modeling the Evolution of Disk Galaxies. I. The Chemodynamical Method and the Galaxy Model. *ApJ*, 476(2):544.
- Sánchez, S.F., Kennicutt, R.C., Gil de Paz, A., et al., 2012. CALIFA, the Calar Alto Legacy Integral Field Area survey. I. Survey presentation. *A&A*, 538:A8.
- Sánchez, S.F., Rosales-Ortega, F.F., Iglesias-Páramo, J., et al., 2014. A characteristic oxygen abundance gradient in galaxy disks unveiled with CALIFA. *A&A*, 563:A49.
- Sánchez Almeida, J., Caon, N., Muñoz-Tuñón, C., et al., 2018. Local anticorrelation between star formation rate and gas-phase metallicity in disc galaxies. *MNRAS*, 476(4):4765.
- Sánchez-Blázquez, P., Rosales-Ortega, F.F., Méndez-Abreu, J., et al., 2014. Stellar population gradients in galaxy discs from the CALIFA survey. The influence of bars. *A&A*, 570:A6.
- Sánchez-Menguiano, L., Sánchez, S.F., Pérez, I., et al., 2016. Shape of the oxygen abundance profiles in CALIFA face-on spiral galaxies. *A&A*, 587:A70.
- Sánchez-Menguiano, L., Sánchez, S.F., Pérez, I., et al., 2018. The shape of oxygen abundance profiles explored with MUSE: evidence for widespread deviations from single gradients. *A&A*, 609:A119.
- Sanders, R.L., Shapley, A.E., Jones, T., et al., 2021. The MOSDEF Survey: The Evolution of the Mass-Metallicity Relation from  $z = 0$  to  $z 3.3$ . *ApJ*, 914(1):19.
- Savaglio, S., Glazebrook, K., Le Borgne, D., et al., 2005. The Gemini Deep Deep Survey. VII. The Redshift Evolution of the Mass-Metallicity Relation. *ApJ*, 635(1):260.
- Schaerer, D., Marques-Chaves, R., Xiao, M., et al., 2024a. Discovery of a new N-emitter in the epoch of reionization. *A&A*, 687:L11.
- Schaerer, D. et al., 2024b. . *A&A*, 687:L11.
- Schaye, J., Crain, R.A., Bower, R.G., et al., 2015. The EAGLE project: simulating the evolution and assembly of galaxies and their environments. *MNRAS*, 446(1):521.
- Schechter, P., 1976. An analytic expression for the luminosity function for galaxies. *ApJ*, 203:297.
- Searle, L., 1971. Evidence for Composition Gradients across the Disks of Spiral Galaxies. *ApJ*, 168:327.

- Sedov, L.I., 1959. *Similarity and Dimensional Methods in Mechanics*.
- Senchyna, P. et al., 2024. . *ApJ*, 966(1):92.
- Sharda, P., Ginzburg, O., Krumholz, M.R., et al., 2024. The interplay between feedback, accretion, transport, and winds in setting gas-phase metal distribution in galaxies. *MNRAS*, 528(2):2232.
- Sharda, P., Krumholz, M.R., Wisnioski, E., et al., 2021. On the origin of the mass-metallicity gradient relation in the local Universe. *MNRAS*, 504(1):53.
- Sharples, R., Bender, R., Agudo Berbel, A., et al., 2013. First Light for the KMOS Multi-Object Integral-Field Spectrometer. *The Messenger*, 151:21.
- Silk, J., 2013. Unleashing Positive Feedback: Linking the Rates of Star Formation, Supermassive Black Hole Accretion, and Outflows in Distant Galaxies. *ApJ*, 772(2):112.
- Simons, R.C., Papovich, C., Momcheva, I., et al., 2021. CLEAR: The Gas-phase Metallicity Gradients of Star-forming Galaxies at  $0.6 < z < 2.6$ . *ApJ*, 923(2):203.
- Smith, M.C., Sijacki, D., and Shen, S., 2018. Supernova feedback in numerical simulations of galaxy formation: separating physics from numerics. *MNRAS*, 478(1):302.
- Somerville, R.S. and Davé, R., 2015. Physical Models of Galaxy Formation in a Cosmological Framework. *Annual Review of Astronomy and Astrophysics*, 53:51.
- Somerville, R.S., Lee, K., Ferguson, H.C., et al., 2004. Cosmic Variance in the Great Observatories Origins Deep Survey. *ApJ*, 600(2):L171.
- Speagle, J.S., Steinhardt, C.L., Capak, P.L., et al., 2014. A Highly Consistent Framework for the Evolution of the Star-Forming “Main Sequence” from  $z \sim 0-6$ . *ApJ*, 214(2):15.
- Spolaor, M., Kobayashi, C., Forbes, D.A., et al., 2010. . *Monthly Notices of the Royal Astronomical Society*, 408(1):272.
- Springel, V., Di Matteo, T., and Hernquist, L., 2005. Modelling feedback from stars and black holes in galaxy mergers. *MNRAS*, 361(3):776.
- Springel, V. and Hernquist, L., 2002. Cosmological smoothed particle hydrodynamics simulations: the entropy equation. *MNRAS*, 333(3):649.
- Springel, V. and Hernquist, L., 2003. Cosmological smoothed particle hydrodynamics simulations: a hybrid multiphase model for star formation. *MNRAS*, 339(2):289.
- Springel, V., Pakmor, R., Pillepich, A., et al., 2018. First results from the IllustrisTNG simulations: matter and galaxy clustering. *MNRAS*, 475(1):676.

- Springel, V., White, S.D.M., Tormen, G., et al., 2001a. Populating a cluster of galaxies - I. Results at  $z=0$ . *MNRAS*, 328(3):726.
- Springel, V., Yoshida, N., and White, S.D.M., 2001b. GADGET: a code for collisionless and gasdynamical cosmological simulations. *NewA*, 6(2):79.
- Stacy, A. and Bromm, V., 2013. Constraining the statistics of Population III binaries. *MNRAS*, 433(2):1094.
- Stanghellini, L. and Haywood, M., 2010. The Galactic Structure and Chemical Evolution Traced by the Population of Planetary Nebulae. *ApJ*, 714(2):1096.
- Stanway, E.R. and Eldridge, J.J., 2018. Re-evaluating old stellar populations. *MNRAS*, 479(1):75.
- Stefanon, M., Bouwens, R.J., Labbé, I., et al., 2021. Galaxy Stellar Mass Functions from  $z=10$  to  $z=6$  using the Deepest Spitzer/Infrared Array Camera Data: No Significant Evolution in the Stellar-to-halo Mass Ratio of Galaxies in the First Gigayear of Cosmic Time. *ApJ*, 922(1):29.
- Stevens, A.R.H., Sinha, M., Rohl, A., et al., 2024. DARK SAGE: Next-generation semi-analytic galaxy evolution with multidimensional structure and minimal free parameters. *Publications of the Astron. Soc. of Australia*, 41:e053.
- Stott, J.P., Sobral, D., Swinbank, A.M., et al., 2014a. A relationship between specific star formation rate and metallicity gradient within  $z \sim 1$  galaxies from KMOS-HiZELS. *MNRAS*, 443(3):2695.
- Stott, J.P., Sobral, D., Swinbank, A.M., et al., 2014b. A relationship between specific star formation rate and metallicity gradient within  $z \sim 1$  galaxies from KMOS-HiZELS. *MNRAS*, 443(3):2695.
- Sutherland, R.S. and Dopita, M.A., 1993. Cooling Functions for Low-Density Astrophysical Plasmas. *ApJ*, 88:253.
- Swinbank, A.M., Sobral, D., Smail, I., et al., 2012. The properties of the star-forming interstellar medium at  $z=0.84-2.23$  from HiZELS: mapping the internal dynamics and metallicity gradients in high-redshift disc galaxies. *MNRAS*, 426(2):935.
- Symbalisty, E. and Schramm, D.N., 1982. Neutron Star Collisions and the r-Process. *Astrophysics Letters*, 22:143.
- Symbalisty, E.M.D., 1984. Magnetorotational iron core collapse. *Astrophysical Journal*, 285:729.
- Tacchella, S., Finkelstein, S.L., Bagley, M., et al., 2022. On the Stellar Populations of Galaxies at  $z=9-11$ : The Growth of Metals and Stellar Mass at Early Times. *ApJ*, 927(2):170.
- Takahashi, K. et al., 2018. . *ApJ*, 857(2):111.

- Tapia-Contreras, B., Tissera, P.B., Sillero, E., et al., 2025. Insight into the physical processes that shape the metallicity profiles in galaxies. *arXiv e-prints*, arXiv:2502.02080.
- Taylor, G., 1950. The Formation of a Blast Wave by a Very Intense Explosion. I. Theoretical Discussion. *Proceedings of the Royal Society of London Series A*, 201(1065):159.
- Taylor, P. and Kobayashi, C., 2014. Seeding black holes in cosmological simulations. *MNRAS*, 442(3):2751.
- Taylor, P. and Kobayashi, C., 2015. The effects of AGN feedback on present-day galaxy properties in cosmological simulations. *MNRAS*, 448(2):1835.
- Taylor, P. and Kobayashi, C., 2016. Time evolution of galaxy scaling relations in cosmological simulations. *MNRAS*, 463(3):2465.
- Taylor, P. and Kobayashi, C., 2017. The metallicity and elemental abundance gradients of simulated galaxies and their environmental dependence. *MNRAS*, 471(4):3856.
- Taylor, P., Kobayashi, C., and Kewley, L.J., 2020. Oxygen loss from simulated galaxies and the metal flow main sequence: predicting the dependence on mass and environment. *MNRAS*, 496(4):4433.
- Tegmark, M., Silk, J., Rees, M.J., et al., 1997. How Small Were the First Cosmological Objects? *ApJ*, 474:1.
- Tinsley, B.M., 1980. Evolution of the Stars and Gas in Galaxies. *Fundamental Cosmic Physics*, 5:287.
- Tissera, P.B., Rosas-Guevara, Y., Sillero, E., et al., 2022. The evolution of the oxygen abundance gradients in star-forming galaxies in the EAGLE simulations. *MNRAS*, 511(2):1667.
- Tomczak, A.R., Quadri, R.F., Tran, K.V.H., et al., 2014. Galaxy Stellar Mass Functions from ZFOURGE/CANDELS: An Excess of Low-mass Galaxies since  $z = 2$  and the Rapid Buildup of Quiescent Galaxies. *ApJ*, 783(2):85.
- Topping, M.W., Stark, D.P., Senchyna, P., et al., 2024a. Metal-poor star formation at  $z > 6$  with JWST: new insight into hard radiation fields and nitrogen enrichment on 20 pc scales. *MNRAS*, 529(4):3301.
- Topping, M.W. et al., 2024b. . *MNRAS*, 529(4):3301.
- Torrey, P., Vogelsberger, M., Marinacci, F., et al., 2019. The evolution of the mass-metallicity relation and its scatter in IllustrisTNG. *MNRAS*, 484(4):5587.
- Tremonti, C.A., Heckman, T.M., Kauffmann, G., et al., 2004. The Origin of the Mass-Metallicity Relation: Insights from 53,000 Star-forming Galaxies in the Sloan Digital Sky Survey. *ApJ*, 613(2):898.

- Trujillo-Gomez, S., Klypin, A., Primack, J., et al., 2011. Galaxies in  $\Lambda$ CDM with Halo Abundance Matching: Luminosity-Velocity Relation, Baryonic Mass-Velocity Relation, Velocity Function, and Clustering. *ApJ*, 742(1):16.
- Umeda, H. and Nomoto, K., 2002. Nucleosynthesis of Zinc and Iron Peak Elements in Population III Type II Supernovae: Comparison with Abundances of Very Metal Poor Halo Stars. *ApJ*, 565(1):385.
- van der Wel, A., Franx, M., van Dokkum, P.G., et al., 2014. 3D-HST+CANDELS: The Evolution of the Galaxy Size-Mass Distribution since  $z = 3$ . *ApJ*, 788(1):28.
- Venturi, G., Carniani, S., Parlanti, E., et al., 2024. Gas-phase metallicity gradients in galaxies at  $z \sim 6 - 8$ . *arXiv e-prints*, arXiv:2403.03977.
- Vincenzo, F. and Kobayashi, C., 2018. . *MNRAS*, 478(1):155.
- Vincenzo, F. and Kobayashi, C., 2020. Stellar migrations and metal flows - Chemical evolution of the thin disc of a simulated Milky Way analogous galaxy. *MNRAS*, 496(1):80.
- Vink, J.S., 2022. Theory and Diagnostics of Hot Star Mass Loss. *Annual Review of Astronomy and Astrophysics*, 60:203.
- Vogelsberger, M., Genel, S., Springel, V., et al., 2014. Introducing the Illustris Project: simulating the coevolution of dark and visible matter in the Universe. *MNRAS*, 444(2):1518.
- Wanajo, S., Janka, H.T., and Kubono, S., 2011. Uncertainties in the  $\nu p$ -process: Supernova Dynamics Versus Nuclear Physics. *ApJ*, 729(1):46.
- Wanajo, S., Sekiguchi, Y., Nishimura, N., et al., 2014. Production of All the r-process Nuclides in the Dynamical Ejecta of Neutron Star Mergers. *ApJ*, 789(2):L39.
- Wang, X., Jones, T., Vulcani, B., et al., 2022. Early Results from GLASS-JWST. IV. Spatially Resolved Metallicity in a Low-mass  $z = 3$  Galaxy with NIRISS. *ApJ*, 938(2):L16.
- Wang, X., Jones, T.A., Treu, T., et al., 2017. The Grism Lens-amplified Survey from Space (GLASS). X. Sub-kiloparsec Resolution Gas-phase Metallicity Maps at Cosmic Noon behind the Hubble Frontier Fields Cluster MACS1149.6+2223. *ApJ*, 837(1):89.
- Ward, E., de la Vega, A., Mobasher, B., et al., 2024. Evolution of the Size–Mass Relation of Star-forming Galaxies Since  $z = 5.5$  Revealed by CEERS. *ApJ*, 962(2):176.
- Watanabe, K., Ouchi, M., Nakajima, K., et al., 2024. EMPRESS. XIII. Chemical Enrichment of Young Galaxies Near and Far at  $z \sim 0$  and 4–10: Fe/O, Ar/O, S/O, and N/O Measurements with a Comparison of Chemical Evolution Models. *ApJ*, 962(1):50.

- Whitaker, K.E., van Dokkum, P.G., Brammer, G., et al., 2012. The Star Formation Mass Sequence Out to  $z = 2.5$ . *ApJ*, 754(2):L29.
- White, S.D.M., 1978. Simulations of merging galaxies. *MNRAS*, 184:185.
- White, S.D.M. and Frenk, C.S., 1991. Galaxy Formation through Hierarchical Clustering. *ApJ*, 379:52.
- White, S.D.M. and Rees, M.J., 1978. Core condensation in heavy halos: a two-stage theory for galaxy formation and clustering. *MNRAS*, 183:341.
- Worthey, G., Faber, S.M., and Gonzalez, J.J., 1992. MG and Fe Absorption Features in Elliptical Galaxies. *ApJ*, 398:69.
- Wuyts, E., Wisnioski, E., Fossati, M., et al., 2016. The Evolution of Metallicity and Metallicity Gradients from  $z = 2.7$  to 0.6 with KMOS<sup>3D</sup>. *ApJ*, 827(1):74.
- Yabe, K., Ohta, K., Iwamuro, F., et al., 2012. NIR Spectroscopy of Star-Forming Galaxies at  $z \sim 1.4$  with Subaru/FMOS: The Mass-Metallicity Relation. *Publications of the ASJ*, 64:60.
- Yates, R.M., Henriques, B.M.B., Fu, J., et al., 2021. L-GALAXIES 2020: The evolution of radial metallicity profiles and global metallicities in disc galaxies. *MNRAS*, 503(3):4474.
- Yates, R.M. and Kauffmann, G., 2014. Dilution in elliptical galaxies: implications for the relation between metallicity, stellar mass and star formation rate. *MNRAS*, 439(4):3817.
- Yoshida, N., Abel, T., Hernquist, L., et al., 2003. Simulations of Early Structure Formation: Primordial Gas Clouds. *ApJ*, 592(2):645.
- Yuan, T.T., Kewley, L.J., Swinbank, A.M., et al., 2011. Metallicity Gradient of a Lensed Face-on Spiral Galaxy at Redshift 1.49. *ApJ*, 732(1):L14.
- Zahid, H.J., Kudritzki, R.P., Conroy, C., et al., 2017. Stellar Absorption Line Analysis of Local Star-forming Galaxies: The Relation between Stellar Mass, Metallicity, Dust Attenuation, and Star Formation Rate. *ApJ*, 847(1):18.
- Zaritsky, D., Kennicutt, Robert C., J., and Huchra, J.P., 1994. H II Regions and the Abundance Properties of Spiral Galaxies. *ApJ*, 420:87.
- Zheng, Z., Wang, H., Ge, J., et al., 2017. SDSS-IV MaNGA: environmental dependence of stellar age and metallicity gradients in nearby galaxies. *MNRAS*, 465(4):4572.